



The Influence of Ride Control Systems on the Motion and Load Response of a Hydroelastic Segmented Catamaran Model

by

Javad AlaviMehr

B.E., Persian Gulf University (2003)

M.E., Sharif University of Technology (2005)

Submitted in fulfilment of the requirements for the degree of
Doctor of Philosophy

at the

UNIVERSITY OF TASMANIA

August 2016

Statement of Originality and Authority of Access

This thesis contains no material that has been accepted for a degree or diploma by the University of Tasmania or any other institution, and to the best of my knowledge and belief no material previously published or written by another person except where due acknowledgement is made in the text of the thesis.

The thesis is not to be made available for loan or copying for two years following the date this statement was signed. Following that time the thesis may be made available for loan and limited copying in accordance with the *Copyright Act 1968*, but only subject to the confidentiality agreement in place between the University of Tasmania, INCAT Tasmania and Revolution Design.

Javad AlaviMehr

Abstract

The operation of high-speed catamarans in large waves can produce significant vessel motions that can lead to passenger discomfort as well as extreme loadings during full bow immersion and wave slam impact. This not only can generate large bending loads on the hull structure but also has significant effects on the fatigue life of the vessel. These large loads and motions can be effectively reduced through the implementation of a Ride Control System (RCS) that can significantly reduce the extreme loads sustained by the hull girder and reduce the incidence of motion sickness for passengers on-board the vessel. Although ride control systems have been implemented on full-scale catamaran vessels, the parameters that influence the response have not been previously quantified partly due to the limitations of testing at full-scale. To accurately investigate these parameters it is needed to undergo testing in controlled conditions and to this end a 2.5 m scaled catamaran model has been developed with an active ride control system based on the 112 m INCAT catamaran to investigate the system parameters influencing the response of the vessel. The 2.5 m hydroelastic segmented catamaran model was set-up with an active T-Foil and stern tab ride control system specifically for towing tank testing at the Australian Maritime College (AMC) to determine the motions and loads response in headseas. Step and frequency responses of the ride control system were first investigated by calm water open-loop tests to determine the control gains needed for closed-loop active control tests. Appropriate combinations of the control surface deflections were then determined to produce pure heave and pure pitch response forming the basis for setting the gains of the ride control system to implement different control algorithms in terms of the heave and pitch motions in encountered waves. Two hydrostatic methods were applied to predict the T-Foil and stern tab responses based on a static load experiment and a hydrostatic prediction and there was close agreement between the two outcomes. This was extended by a dynamic prediction of the response of the moving model based on a two degree of freedom rigid body analysis using strip theory. A series of model tests in head seas at different wave heights and frequencies was then undertaken at the AMC towing tank for different ride control conditions including without RCS, passive RCS and active RCS to measure the heave and pitch motions as well as the centre bow slam force and the demihull slam induced bending moments. Three different ride control algorithms of heave control, local control and pitch control were developed to activate the model scale ride control surfaces in a closed loop control system configuration. The response amplitude operators (RAOs) as well as the response phase operators (RPOs) of the model were evaluated from the heave and pitch data. In addition to the RAOs and RPOs, the amplitude and phase of control surfaces were analysed in order to present the range of control surface deflection as well as the phase lag between the control surfaces deflection and the model motions. Comparing the results of the model without RCS with the results of the model with a passive RCS it was found that the deployment of the T-Foil to a fixed position and acting as a passive control surface reduces the peak heave and pitch motions. As expected heave

and pitch were more strongly reduced by their respective control algorithms. This was more evident in the pitch control mode where it significantly reduced the pitch RAO. The centre bow slam force and the demihull slam induced bending moments were also significantly reduced by implementing the pitch control mode. The motion and load results obtained through this unique and comprehensive investigation of a catamaran model fitted with the model scale ride control system have clearly demonstrated the positive effects of using improved ride control algorithms on the vessel motions and loads response. This consequently has a direct impact on the design of future catamaran vessels allowing ship designers to optimise the structural design of the vessel whilst improving passenger comfort and reducing the incidence of motion sickness in particular when operating in larger waves.

Acknowledgements

I would like to express my acknowledgement towards all my friends and colleagues at the University of Tasmania, University College London, Australian Maritime College, Revolution Design and INCAT Tasmania for their assistance, support and encouragement during the course of this project. In particular, I would like to thank the following people:

- Dr Jason Lavroff at the University of Tasmania for his valuable support, enthusiasm, encouragement and technical input throughout the project.
- Professor Mike Davis at the University of Tasmania for his valuable guidance, excellent technical input, professional experiences, intelligent suggestions and great project direction. Professor Mike Davis has been a great source of assistance during the course of this project and it is just simple to say without his support a significant part of this project would not have seen the light.
- Dr Damien Holloway at the University of Tasmania for his valuable technical input and great assistance in writing of thesis and academic papers.
- Professor Giles Thomas at the University College London for his valuable technical input and great assistance in writing of thesis and academic papers.

I would like to extend my special thanks to those people who assisted with the instrumentation, manufacturing, programming and testing of the hydroelastic segmented catamaran model. In particular, I would like to acknowledge Peter Seward, Calverly Gerard, James Lamont, Bernard Chenery, David Morley and Andrew Bylett at the University of Tasmania and also Dr Walid Amin, Gregor Macfarlane, Kirk Myer and Tim Lilienthal at the Australian Maritime College towing tank.

I would also like to thank my friends at the University of Tasmania and Australian Maritime College who were all involved with this project through different PhD research topics. In particular, I would like to make a special mention of Jason McVicar, Jalal R. Shahraki, Babak Shabani and Gary Davidson.

Finally, I would like to thank my partner Sima for her motivation and support throughout the whole course of the project, my parents for their great support throughout my whole life, my brothers for their moral support and my little son Nickan who has been a source of great strength and inspiration.

This research project was in collaboration between the University of Tasmania, Australian Maritime College, Revolution Design and INCAT Tasmania. The support of the Australian Research Council and INCAT Tasmania is gratefully acknowledged.

Contents

1	Introduction	1
1.1	Background	1
1.1.1	Wave loads on catamarans	2
1.1.2	Ride control systems	3
1.1.3	Research objectives	7
1.2	Scope of work	8
2	Hydroelastic Segmented Catamaran Model Set-up	10
2.1	Introduction	10
2.2	Centre bow calibration and modification	11
2.2.1	Introduction	11
2.2.2	Review and modification of the existing instrumentation	16
2.2.3	Calibration tests	28
2.3	Conclusions	32
3	Low Reynolds Number Performance of a Model Scale T-Foil	34
3.1	Introduction	34
3.2	Apparatus and instrumentation	36
3.3	Calibration	40
3.4	Experimental tests and results	42
3.5	Comparison of test results with aerofoil theory and data	46
3.5.1	Static tests	46
3.5.2	Dynamic tests	49
3.6	Conclusions	55
4	Open-Loop Responses of the Catamaran Model to the Ride Control System	57
4.1	Introduction	57
4.2	Theoretical prediction of model responses	58
4.2.1	Hydrostatic determination of steady state step response	58
4.2.2	Dynamic prediction of response of moving model using strip theory	61
4.3	Model set-up and instrumentation	64

4.4	Step responses results	68
4.5	Frequency responses results	84
4.5.1	Amplitude responses	84
4.5.2	Phase responses	85
4.6	Conclusions	89
5	Closed-Loop Influence of the Ride Control System on the Model Motion Responses	91
5.1	Introduction	91
5.2	Ride control algorithms	91
5.2.1	Pitch control	93
5.2.2	Heave control	94
5.2.3	Local control	95
5.2.4	Nonlinear control algorithms	95
5.3	Motion tests and analysis	96
5.4	Ride control system motions response	99
5.4.1	Uncertainty analysis	99
5.4.2	Response Amplitude Operators (RAOs)	99
5.4.3	Response Phase Operators (RPOs)	101
5.4.4	Acceleration response	110
5.4.5	Control surface response amplitude	111
5.5	Conclusions	118
6	Closed-Loop Influence of the Ride Control System on the Model Load Responses	120
6.1	Introduction	120
6.2	Time record data analysis	121
6.3	Dynamic structural loads analysis	124
6.3.1	Centre bow slamming forces	126
6.3.2	Demihull slam induced bending moments	139
6.4	Slamming kinematics data analysis	149
6.4.1	Relative bow immersion	151
6.4.2	Relative bow velocity	151
6.4.3	Slam duration and impulse	156
6.5	Slam induced strain energy analysis	158
6.5.1	Peak strain energy of the centre bow elastic links	159
6.5.2	Peak strain energy of the demihull elastic links	159
6.5.3	Total peak strain energy of the centre bow and demihull elastic links . . .	159
6.6	Conclusions	163

7	Conclusions	164
7.1	Summary	164
7.1.1	Steady and unsteady lift performance of low Reynolds number T-Foil . .	164
7.1.2	Open-loop hull step and frequency responses to control actions in calm water	165
7.1.3	Motion responses to waves with feedback ride control	167
7.1.4	Load responses to waves with feedback ride control	168
7.1.5	Key outcome	169
7.2	Recommendations for future work	169

List of Figures

1.1	INCAT Tasmania 112 m wave-piercing catamaran: Hull 066 - KatExpress 1. . . .	1
1.2	INCAT Tasmania 112 m wave-piercing catamaran: Hull 067 - KatExpress 2. . . .	2
1.3	Location of the T-Foil and the trim tabs on a 112 m INCAT Tasmania high-speed wave-piercing catamaran.	4
1.4	Full scale T-Foil prior to installation on a 112 m INCAT Tasmania high-speed wave-piercing catamaran.	5
1.5	Schematic diagram of a retractable T-Foil.	5
2.1	Schematic diagram of hydroelastic segmented catamaran model.	11
2.2	Elastic link used to connect the segments.	12
2.3	National Instruments Compact RIO.	12
2.4	Schematic diagram of the centre bow transverse beam showing the force acting on each beam.	13
2.5	Schematic diagram of the centre bow transverse beams for the evaluation of the total force acting on the centre bow and its location.	13
2.6	The model set-up on a horizontal flat bench for calibration.	14
2.7	Loading beam installed on the centre bow to apply load at six positions.	15
2.8	Locations of the applied calibration loads on the model.	15
2.9	Photograph of an elastic link instrumented with strain gauges.	16
2.10	Raw strain gauge data for calibration loads applied at the aft transverse beam. .	17
2.11	Photograph of the new strain gauge installed on the aft starboard elastic links. .	18
2.12	Differential microstrain acquired by cRIO chassis using NI 9237 modules showing about 120 microstrain noise during acquisition time.	18
2.13	Photograph of the new NI 9174-USB cDAQ chassis with four NI modules consisting of one NI 9263 AO, one NI 9201 AI and two NI 9237 strain gauge modules. .	19
2.14	Differential microstrain acquired by the new NI cDAQ chassis using the new NI 9237 Modules showing 3-4 microstrain noise during the acquisition time.	20
2.15	Centre bow calibration results: measured load as a function of the calibration applied load.	21
2.16	Distance of the measured loads from the aft transverse beam vs distance of the applied loads from the aft transverse beam.	21

2.17	Bent shape of the transverse beam showing the induced sideways force.	22
2.18	Schematic diagram of the transverse beams and backbone beams: (a) unloaded. (b) loaded and deformed.	22
2.19	Schematic diagram of the transverse beam showing induced force and bending moment.	24
2.20	Schematic diagram of the horizontal slot on the pin bush.	24
2.21	Photograph of the 1 mm horizontal slot on the pin bush.	24
2.22	CAD design of the new pin joint mount.	25
2.23	Photograph of the manufactured new pin joint mount - Part 1 which was mounted on the backbone beam.	25
2.24	Photograph of the manufactured new pin joint mount - Part 2 which was mounted on the transverse beam.	26
2.25	Photograph of the previous pin joint mount (left) and the new pin joint mount (right) - Part 1 which was mounted on the backbone beam.	26
2.26	Photograph of the previous pin joint mount (left) and the new pin joint mount (right) - Part 2 which was mounted on the transverse beam.	27
2.27	Photograph of the new pin joint mounts installed on the centre bow.	27
2.28	Catamaran model centre bow calibration results by using the new instrumenta- tion: measured load as a function of the calibration applied load.	29
2.29	Catamaran model centre bow calibration results by using the new instrumenta- tion: corrected measured load as a function of the calibration applied load. . . .	31
2.30	Distance of the corrected measured loads from the aft transverse beam vs distance of the applied load from the aft transverse beam.	31
3.1	Electrically activated model scale T-Foil developed for the 2.5 m hydroelastic segmented catamaran model.	35
3.2	University of Tasmania water tunnel.	37
3.3	Circulating water tunnel flow constriction flap (flow is from left to right). . . .	37
3.4	AMTI 6 DOF load cell-Model MC3A-100.	38
3.5	Load cell set-up on top of the T-Foil.	39
3.6	T-Foil and load cell set-up in the circulating water tunnel (flow is left to right). .	39
3.7	Relationship between T-Foil angle of attack and output voltage from the poten- tiometer.	40
3.8	Relationship between T-Foil angle of attack and input voltage to the servo-motor.	41
3.9	Relationship between lift force and load-cell output voltage measuring force in the vertical z-axis direction, F_z	41
3.10	Relationship between drag force and load-cell output voltage measuring force in the horizontal y-axis direction, F_y	42

3.11	Lift force measured on the T-Foil at fixed angles of attack for static tests undertaken at water flow velocities of 1.82 m/s, 2.30 m/s and 2.70 m/s.	43
3.12	Drag force measured on the T-Foil at fixed angles of attack for static tests undertaken at water flow velocities of 1.82 m/s, 2.30 m/s and 2.70 m/s.	43
3.13	Lift (L), and Drag (D), forces measured at a flow velocity of 1.82 m/s, frequency of 1.5 Hz and demand T-Foil incidence (α) range of $\pm 15^\circ$	44
3.14	Ratio of measured angle of attack to demand angle of attack at three flow velocities of 1.82 m/s, 2.30 m/s and 2.70 m/s and also three demand T-Foil incidence (α) ranges of $\pm 15^\circ$, $\pm 10^\circ$ and $\pm 5^\circ$	45
3.15	Phase lag at three flow velocities of 1.82 m/s, 2.30 m/s and 2.70 m/s and also three demand T-Foil incidence (α) ranges of $\pm 15^\circ$, $\pm 10^\circ$ and $\pm 5^\circ$	46
3.16	T-Foil static lift coefficient at different angles of attack and water flow velocities of 1.82 m/s, 2.30 m/s and 2.70 m/s.	47
3.17	T-Foil static drag coefficient at different angles of attack and water flow velocities of 1.82 m/s, 2.30 m/s and 2.70 m/s.	47
3.18	T-Foil lift-to-drag ratio at different angles of attack and water flow velocities of 1.82 m/s, 2.30 m/s and 2.70 m/s.	48
3.19	Comparison between experimental lift coefficient and quasi-static lift coefficient at water flow velocity of 1.82 m/s, frequency of 1.5 Hz and demand T-Foil incidence (α) range of $\pm 15^\circ$	49
3.20	Comparison of T-Foil angle of attack (left) and lift coefficient (right) at frequencies of 0.5 Hz, 1.5 Hz and 2.5 Hz, water flow velocity of 1.82 m/s with demand T-Foil incidence (α) range of $\pm 15^\circ$	51
3.21	Comparison of T-Foil angle of attack (left) and lift coefficient (right) at frequencies of 0.5 Hz, 1.5 Hz and 2.5 Hz, water flow velocity of 2.70 m/s with demand T-Foil incidence (α) range of $\pm 15^\circ$	52
3.22	Comparison of T-Foil angle of attack (left) and lift coefficient (right) at frequencies of 0.5 Hz, 1.5 Hz and 2.5 Hz, water flow velocity of 2.70 m/s with demand T-Foil incidence (α) range of $\pm 10^\circ$	53
3.23	Comparison of T-Foil angle of attack (left) and lift coefficient (right) at frequencies of 0.5 Hz, 1.5 Hz and 2.5 Hz, water flow velocity of 2.70 m/s with demand T-Foil incidence (α) range of $\pm 5^\circ$	54
4.1	Schematic diagram showing the sign convention for sinkage (heave), trim (pitch), T-Foil deflection and stern tabs deflection.	58
4.2	Heave added mass and damping for floating semi-circular cylinder.	63
4.3	3D CAD design of electrically activated model scale stern tabs.	65
4.4	Electrically activated model scale stern tabs developed for the 2.5 m hydroelastic segmented catamaran model.	65

4.5	Stern tabs installed at the stern of the model.	66
4.6	T-Foil installed on the aft section of the centre bow of the model.	66
4.7	T-Foil electrical actuator installed on the aft section of the centre bow of the model.	67
4.8	The model attached to the moving carriage in the AMC towing tank.	68
4.9	Sinkage response to T-Foil deflection of $\pm 15^\circ$ at model speed of 2.89 m/s.	69
4.10	Trim response to T-Foil deflection of $\pm 15^\circ$ at model speed of 2.89 m/s.	69
4.11	Sinkage response to T-Foil deflection of $\pm 10^\circ$ at model speed of 2.89 m/s.	70
4.12	Trim response to T-Foil deflection of $\pm 10^\circ$ at model speed of 2.89 m/s.	70
4.13	Sinkage response to T-Foil deflection of $\pm 5^\circ$ at model speed of 2.89 m/s.	71
4.14	Trim response to T-Foil deflection of $\pm 5^\circ$ at model speed of 2.89 m/s.	71
4.15	Sinkage response to stern tabs deflection of $\pm 18^\circ$ at model speed of 2.89 m/s.	73
4.16	Trim response to stern tabs deflection of $\pm 18^\circ$ at model speed of 2.89 m/s.	73
4.17	Sinkage response to stern tabs deflection of $\pm 10^\circ$ at model speed of 2.89 m/s.	74
4.18	Trim response to stern tabs deflection of $\pm 10^\circ$ at model speed of 2.89 m/s.	74
4.19	Sinkage response to stern tabs deflection of $\pm 5^\circ$ at model speed of 2.89 m/s.	75
4.20	Trim response to stern tabs deflection of $\pm 5^\circ$ at model speed of 2.89 m/s.	75
4.21	Model responses to maximum step movements of RCS when activated together to produce maximum trim change: (a) model speed of 2.89 m/s, (b) model speed of 2.50 m/s, (c) model speed of 2.0 m/s, (d) model speed of 1.53 m/s. First step: T-Foil deflection of $+15^\circ$ and stern tabs deflection of -18° . Second step: T-Foil deflection of -15° and stern tabs deflection of $+18^\circ$	78
4.22	Model responses to maximum step movements of RCS when activated together to produce maximum sinkage change: (a) model speed of 2.89 m/s, (b) model speed of 2.50 m/s, (c) model speed of 2.0 m/s, (d) model speed of 1.53 m/s. First step: T-Foil deflection of $+15^\circ$ and stern tabs deflection of $+18^\circ$. Second step: T-Foil deflection of -15° and stern tabs deflection of -18°	79
4.23	Photo of the model running at the low speed of 1.53 m/s when the stern tabs and the T-Foil are deflected at -18° and -15° respectively.	80
4.24	Photo of the model running at the high speed of 2.89 m/s when the stern tabs and the T-Foil are deflected at -18° and -15° respectively.	80
4.25	Model responses to step movements of RCS surfaces when activated together to produce pure sinkage excitation (T-Foil deflection of $+15^\circ$ and stern tabs deflection of $+10^\circ$): (a) model speed of 2.89 m/s, (b) model speed of 2.50 m/s, (c) model speed of 2.0 m/s, (d) model speed of 1.53 m/s.	82
4.26	Model responses to step movements of RCS surfaces when activated together to produce pure trim excitation (T-Foil deflection of -8° and stern tabs deflection of $+18^\circ$): (a) model speed of 2.89 m/s, (b) model speed of 2.50 m/s, (c) model speed of 2.0 m/s, (d) model speed of 1.53 m/s.	83

4.27	Heave response of the model in calm water at a model speed of 2.89 m/s excited by T-Foil deflection of $\pm 10^\circ$ at a frequency of 1.25 Hz with the stern tabs fixed at $+9^\circ$.	84
4.28	Heave range of the model excited by different combinations of the control surfaces at different frequencies in calm water at a model speed of 2.89 m/s.	86
4.29	Pitch range of the model excited by different combinations of the control surfaces at different frequencies in calm water at a model speed of 2.89 m/s.	86
4.30	Phase lag between the motions as well as the control surface deflections for the T-Foil full range mode at different frequencies in calm water at a model speed of 2.89 m/s.	87
4.31	Phase lag between the motions as well as the control surface deflections for the stern tabs full range mode at different frequencies in calm water at a model speed of 2.89 m/s.	87
4.32	Phase lag between the motions as well as the control surface deflections for the pitch excitation mode at different frequencies in calm water at a model speed of 2.89 m/s.	88
4.33	Phase lag between the motions as well as the control surface deflections for the heave excitation mode at different frequencies in calm water at a model speed of 2.89 m/s.	89
5.1	Time records at a model test speed of 2.89 m/s ($Fr = 0.608$), wave height of 90 mm, dimensionless wave encounter frequency $\omega_e^* = 3.182$ and passive RCS mode.	98
5.2	Time records at a model test speed of 2.89 m/s ($Fr = 0.608$), wave height of 90 mm, dimensionless wave encounter frequency $\omega_e^* = 3.182$ and pitch control mode.	98
5.3	Pitch RAO at model speed of 2.89 m/s ($Fr = 0.608$) and wave height of 60 mm showing error bars.	100
5.4	Heave RAO at model speed of 2.89 m/s ($Fr = 0.608$) and wave height of 60 mm showing error bars.	100
5.5	Pitch RAO at model speed of 2.89 m/s ($Fr = 0.608$) and wave height of 60 mm.	103
5.6	Pitch RAO at model speed of 2.89 m/s ($Fr = 0.608$) and wave height of 90 mm.	103
5.7	Heave RAO at model speed of 2.89 m/s ($Fr = 0.608$) and wave height of 60 mm.	104
5.8	Heave RAO at model speed of 2.89 m/s ($Fr = 0.608$) and wave height of 90 mm.	104
5.9	Pitch RPO (pitch phase lag relative to encountered wave at the LCG) at model speed of 2.89 m/s ($Fr = 0.608$) and wave height of 60 mm.	105
5.10	Pitch RPO (pitch phase lag relative to encountered wave at the LCG) at model speed of 2.89 m/s ($Fr = 0.608$) and wave height of 90 mm.	105

5.11	Heave RPO (heave phase lag relative to encountered wave at the LCG) at model speed of 2.89 m/s ($Fr = 0.608$) and wave height of 60 mm.	106
5.12	Heave RPO (heave phase lag relative to encountered wave at the LCG) at model speed of 2.89 m/s ($Fr = 0.608$) and wave height of 90 mm.	106
5.13	Phase lag of T-Foil relative to pitch motion at model speed of 2.89 m/s ($Fr = 0.608$) and wave height of 60 mm.	107
5.14	Phase lag of T-Foil relative to pitch motion at model speed of 2.89 m/s ($Fr = 0.608$) and wave height of 90 mm.	107
5.15	Phase lag of stern tabs relative to pitch motion at model speed of 2.89 m/s ($Fr = 0.608$) and wave height of 60 mm.	108
5.16	Phase lag of stern tabs relative to pitch motion at model speed of 2.89 m/s ($Fr = 0.608$) and wave height of 90 mm.	108
5.17	Phase lag between T-Foil and stern tabs deflection at model speed of 2.89 m/s ($Fr = 0.608$) and wave height of 60 mm.	109
5.18	Phase lag between T-Foil and stern tabs deflection at model speed of 2.89 m/s ($Fr = 0.608$) and wave height of 90 mm.	109
5.19	Dimensionless heave acceleration at LCG (37% LOA from the stern) at model speed of 2.89 m/s ($Fr = 0.608$) and wave height of 60 mm.	113
5.20	Dimensionless heave acceleration at LCG (37% LOA from the stern) at model speed of 2.89 m/s ($Fr = 0.608$) and wave height of 90 mm.	113
5.21	Dimensionless vertical acceleration at the longitudinal location of the T-Foil (80% LOA from the stern) at model speed of 2.89 m/s ($Fr = 0.608$) and wave height of 60 mm.	114
5.22	Dimensionless vertical acceleration at the longitudinal location of the T-Foil (80% LOA from the stern) at model speed of 2.89 m/s ($Fr = 0.608$) and wave height of 90 mm.	114
5.23	Dimensionless vertical acceleration at the longitudinal location of the stern tabs at model speed of 2.89 m/s ($Fr = 0.608$) and wave height of 60 mm.	115
5.24	Dimensionless vertical acceleration at the longitudinal location of the stern tabs at model speed of 2.89 m/s ($Fr = 0.608$) and wave height of 90 mm.	115
5.25	T-Foil deflection range at model speed of 2.89 m/s ($Fr = 0.608$) and wave height of 60 mm.	116
5.26	T-Foil deflection range at model speed of 2.89 m/s ($Fr = 0.608$) and wave height of 90 mm.	116
5.27	Stern tabs deflection range at model speed of 2.89 m/s ($Fr = 0.608$) and wave height of 60 mm.	117
5.28	Stern tabs deflection range at model speed of 2.89 m/s ($Fr = 0.608$) and wave height of 90 mm.	117

6.1	Time records showing kinematic data at model speed of 2.89 m/s ($Fr = 0.608$), wave height of 90 mm, ω_e^* of 4.581 and passive RCS mode.	122
6.2	Time records showing kinematic data at model speed of 2.89 m/s ($Fr = 0.608$), wave height of 90 mm, ω_e^* of 4.581 and pitch control mode.	123
6.3	Error bars for centre bow total sagging force at a model test speed of 2.89 m/s ($Fr = 0.608$) and wave height of 60 mm.	125
6.4	Error bars for demihull slam induced sagging bending moment at the forward segment position at a model test speed of 2.89 m/s ($Fr = 0.608$) and wave height of 60 mm.	125
6.5	Designation of centre bow entry and total centre bow force using data obtained at model speed of 2.89 m/s ($Fr = 0.608$), wave height of 90 mm, ω_e^* of 4.581 and pitch control mode.	126
6.6	Centre bow entry force at model speed of 2.89 m/s ($Fr = 0.608$) and wave height of 60 mm.	127
6.7	Centre bow entry force at model speed of 2.89 m/s ($Fr = 0.608$) and wave height of 90 mm.	127
6.8	Dimensionless centre bow entry force at model speed of 2.89 m/s ($Fr = 0.608$) and wave height of 60 mm.	128
6.9	Dimensionless centre bow entry force at model speed of 2.89 m/s ($Fr = 0.608$) and wave height of 90 mm.	128
6.10	Centre bow total sagging force at model speed of 2.89 m/s ($Fr = 0.608$) and wave height of 60 mm.	130
6.11	Centre bow total sagging force at model speed of 2.89 m/s ($Fr = 0.608$) and wave height of 90 mm.	130
6.12	Dimensionless centre bow total sagging force at model speed of 2.89 m/s ($Fr = 0.608$) and wave height of 60 mm.	131
6.13	Dimensionless centre bow total sagging force at model speed of 2.89 m/s ($Fr = 0.608$) and wave height of 90 mm.	131
6.14	Centre bow total hogging force at model speed of 2.89 m/s ($Fr = 0.608$) and wave height of 60 mm.	133
6.15	Centre bow total hogging force at model speed of 2.89 m/s ($Fr = 0.608$) and wave height of 90 mm.	133
6.16	Dimensionless centre bow total hogging force at model speed of 2.89 m/s ($Fr = 0.608$) and wave height of 60 mm.	134
6.17	Dimensionless centre bow total hogging force at model speed of 2.89 m/s ($Fr = 0.608$) and wave height of 90 mm.	134
6.18	Sagging slam force at model speed of 2.89 m/s ($Fr = 0.608$) and wave height of 60 mm.	135

6.19	Sagging slam force at model speed of 2.89 m/s ($Fr = 0.608$) and wave height of 90 mm.	135
6.20	Dimensionless sagging slam force at model speed of 2.89 m/s ($Fr = 0.608$) and wave height of 60 mm.	136
6.21	Dimensionless sagging slam force at model speed of 2.89 m/s ($Fr = 0.608$) and wave height of 90 mm.	136
6.22	Centre bow total sagging force position from the transom at model speed of 2.89 m/s ($Fr = 0.608$) and wave height of 60 mm.	137
6.23	Centre bow total sagging force position from the transom at model speed of 2.89 m/s ($Fr = 0.608$) and wave height of 90 mm.	137
6.24	Centre bow total hogging force position from the transom at model speed of 2.89 m/s ($Fr = 0.608$) and wave height of 60 mm.	138
6.25	Centre bow total hogging force position from the transom at model speed of 2.89 m/s ($Fr = 0.608$) and wave height of 90 mm.	138
6.26	Demihull slam induced sagging bending moment at the forward segment position at model speed of 2.89 m/s ($Fr = 0.608$) and wave height of 60 mm.	140
6.27	Demihull slam induced sagging bending moment at the forward segment position at model speed of 2.89 m/s ($Fr = 0.608$) and wave height of 90 mm.	140
6.28	Demihull slam induced hogging bending moment at the forward segment position at model speed of 2.89 m/s ($Fr = 0.608$) and wave height of 60 mm.	141
6.29	Demihull slam induced hogging bending moment at the forward segment position at model speed of 2.89 m/s ($Fr = 0.608$) and wave height of 90 mm.	141
6.30	Demihull slam induced sagging bending moment at the aft segment position at model speed of 2.89 m/s ($Fr = 0.608$) and wave height of 60 mm.	142
6.31	Demihull slam induced sagging bending moment at the aft segment position at model speed of 2.89 m/s ($Fr = 0.608$) and wave height of 90 mm.	142
6.32	Demihull slam induced hogging bending moment at the aft segment position at model speed of 2.89 m/s ($Fr = 0.608$) and wave height of 60 mm.	143
6.33	Demihull slam induced hogging bending moment at the aft segment position at model speed of 2.89 m/s ($Fr = 0.608$) and wave height of 90 mm.	143
6.34	Dimensionless demihull slam induced sagging bending moment at the forward segment position at model speed of 2.89 m/s ($Fr = 0.608$) and wave height of 60 mm.	145
6.35	Dimensionless demihull slam induced sagging bending moment at the forward segment position at model speed of 2.89 m/s ($Fr = 0.608$) and wave height of 90 mm.	145
6.36	Dimensionless demihull slam induced hogging bending moment at the forward segment position at model speed of 2.89 m/s ($Fr = 0.608$) and wave height of 60 mm.	146

6.37	Dimensionless demihull slam induced hogging bending moment at the forward segment position at model speed of 2.89 m/s ($Fr = 0.608$) and wave height of 90 mm.	146
6.38	Dimensionless demihull slam induced sagging bending moment at the aft segment position at model speed of 2.89 m/s ($Fr = 0.608$) and wave height of 60 mm. . .	147
6.39	Dimensionless demihull slam induced sagging bending moment at the aft segment position at model speed of 2.89 m/s ($Fr = 0.608$) and wave height of 90 mm. . .	147
6.40	Dimensionless demihull slam induced hogging bending moment at the aft segment position at model speed of 2.89 m/s ($Fr = 0.608$) and wave height of 60 mm. . .	148
6.41	Dimensionless demihull slam induced hogging bending moment at the aft segment position at model speed of 2.89 m/s ($Fr = 0.608$) and wave height of 90 mm. . .	148
6.42	Designation of kinematics parameters using data obtained at model speed of 2.89 m/s ($Fr = 0.608$), wave height of 90 mm, ω_e^* of 6.272 and pitch control mode.	150
6.43	Maximum relative bow immersion at model speed of 2.89 m/s ($Fr = 0.608$) and wave height of 60 mm.	152
6.44	Maximum relative bow immersion at model speed of 2.89 m/s ($Fr = 0.608$) and wave height of 90 mm.	152
6.45	Relative bow immersion at the instant of sagging slam force at model speed of 2.89 m/s ($Fr = 0.608$) and wave height of 60 mm.	153
6.46	Relative bow immersion at the instant of sagging slam force at model speed of 2.89 m/s ($Fr = 0.608$) and wave height of 90 mm.	153
6.47	Maximum relative bow velocity at model speed of 2.89 m/s ($Fr = 0.608$) and wave height of 60 mm.	154
6.48	Maximum relative bow velocity at model speed of 2.89 m/s ($Fr = 0.608$) and wave height of 90 mm.	154
6.49	Relative bow velocity at the instant of sagging slam force at model speed of 2.89 m/s ($Fr = 0.608$) and wave height of 60 mm.	155
6.50	Relative bow velocity at the instant of sagging slam force at model speed of 2.89 m/s ($Fr = 0.608$) and wave height of 90 mm.	155
6.51	Slam impulse integration time at model speed of 2.89 m/s ($Fr = 0.608$) and wave height of 60 mm.	156
6.52	Slam impulse integration time at model speed of 2.89 m/s ($Fr = 0.608$) and wave height of 90 mm.	157
6.53	Absolute slam impulse at model speed of 2.89 m/s ($Fr = 0.608$) and wave height of 60 mm.	157
6.54	Absolute slam impulse at model speed of 2.89 m/s ($Fr = 0.608$) and wave height of 90 mm.	158
6.55	Peak strain energy of the centre bow elastic links at model speed of 2.89 m/s ($Fr = 0.608$) and wave height of 60 mm.	160

6.56	Peak strain energy of the centre bow elastic links at model speed of 2.89 m/s ($Fr = 0.608$) and wave height of 90 mm.	160
6.57	Peak strain energy of the demihull elastic links at model speed of 2.89 m/s ($Fr = 0.608$) and wave height of 60 mm.	161
6.58	Peak strain energy of the demihull elastic links at model speed of 2.89 m/s ($Fr = 0.608$) and wave height of 90 mm.	161
6.59	Total peak strain energy of the centre bow and demihull elastic links at model speed of 2.89 m/s ($Fr = 0.608$) and wave height of 60 mm.	162
6.60	Total peak strain energy of the centre bow and demihull elastic links at model speed of 2.89 m/s ($Fr = 0.608$) and wave height of 90 mm.	162

List of Tables

2.1	Centre bow instrumentation error on the basis of the data collected during the centre bow calibrations.	29
2.2	Calibration factors for the magnitude of the load on each transverse beam for six applied load positions.	30
2.3	Calibration factors for the magnitude of the measured loads on each transverse beam at three parts of the centre bow.	33
3.1	Specifications of the full scale 112 m INCAT catamaran and 2.5 m scaled model T-Foil.	35
4.1	Hydrostatic sinkage and trim stiffness calculation by applying a 1.5 kg mass at the location of T-Foil on the catamaran model at zero speed in calm water. . . .	59
4.2	Hydrostatic sinkage and trim stiffness calculation by applying a 1.5 kg mass on the model centreline at longitudinal location of stern tabs at zero speed in calm water.	59
4.3	Prediction of model responses to load applied at the location of T-Foil and stern tabs by static load experiment and hydrostatic prediction.	60
4.4	Specifications of the full scale INCAT catamaran and the scaled model.	64
4.5	Specifications of the full scale 112 m INCAT catamaran and 2.5 m scaled model stern tabs.	64
5.1	Towing tank catamaran model RCS test conditions.	97

List of Publications

Copies of following publications which are relevant to the thesis are attached to the thesis.

- J. AlaviMehr, M. R. Davis and J. Lavroff. Low Reynolds Number Performance of a Model Scale T-Foil. *Royal Institution of Naval Architects. Transactions. Part A3. International Journal of Maritime Engineering*, vol. 157, pp. A175-A187, 2015.
- J. AlaviMehr, M. R. Davis, J. Lavroff, D. S. Holloway and G. A. Thomas. Response of a High-Speed Wave-Piercing Catamaran to an Active Ride Control System. *Royal Institution of Naval Architects. Transactions. Part A3. International Journal of Maritime Engineering*, In Press, 2016.
- J. AlaviMehr, J. Lavroff, M. R. Davis, D. S. Holloway and G. A. Thomas. Motion Response to Waves of a High-Speed Catamaran with Feedback Ride Control. *Submitted to Journal of Ship Research*, Manuscript ID JSR-06-16-0041, 2016.
- J. AlaviMehr, J. Lavroff, M. R. Davis, D. S. Holloway and G. A. Thomas. An Experimental Investigation of Ride Control Algorithms to Mitigate Wave Impact Loads on High-Speed Catamarans. *Submitted to Journal of Ship Research*, Manuscript ID JSR-07-16-0046, 2016.
- J. R. Shahraki, M. R. Davis, B. Shabani, J. AlaviMehr, G. A. Thomas, J. Lavroff. and W. Amin. Mitigation of Slamming of Large Wave-Piercing Catamarans. *30th Symposium on Naval Hydrodynamics, Hobart, Tasmania, Australia*, , 2014.

Nomenclature

General

- Dimensionless parameters signified by superscript asterisk
- Over dots represent differentiation with respect to time

Chapter 2

Roman symbols

a	Distance between centre of elastic link and centreline of the demihull pin joint mount (m)
b	Distance between centre of starboard and port elastic links of centre bow transverse beams (m)
c	Distance between centreline of forward and aft centre bow transverse beams (m)
d	Position of force acting on each centre bow transverse beam measured from the centreline of the port demihull pin joint mount (m)
E	Elastic modulus (N/m ²)
F	Calibration load acting on each transverse beam (N)
F_1	Calibration load acting on centre bow forward transverse beam (N)
F_2	Calibration load acting on centre bow aft transverse beam (N)
F_T	Total calibration load acting on centre bow (N)
I	Second moment of area of cross section (m ⁴)
M	Bending moment (N.m)
M_1	Moment acting on port elastic link of centre bow transverse beam (N.m)
M_2	Moment acting on starboard elastic link of centre bow transverse beam (N.m)
x_F	Position of total calibration load acting on centre bow measured from the centreline of the aft transverse beam (m)
y_l	Distance between strain gauges on an elastic link (m)

Greek letters

ϵ	Differential strain measured on elastic link
------------	--

Chapter 3

Roman symbols

a	Dimensionless parameter which determines the location of a point that vertical motion of T-Foil is referenced to
AR	T-Foil aspect ratio
b	T-Foil semi-chord length (m)
C_D	T-Foil drag coefficient
C_L	T-Foil lift coefficient
$C_{L\alpha}$	T-Foil lift-coefficient derivative ($dC_L/d\alpha$) (dimensionless)
D	T-Foil drag force (N)
f	T-Foil actuation frequency (Hz)
F_y	Load-cell output voltage in the horizontal y-axis direction (V)
F_z	Load-cell output voltage in the vertical z-axis direction (V)
h	T-Foil vertical displacement (m)
k	T-Foil reduced frequency ($b\omega/V$)
L	T-Foil lift force (N)
L/D	T-Foil lift-to-drag ratio
S	T-Foil planform area (m^2)
V	Water flow velocity (m/s)
V_{in}	Stepper-motor input voltage (V)
V_{out}	Potentiometer output voltage (V)

Greek letters

α	T-Foil pitch angle of attack (degree)
ω	T-Foil actuation angular frequency ($2\pi f$)
ρ	Density of water (kg/m^3)

Chapter 4

Roman symbols

A_{WP}	Model equilibrium waterplane area (m^2)
d_{CF}	Distance of centre of pressure of the control surface forward of the model LCF (m)
d_{CG}	Distance of centre of pressure of the control surface forward of the model LCG (m)
d_{FG}	Distance of the model LCF forward of the LCG (m)
f_{ST}	Stern tabs lift factor (N/radian)
f_{TF}	T-Foil lift factor (N/radian)
g	Gravitational acceleration (m/s^2)

I_{CF}	Second moment of area of waterplane about a transverse axis passing through the centre of flotation (m^4)
L	Control surface lift force (N)
LCF	Longitudinal Centre of Flotation (m)
LCG	Longitudinal Centre of Gravity (m)
S	Control surface planform area (m^2)
U	Model forward speed (m/s)
x_{ST}	Distance between centre of pressure of the stern tabs and LCG (m)
x_{TF}	Distance between centre of pressure of the T-Foil and LCG (m)

Greek letters

α_{ST}	Stern tabs deflection (radian)
α_{TF}	T-Foil deflection (radian)
η_3	Model heave (sinkage) (m)
η_5	Model pitch (trim) (radian)
ρ	Density of water (kg/m^3)
ω	Motion frequency ($2\pi f$)

Chapter 5

Roman symbols

$C_{L\alpha}$	Control surfaces lift-coefficient derivative ($dC_L/d\alpha$) (dimensionless)
Fr	Froude number based on hull waterline length
g	Gravitational acceleration (m/s^2)
H	Model heave at LCG (m, positive up)
H^*	Dimensionless model heave at LCG (heave/wave amplitude)
l	Length of model waterline (m)
LCG	Longitudinal Centre of Gravity
L_{ST}	Stern tab lift force (N)
L_{TF}	T-Foil lift force (N)
P	Model pitch about LCG (radian, positive bow down)
P^*	Dimensionless model pitch at LCG (pitch/wave slope)
S_{ST}	Stern tab planform area (m^2)
S_{TF}	T-Foil planform area (m^2)
$ST0$	Stern tab initial angle of attack (radian, positive producing upward lift)
$TF0$	T-Foil initial angle of attack (radian, positive producing upward lift)
U	Model forward speed (m/s)
x_{ST}	Distance between centre of pressure of the stern tabs and LCG (m)

x_{TF} Distance between centre of pressure of the T-Foil and LCG (m)

Greek letters

α_{ST} Stern tabs angular deflection (radian, positive producing upward lift)

α_{STd} Control system demand stern tabs angular deflection (radian, positive producing upward lift)

α_{TF} T-Foil angular deflection (radian, positive producing upward lift)

α_{TFd} Control system demand T-Foil angular deflection (radian, positive producing upward lift)

ζ Wave amplitude (m)

λ Wave length (m)

ρ Density of water (kg/m³)

ω_0 Wave frequency in fixed coordinate (radian/s)

ω_e Wave encounter frequency (radian/s)

ω_e^* Dimensionless wave encounter frequency

Chapter 6

Roman symbols

E_ϵ Elastic hinge strain energy (J)

Fr Froude number based on hull waterline length

F Force (N)

g Gravitational acceleration (m/s²)

h Cross-section height of elastic link (m)

h_{max} Maximum relative bow immersion (m)

h_s Relative bow immersion at peak sagging slam force (m)

I_s Slam impulse (Ns)

k_{eff} Effective stiffness of elastic link (Nm/rad)

k_{th} Theoretical stiffness of elastic link (Nm/rad)

L Model length (m)

l_b Length of elastic link (m)

LCG Longitudinal Centre of Gravity (m)

M Bending moment (Nm)

V_{max} Maximum relative bow velocity (m/s)

Greek letters

ζ Wave amplitude (m)

Δt_s Slam impulse integration time (s)

ρ Density of water (kg/m³)

ϵ Differential strain measured on the strain gauges

ω_e Wave encounter frequency ($2\pi f$)

Chapter 1

Introduction



Figure 1.1: INCAT Tasmania 112 m wave-piercing catamaran: Hull 066 - KatExpress 1.

1.1 Background

Worldwide demand for fast sea transportation has led to an on-going development of large high-speed and lightweight marine vessels for both commercial and military applications [1]. Different types of high-speed craft have been developed to satisfy this requirement, but catamarans have proven to be most popular due to their large deck area, high hydrostatic and hydrodynamic stability, their ability to provide lightweight Roll-on-Roll-off (Ro-Ro) vessels and relatively large deadweight to displacement ratios [2].

INCAT Tasmania carried out the original development of high-speed wave piercing catamarans in the late 1970s and 1980s up to 40m in length [3]. INCAT then produced a 74m length high-speed catamaran in 1990 that was the first catamaran capable of transporting vehicles [3].

1.1.1 Wave loads on catamarans

Catamaran vessels operating at high-speed often experience slam events and associated large wave loads when the vessel motion causes an impact between the cross deck structure and the water surface [4]. The most common design of catamaran is a twin hull configuration consisting of a flat wet-deck section joining the two demihulls. Although this hull form is effective during operation in smaller waves, it is prone to deck diving in larger waves due to little reserve buoyancy in the forward part of the vessel. This causes the flat wet-deck to make contact with the water surface, leading to very large impulsive slam loads on the hull structure [5–7] and in severe cases green water over the bow and substantial structural damage.

A unique configuration of high-speed wave-piercing catamarans has been developed by INCAT Tasmania [8] with a prominent centre bow located at the vessel centreline between the wave-piercer demihulls designed to effectively eliminate deck diving in following seas. The centre bow provides forward buoyancy to the front of the vessel during wave slam impact [3]. Figure 1.1 shows a 112 m INCAT Tasmania high-speed wave-piercing catamaran, KatExpress 1 built in 2009 and Figure 1.2 shows a 112 m INCAT Tasmania high-speed wave-piercing catamaran, KatExpress 2 built in 2013 [8].



Figure 1.2: INCAT Tasmania 112 m wave-piercing catamaran: Hull 067 - KatExpress 2.

There have been prior studies of structural loads relevant to this type of fast ship and the problem has been investigated both experimentally and numerically.

In 2005, a time domain method was developed by Davis et al. to predict the nonlinear wave loads and was validated by the measured loads in sea trials of an 86 m catamaran [9]. Davidson et al. presented the results of studies into the calculation of global loads on a 112 m wave-piercing catamaran design in 2006 [10]. In 2006, the methodology of global load verification for an INCAT 98 m class catamaran was investigated by Roberts et al. [11] and research into global load predictions for larger designs was carried out. Computational modelling of wet deck slam loads of an INCAT 96 m wave-piercing catamaran with reference to sea trial data was conducted by Davis et al. in 2007 [12].

In 2009, slamming loads on large high-speed wave piercers were investigated by Amin et al. using a reverse engineering method in conjunction with trials data and finite element analysis [13]. The vibratory response of high-speed catamarans to slamming was investigated by Lavroff et al. in 2009 [14] through hydroelastic segmented model experiments. This work using hydroelastic segmented model experiments was extended by Lavroff et al. to determine the wave slamming loads on high-speed catamarans in 2011 [15], and 2013 [16].

In 2011, the slam events of high-speed catamarans in irregular waves were characterised through towing tank testing of a hydroelastic segmented model by Thomas et al. [2], with further work conducted by French et al. in 2013 [17].

Mitigation of slamming of large wave-piercing catamarans was investigated by Shahraki et al. in 2016 [18] and it was found that increases of wet deck height reduce impulsive slam loadings but lead to increased motions. Shahraki et al. also found that shorter centre bows reduce slam loadings and also reduce the vessel pitch motions [18].

Although there have been many investigations into catamaran structural loads through numerical computations, model experiment and full-scale sea trials, the influence of ride control systems on structural loads has not been investigated.

1.1.2 Ride control systems

High-speed catamarans, due to their slender twin hull geometry and high operating Froude number [19], frequently experience large heave and pitch motions and accelerations that are different to those of conventional monohulls. Catamarans experience smaller but more rapid rolling motions due to their high metacentric height, compared to large and relatively slow rolling motions of monohulls [19]. Increases in the operating speed of catamarans generally exacerbates vessel motions due to increase of Froude number which leads to passenger discomfort, sea sickness and potential structural damage when operating in severe conditions and higher sea states. A motion control system is therefore required to reduce these large motions, increase passenger comfort and improve the vessel performance.

Incat Tasmania [8] uses active motion control systems for its high-speed wave piercing

catamarans to reduce vessel motions and dynamic structural loads, improve passenger comfort and increase the range of operability. These active Ride Control Systems (RCS) consist of two active trim tabs located at the stern of the vessel demihulls and a retractable T-Foil mounted on the centreplane at the aft end of the centre bow. Figure 1.3 shows the location of the T-Foil and the stern tabs on a 112 m INCAT Tasmania high-speed wave-piercing catamaran [8]. Figure 1.4 shows a full scale T-Foil prior to installation on a 112 m INCAT Tasmania high-speed wave-piercing catamaran [8].

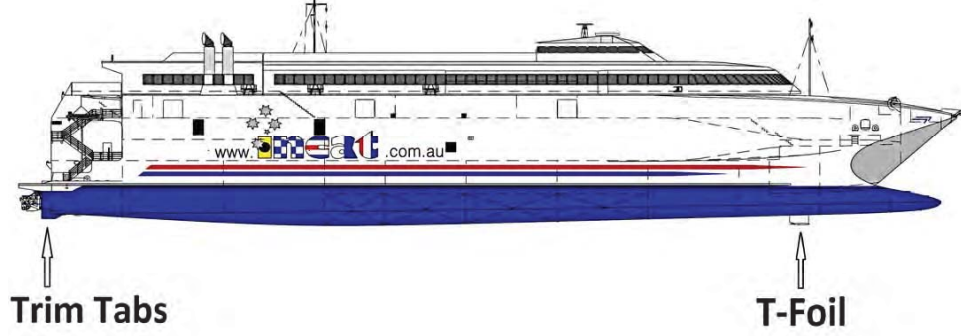


Figure 1.3: Location of the T-Foil and the trim tabs on a 112 m INCAT Tasmania high-speed wave-piercing catamaran.

The T-Foil generates a vertical force, either upward or downward, to reduce heave and pitch motions. Retracting the T-Foil into the hull helps to reduce resistance in calm water. Figure 1.5 shows a schematic diagram of a retractable T-Foil. The trim tabs installed at the stern of the vessel demihulls, hereafter called stern tabs, produce a lift force at the transom to retain the desired vessel dynamic trim and reduce pitch and heave motion in combination with the T-Foil. The stern tabs can also resist the vessel roll motion when they are operated differentially.

By controlling motions, particularly pitch, bow entry and slamming can be minimized [20]. These are major structural loads that can be significantly reduced through the implementation of motions control [21].

Some prior studies of ride control systems relevant to this type of fast ships have been carried out through experimental and numerical investigation.

In 1994, ride control of surface effect ships was studied by Sorensen et al. [22] using distributed control for active damping of heave and pitch acceleration. Sorensen et al. developed a distributed ride control system based on the theory of passive system, and proposed a proportional pressure feedback controller [22]. Their full scale experiments showed improvement in ride quality when using a ride control system which provides dissipation of energy around the resonance frequencies [22].

In 1995, the development of a ride control system for fast ferries [23] and the role of simulation in this development [24] were investigated by Haywood et al. In 2015, Haywood et al. reviewed the different ride control devices including fins, trim tabs, interceptors, retractable



Figure 1.4: Full scale T-Foil prior to installation on a 112 m INCAT Tasmania high-speed wave-piercing catamaran.

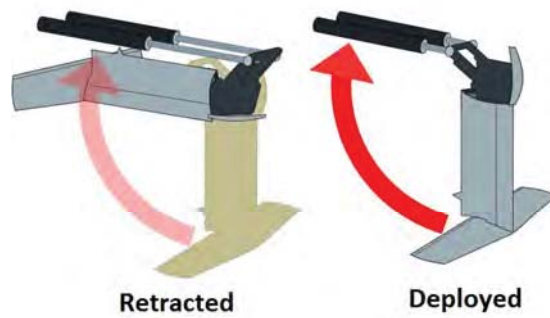


Figure 1.5: Schematic diagram of a retractable T-Foil.

T-Foils and lifting foils by studying technical aspects, costs, ease of installation, operational and maintenance requirements and material [25].

In 2000, Esteban et al. investigated the vertical acceleration reduction of a monohull fast ferry with the control of flaps and T-Foil by control-oriented modelling [26]. This work was extended in 2001 by Esteban et al. to attenuate the ship's vertical motions by a simulation tool using MATLAB and SIMULINK [27]. This numerical investigation was extended in 2001 by experimental study conducted by Giron-Sierra et al. [28]; however, these experiments only studied the reduction of the acceleration and MSI. In 2002, Giron-Sierra et al. studied the control of the actuators for vertical motion damping [29] and concluded that not only did the MSI need to be minimized, but other objectives such as reduced control effort, vibrations and cavitation should be considered [29]. In 2002, Esteban et al. investigated the multiobjective optimization of control by designing a Genetic Algorithm method [30]. In 2003, a complete control-oriented model was used by Giron-Sierra et al. [31] to study PID control of fast ferries and it was shown that moving controlled actuators can have an important stabilisation effect. In 2004, Esteban et al. developed the control-oriented model of the vertical motions of the fast ferry by a methodology based on MATLAB tools using experiments and CAD-based programs [32].

Decreasing of the motion sickness incidence in a high speed ferry using different multivariable classic controllers was studied by Aranda et al. in 2001 [33] and it was concluded as the wave induced vertical accelerations are greater in the higher sea states, the work of the actuators is less effective because they have to compensate higher forces and momentums [33]. In addition, Aranda et al. have carried out the design of a multivariable robust controller to decrease the motion sickness incidence in high speed ferries in 2005 [34]. The design of a monovariable robust controller in order to reduce the vertical movement on a high-speed ferry have been undertaken by Diaz et al. with quantitative feedback theory (QFT) [35, 36] where it was concluded the QFT monovariable robust design is useful as it reduces MSI in an acceptable way using a sole actuator, the T-Foil [35]. De la Cruz, Giron-Sierra, Esteban et al. have investigated the smoothing of the vertical motions of a monohull fast ferry with the control of flaps and T-Foil by control-oriented modelling and some experimental evaluation [26–32, 37–48] and have concluded that moving controlled actuators can have an important stabilisation effect. They have dedicated their first step of their research to modelling. This step has been based on CAD-based simulations and experiments with a scaled-down replica. The main result of their first step was the development of a simulation tool, where control alternatives were studied before real application. The next step of their research was experimental tests of appendages and control where they concluded there was a considerable reduction of the MSI at the normal operational conditions of the ship (small or moderate waves).

In 2002, reduction of the vertical motion of a round-bilge boat in waves by design of controllable transom flaps was investigated by Wu-Qiang et al. [49] and this was evaluated by some model tests. However, an oscillating flap was used instead of a controllable flap for evaluation of the effects of flaps on pitch reduction of the model [49]. These model experiments have shown

that using an oscillating flap would reduce pitch motion, if a suitable phase could be established between flap exciting forces and wave disturbances [49].

In 2004, Sclavounos et al. studied the seakeeping performance of a foil-assisted high-speed monohull vessel using a state-of-the-art three-dimensional Rankine panel method [50] where it was found that the most efficient location for the hydrofoil is at the ship bow leading to a 50% reduction of the root mean square values of the heave and pitch motions in a Joint North Sea Wave Project (JONSWAP) spectrum [50].

In 2011, seakeeping simulations for a high speed wave piercing catamaran with an active ride control system was carried out by Hughes et al. using the Large Amplitude Motion Program (LAMP), a time domain potential flow panel code that solves the 3-D wave-body hydrodynamics and rigid-body dynamics problems [51]. Hughes et al. concluded that the LAMP predictions show a significant benefit from actively controlled trim tabs and T-Foils for reducing both pitch and roll motions [51].

In 2011, Rijikens et al. developed a computational tool for the design and optimization of the ride control systems for high speed planing monohulls [52] where their simulations demonstrated improvement in motion behaviour of a fast planing vessel with a ride control system sailing in head waves [52]. Rijikens et al. also investigated the hydrodynamic performance of a new transom-interceptor configuration to control the motion behaviour of a fast ship in waves in 2013 [53] where it was found that the new transom interceptor configuration leads to reduction of accelerations which contributes to a more favourable sea keeping performance of the ship [53].

1.1.3 Research objectives

Although some investigations into ship motions and loads as well as ship motion control systems on fast ships have been undertaken by numerical computations, model experiment and full-scale sea trials [2–7, 9–110], there is still limited knowledge on the mechanisms of the whole motion control system and also the influence of the ride control systems on the motions and structural loads of the vessel has had only limited research undertaken. In particular, the best control algorithm for linking detected ship motions to control surface activity has yet to be determined. In order to understand and optimise the motion control system further investigation is therefore required to accurately determine the effect of the control algorithm on the ship motions and loads. The overall objective of the current research is to evaluate the effect of the ride control algorithm on motions and loads in waves under more controlled conditions than is possible at full scale. The motions and loads data at model scale, in conjunction with full scale sea trials data and numerical computations will ultimately assist in the optimisation of motion control system algorithms to improve ship motions, passenger comfort and reduce structural loads.

1.2 Scope of work

The present study seeks to identify the influence of ride control systems on the motions and loads response of an existing 1/44.8 scale 2.5 m hydroelastic segmented catamaran model of the 112 m INCAT Tasmania high-speed wave-piercing catamaran in head seas. The scope of work undertaken during this research project is thus summarised as follows:

- The 2.5 m hydroelastic segmented catamaran model was calibrated, modified and set up prior to the installation of the model scale ride control system.
- A model scale T-Foil and two model scale stern tabs were developed to fit to the catamaran model.
- The lift and drag characteristics as well as the frequency response of the model scale T-Foil were studied by both static and dynamic tests (AlaviMehr et al. [111]).
- The step and frequency responses of the catamaran model to the ride control system were investigated by calm water open-loop test in order to assist with the closed-loop active control system (AlaviMehr et al. [112]) and the relative control gains that are to be used with different control algorithms.
- An appropriate combination of control movements to excite the model only in heave or only in pitch was investigated in order to form the basis of setting the gains of the ride control system to implement different control algorithms, such as pitch control, local control and heave control (AlaviMehr et al. [112]).
- A numerical two Degree of Freedom (DOF) rigid-body simulation was developed to theoretically evaluate the experimental step and frequency response results (AlaviMehr et al. [112]).
- A series of towing tank model tests was carried out in regular waves at different wave heights and frequencies in order to investigate the influence of different ride control algorithms on the motions response of the catamaran model (AlaviMehr et al. [113]).
- Six different algorithms were developed to activate the model scale ride control surfaces in a closed loop control system: heave control, local control and pitch control, each in a linear and nonlinear version. These were compared with a passive and no ride control system (AlaviMehr et al. [113]).
- The heave and pitch motions of the catamaran model were measured and presented as Response Amplitude Operators (RAOs), acceleration response and Response Phase Operators (RPOs) (AlaviMehr et al. [113]).
- The influence of the ride control system on the model structural loads including centre bow forces and demihull bending moments was investigated by analysing the data obtained

from the strain gauges installed on the model centre bow and demihull links (AlaviMehr et al. [114]).

- The position of the centre bow slam force from the transom were presented as a function of wave height and wave encounter frequency for different ride control algorithms (AlaviMehr et al. [114]).
- The centre bow motion during the slamming process was investigated by using the heave and pitch motions data obtained during the towing tank tests performed in regular seas in order to study the slamming kinematics.
- A strain energy analysis was carried out in order to investigate the energy of the slam force transmitted to the centre bow and demihull elastic links of the catamaran model.
- Conclusions are drawn and recommendations made on the optimum ride control algorithm against a variety of objectives.

Chapter 2

Hydroelastic Segmented Catamaran Model Set-up

2.1 Introduction

The model used for this research project is the Hydroelastic Segmented Catamaran Model (HSM) which was designed, built and used by a team at the University of Tasmania. A check up, calibration, modification and set-up was performed prior to installing the model scale ride control system into the HSM. This chapter presents details of the HSM set-up including modification of instrumentation and calibration. The HSM was designed and constructed in order to represent the identical scaled dimensions of the 112 m INCAT catamaran vessel with a design displacement of 2500 t. A scale ratio of 1/44.8 was defined on the basis of criteria such as towing tank size and capabilities, which led to a model with the length of 2.5 m and mass of 27.8 kg [3]. This model, which is conceptually a combination of the hydroelastic model type and the segmented hull type, was designed to simulate ship hydroelasticity and to measure motions, wave-induced loads and structural vibratory responses [115]. In order to achieve this, the catamaran model was developed using rigid segments and elastic connections [3]. The HSM was segmented into seven separate rigid body sections, with each demihull segmented into three distinct parts consisting of aft, midship and forward segments. Another section was located between the starboard and port forward demihulls, defined as the centre bow. The centre bow was separated from the forward demihulls in order to isolate the slamming loads acting on the bow of the model [3]. There are two longitudinal aluminium backbone beams, two midship transverse beams and two centre bow transverse beams. The separate segments of the hull were joined using aluminium elastic links (Figure 2.1 from Lavroff [3]).

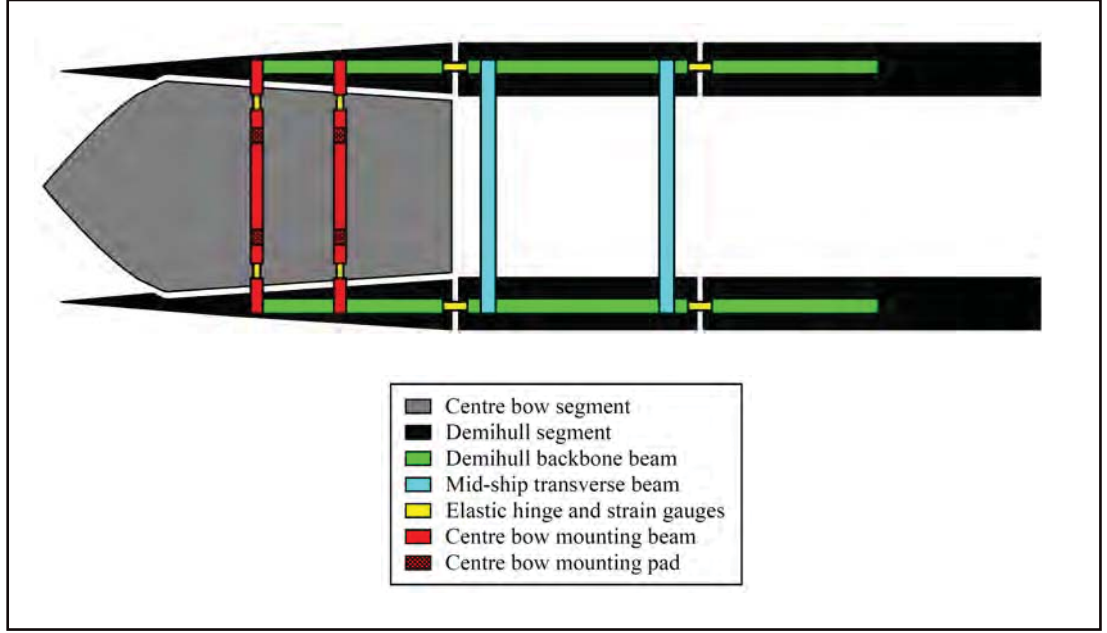


Figure 2.1: Schematic diagram of hydroelastic segmented catamaran model.

2.2 Centre bow calibration and modification

2.2.1 Introduction

As can be seen in Figure 2.1, the elastic links were located in each of the centre bow transverse beams to either side of the main vessel centreline and were fitted with strain gauges to measure the bending strains. Figure 2.2 (from Lavroff [3]) shows the elastic link. The elastic links had a rectangular section with strain gauges mounted on top and bottom surfaces. Each pair of strain gauges was installed in a half bridge configuration so that the strain differential indicated the bending moment of the link. The strain differential measured at each elastic link was then a function of the bending moment and the elastic link cross section properties given by:

$$\epsilon = \frac{My_l}{EI} \quad (2.1)$$

where ϵ = differential strain measured on the elastic link, M = bending moment, y_l = distance between strain gauges on a link (depth of the flexible link cross section), E = elastic modulus and I = second moment of area of the link cross section about its axis of bending. Therefore, the bending moment of each elastic link could be easily calculated by acquiring the differential strain on each elastic link and using the link properties, hence

$$M = \epsilon \frac{EI}{y_l} \quad (2.2)$$

The microstrain signal was acquired using the National Instruments Compact RIO (cRIO) shown in Figure 2.3. There were four slots located on the cRIO chassis to accommodate the

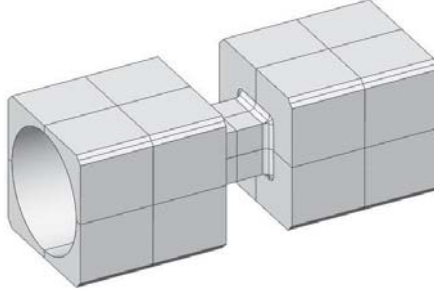


Figure 2.2: Elastic link used to connect the segments.

cRIO signal conditioning modules. The modules consisted of $2 \times$ NI cRIO-9215 analog modules and $2 \times$ NI 9237 strain gauge modules. The strains measured in the centre bow were acquired by $2 \times$ NI 9237 strain gauge modules labeled slot A and slot B.



Figure 2.3: National Instruments Compact RIO.

With reference to Figure 2.1, the applied load acting on the centre bow of the catamaran model was distributed between the two centre bow transverse beams. Figure 2.4 shows a schematic diagram of the applied load acting on each centre bow transverse beam. Each transverse beam incorporated two elastic links located on the starboard and port sides at locations with bending moments M_1 and M_2 . Both outboard ends of the transverse beam were mounted to pinned connections that were hard mounted to the port and starboard demihull backbone beams. Strain gauges were installed on each of the elastic links and were separated by a distance, b . The port and starboard strain gauge measurement positions were located at a distance, a , from the pinned connections. Strains were measured at each of the elastic links for the evaluation of bending moments, M_1 and M_2 . The force acting on the forward or aft transverse beam, F , and the force position, d , were calculated on the basis of the magnitude and position of the measured bending moments:

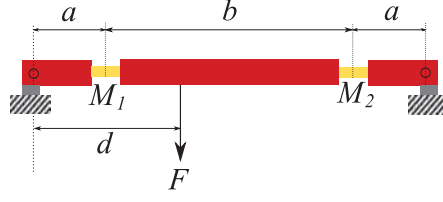


Figure 2.4: Schematic diagram of the centre bow transverse beam showing the force acting on each beam.

$$F = \frac{M_1 + M_2}{a} \quad (2.3)$$

$$d = \frac{M_2(2a + b)}{M_1 + M_2} \quad (2.4)$$

In calibration tests the loading would be symmetric and so $d = (2a + b)/2$ should apply subject to accuracy of the measurement system. Figure 2.5 shows a schematic diagram of the transverse beams for the evaluation of the total force acting on the centre bow. The forward and aft transverse beams were pinned to the port and starboard demihull backbone beams and separated by spacing, c . The total force acting on the centre bow, F_T , was the summation of the forces acting on the forward transverse beam, F_1 , and the aft transverse beam, F_2 (2.5). The longitudinal position of the total force, x_F , was calculated based on these known parameters (2.6),

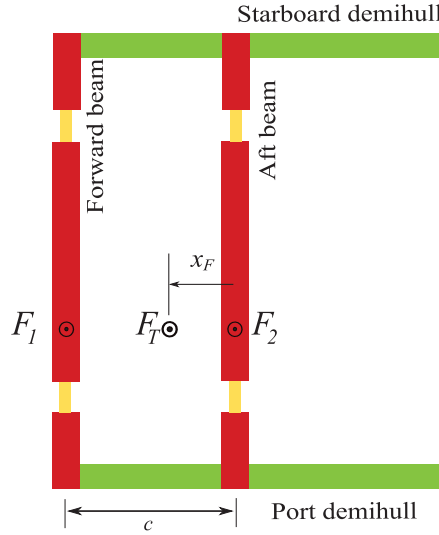


Figure 2.5: Schematic diagram of the centre bow transverse beams for the evaluation of the total force acting on the centre bow and its location.

$$F_T = F_1 + F_2 \quad (2.5)$$

$$x_F = \frac{F_1}{F_1 + F_2} c \quad (2.6)$$

For the centre bow calibration the HSM was turned upside down and placed on a horizontal flat bench so that the centre bow was free to move in the vertical direction (Figure 2.6). Calibration loads were applied to the centreline of the HSM at six positions on the centre bow using a loading beam including six hooks (Figure 2.7). Figure 2.8 shows a schematic diagram of the locations of the applied calibration loads on the catamaran model. Loads were applied in the range of 0 – 25 kg in 2.5 – 5 kg increments depending upon the location of the load and the magnitude of the strain gauge response so as to remain within the yield strain of the centre bow forward transverse beam elastic link instrumentation. The aluminium used for the manufacture of the elastic links was a 6060 T5 grade alloy with a yield strain of approximately 1471 microstrain [3].



Figure 2.6: The model set-up on a horizontal flat bench for calibration.

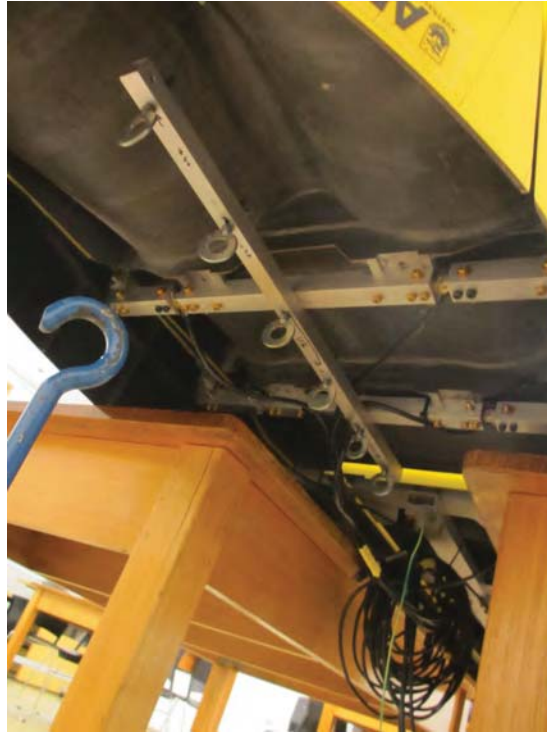


Figure 2.7: Loading beam installed on the centre bow to apply load at six positions.

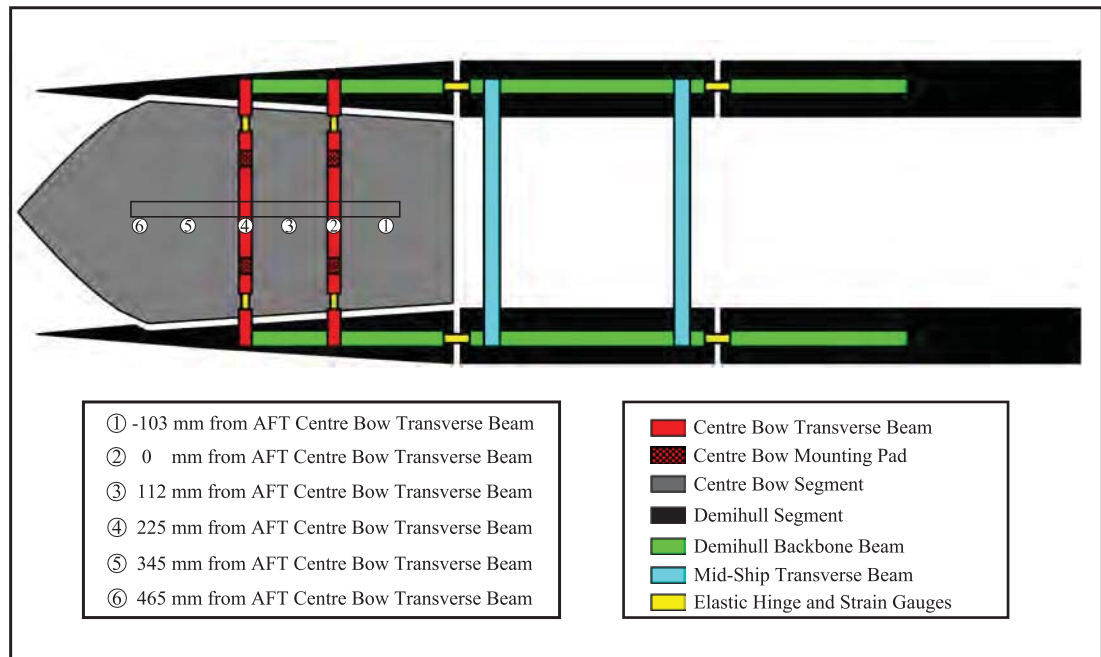


Figure 2.8: Locations of the applied calibration loads on the model.

2.2.2 Review and modification of the existing instrumentation

Review of the strain gauges

Strain gauges were installed on the elastic links to measure the load induced strains and the structural bending moments. Figure 2.9 shows a photograph of the elastic link instrumented with strain gauges. The existing strain gauge system was checked in detail as it had suffered



Figure 2.9: Photograph of an elastic link instrumented with strain gauges.

water exposure and the previous user had reported problems of electronic drift and noise. Figure 2.10 shows the raw microstrain data obtained from the centre bow elastic links for calibration loads applied at the aft centre bow transverse beam. It should be noted that the measured strain data shown for all calibration tests was the average magnitude of the differential strain measured on the elastic links. Although the calibration loads were applied at the centreline of the model it was found from the raw data presented in Figure 2.10 that there was some asymmetric bending at the forward port and starboard elastic links, as well as the aft port and aft starboard elastic links. In contrast, the forward port and aft starboard elastic links produced symmetric bending which showed that their strain gauges were communicating with each other. After investigating this issue by using a multimeter it was found that the strain gauges installed on the forward port and aft starboard elastic links were electrically connected to the elastic links and they needed to be isolated.

Modification of the strain gauges

As explained above, it was found that the strain gauges installed on the forward port and aft starboard elastic links were electrically connected to the elastic links and they were communi-

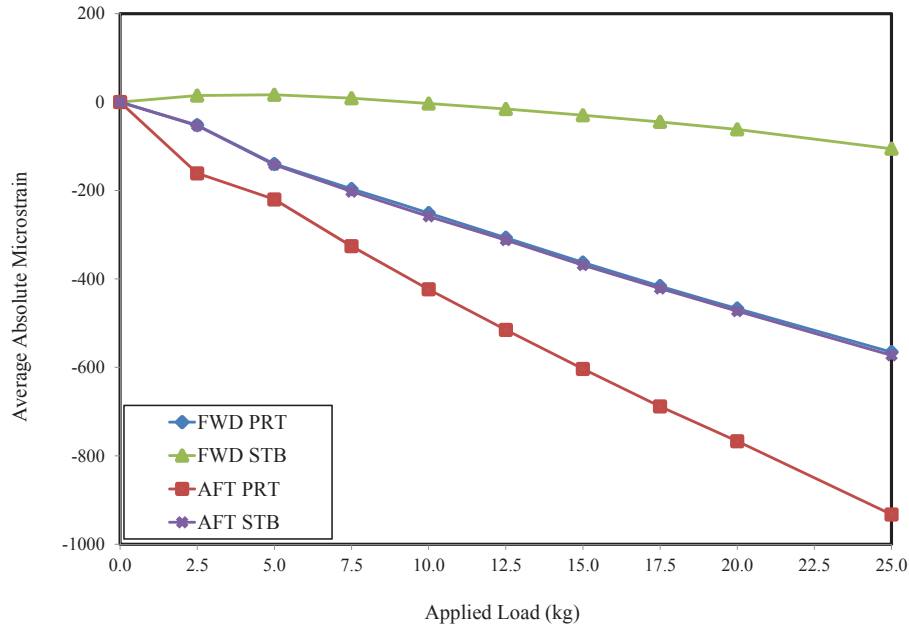


Figure 2.10: Raw strain gauge data for calibration loads applied at the aft transverse beam.

cating with each other. As the acquired microstrain via those strain gauges were not correct, they were replaced by new strain gauges. Figure 2.11 shows a photograph of the new strain gauge installed on the aft starboard elastic links. By checking the new strain gauges before continuing the calibration tests, it was found that the new strain gauges were working properly.

Review of the cRIO chassis and NI 9237 modules

As explained in Section 2.2.1, the strains measured in the centre bow were acquired by $2 \times$ NI 9237 strain gauge modules inserted in two slots (A and B) of the National Instruments Compact RIO (cRIO). During the calibration tests, it was observed that the acquired data were noisy and the solution to this problem was to ground the elastic link by attaching a cable to the aluminium frame and connecting it to earth as the elastic link and the aluminium frame had acted as an antenna and received electrical noise that was in the surrounding area. Although the resulting output signal noise was subsequently reduced by the grounding of the elastic links, the results were still unreasonable as sometimes the observed noise during the data acquisition was about 120 microstrain, as shown in Figure 2.12.

New NI compact DAQ chassis and new NI 9237 modules

At discussed above, it was observed that the acquired data via cRIO chassis and NI 9237 modules were noisy as sometimes the observed noise was about 120 microstrain during the

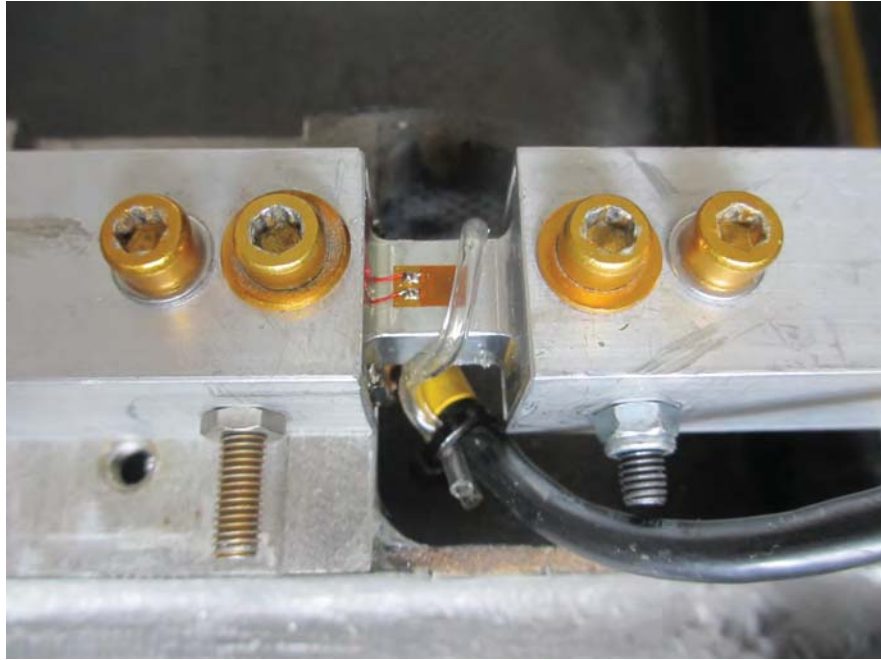


Figure 2.11: Photograph of the new strain gauge installed on the aft starboard elastic links.

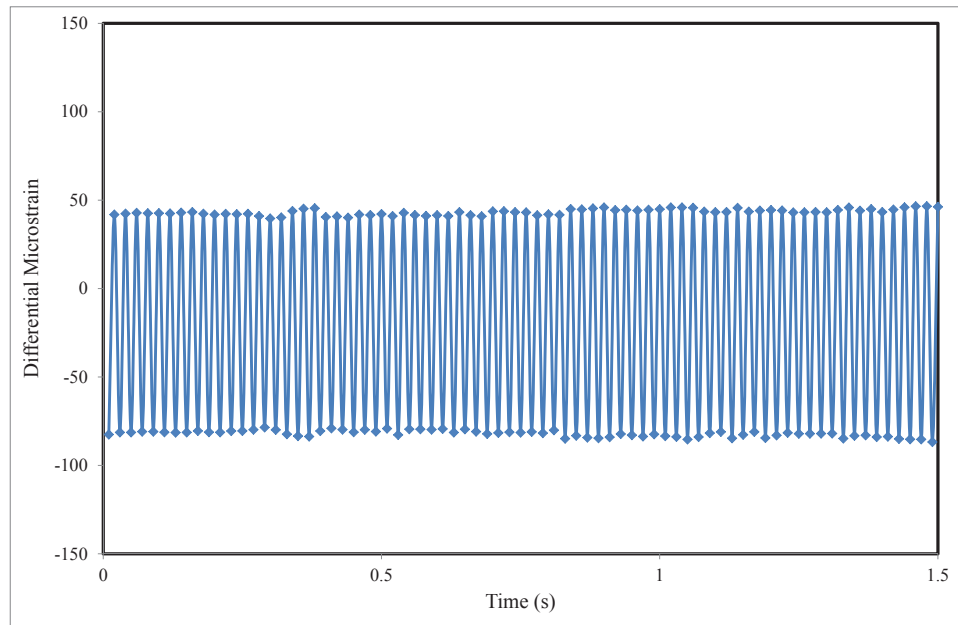


Figure 2.12: Differential microstrain acquired by cRIO chassis using NI 9237 modules showing about 120 microstrain noise during acquisition time.

acquisition time. Therefore, a new National Instruments (NI) 9174-USB compact DAQ (cDAQ) chassis with four NI modules consisting of one NI 9263 Analogue Output (AO), one NI 9201 Analogue Input (AI) and two NI 9237 strain gauge modules was purchased. The new NI cDAQ 9174 chassis, which is shown in Figure 2.13, was connected to the computer through a USB connection and a LabVIEW program was written to acquire data (whereas the cRIO chassis had its own program inside the chassis and it was connected to the computer via an Ethernet cable). Figure 2.14 shows the differential microstrain acquired by the new NI cDAQ chassis using the new NI 9237 Modules. As can be seen, the observed noise during the acquisition time was about 3 – 4 microstrain. In addition, by comparing the Figure 2.14 and Figure 2.12 it can be seen that the observed noise using the cRIO and the previous NI 9237 modules was alternated between two values. This demonstrated that the cRIO and the previous NI 9237 modules were not working properly.



Figure 2.13: Photograph of the new NI 9174-USB cDAQ chassis with four NI modules consisting of one NI 9263 AO, one NI 9201 AI and two NI 9237 strain gauge modules.

Review of the pin joint mounts

Figure 2.15 shows the loads measured by the strain gauge when different loads were applied at varying locations on the centre bow. As can be seen there was a large deviation from the 1:1 line and the magnitudes of measured loads were not satisfactorily accurate. In addition, Figure 2.16 shows a significant deviation in the distance of the measured loads from the aft transverse beam compared with the distance of the applied loads from the aft transverse beam. The large scatter in the results is (as explained earlier in relation to Figure 2.10) due to asymmetric bending at the forward port and forward starboard elastic links as well as the aft port and aft

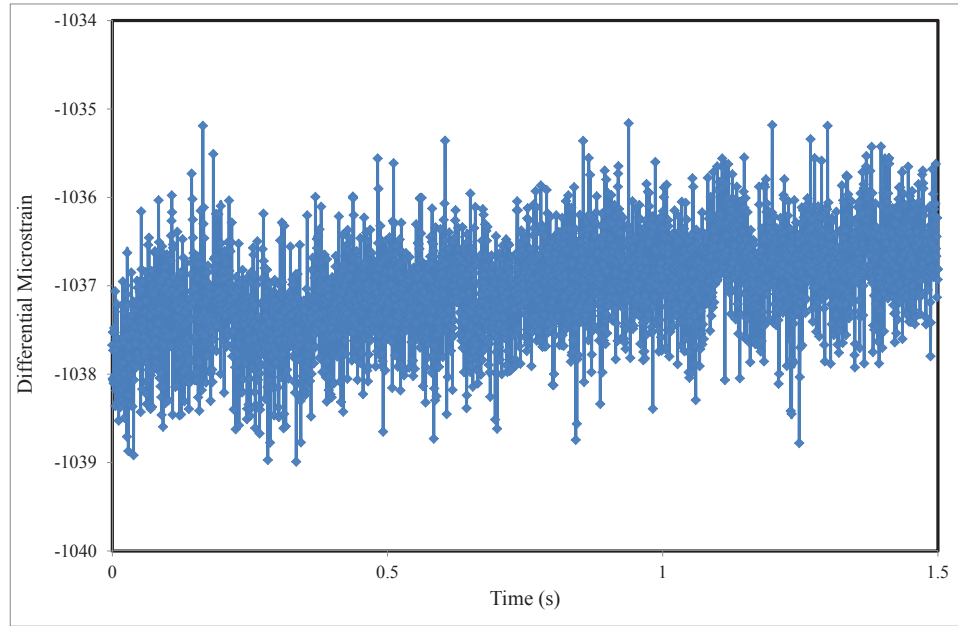


Figure 2.14: Differential microstrain acquired by the new NI cDAQ chassis using the new NI 9237 Modules showing 3-4 microstrain noise during the acquisition time.

starboard elastic links.

To investigate all the above mentioned problems, the loading beam (shown in Figure 2.7) and the centre bow were removed and the loads were applied to the centre bow transverse beams directly. In this case, a 6 kg load was applied on the aft transverse beam and the microstrain was measured for both transverse beams. The measured average strain on the aft transverse beam was 280 microstrain and the measured average strain on the forward transverse beam was 50 microstrain whereas the load was applied just to the aft transverse beam and the strain gauges on the unloaded forward transverse beam should not show any strain. The same result was obtained by applying the load on the forward transverse beam and measuring the microstrain on the aft transverse beam. It was concluded that the two transverse beams were constrained and the load on one beam affected the other beam. To check this issue, all the 6 mm bolts at the pin joint mounts were replaced by 5 mm bolts in order to loosen the pin joint mounts. In this case, again a 6 kg load was applied on the aft transverse beam and the microstrain was measured for both transverse beams. The measured average strain on the aft transverse beam was 284 microstrain and the measured average strain on the forward transverse beam was 2 microstrain. Also, a 6 kg load was applied on the forward transverse beam and the microstrain was measured for both transverse beams. The measured average strain on the aft transverse beam was 4 microstrain and the measured average strain on the forward transverse beam was 282 microstrain. It was concluded that when a transverse beam was loaded it deformed in

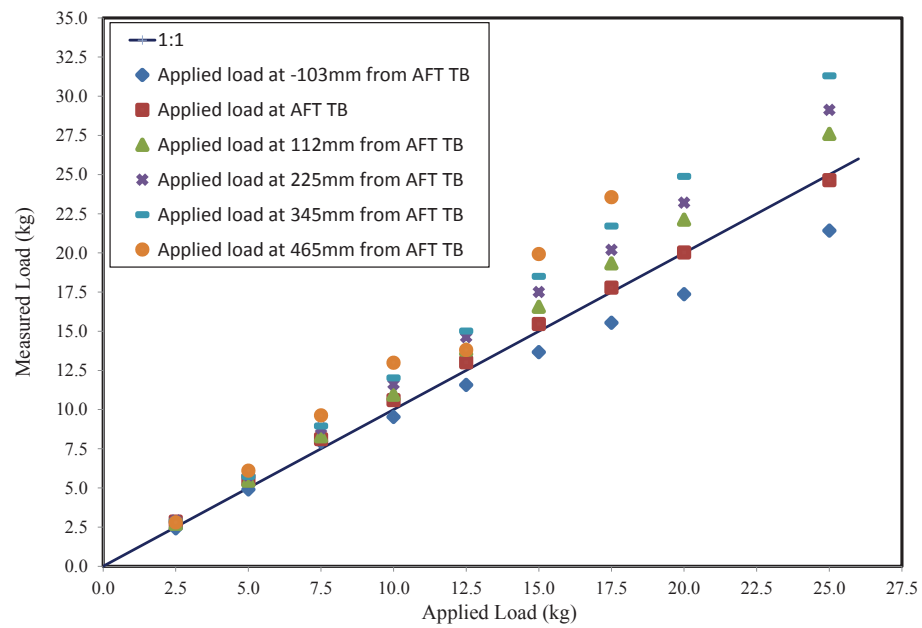


Figure 2.15: Centre bow calibration results: measured load as a function of the calibration applied load.

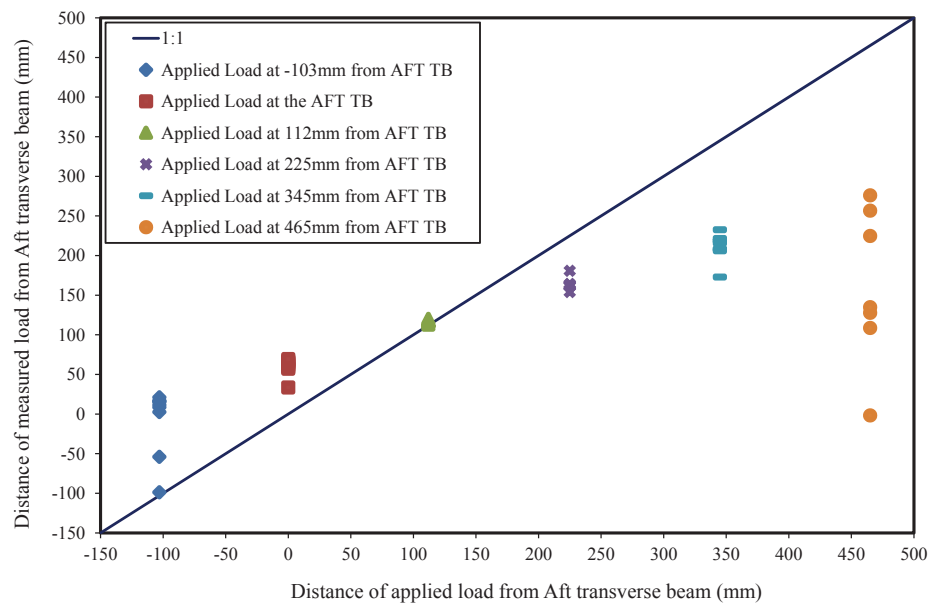


Figure 2.16: Distance of the measured loads from the aft transverse beam vs distance of the applied loads from the aft transverse beam.

bending shape and the pin joints displaced sideways a small amount owing to the rigid right angle connection at the transverse beam end (Figure 2.17). This caused a force (F') in a horizontal direction on the backbone beams and as can be seen in Figure 2.18 this induced force (F') could be transferred to the unloaded transverse beam through its pin joint mounts. Thus the induced force (F') on the unloaded transverse beam caused a bending moment on the beam as the pin joints were not in the same plane of the elastic links installed on the transverse beams (Figure 2.19). Although the above-mentioned constraint on the beam was

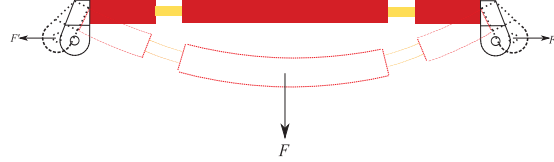


Figure 2.17: Bent shape of the transverse beam showing the induced sideways force.

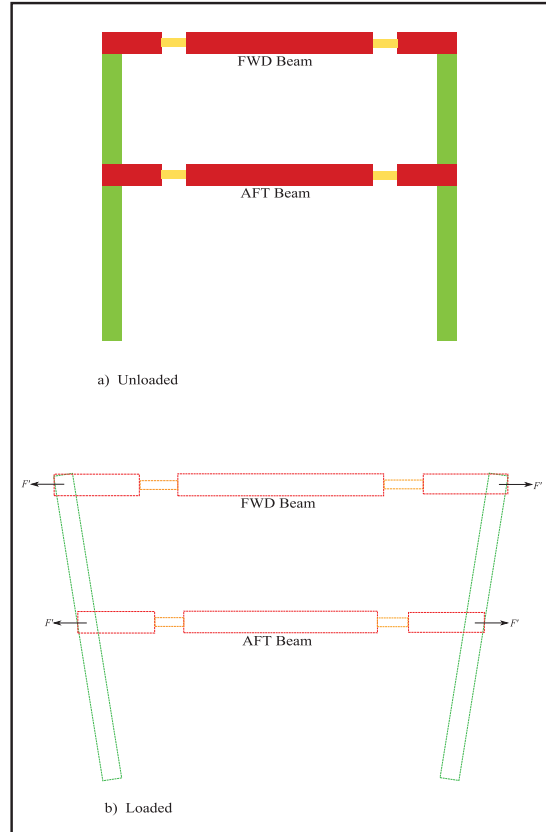


Figure 2.18: Schematic diagram of the transverse beams and backbone beams: (a) unloaded. (b) loaded and deformed.

solved by using the thinner bolts for the pin joint mounts, these loose bolts should not be used for the pin joint mounts during the model testing in the towing tank as the pin joints should not be free to have vertical motions on waves. To resolve this issue, all the pin joint mounts were fixed using previous 6 mm bolts and a 1 mm slot was made on one pin bush to make

that pin free to move horizontally (Figure 2.20). Figure 2.21 shows a photograph of the pin joint mount showing a 1 mm slot on the pin bush. Although better results were obtained by making the slot on the pin bush of the pin joint mount, the pin joint mounts still needed to be changed as the resultant transverse horizontal force on the pins when the sideways movement was resisted by the backbone beams contributed an additional moment to the elastic link since the elastic link was above the horizontal plane of the pin as shown in Figure 2.19. When the forward centre bow transverse beam and the aft centre bow transverse beam have different loads there was a difference in the moments of the two transverse beams. The end result was that the force appeared to be nearer to the midpoint between two transverse beams than it actually was. The resolution was to relocate the pin joints at the same level as the transverse beams by moving the pivot points upwards and away from the backbone beams to the level of the transverse beams. Thus any sideways loads due to small model deformations under load will not contribute bending to the elastic links but just a compression force which would be balanced out by the strain gauges which were set up to indicate differential strain and thus to show only moments and not compression in the elastic links.

Modification of the pin joint mounts

As explained above, when a transverse beam was loaded it deformed into a bent shape and the pin joints displaced sideways a small amount owing to the rigid right angle connection at the transverse beam end, which induced a lateral force in the backbone beams and this induced force could be transferred to the unloaded transverse beam through its pin joint mounts. Thus the induced force on the unloaded transverse beam caused a bending moment on the beam, as the pin joints were not in the horizontal plane of the elastic links installed on the transverse beams. As shown in Figure 2.19, the horizontal plane of the pin joints was a distance of h from the horizontal plane of the elastic links installed on the transverse beam. This can be seen also in the shown photograph of the existing pin joint mount in the Figure 2.21. Therefore, it was decided to design a new pin joint mount having the pin joint and the beam in one horizontal plan. Figure 2.22 shows the CAD design of the new pin joint mount including two parts. Figure 2.23 shows the photograph of the manufactured new pin joint mount (Part 1) which was mounted on the backbone beam and Figure 2.24 shows the photograph of the manufactured new pin joint mount (Part 2) which was mounted on the transverse beam. Figures 2.25 and 2.26 show photographs of the same parts of the previous pin joint mounts and the new pin joint mounts for comparison. In addition to the different pin joint position, the new pin joint mounts were lighter than the previous pin joint mounts as the total weight of the four pin joint mounts was decreased by 200 g. Figure 2.27 shows a photograph of the new pin joint mounts installed on the centre bow.

To compare the results between the new pin joint mount configuration and the old pin joint mount configuration, all the calibration test conditions were repeated. The loading beam (shown in figure 2.7) and the centre bow were removed and the loads were applied to the centre bow



Figure 2.19: Schematic diagram of the transverse beam showing induced force and bending moment.

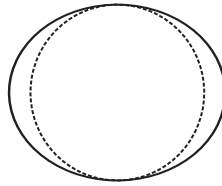


Figure 2.20: Schematic diagram of the horizontal slot on the pin bush.



Figure 2.21: Photograph of the 1 mm horizontal slot on the pin bush.

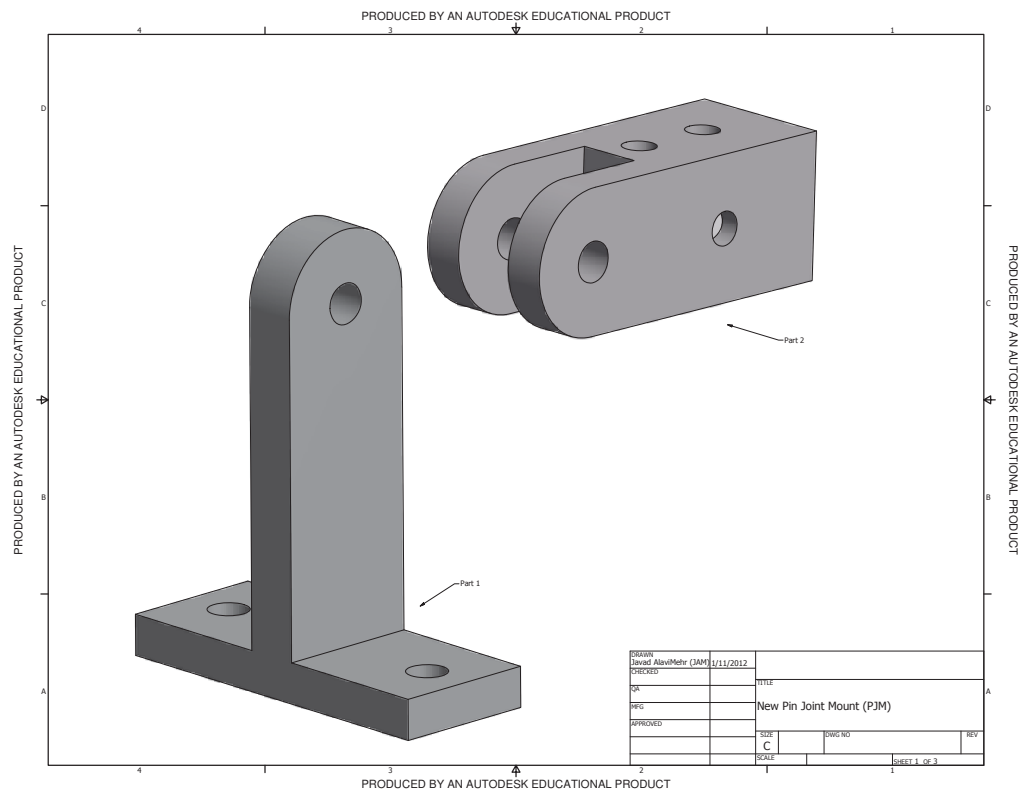


Figure 2.22: CAD design of the new pin joint mount.

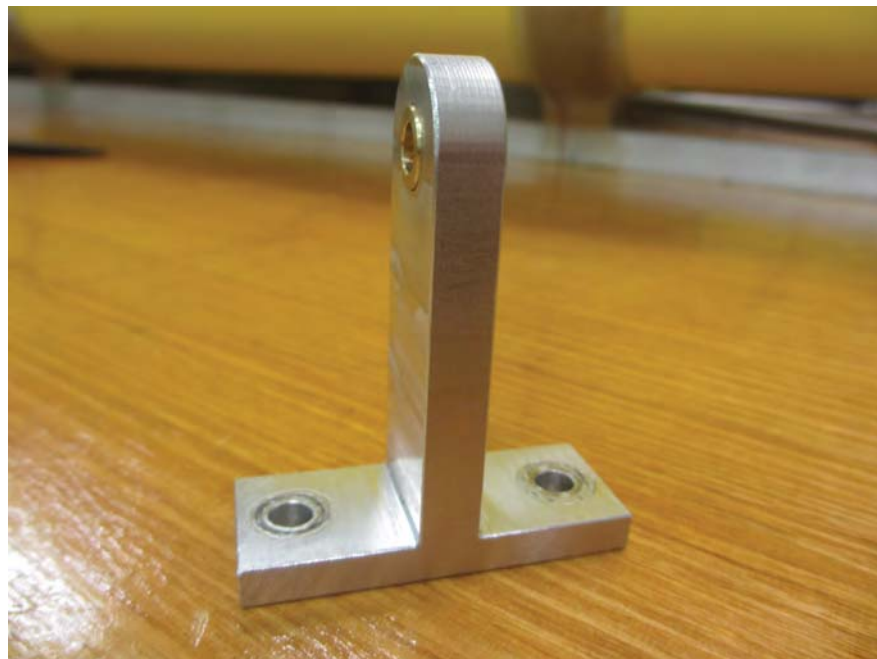


Figure 2.23: Photograph of the manufactured new pin joint mount - Part 1 which was mounted on the backbone beam.



Figure 2.24: Photograph of the manufactured new pin joint mount - Part 2 which was mounted on the transverse beam.

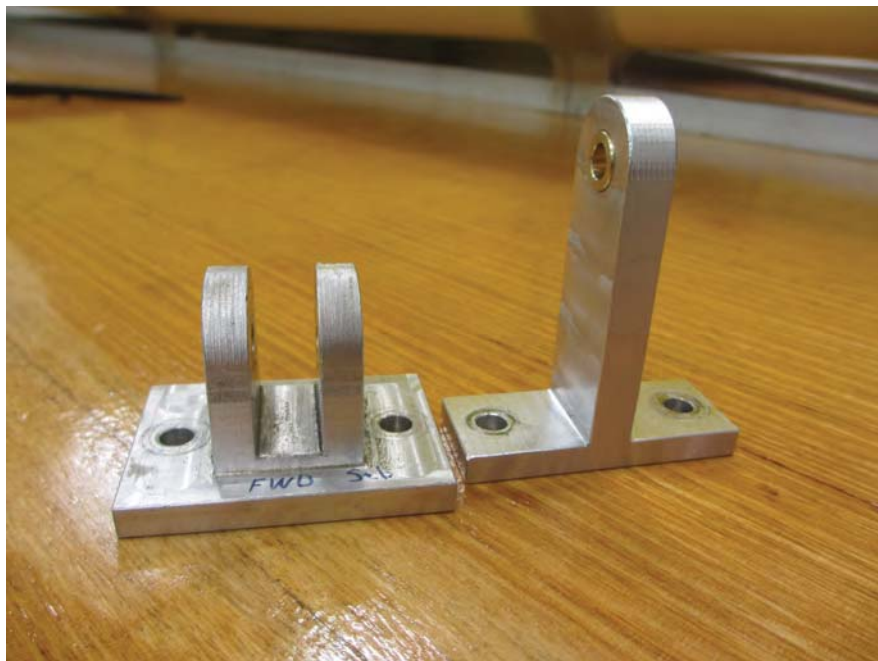


Figure 2.25: Photograph of the previous pin joint mount (left) and the new pin joint mount (right) - Part 1 which was mounted on the backbone beam.



Figure 2.26: Photograph of the previous pin joint mount (left) and the new pin joint mount (right) - Part 2 which was mounted on the transverse beam.

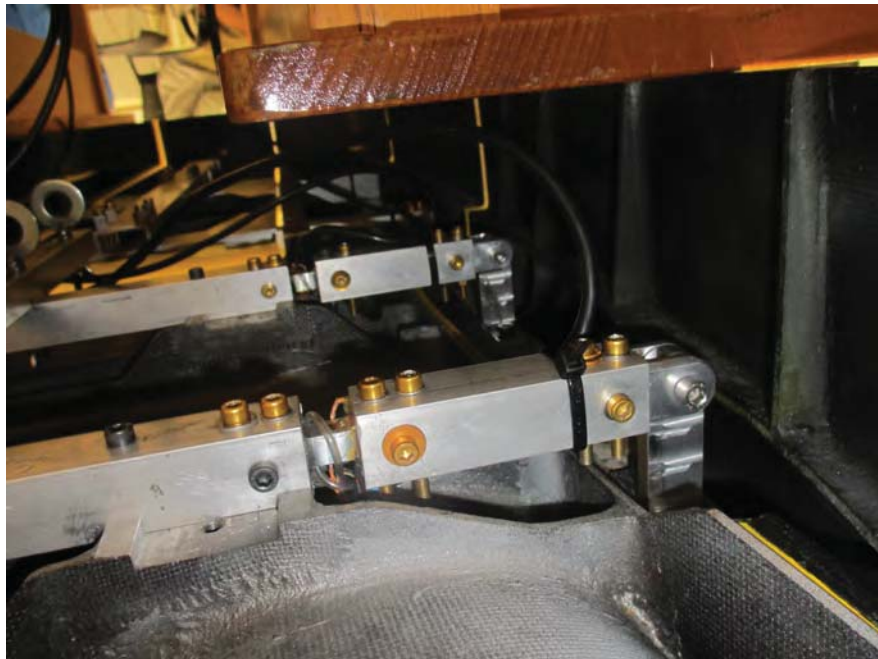


Figure 2.27: Photograph of the new pin joint mounts installed on the centre bow.

transverse beams directly. In this case, a 6 kg load was applied on the aft transverse beam and the microstrain was measured for both transverse beams. The measured average strain on the aft transverse beam was about 300 microstrain and the measured average strain on the forward transverse beam was about 0.5 microstrain. A similar result was observed by applying the load on the forward transverse beam and measuring the microstrain on the aft transverse beam as a 6 kg load was applied on the forward transverse beam and the microstrain was measured for both transverse beams. The measured average strain on the aft transverse beam was about 1.5 microstrain and the measured average strain on the forward transverse beam was about 299 microstrain. Following this reasonable outcome after replacing the new pin joint mounts, it was decided to repeat the full calibration tests using the new configuration.

2.2.3 Calibration tests

In order to commence the centre bow calibration tests following the modifications, the HSM was turned upside down and placed on a horizontal flat bench as the centre bow was free to move in the vertical direction (Figure 2.6). Calibration loads were applied to the centre line of the HSM at six positions on the centre bow using a loading beam including six hooks (Figure 2.7). Figure 2.8 shows the schematic diagram of the HSM showing the locations of the applied calibration loads. Calibration loads were applied at -103 mm, 0 mm, 112 mm, 225 mm, 345 mm and 465 mm from the aft centre bow transverse beam as shown in Figure 2.8. Loads were applied in the range of 0 – 25 kg at 2.5 kg increments depending upon the location of the load and the magnitude of the strain gauge response to remain within the yield strain of the centre bow forward transverse beam elastic links instrumentation. In order to avoid any drift error during the data acquisition, the microstrain was acquired twice for each load at each position; first when it was loaded and the second when it was unloaded. Then the difference of two data values was considered as the absolute microstrain for that load at that position. Figure 2.28 shows the results of the catamaran model centre bow calibrations showing the measured loads on the basis of the Equations 2.3 and 2.5. In addition, Table 2.1 shows the centre bow instrumentation error using Root Mean Square (RMS) method on the basis of the data collected during the centre bow calibrations.

It can be seen that there is a small systematic discrepancy between the applied loads on the centre bow and the relative measured loads. This is attributed to the characteristics of the elastic links which influence the measured loads. The results of Figure 2.28 can then be used as a calibration of the elastic links, the true loads being 5% smaller than the measured loads. The centre bow calibration data for each load case was analysed using a spreadsheet and calibration factors were evaluated for the magnitude of the applied calibration load. The calibration factors were evaluated for the magnitude of the load on each transverse beam individually. Thus, twelve calibration factors were obtained as the loads were applied at six positions of the centre bow and the forces were measured at both forward and aft transverse beams for each

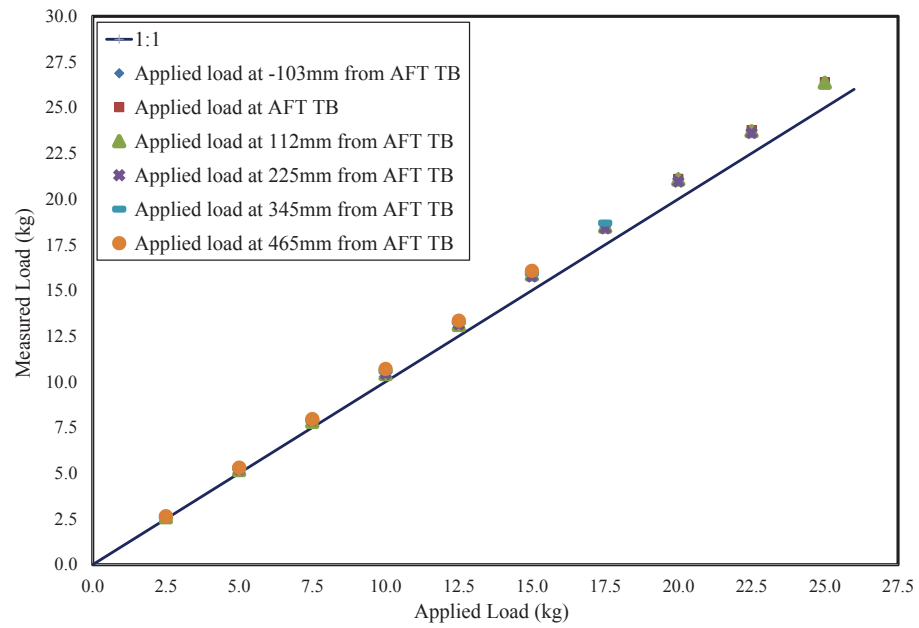


Figure 2.28: Catamaran model centre bow calibration results by using the new instrumentation: measured load as a function of the calibration applied load.

Table 2.1: Centre bow instrumentation error on the basis of the data collected during the centre bow calibrations.

Centre bow calibration			
Applied load	Measured load (kg)		RMS error
(kg)	Minimum	Maximum	(kg)
2.5	2.56	2.65	0.11
5.0	5.17	5.31	0.25
7.5	7.81	7.96	0.39
10.0	10.42	10.70	0.58
12.5	13.11	13.35	0.74
15.0	15.76	16.08	0.93
17.5	18.40	18.69	1.06
20.0	20.95	21.20	1.08
22.5	23.62	23.76	1.19
25.0	26.36	26.38	1.37
Average (kg)			0.77

applied load position. Table 2.2 shows the calibration factors for the magnitude of the load on each transverse beam for six applied load positions. Figure 2.29 shows the results of the cata-

Table 2.2: Calibration factors for the magnitude of the load on each transverse beam for six applied load positions.

Applied load position	Calibration Factors for	
Distance from AFT transverse beam (mm)	Measured load on FWD transverse beam	Measured load on AFT transverse beam
-103	0.95888	1.02751
0	1.00000	1.03538
112	1.05086	1.03897
225	1.01114	1.00000
345	1.01018	0.91531
465	1.01183	0.95992

maran model centre bow calibrations showing the measured load corrected by the calibration factors. It can be seen in Figure 2.29 that the magnitude of the measured loads corrected by the calibration factors are close to the magnitude of the applied loads. Also, Figure 2.30 shows the results of the catamaran model centre bow calibrations showing the position of the measured loads corrected by the calibration factors. It can be seen in Figure 2.30 that the position of the measured loads corrected by the calibration factors are in close agreement with the position of the applied loads. Clearly the altered design of the transverse beams, with the pivot point in the same plane as the transverse beam, successfully corrected the identification of the location of the applied force on the basis of the measured bending moment of the transverse beams.

The static loading tests on the model showed that the method used as illustrated in Figures 2.4 and 2.5 correctly identified the fore and aft location of the load on the bow using Equations 2.5 and 2.6 and that the pin mountings on the demihulls did not therefore transmit a significant torsional moment to the transverse bow support beams.

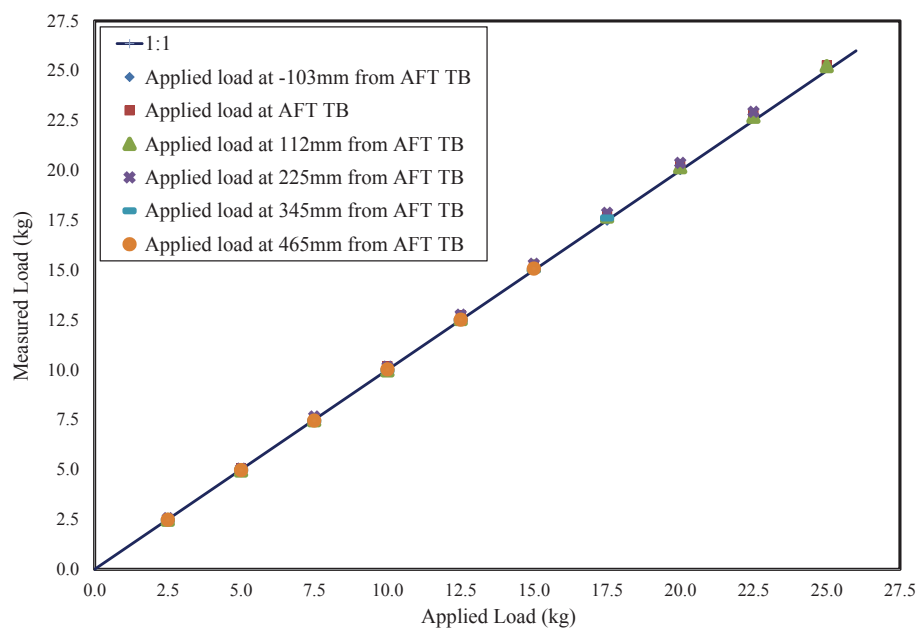


Figure 2.29: Catamaran model centre bow calibration results by using the new instrumentation: corrected measured load as a function of the calibration applied load.

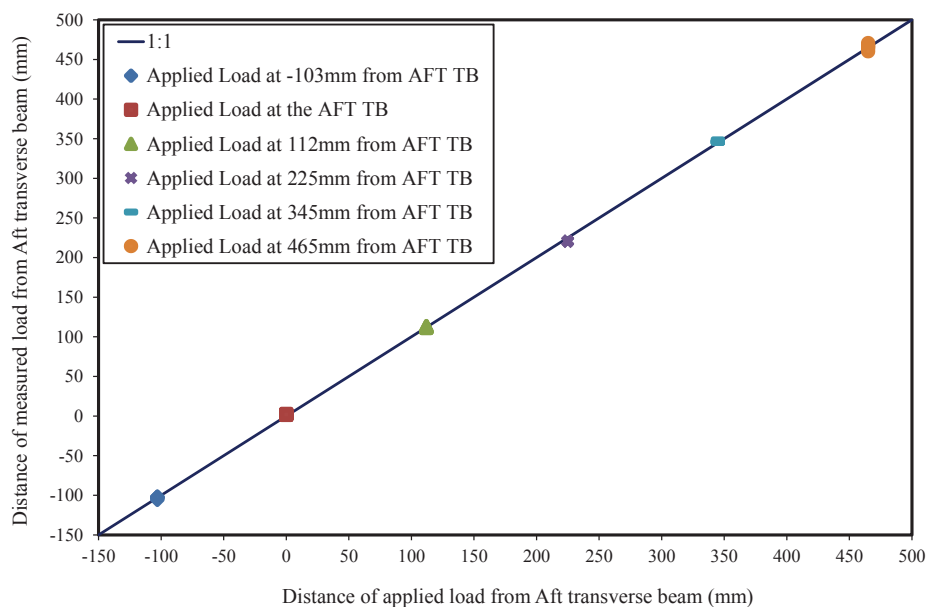


Figure 2.30: Distance of the corrected measured loads from the aft transverse beam vs distance of the applied load from the aft transverse beam.

2.3 Conclusions

During the calibration process of the centre bow of the 2.5 m hydroelastic segmented catamaran model it was found that the existing instrumentation needed to be replaced and that the layout of the transverse beams pin joint mounts needed to be revised. These modifications are summarised as follow.

The original strain gauges installed on the forward port and aft starboard elastic links were electrically connected to the elastic links and they were communicating with each other. As the acquired microstrain via those strain gauges were not correct, they were replaced by new strain gauges.

The acquired data via cRIO chassis and NI 9237 Modules were noisy as sometimes the observed noise was about 120 microstrain during the acquisition time. Therefore, a new National Instruments (NI) 9174-USB compact DAQ (cDAQ) chassis with four NI modules consisting of one NI 9263 Analogue Output (AO), one NI 9201 Analogue Input (AI) and two NI 9237 strain gauge modules were purchased. The new NI cDAQ 9174 chassis was connected to the computer through USB connection and a LabVIEW program was written to acquire data whereas the cRIO chassis had its own program inside the chassis and it was connected to the computer via Ethernet cable. Using the new NI cDAQ 9174 chassis and $2 \times$ NI 9237 strain gauge modules, the observed noise during the acquisition time was about 3 – 4 microstrain.

When a transverse beam was loaded it deformed in bending and the pin joints displaced sideways a small amount owing to the rigid right angle connection at the transverse beam end. This induced a force in the backbone beams and which was transferred to the unloaded transverse beam through its pin joint mounts. Thus the induced force on the unloaded transverse beam caused a bending moment on the beam as the pin joints were not in the horizontal plane of the elastic links installed on the transverse beams. Therefore, a new pin joint mount was designed having the pin joint and the beam in one horizontal plane. In addition to the different pin joint position, the new pin joint mounts were lighter than the previous pin joint mounts as the total mass of the four pin joint mounts was decreased by 200 g.

The centre bow calibration data for each load case was analysed using a spreadsheet and calibration factors were evaluated for the magnitude of the applied calibration load. The calibration factors were evaluated for the magnitude of the load on each transverse beam individually and then they were used for the correction of the measured load as well as the position of the measured load. It can be concluded from Table 2.2 that the position of the measured loads can be categorized in three parts. These categories are included of the aftward of the AFT transverse beam, between two transverse beams and forward of the FWD transverse beam. Then the calibration factors for the magnitude of the measured force on each transverse beam could be applied to correct the slam force observed at each part of the centre bow. Table 2.3 shows these calibration factors for the magnitude of the loads on each transverse beam at three locations on the centre bow.

Table 2.3: Calibration factors for the magnitude of the measured loads on each transverse beam at three parts of the centre bow.

Observed load position	Calibration Factors for	
	Measured load on FWD transverse beam	Measured load on AFT transverse beam
Aftward of the AFT transverse beam	0.95888	1.03144
Between two transverse beams	1.03100	1.03717
Forward of the FWD transverse beam	1.01105	0.93762

Therefore, the relevant calibration factors should be applied to correct the magnitude of the measured force on each transverse beam depending on the location of the measured force. The corrected measured forces on each transverse beam should then be applied to calculate the magnitude of the true slam force as well as its true location.

Chapter 3

Low Reynolds Number Performance of a Model Scale T-Foil

3.1 Introduction

Although active ride control systems have been installed on all full scale 112 m INCAT Tasmania wave-piercer catamarans, the 2.5 m hydroelastic segmented model did not originally include an active ride control system in the previous model tests [3,115]; stern tabs were statically mounted to correct bow up trim at speed and no T-Foil was fitted to the model. Therefore a model scale T-Foil was developed to fit to the model and the fixed tabs were replaced with moveable tabs. Figure 3.1 shows a photograph of the electrically activated model T-Foil, while Table 3.1 shows its specification. It is to be noted that the model scale T-Foil was pivoted within the model foil itself at the base of a rigid mounting strut whereas the full scale T-Foil and strut (Figure 1.4) were rigidly connected and were both mounted on a pivot within the hull. The model configuration was chosen so that the model pivot was located slightly ahead of the model T-Foil centre of pressure thereby minimising the power required to move the model foil. Given the limited power of the model servo-motor this arrangement maximised the response rate of the model system.

In order to optimise the ride control system and design an appropriate algorithm to control ship motions, it is necessary to effectively activate the control surfaces according to vessel response. Some studies of the lifting performance of model scale stern tabs have been previously undertaken at the University of Tasmania [107,108]. The present work investigates the lift and drag characteristics as well as the frequency response of the model T-Foil by both static and dynamic tests. As the T-Foil is to be used in the ride control system and its angle of attack is to be changed based on the measured unsteady heave and pitch motion and designated algorithms,

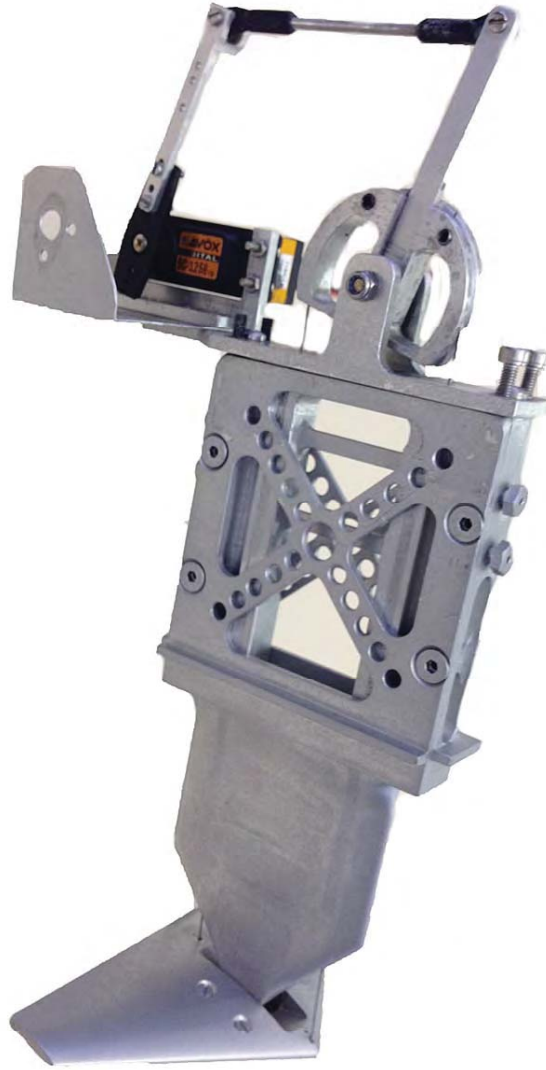


Figure 3.1: Electrically activated model scale T-Foil developed for the 2.5 m hydroelastic segmented catamaran model.

Table 3.1: Specifications of the full scale 112 m INCAT catamaran and 2.5 m scaled model T-Foil.

	112 m full-scale (m)	2.5 m model scale (mm)
Chord	2.63	58.68
Span	6.30	140.63

it was important to conduct dynamic tests on the T-Foil to investigate its performance prior to installation for testing on the 2.5 m hydroelastic catamaran model.

Owing to the small size of the model scale T-Foil the fluid flow characteristics are such that it operates at low Reynolds number and this creates uncertainty in predicting its lift performance. Predictions of lift performance are also complicated by the relatively low aspect ratio of the planform ($AR = 3.6$) which tapers strongly towards the foil tips. At a model test speed of approximately 2.7 m/s, simulating a full-scale speed of 35 knots, the T-Foil Reynolds number is 1.05×10^5 which is sufficiently large that the lift performance is not expected to be diminished by laminar separation [116]. In the present investigation the combined effect of both low Reynolds number and low aspect ratio on T-Foil performance for a realistic design is to be confirmed in terms of similar research on two dimensional low Reynolds number foils [117–120] and low aspect ratio lifting wing theory. It was expected from previous investigations that this model scale T-Foil will perform acceptably as a control surface on the bow of the 2.5 m model, but the precise detail of the lifting performance needed to be de ascertained. Whilst the primary application considered here is for the INCAT Tasmania wave piercing configuration, similar ride control systems can of course be applied to other types of vessels such as Trimarans and SWATHs. Foil immersion is in general sufficiently deep that Froude number is not significantly relevant to the performance of a submerged T-Foil.

To test the performance of the T-Foil prior to installing on the catamaran model, the T-Foil was instrumented to measure its lift and drag as well as its dynamic responses. This was undertaken as a function of angle of attack and water flow speed in a closed circuit circulating water tunnel.

3.2 Apparatus and instrumentation

All the experimental tests on the individual T-Foil were carried out in a closed circuit circulating water tunnel in the University of Tasmania Hydraulics Laboratory (Figure 3.2 from Barton [121]). The water tunnel has a working section with length of 1000 mm, width of 600 mm and a usable depth of 200 mm. The T-Foil model tests needed to be conducted in an open working section so that the free surface was at atmospheric pressure. When operated with an open working section, the water tunnel had not previously achieved velocities above 1.2 m/s with an acceptable flow quality [107]. However, a significant increase of velocity was achieved in the flow by Bell et al. [107] using a flow constriction flap as shown in Figure 3.3. A maximum flow velocity of 2.7 m/s was achieved by changing the angle of the constriction flap, hence the water depth.

T-Foil lift and drag force measurements were carried out using an AMTI 6 Degree of Freedom (DOF) load cell shown in Figure 3.4. The load cell was assembled on top of the T-Foil as shown in Figure 3.5. Figure 3.6 shows the set-up of the T-Foil and the load cell in the water tunnel. Using a LabVIEW program, the load cell output signals were acquired by a National

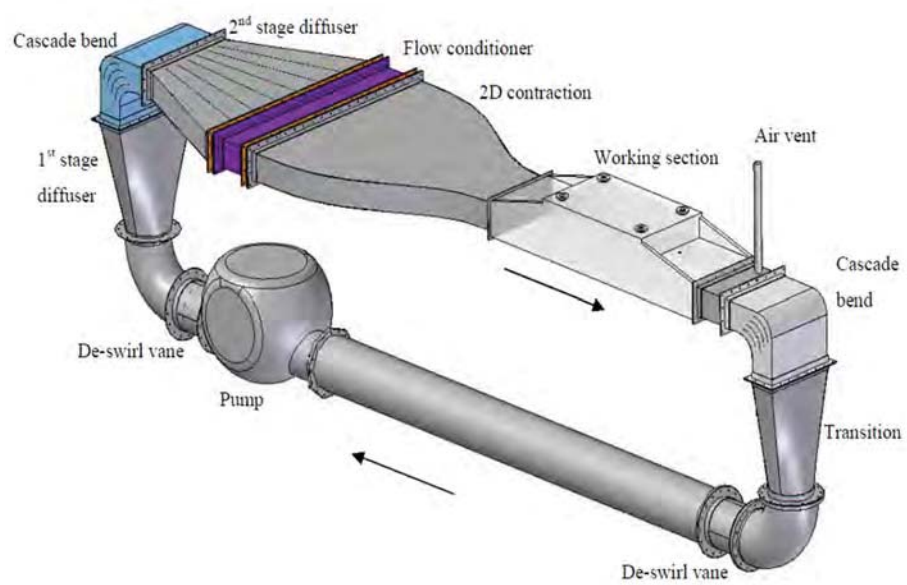


Figure 3.2: University of Tasmania water tunnel.



Figure 3.3: Circulating water tunnel flow constriction flap (flow is from left to right).

Instruments (NI) PCI-6221 DAQ card through an AMTI amplifier.



Figure 3.4: AMTI 6 DOF load cell-Model MC3A-100.

A servo-motor was used to activate the T-Foil and a potentiometer was used to measure the angular position of the T-Foil control surface. A National Instruments (NI) 9174-USB compact DAQ (cDAQ) chassis with two NI modules, NI 9263 Analogue Output (AO) and NI 9201 Analogue Input (AI), was used whilst running LabVIEW for both static and dynamic tests. The T-Foil angle of attack was demanded through the NI 9263 AO module and the NI 9201 AI module was used to acquire the potentiometer voltage in order to measure the actual instantaneous T-Foil angle of attack. The channel related to the potentiometer voltage in the NI 9201 AI module was directly connected to an AI channel of the NI PCI-6221 DAQ card in order to measure the true T-Foil angle of attack during force measurements.



Figure 3.5: Load cell set-up on top of the T-Foil.



Figure 3.6: T-Foil and load cell set-up in the circulating water tunnel (flow is left to right).

3.3 Calibration

Calibrations of the servo-motor and the potentiometer were carried out in order to find a relationship between demand voltage for the servo-motor and T-Foil angle of attack, and a relationship between output voltage from the potentiometer and T-Foil angle of attack. The T-Foil angle of attack was measured by a digital inclinometer with a resolution of 0.05° . The digital inclinometer was calibrated and oriented relative to the apparatus as the T-Foil chord line was parallel to the water surface at 0° . Figures 3.7 and 3.8 show the calibration graphs for potentiometer and servo-motor respectively, the system had good linearity. Equations 3.1 and 3.2 show these relationships respectively:

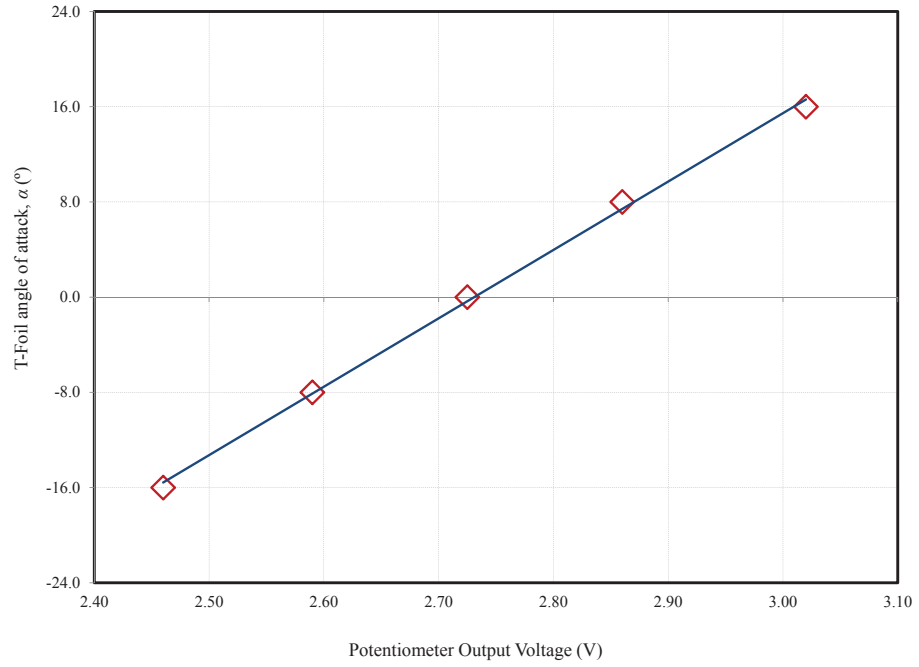


Figure 3.7: Relationship between T-Foil angle of attack and output voltage from the potentiometer.

$$\alpha = (57.46 \times V_{out}) - 156.93 \quad (3.1)$$

$$\alpha = (80.00 \times V_{in}) - 244.00. \quad (3.2)$$

The load cell was calibrated by applying a static load in the vertical (z -axis) direction of the load cell to find a relationship between lift and output voltage from the channel related to the force in the z -axis direction, F_z . Similar tests were carried out by applying static loads in the y -axis direction of the load cell to find a relationship between drag and output voltage from the channel related to the force in the horizontal y -axis direction, F_y . Figures 3.9 and 3.10 show the calibration graphs for lift and drag respectively. These both show good linearity. Equations 3.3 and 3.4 show these relationships respectively:

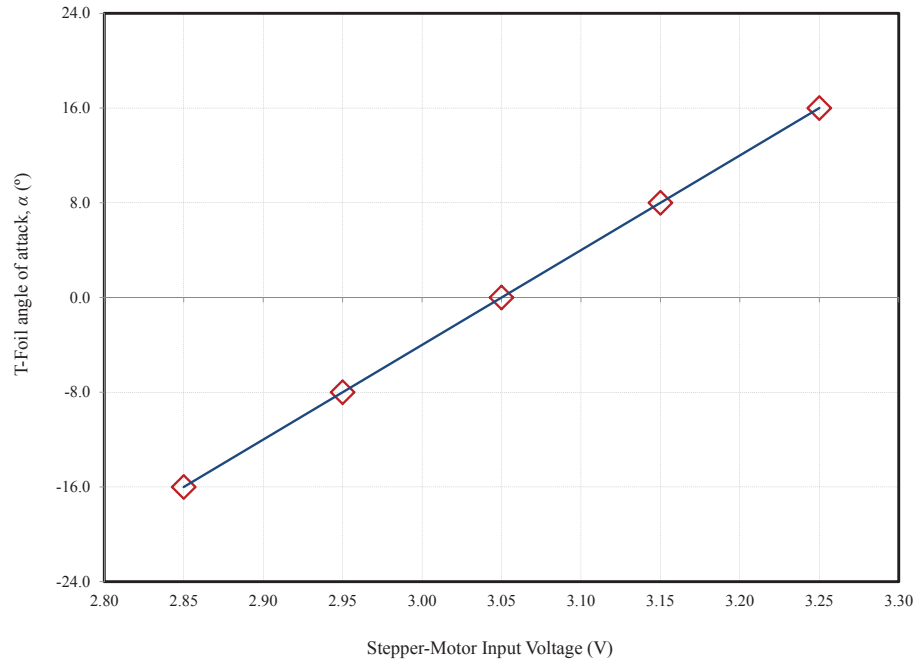


Figure 3.8: Relationship between T-Foil angle of attack and input voltage to the servo-motor.

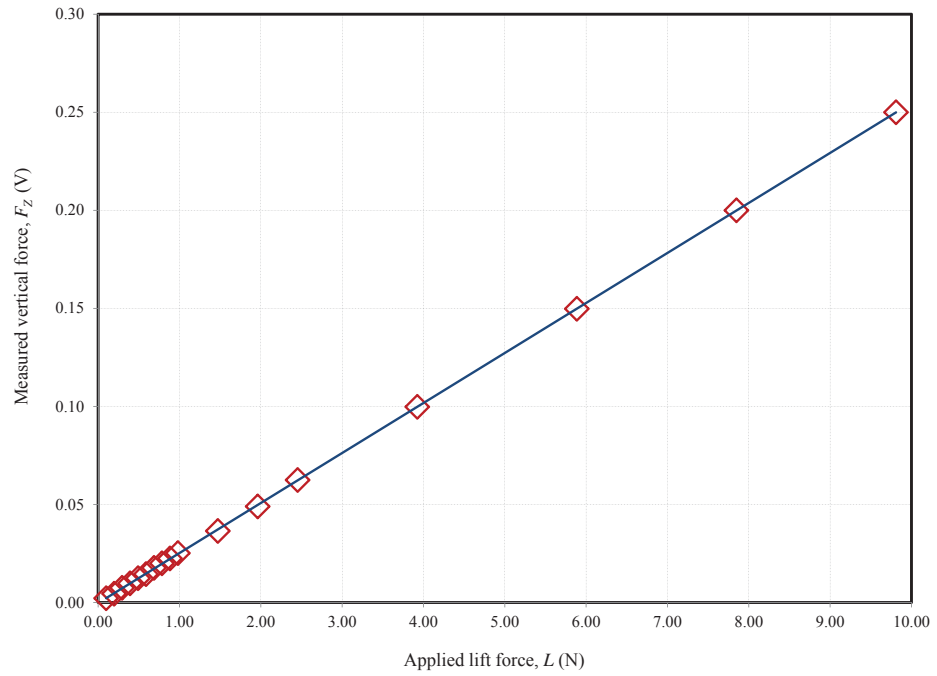


Figure 3.9: Relationship between lift force and load-cell output voltage measuring force in the vertical z-axis direction, F_z .

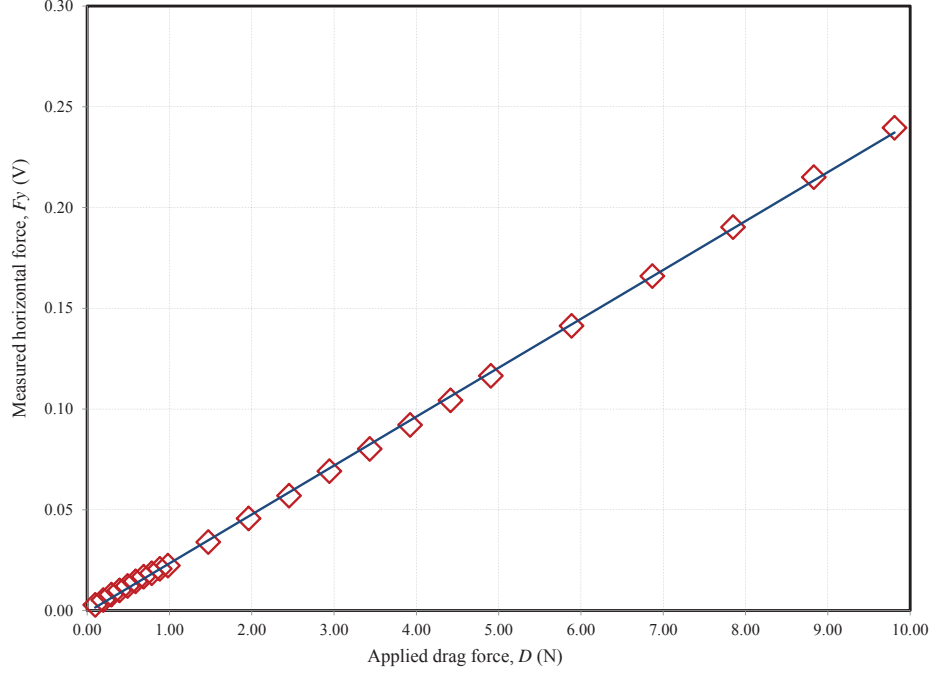


Figure 3.10: Relationship between drag force and load-cell output voltage measuring force in the horizontal y-axis direction, F_y .

$$F_z = (0.025503 \times L) - 0.000255 \quad (3.3)$$

$$F_y = (0.024268 \times D) - 0.000871. \quad (3.4)$$

3.4 Experimental tests and results

After installation of the T-Foil and the load cell in the water tunnel, the static tests were carried out at three different water flow velocities: a low speed, 1.82 m/s, a medium speed, 2.30 m/s and a high speed, 2.70 m/s. The flow velocities were selected on the basis of the forward test speeds required for the 2.5 m catamaran model for future testing of motion control response in head-seas. For each water flow velocity, the T-Foil angle of attack was fixed at 10 different angles ranging from -15° to $+15^\circ$ in 3° increments and the magnitude of both lift and drag were measured. The magnitudes of force are shown in Figures 3.11 and 3.12 for lift and drag respectively, using a sign convention where the T-Foil angle of attack (α) from the port side is positive clockwise with a left to right flow and the generated lift force is positive upwards. The lift and drag coefficients are to be discussed in Section 3.5. These dimensional results can be compared directly to the lift results for stern tabs [107] in assessing the combined performance of a T-Foil and stern tabs.

In addition to the static tests, dynamic tests were carried out on the T-Foil in the water tunnel at the three water flow velocities as mentioned above. Three ranges of angle of attack

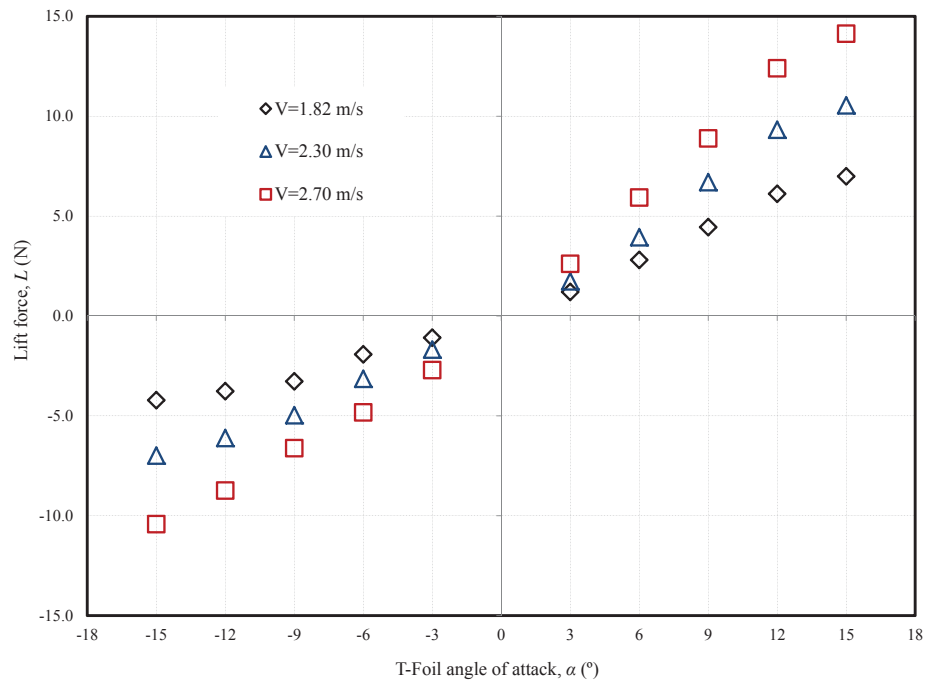


Figure 3.11: Lift force measured on the T-Foil at fixed angles of attack for static tests undertaken at water flow velocities of 1.82 m/s, 2.30 m/s and 2.70 m/s.

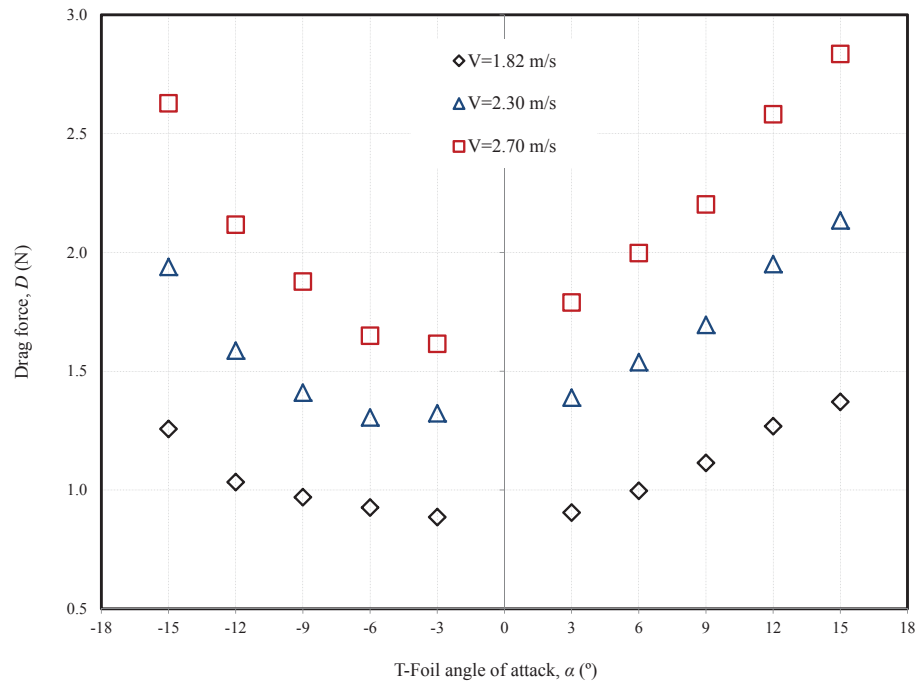


Figure 3.12: Drag force measured on the T-Foil at fixed angles of attack for static tests undertaken at water flow velocities of 1.82 m/s, 2.30 m/s and 2.70 m/s.

consisting $\pm 5^\circ$, $\pm 10^\circ$ and $\pm 15^\circ$ were tested for each flow velocity. All these tests were done at 18 different frequencies ranging from 0.5 Hz to 9 Hz in 0.5 Hz increments. The aim of these dynamic tests was to measure the dynamic forces on the T-Foil to compare to static forces as well as to define the T-Foil frequency response. Figure 3.13 shows a sample of measured dynamic forces at a flow velocity of 1.82 m/s, a frequency of 1.5 Hz and a demand T-Foil incidence (α) range of $\pm 15^\circ$.

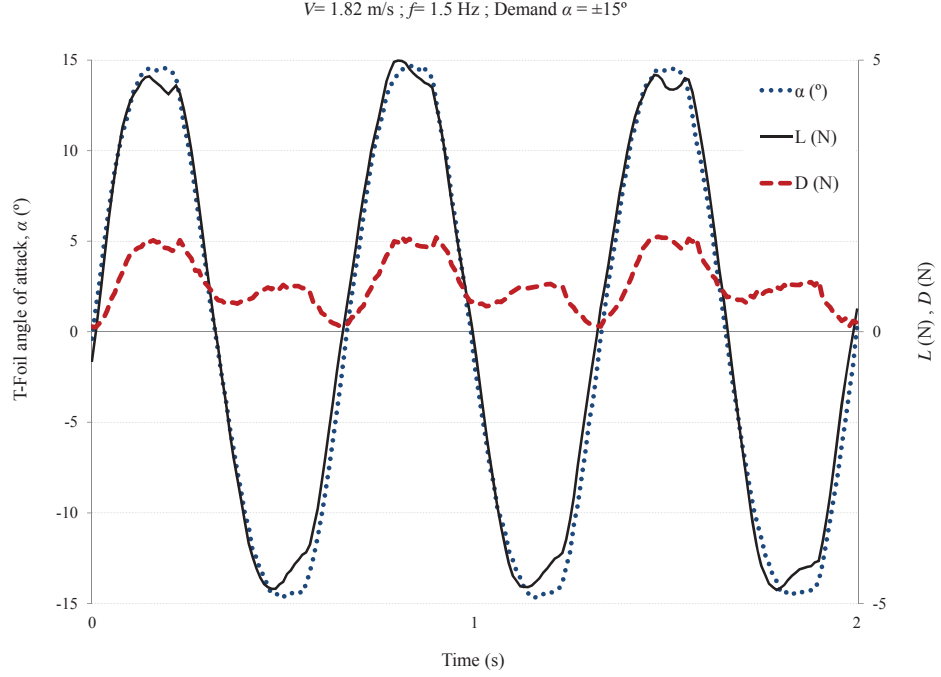


Figure 3.13: Lift (L), and Drag (D), forces measured at a flow velocity of 1.82 m/s, frequency of 1.5 Hz and demand T-Foil incidence (α) range of $\pm 15^\circ$.

The local slightly non-sinusoidal form in the immediate vicinity of the peak and trough of the measured lift can be explained on the basis of the mechanical operation of the servo-motor used to drive the T-Foil, where there is a dead-space in the servo-motor gearbox as well as slack in the connections between the motor and T-Foil. It should be noted that the unsteady fluid dynamics will be discussed in Section 3.5.2.

The results of the frequency response tests included the ratio of the measured angle of attack divided by the demand angle of attack. Also, the phase lag between demand and T-Foil movement was measured. Figures 3.14 and 3.15 show these results at the three different flow velocities of 1.82 m/s, 2.30 m/s and 2.70 m/s and also three different demand T-Foil incidence (α) ranges of $\pm 15^\circ$, $\pm 10^\circ$ and $\pm 5^\circ$. As can be seen, the ratio of measured angle of attack to the demand angle of attack decreases with increase of frequency, in particular above 4 Hz. It can be seen that this ratio is not exactly equal to unity for the low frequencies, however it is close to unity. This can be explained in terms of the mechanical operation of the T-Foil linkage set-up. As mentioned before, it was found that there is a dead-space in the servo-motor

gearbox which causes the error. When an angle is demanded for the servo-motor, its output angle is not exactly equal to the demand angle. This error is relatively more significant for low demand T-Foil incidence (α) range of $\pm 5^\circ$ as seen in Figure 3.14. In addition, Figure 3.15 shows the observed phase lag between measured angle of attack and demand angle of attack. As can be seen the observed phase lag increases with increase of frequency, the linear increase being indicative of a time delay in the control system. From the slope of this figure the time delay is about 30 ms.

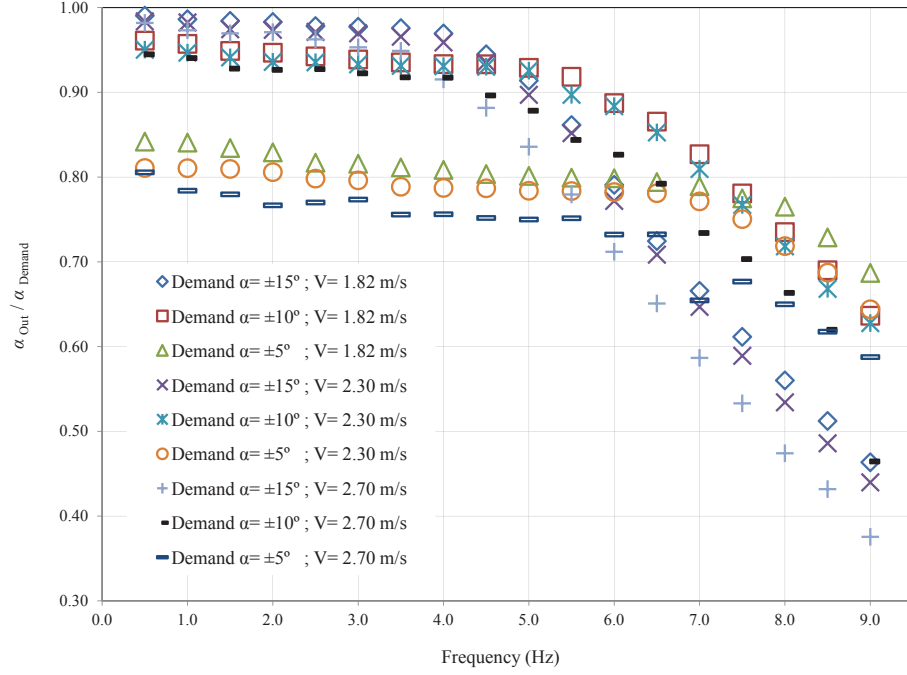


Figure 3.14: Ratio of measured angle of attack to demand angle of attack at three flow velocities of 1.82 m/s, 2.30 m/s and 2.70 m/s and also three demand T-Foil incidence (α) ranges of $\pm 15^\circ$, $\pm 10^\circ$ and $\pm 5^\circ$.

Referring to the previous studies on the INCAT Tasmania hydroelastic segmented model [122–124], it was found that peak motions and peak loads occurred at the frequencies between 1 Hz and 1.5 Hz. Considering this range of frequencies for a demand T-Foil incidence (α) range of $\pm 10^\circ$, which is close to the maximum full-scale range, it can be seen that the ratio of measured angle of attack to demand angle of attack is about 0.95 which is acceptable for such a small model test system. Also, the observed phase lag in this range of frequencies is between 10° and 20° which is due to the servo-motor limitation of time delay.

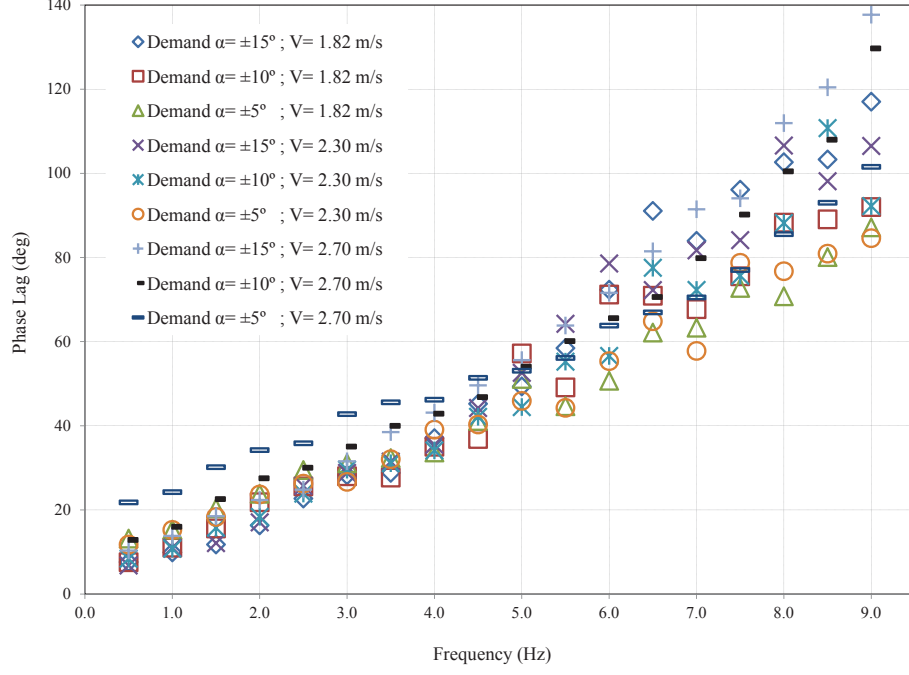


Figure 3.15: Phase lag at three flow velocities of 1.82 m/s, 2.30 m/s and 2.70 m/s and also three demand T-Foil incidence (α) ranges of $\pm 15^\circ$, $\pm 10^\circ$ and $\pm 5^\circ$.

3.5 Comparison of test results with aerofoil theory and data

3.5.1 Static tests

From the measured forces during the T-Foil model tests in the water tunnel, lift coefficients and drag coefficients in the static tests were investigated. Equations 3.5 and 3.6 were used to calculate the lift coefficients and drag coefficients respectively:

$$C_L = \frac{L}{\frac{1}{2}\rho V^2 S} \quad (3.5)$$

$$C_D = \frac{D}{\frac{1}{2}\rho V^2 S}. \quad (3.6)$$

Figures 3.16 and 3.17 show the magnitude of lift coefficients and drag coefficients of the T-Foil obtained from the static tests at various water flow velocities. In addition, the lift-to-drag ratio is plotted for different angles of attack in Figure 3.18.

As can be seen in Figure 3.16, the relationship between lift coefficient and angle of attack is not exactly linear. However, the relationship was considered sufficiently close to linear to calculate an average model T-Foil lift-coefficient derivative ($\frac{dC_L}{d\alpha}$) over the incidence range of ± 15 degrees. This slope was found to be $C_{L\alpha} = 2.45$ per radian and was considered appropriate to calculate a quasi-static lift coefficient for the dynamic tests as the basis of comparison with

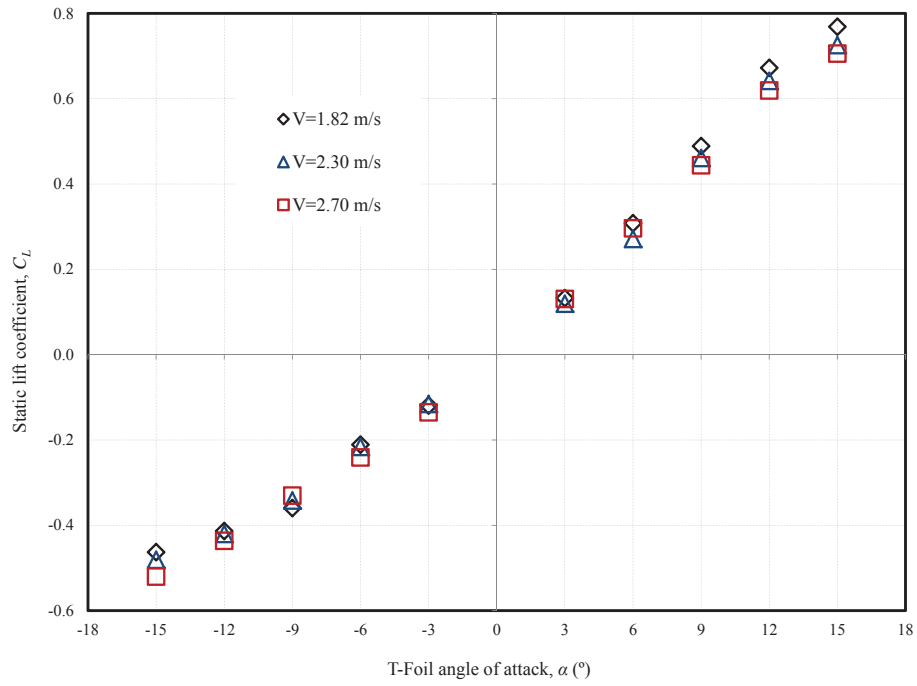


Figure 3.16: T-Foil static lift coefficient at different angles of attack and water flow velocities of 1.82 m/s, 2.30 m/s and 2.70 m/s.

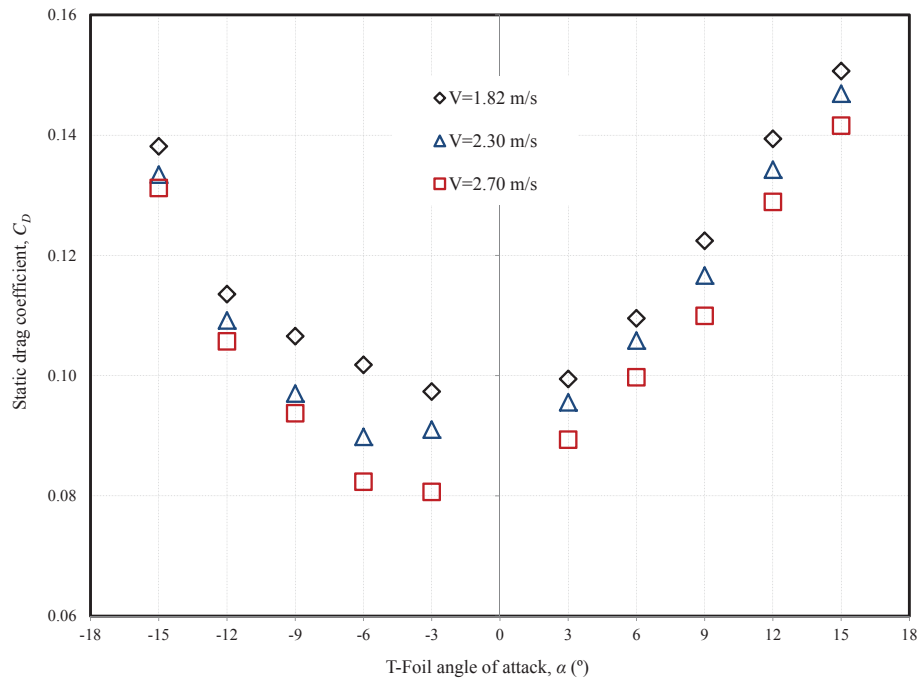


Figure 3.17: T-Foil static drag coefficient at different angles of attack and water flow velocities of 1.82 m/s, 2.30 m/s and 2.70 m/s.

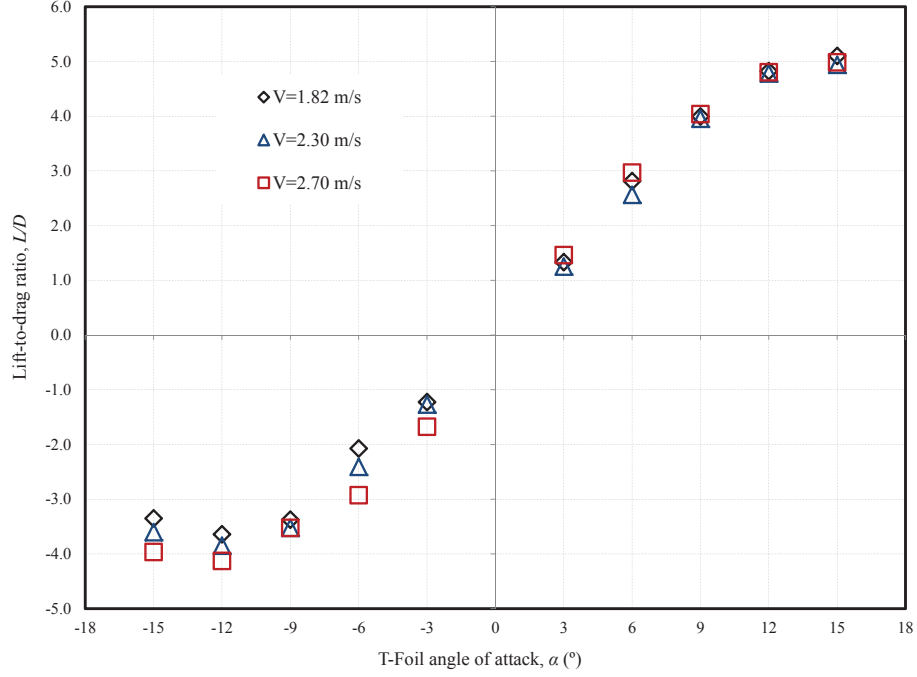


Figure 3.18: T-Foil lift-to-drag ratio at different angles of attack and water flow velocities of 1.82 m/s, 2.30 m/s and 2.70 m/s.

measured dynamic lift coefficients.

It is known that the lift curve slope reduces as aspect ratio reduces. This is due to the downwash produced, which reduces the effective angle of attack of the foil. Glauert [125] has investigated the effect of aspect ratio on the slope of the lift curve for both elliptic and rectangular aerofoils. Although the T-Foil used here is neither elliptic nor rectangular in planform, the foil is approximately intermediate in geometry between these. Further, the results obtained using Glauert's equations for aspect ratio of $AR = 3.6$ varied only slightly, being 3.89 per radian for the rectangular planform and 4.04 per radian for the elliptic planform on the basis of a two dimensional section lift curve slope of 2π per radian. It is also noted that Ol et al. [118] measured a two dimensional lift curve slope very close to 2π per radian at a Reynolds number of 6×10^4 , less than the Reynolds number of the T-Foil tested here, which was 1.05×10^5 based on the average chord. Therefore it can be expected that the present T-Foil two dimensional section would also have a lift curve slope close to 2π per radian. The possible causes of the rather lower three dimensional $C_{L\alpha} = 2.45$ per radian measured on the model T-Foil are the presence of the T-Foil strut, which obstructs the upper surface; the hinge mount, which penetrates the foil to the lower surface; and the precise design of the T-Foil outboard ends, which are approximately rectangular and smoothly contoured. The T-Foil strut in particular may be the cause of the asymmetry of the lift curve for positive and negative angles of attack.

3.5.2 Dynamic tests

The quasi-static lift coefficient was calculated by multiplying the T-Foil lift-coefficient derivative ($\frac{dC_L}{d\alpha}$) with the measured angles of attack. Figure 3.19 shows a sample comparison between quasi-static lift coefficient and dynamic lift coefficient at a water flow velocity of 1.82 m/s, frequency of 1.5 Hz and demand T-Foil incidence (α) range of $\pm 15^\circ$. Although this graph shows good agreement between experimental lift coefficient and quasi-static lift coefficient, there is a deviation at the peaks when the T-Foil reaches the maximum and minimum angle of attack.

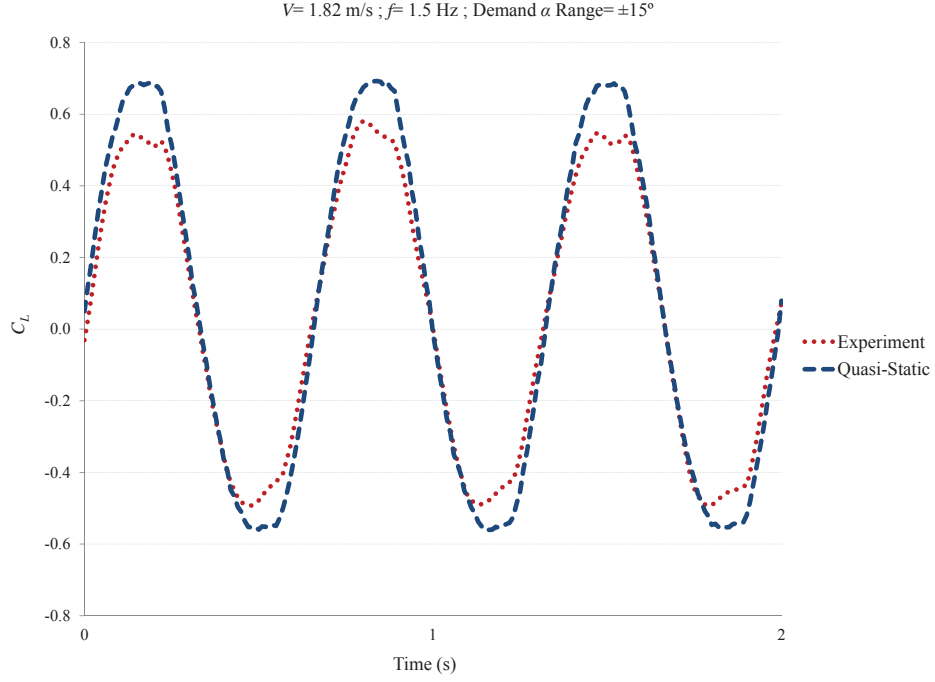


Figure 3.19: Comparison between experimental lift coefficient and quasi-static lift coefficient at water flow velocity of 1.82 m/s, frequency of 1.5 Hz and demand T-Foil incidence (α) range of $\pm 15^\circ$.

As the results presented in Figure 3.19 were obtained through experiments, it was decided to compare these results with theoretical calculations. Therefore, Theodorsen's Unsteady Thin Airfoil Theory [126] was applied to conduct the theoretical calculations for dynamic lift effects.

According to Theodorsen's theory, the lift which contains both circulatory and non-circulatory terms is given by [126] in the form

$$L = 2\pi\rho V b C(k) \left[\dot{h} + V\alpha + b \left(\frac{1}{2} - a \right) \dot{\alpha} \right] + \pi\rho b^2 (\ddot{h} + V\dot{\alpha} - ba\ddot{\alpha}). \quad (3.7)$$

In this expression $C(k)$ is a complex-valued function of the reduced frequency k defined as

$$C(k) = \frac{H_1^{(2)}(k)}{H_1^{(2)}(k) + iH_0^{(2)}(k)}, \quad (3.8)$$

where $H_n^{(2)}(k)$ are Hankel functions of the second kind, which can be represented in terms of Bessel functions of the first and second kind,

$$H_n^{(2)}(k) = J_n(k) - iY_n(k). \quad (3.9)$$

The function $C(k)$ is called Theodorsen's function and is real and equal to unity for the steady case (i.e., for $k=0$).

Three different values for the unsteady lift coefficient are now considered: the Theodorsen prediction based on a steady lift curve slope of 2.45 per radian, direct experimental data from the unsteady water tunnel tests and quasi-static values obtained from the static water tunnel tests. The latter would only be expected to apply at low frequencies.

These results are to be compared at two different water flow velocities of 1.82 m/s and 2.70 m/s and three different frequencies of 0.5 Hz, 1.5 Hz and 2.5 Hz. The flow velocities and frequency of T-Foil deflection were selected on the basis of the forward test speeds and wave frequencies required for the 2.5 m catamaran model for future testing of motion control response in head-seas.

In addition, results are presented for three different demand T-Foil incidence (α) ranges of $\pm 15^\circ$, $\pm 10^\circ$ and $\pm 5^\circ$ for flow velocity of 2.7 m/s. Figures 3.20 to 3.23 show these results as well as the amplitude response of the foil angle of attack for each case. The left panel of each figure shows the comparison of the demand angle of attack with measured angle of attack. The selected frequencies (0.5, 1.5 and 2.5 Hz) are in the range for which model testing will take place and relatively small magnitude and phase errors are expected between actual movement and demand movement within this as previously discussed.

The results for the response amplitude of the angle of attack show a small deviation in the measured range of the angle of attack compared with the demand range of the angle of attack. These results are expected based on the frequency response presented in Figure 3.14. Figures 3.20 and 3.21 show that Theodorsen's theory somewhat underpredicts the magnitude of unsteady lift at the highest frequency, but the quasi-static calculation overpredicts the magnitude of unsteady lift at all frequencies. These results show that the Theodorsen's theory prediction is relatively close to the experimental magnitude of unsteady lift at a frequency of 1.5 Hz which is the frequency that the INCAT Tasmania model encounters peak motions during tank tests [123]. As can be seen, there is no significant difference in the results between the two different flow velocities (Figures 3.20 and 3.21). Thus, it was decided to focus on the higher water flow velocity of 2.7 m/s as it is close to the design speed of the catamaran model.

Figure 3.22 shows the results at frequencies of 0.5 Hz, 1.5 Hz and 2.5 Hz, water flow velocity of 2.70 m/s and demand T-Foil incidence (α) range of $\pm 10^\circ$. The results for the response amplitude of the angle of attack (left panel) show 5% to 10% deviation in the measured range of the angle of attack compared with the demand range of the angle of attack, which was expected given the frequency response presented in Figure 3.14. The results for the unsteady lift

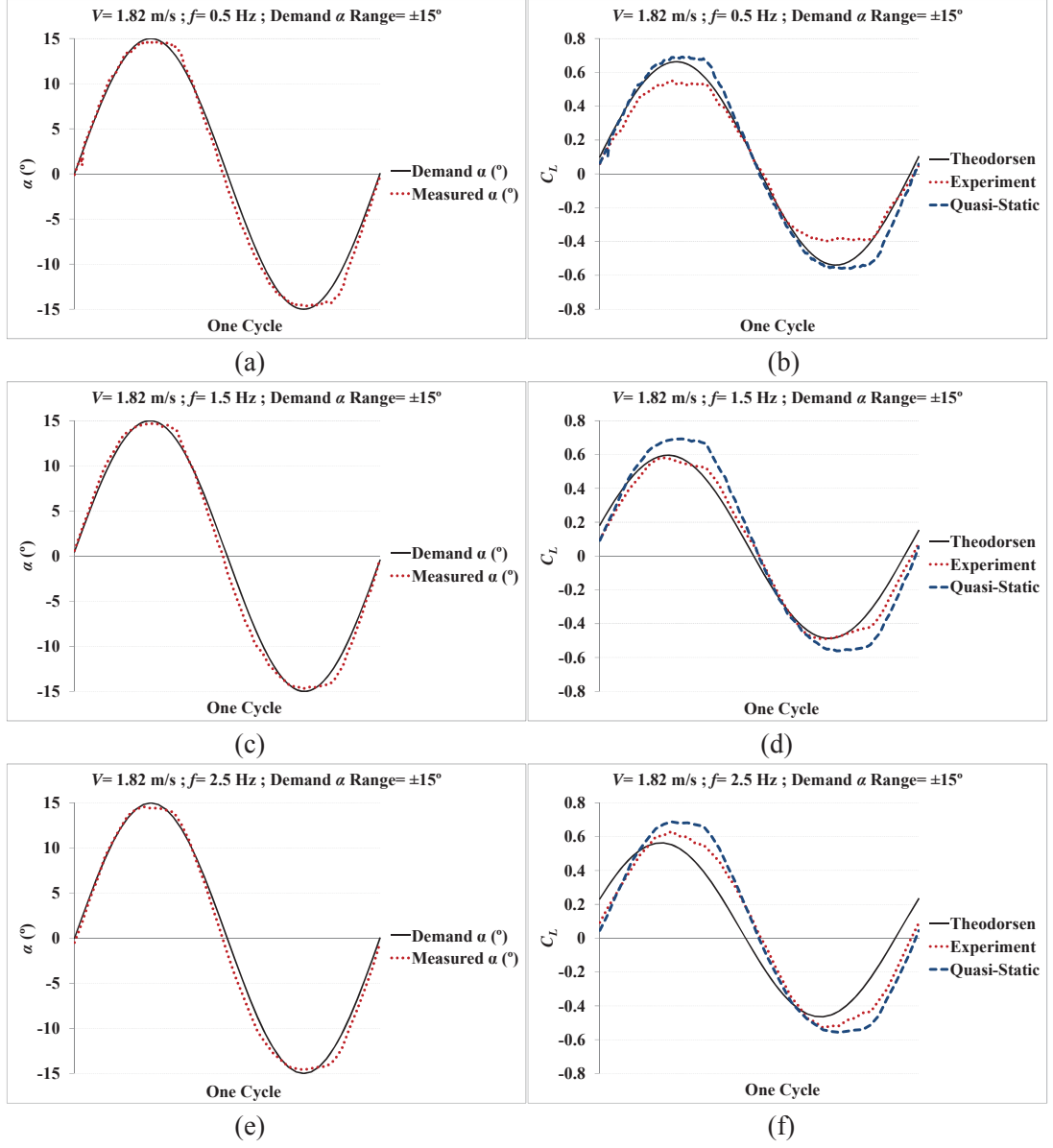


Figure 3.20: Comparison of T-Foil angle of attack (left) and lift coefficient (right) at frequencies of 0.5 Hz, 1.5 Hz and 2.5 Hz, water flow velocity of 1.82 m/s with demand T-Foil incidence (α) range of $\pm 15^\circ$.

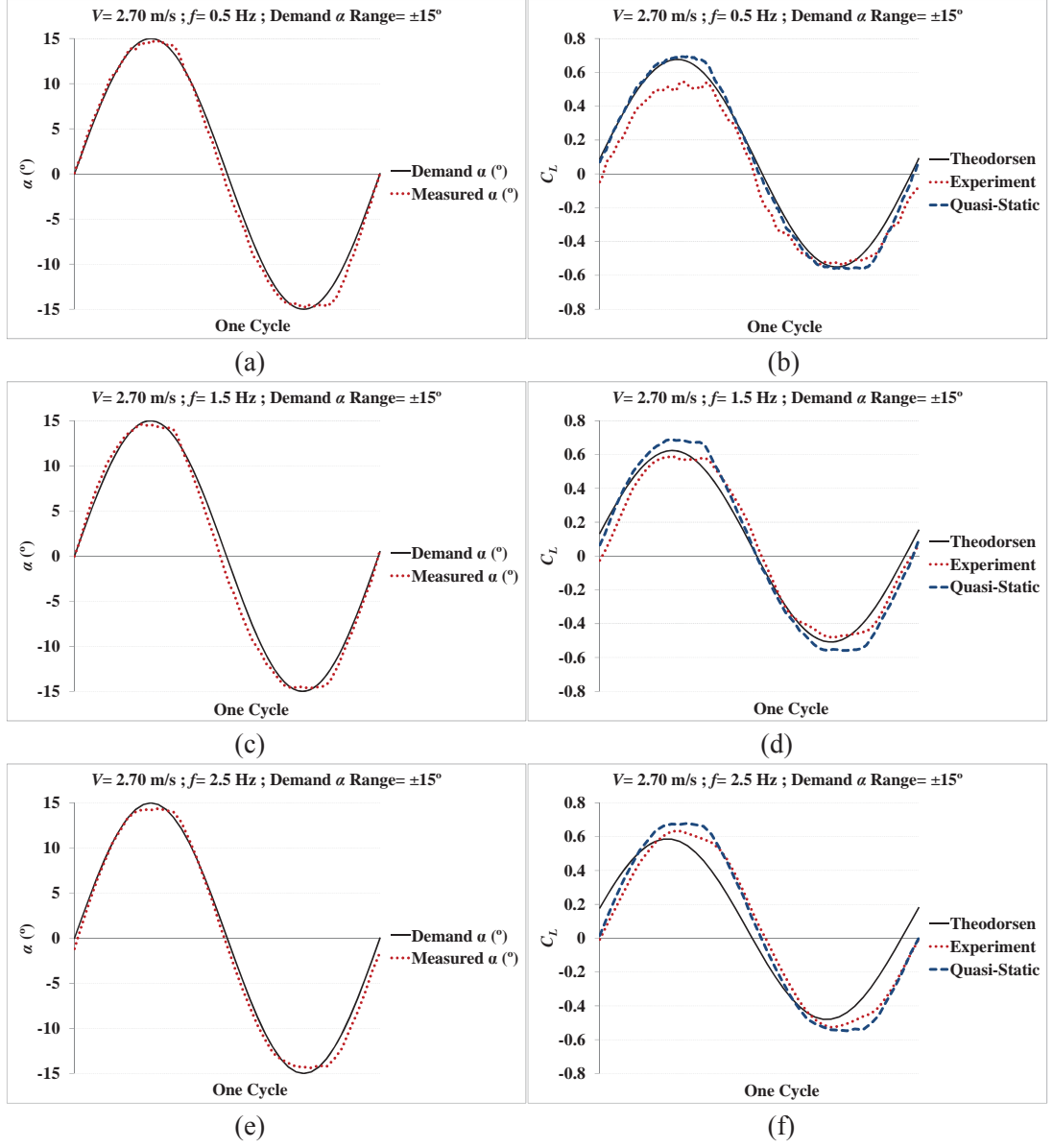


Figure 3.21: Comparison of T-Foil angle of attack (left) and lift coefficient (right) at frequencies of 0.5 Hz, 1.5 Hz and 2.5 Hz, water flow velocity of 2.70 m/s with demand T-Foil incidence (α) range of $\pm 15^\circ$.

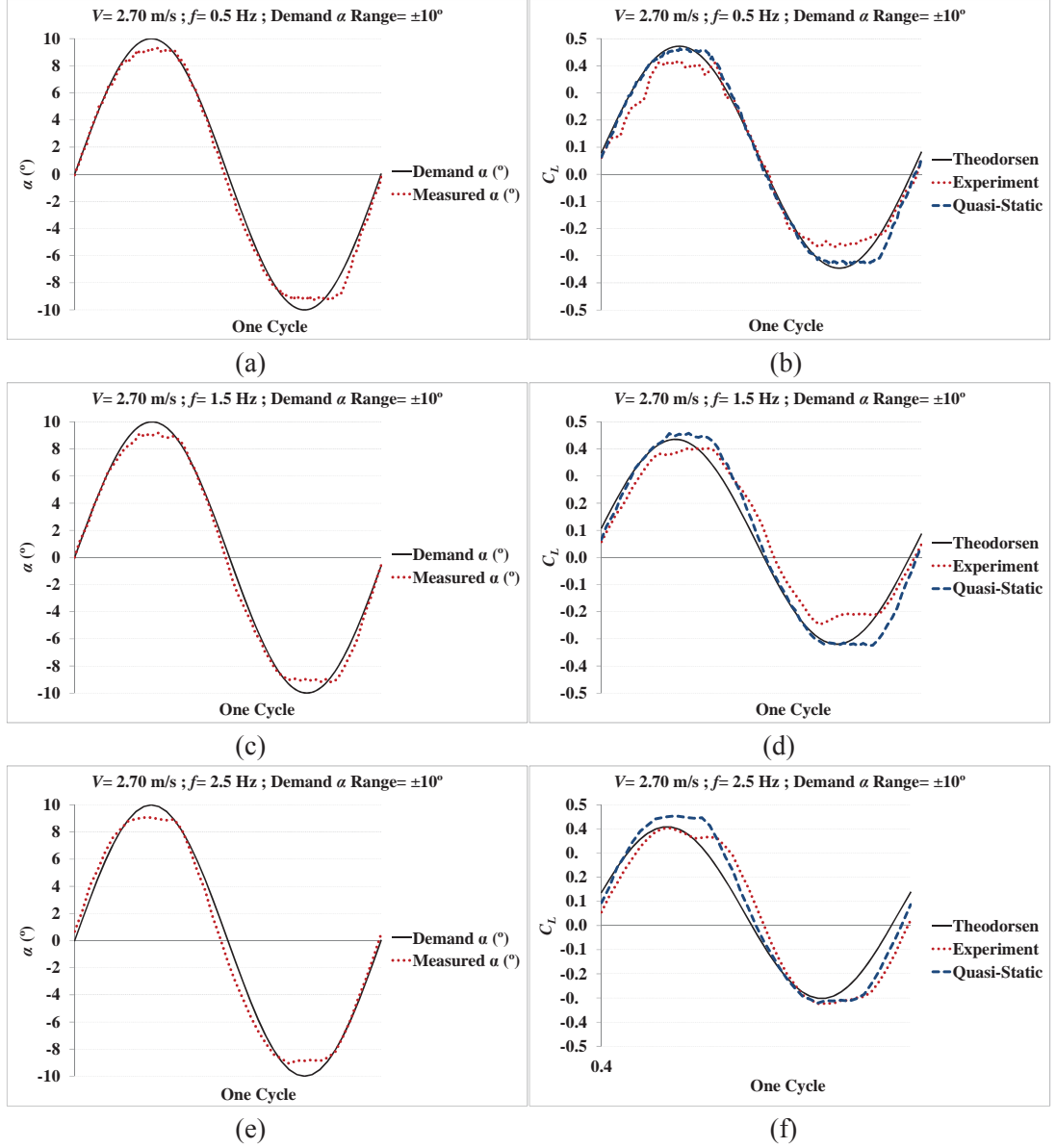


Figure 3.22: Comparison of T-Foil angle of attack (left) and lift coefficient (right) at frequencies of 0.5 Hz, 1.5 Hz and 2.5 Hz, water flow velocity of 2.70 m/s with demand T-Foil incidence (α) range of $\pm 10^\circ$.

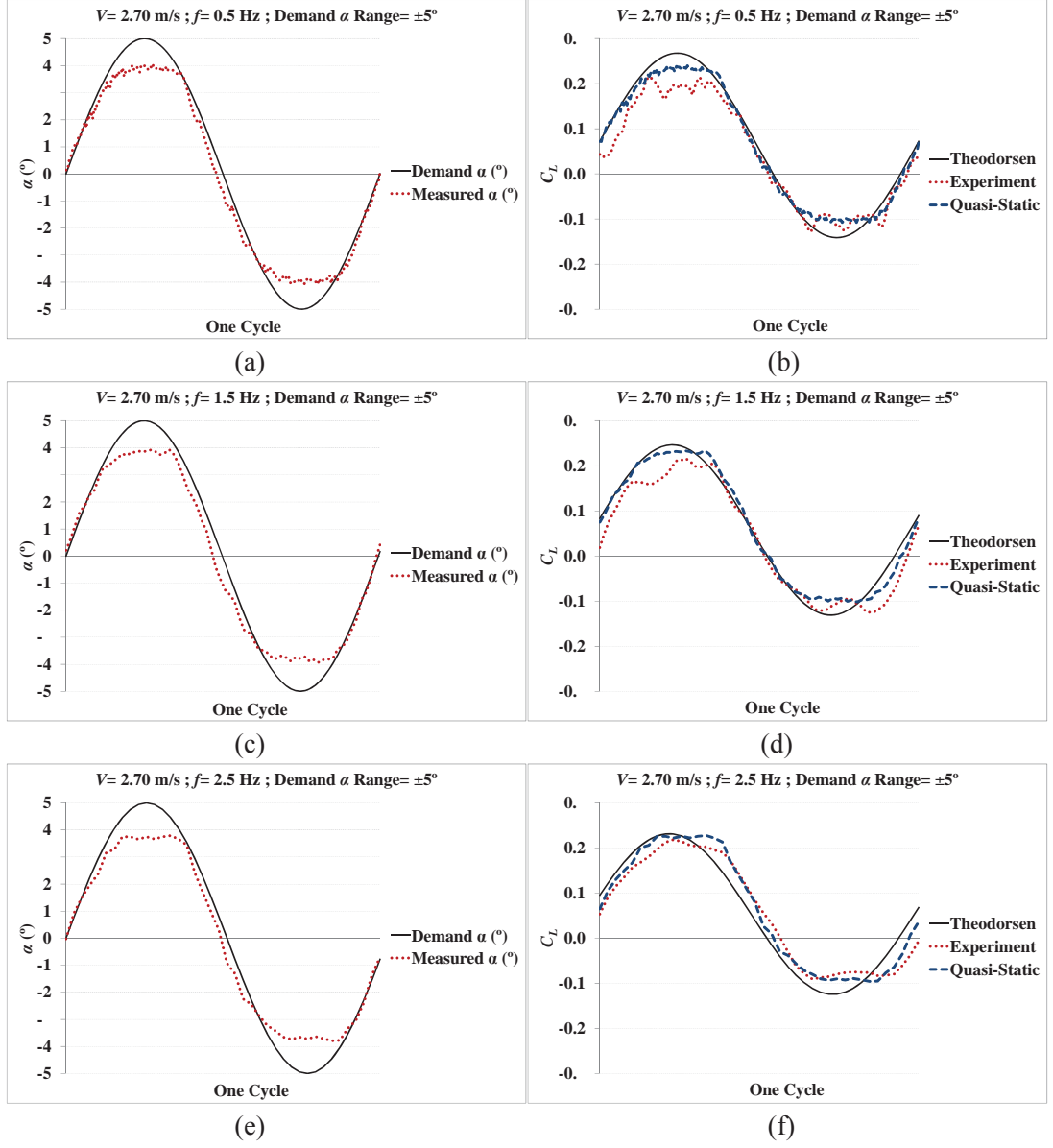


Figure 3.23: Comparison of T-Foil angle of attack (left) and lift coefficient (right) at frequencies of 0.5 Hz, 1.5 Hz and 2.5 Hz, water flow velocity of 2.70 m/s with demand T-Foil incidence (α) range of $\pm 5^\circ$.

coefficient (right panel) show that the Theodorsen theory somewhat overpredicts the magnitude of unsteady lift at the lowest frequency, however the quasi-static calculation again overpredicts the magnitude of unsteady lift at all frequencies. These results show that the Theodorsen theory prediction is relatively close to the experimental magnitude of unsteady lift at frequency of 1.5 Hz with a discrepancy of 3% at the peak and 11% at the trough.

Figure 3.23 shows the results at frequencies of 0.5 Hz, 1.5 Hz and 2.5 Hz, water flow velocity of 2.70 m/s and demand T-Foil incidence (α) range of $\pm 5^\circ$. The results for the response amplitude of the angle of attack (left panel) show about 20% deviation in the measured range of the angle of attack compared with the demand range of the angle of attack, which again was expected given the frequency response presented in Figure 3.14. As explained previously, this discrepancy is due to mechanical operation of the T-Foil actuator which introduced a dead-space in the servo-motor gearbox. This slack causes an error when an angle is demanded for the servo-motor and its response is not exactly equal to the demand angle. This error is relatively more significant for the low demand T-Foil incidence (α) range of $\pm 5^\circ$ as the ratio of response deflection to the demand deflection decreases with decreasing range of the demand control angle range. The results for the unsteady lift coefficients (right panel) with a $\pm 5^\circ$ range show that the Theodorsen theory somewhat overpredicts the magnitude of unsteady lift at all frequencies in this case. However the quasi-static calculation is relatively close to the experimental magnitude of unsteady lift at all frequencies. These outcomes are all related to imperfections in the mechanism becoming relatively larger for small movements.

In general, it can be said that there is an acceptable agreement between experimental data and theoretical data. Thus, it is acceptable to use the Theodorsen theory in combination with the quasi-static calculation to predict the dynamic lift coefficients in numerical simulations of motion control systems as the basis for evaluating appropriate control algorithms.

3.6 Conclusions

Under steady conditions the effect of low Reynolds number on lift performance is not very significant and the results obtained here show that the model scale T-Foil performs adequately to act as a control surface on the bow of a 2.5 m INCAT Tasmania catamaran model. Similar results were found at different water flow velocities and it is evident that the T-Foil performance is not diminished due to the effect of low operating Reynolds number. The lift curve slope of the T-Foil was found to be 2.45 per radian, which is 61% of the value for an ideal foil of the same aspect ratio with elliptic load distribution.

Under unsteady conditions, the magnitude of the measured angle of attack as a ratio to the demand angle of attack decreases as the frequency increases. This ratio is close to but not exactly unity for the range of frequencies up to 4 Hz for which model testing will be conducted. This small deviation from unity can be explained on the basis of the mechanical operation of the servo-motor used to drive the T-Foil where there is a dead-space in the servo-motor gearbox

as well as slack in the connections between the motor and T-Foil. This error is relatively more significant for the lower demand angle range and is due to an absolute error of about $\pm 0.5^\circ$ caused by the mechanical linkage of the model.

The observed phase lag between measured angle of attack and demand angle of attack increases with increasing frequency, reaching about 30° at 4 Hz. The phase lag increases approximately in proportion to frequency and thus appears to be caused by time delay limitations in the servo-motor actuation system.

It was found that there is a generally moderately good agreement between the temporal variation of experimentally measured lift coefficients and theoretical lift coefficients derived from a combination of the static lift curve slope and the Theodorsen theory for unsteady lift. This leads to the conclusion that it is acceptable to use the Theodorsen theory for the effect of frequency in combination with quasi-static predictions at low frequency to predict the dynamic lift coefficients of model scale T-Foil.

The general conclusion of this investigation is that the unsteady performance of the low Reynolds number model scale T-Foil with a relatively low aspect ratio is adequate for application to scale model towing tank tests. It is therefore anticipated that tank testing of a complete 2.5 m catamaran model fitted with a model RCS system will lead to the identification of the effect of motion control algorithms for reducing ship motions and thus contribute significantly to improvement of passenger comfort and reduction of structural loads.

Chapter 4

Open-Loop Responses of the Catamaran Model to the Ride Control System

4.1 Introduction

This chapter investigates the step and frequency responses of the 112 m INCAT Tasmania wave-piercing catamaran to the ride control system by towing tank testing of the 2.5 m Hydroelastic Segmented Model (HSM). These calm water open-loop test results are intended to assist in the future studies of closed-loop active control system and the relative control gains to be used with different control algorithms.

A specific purpose of the tests was to find an appropriate combination of control movements to excite the model only in heave or only in pitch. This then forms the basis of setting the gains of the ride control system to implement different control algorithms, such as pitch control, local control and heave control.

In addition to the experimental investigation, two hydrostatic methods were developed to predict the steady state step responses. Furthermore, a numerical two Degree of Freedom (DOF) rigid-body simulation was developed to theoretically evaluate the experimental step and frequency response results. It should be noted that in this study the terms “sinkage” and “trim” are used rather than “heave” and “pitch” in presenting the step responses of the model to the RCS.

4.2 Theoretical prediction of model responses

4.2.1 Hydrostatic determination of steady state step response

Two hydrostatic methods were developed in order to predict the steady state response to the control surface deflections prior to conducting the model tests. These methods ensured that the model scale ride control surfaces can adequately excite the model in heave (sinkage) and pitch (trim) by considering the maximum possible lift of 15 N for the T-Foil and total of 15 N for the stern tabs according to the previous studies on the T-Foil and stern tabs characteristics [107, 111].

The first method, termed the static load experiment, simulated the lift of each control surface by applying a 1.5 kg mass at the longitudinal location of each control surface individually while the model was stationary in calm water. The sinkage and trim stiffness of the model were calculated by measuring the model movements. The sinkage stiffness was calculated by $\frac{M \times g}{Sinkage}$ and the trim stiffness was calculated by $\frac{M \times g \times x}{Trim}$ where M is the mass and x is the longitudinal distance between the mass and the LCG . Figure 4.1 shows a schematic diagram of the model demonstrating the sign convention. Positive control deflections produce upward forces on the hull.

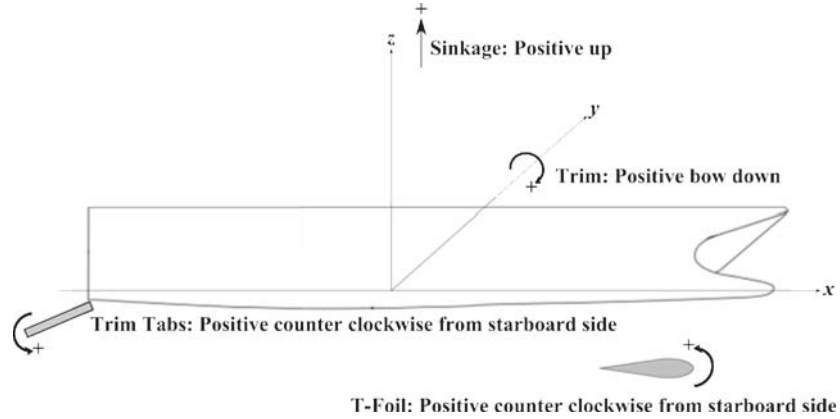


Figure 4.1: Schematic diagram showing the sign convention for sinkage (heave), trim (pitch), T-Foil deflection and stern tabs deflection.

Table 4.1 shows the results when the 1.5 kg mass was applied at the longitudinal location of T-Foil and both model movements at the longitudinal location of T-Foil and stern tabs were measured.

Similarly Table 4.2 shows the results when the 1.5 kg mass was applied at the centreline of the model at the longitudinal location of stern tabs and model movement at the longitudinal location of T-Foil and stern tabs were measured.

The second method was a hydrostatic prediction technique that estimates the theoretical model responses using the waterplane area properties, distances between the LCF , LCG and control surface, and the lift force at each control surface. The sinkage and trim are thus

Table 4.1: Hydrostatic sinkage and trim stiffness calculation by applying a 1.5 kg mass at the location of T-Foil on the catamaran model at zero speed in calm water.

Mass (kg)	1.5
Mass location (m, positive forward of LCG)	1.06
Observed vertical movement at the location of T-Foil (m, positive up)	-0.0135
Observed vertical movement at the location of stern tabs (m, positive up)	0.0060
Sinkage (m, positive up, measured at the LCG)	-0.0031
Trim (degree, positive bow down)	0.5614
Sinkage Stiffness (N/m)	4724.92
Trim stiffness (Nm/degree)	27.77

Table 4.2: Hydrostatic sinkage and trim stiffness calculation by applying a 1.5 kg mass on the model centreline at longitudinal location of stern tabs at zero speed in calm water.

Mass (kg)	1.5
Mass location (m, positive forward of LCG)	-0.93
Observed vertical movement at the location of T-Foil (m, positive up)	0.0060
Observed vertical movement at the location of stern tabs (m, positive up)	-0.0110
Sinkage (m, positive up, measured at the LCG)	-0.0031
Trim (degree, positive bow down)	-0.4894
Sinkage Stiffness (N/m)	4814.29
Trim stiffness (Nm/degree)	27.95

$$\eta_3 = \frac{L}{\rho g A_{WP}} + \eta_5 d_{FG} = \frac{L}{\rho g A_{WP}} \left(1 - \frac{A_{WP} d_{CF} d_{FG}}{I_{CF}} \right), \quad (4.1)$$

$$\eta_5 = \frac{-L d_{CF}}{\rho g I_{CF}}. \quad (4.2)$$

For both methods the T-Foil lift was predicted using the results of Section 3.4, while the stern tabs lift was predicted using the results of Bell et al [107]. These were expressed in terms of a lift-curve coefficient ($\frac{dC_L}{d\alpha}$) and control surface angular deflection (α), where $\frac{dC_L}{d\alpha}$ was found to be 2.45 radian for the T-Foil, 1.72 per radian for the tabs with positive deflection, and 0.40 per radian for the tabs with negative deflection, as discussed in Chapter 3.

Table 4.3 shows the prediction of the model response to T-Foil and stern tab deflections using the sinkage and trim stiffness determined through experimental measurement (Tables 4.1 and 4.2) and the predicted sinkage and trim (equations 4.1 and 4.2) based on the empirically determined lift coefficients [111] and [107]. This table shows good agreement between the two methods for predicting the steady state response to the control surface deflections.

Table 4.3: Prediction of model responses to load applied at the location of T-Foil and stern tabs by static load experiment and hydrostatic prediction.

T-Foil deflection (degrees)	Stern tabs deflection (degrees)	Sinkage (mm)		Trim (degrees)	
		Static load experiment	Hydrostatic prediction	Static load experiment	Hydrostatic prediction
+15	0	3.11	3.10	-0.56	-0.53
+10	0	2.07	2.06	-0.37	-0.36
-10	0	-2.07	-2.06	0.37	0.36
-15	0	-3.11	-3.10	0.56	0.53
0	+18	3.43	3.52	0.55	0.57
0	+10	1.90	1.96	0.30	0.31
0	-10	-0.51	-0.52	-0.08	-0.08
0	-18	-0.91	-0.94	-0.15	-0.15

4.2.2 Dynamic prediction of response of moving model using strip theory

A numerical simulation of the experimental responses of the model to the control surfaces deflections was developed in order to theoretically evaluate the experimental step and frequency response results. The general equations of motion for a six degree of freedom (DOF) rigid-body are [127]

$$\sum_{k=1}^6 [(M_{jk} + A_{jk})\ddot{\eta}_k + B_{jk}\dot{\eta}_k + C_{jk}\eta_k] = \sum F_j \quad (j = 1, \dots, 6) \quad (4.3)$$

where M_{jk} , A_{jk} , B_{jk} , and C_{jk} are the components of the total mass, added mass, damping, and stiffness respectively. The subscripts in $A_{jk}\ddot{\eta}_k$ refer to the force (or moment) component in j -direction due to motion in the k -direction [127], where η_1 = Surge, η_2 = Sway, η_3 = Heave, η_4 = Roll, η_5 = Pitch and η_6 = Yaw.

It is generally accepted that in most conditions the heave and pitch equations are uncoupled from or only weakly coupled to the other degrees of freedom. In any case the experimental setup only allowed two degrees of freedom, therefore a two DOF rigid-body model was considered, as presented in Equations 4.4 and 4.5.

$$[(M + A_{33})\ddot{\eta}_3 + B_{33}\dot{\eta}_3 + C_{33}\eta_3] + [(M_{35} + A_{35})\ddot{\eta}_5 + B_{35}\dot{\eta}_5 + C_{35}\eta_5] = \sum F_3 \quad (4.4)$$

$$[(M_{53} + A_{53})\ddot{\eta}_3 + B_{53}\dot{\eta}_3 + C_{53}\eta_3] + [(I_{55} + A_{55})\ddot{\eta}_5 + B_{55}\dot{\eta}_5 + C_{55}\eta_5] = \sum F_5 \quad (4.5)$$

where, for an origin at the *LCG*

$$M_{35} = M_{53} = 0$$

$$C_{33} = \rho g A_{WP}$$

$$C_{55} = \rho g (I_{cf} + A_{WP} d_{FG}^2)$$

$$C_{35} = C_{53} = -\rho g A_{WP} d_{FG}$$

$$\sum F_3 = (\alpha_{ST} \times f_{ST}) + (\alpha_{TF} \times f_{TF}) + (-\eta_5 \times f_{TF})$$

$$\sum F_5 = (\alpha_{ST} \times f_{ST} \times x_{ST}) + (-\alpha_{TF} \times f_{TF} \times x_{TF}) + (\eta_5 \times f_{TF} \times x_{TF}) .$$

The f_{ST} and f_{TF} are the stern tabs and T-Foil lift factors respectively, calculated as $\frac{1}{2}\rho U^2 S \frac{dC_L}{d\alpha}$. The added mass and damping coefficients were calculated using the following equations presented by Holloway [128], based on the theory of Salvesen et al. [129], with the addition of a T-Foil lift damping coefficient based on the equations presented by Faltinsen [127],

$$\begin{aligned}
A_{33} &= \int a_{33} dx - \frac{U}{\omega^2} b_{33}^A \\
B_{33} &= \int b_{33} dx + U a_{33}^A + \frac{1}{2} \rho U S \frac{dC_L}{d\alpha} \\
A_{35} &= - \int (a_{33} x + \frac{b_{33} U}{\omega^2}) dx - \frac{U}{\omega^2} (a_{33}^A U - b_{33}^A x^A) \\
B_{35} &= - \int (b_{33} x - a_{33} U) dx - U (a_{33}^A x^A + \frac{b_{33}^A U}{\omega^2}) - \frac{1}{2} \rho U S \frac{dC_L}{d\alpha} x_{TF} \\
A_{53} &= - \int (a_{33} x - \frac{b_{33} U}{\omega^2}) dx + \frac{U}{\omega^2} b_{33}^A x^A \\
B_{53} &= - \int (b_{33} x + a_{33} U) dx - U a_{33}^A x^A - \frac{1}{2} \rho U S \frac{dC_L}{d\alpha} x_{TF} \\
A_{55} &= \int a_{33} \left(x^2 + \frac{U^2}{\omega^2} \right) dx + \frac{U x^A}{\omega^2} (a_{33}^A U - b_{33}^A x^A) \\
B_{55} &= \int b_{33} \left(x^2 + \frac{U^2}{\omega^2} \right) dx + U x^A (a_{33}^A x^A + \frac{b_{33}^A U}{\omega^2}) + \frac{1}{2} \rho U S \frac{dC_L}{d\alpha} x_{TF}^2
\end{aligned}$$

where the superscript A refers to the aft or stern section. It should be pointed out that all integrals are from the bow to the stern and evaluated in the present work using Simpson's rule. The two DOF rigid-body model was segmented into 40 sections at the water plane and the sectional coefficients a_{33} and b_{33} were calculated using the added mass and damping for a floating semi-circular cylinder presented by Holloway [128], shown in Figure 4.2 (from Holloway [128]), where R is the cylinder radius, taken to be equal to half the local demihull beam.

It should be noted that using the actual shape of each section involves a complicated integral equation that would require substantial additional work to solve for very minimal improvement in accuracy. Implementing a full boundary element or conformal mapping solution, which is necessary to evaluate more accurate section coefficients for an arbitrarily shaped hull, is outside the scope of this thesis. As the numerical results here are for illustrative purposes, using a semicircular cylinder of diameter equal to the local demihull beam is the most appropriate approximation short of using the full solution [130].

Holloway used a steady periodic Green function panel method and compared this method to an analytical solution described by Ursell in terms an infinite number of equations in an infinite number of unknowns [128]. For the purposes of calculating the sectional coefficients a_{33} and b_{33} , and global coefficients A_{ij} and B_{ij} , which are all frequency dependent, ω was taken to be the experimentally observed natural frequency.

Equations 4.4 and 4.5 can be written in matrix form as

$$\begin{aligned}
\begin{bmatrix} M + A_{33} & A_{35} \\ A_{53} & I_{55} + A_{55} \end{bmatrix} \begin{bmatrix} \ddot{\eta}_3 \\ \ddot{\eta}_5 \end{bmatrix} + \begin{bmatrix} B_{33} & B_{35} \\ B_{53} & B_{55} \end{bmatrix} \begin{bmatrix} \dot{\eta}_3 \\ \dot{\eta}_5 \end{bmatrix} + \begin{bmatrix} C_{33} & C_{35} + f_{TF} \\ C_{53} & C_{55} - f_{TF} \times x_{TF} \end{bmatrix} \begin{bmatrix} \eta_3 \\ \eta_5 \end{bmatrix} \\
= \begin{bmatrix} \alpha_{ST} \times f_{ST} + \alpha_{TF} \times f_{TF} \\ \alpha_{ST} \times f_{ST} \times x_{ST} - \alpha_{TF} \times f_{TF} \times x_{TF} \end{bmatrix} \quad (4.6)
\end{aligned}$$

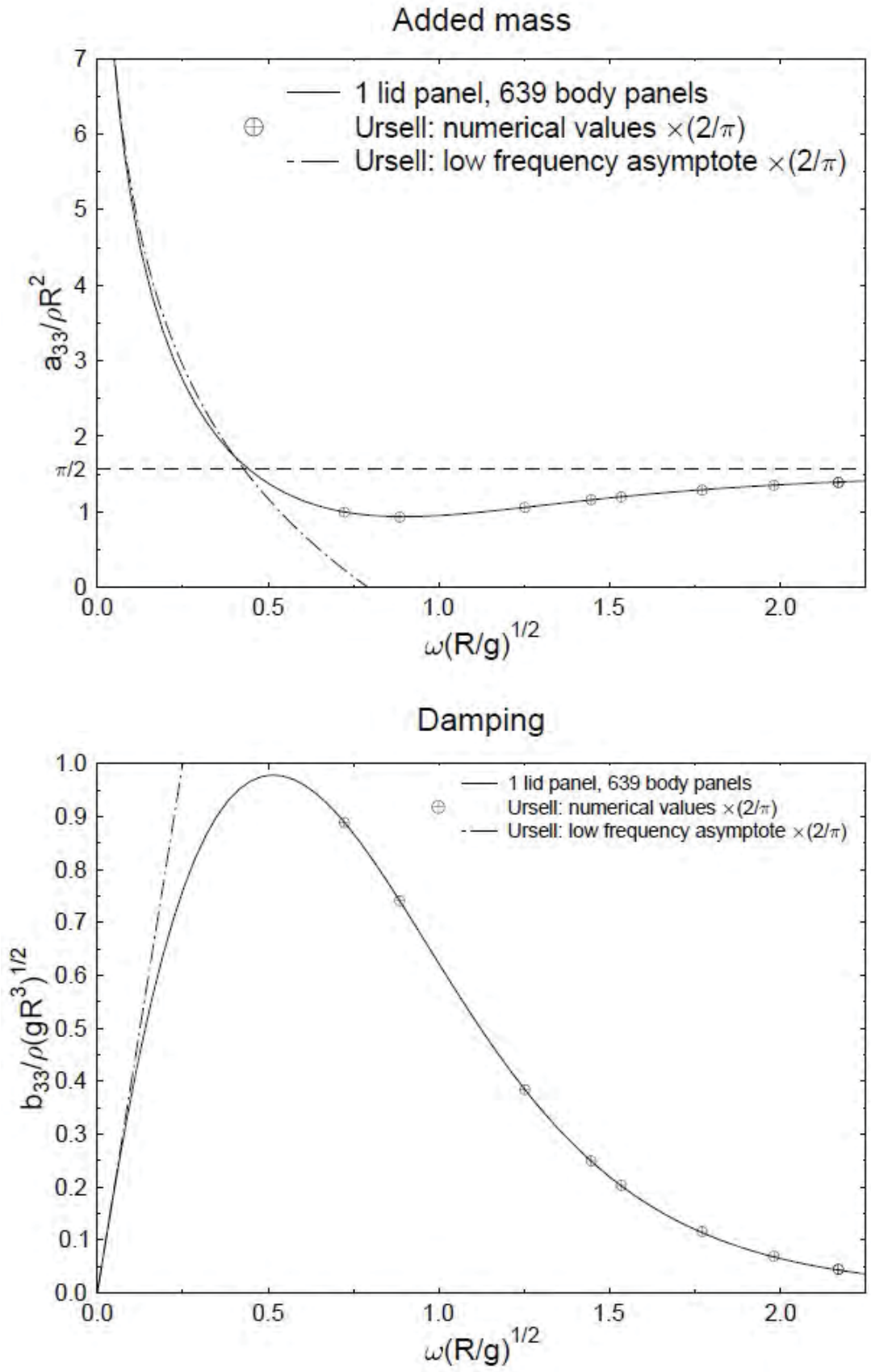


Figure 4.2: Heave added mass and damping for floating semi-circular cylinder.

Equation 4.6 is a function of T-Foil and stern tab deflection. Therefore theoretical sinkage and trim response to the control surfaces deflection, either individually or combined, can be obtained by solving Equation 4.6. A Matlab code using Newmark-beta method was written to solve the Equation 4.6 for different conditions.

4.3 Model set-up and instrumentation

As discussed before, the model used for this research project is the Hydroelastic Segmented Catamaran Model (HSM) which was designed, built and used by a team at the University of Tasmania. Table 4.4 shows the specifications of the full scale catamaran and the scaled model.

Table 4.4: Specifications of the full scale INCAT catamaran and the scaled model.

	Full-scale (m)	Model scale (m)
Length of Overall (LOA)	112.00	2.50
Length of Waterline (LWL)	103.04	2.30
Breadth (B)	30.30	0.68
Breadth of demihulls (BDH)	5.80	0.13
Design Draft (T)	3.33	0.07

In addition to the model scale T-Foil described in Chapter 3, two model scale stern tabs were designed, manufactured and fitted onto the model. Figure 4.3 shows the 3D CAD design of the electrically activated model scale stern tabs, while Figure 4.4 shows a photograph of the electrically activated model stern tabs and Table 4.5 shows their specifications. Three servo-motors were used to independently activate the T-Foil and stern tabs, while three potentiometers measured their angular positions. Figure 4.5 shows the stern tabs installed at the aft end of the model. Figures 4.6 and 4.7 show the T-Foil and its electrical actuator installed on the aft section of the centre bow.

Table 4.5: Specifications of the full scale 112 m INCAT catamaran and 2.5 m scaled model stern tabs.

	112 m full-scale (m)	2.5 m model scale (mm)
Chord	1.50	33.48
Span	5.80	129.46

Experimental testing of the model was conducted at the Australian Maritime College (AMC) towing tank in Launceston, Tasmania, with a model displacement of 28.3 kg simulating a full

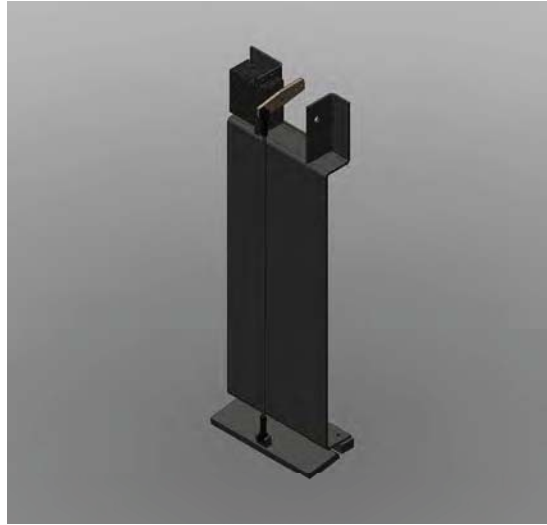


Figure 4.3: 3D CAD design of electrically activated model scale stern tabs.

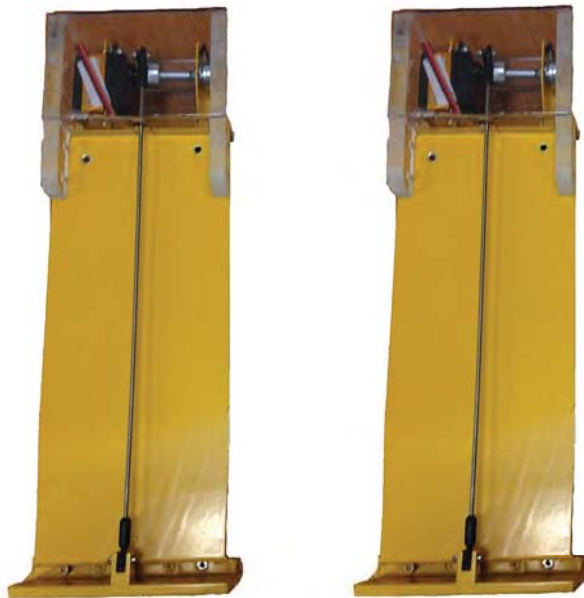


Figure 4.4: Electrically activated model scale stern tabs developed for the 2.5 m hydroelastic segmented catamaran model.



Figure 4.5: Stern tabs installed at the stern of the model.

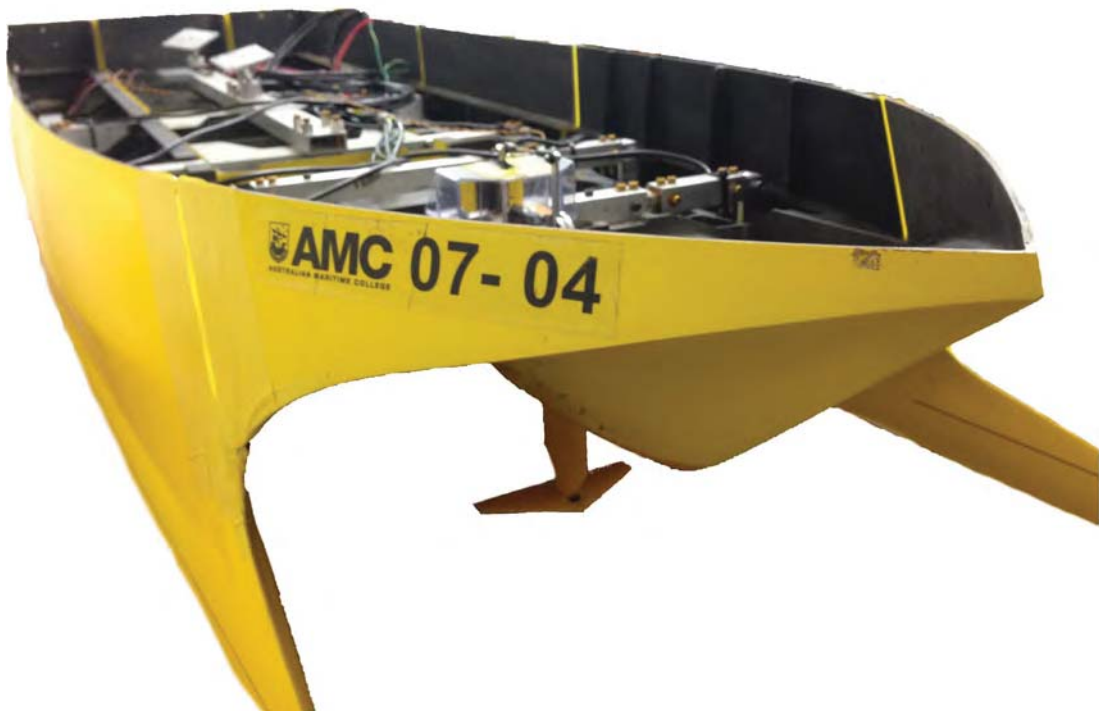


Figure 4.6: T-Foil installed on the aft section of the centre bow of the model.

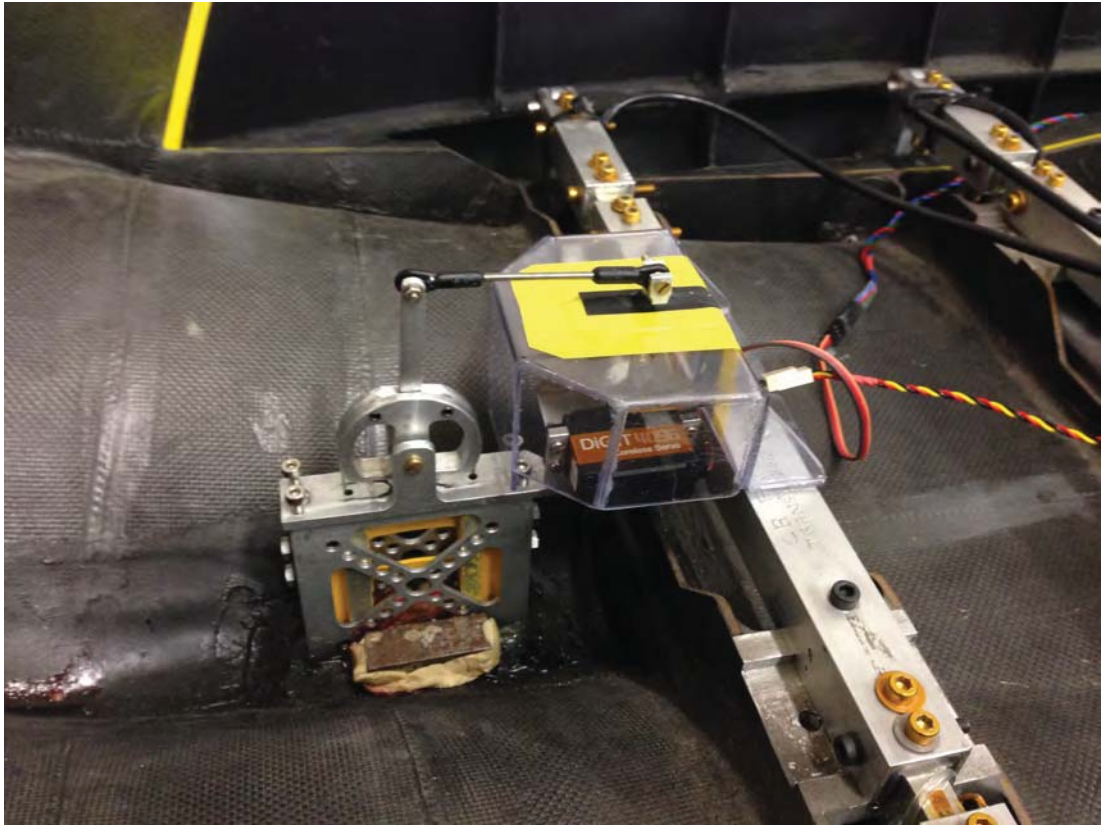


Figure 4.7: T-Foil electrical actuator installed on the aft section of the centre bow of the model.

scale displacement of 2545 tonnes. The towing tank is 100 m long, 3 m wide and 1.4 m deep. The model was attached to the moving carriage using two tow posts mounted forward and aft of the model longitudinal centre of gravity (LCG). Figure 4.8 shows the model attached to the moving carriage. Testing was undertaken in calm water with a primary focus on measuring the responses to the ride control system at a model speed of 2.89 m/s, simulating the full scale speed of 37 knots, while the control surfaces were deflected to various angles with rapid step movements as well as periodic movement.

A National Instruments (NI) 9174-USB compact DAQ (cDAQ) chassis was used with two NI modules, a NI 9263 Analogue Output (AO) and a NI 9201 Analogue Input (AI) as described in Chapter 2. Control surface deflections were demanded through the AO module and the AI module acquired the potentiometer voltage to measure the actual instantaneous deflection of the control surfaces. Three additional voltages including carriage speed, forward Linear Variable Differential Transformer (LVDT) and aft LVDT, were logged using the NI 9201 Analogue Input (AI).

The servo-motors and the potentiometers were calibrated to determine the relationship between demand voltage for the servo-motor and relative deflection of the control surface, and the relationship between the output voltage from the potentiometer and relative deflection of the control surface. During calibration the deflections of the control surfaces were measured using a digital inclinometer with a resolution of 0.05° . The inclinometer was aligned with the



Figure 4.8: The model attached to the moving carriage in the AMC towing tank.

T-Foil chord line and the stern tabs, with 0° corresponding to these being parallel to the water surface.

Although the RCS DAQ system was able to log all the required data, a separate towing carriage data acquisition and signal conditioning system was used simultaneously to cross check the data acquired by the RCS DAQ system. LVDTs were mounted on each tow post and measured the vertical movement in order to calculate model sinkage (heave) and trim (pitch). Two video cameras were set up to record all the runs from bow and stern views.

4.4 Step responses results

The model was first tested in calm water to investigate the step responses of the model to the ride control system. The control surfaces were first deflected individually to different angles to measure the effect of each control surface on sinkage and trim. Deflections of $\pm 15^\circ$, $\pm 10^\circ$ and $\pm 5^\circ$ were applied to the T-Foil and $\pm 18^\circ$, $\pm 10^\circ$ and $\pm 5^\circ$ to the stern tabs. Figure 4.1 shows a schematic diagram of the model demonstrating the sign convention.

Figures 4.9 to 4.20 compare the theoretical and experimental responses to step movements of the control surfaces when activated individually at a model test speed of 2.89 m/s.

As can be seen from Figure 4.9 and 4.10, the maximum deflection range of the T-Foil from $+15^\circ$ to -15° produces a sinkage range of about 7 mm (i.e. from +3.5 to -3.5 mm) and trim

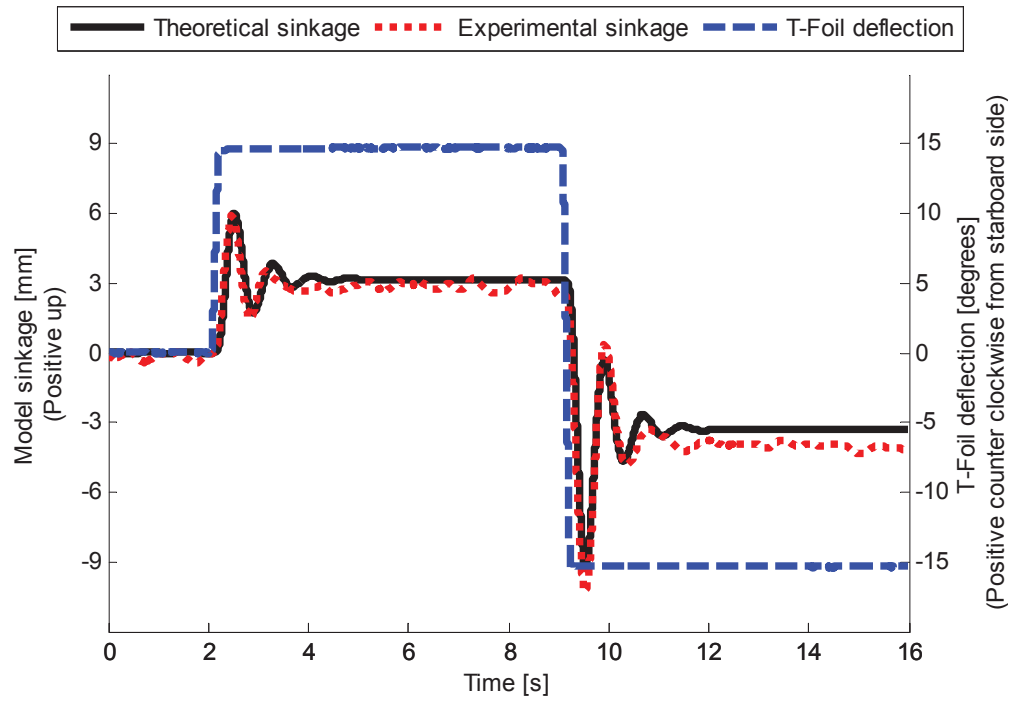


Figure 4.9: Sinkage response to T-Foil deflection of $\pm 15^\circ$ at model speed of 2.89 m/s.

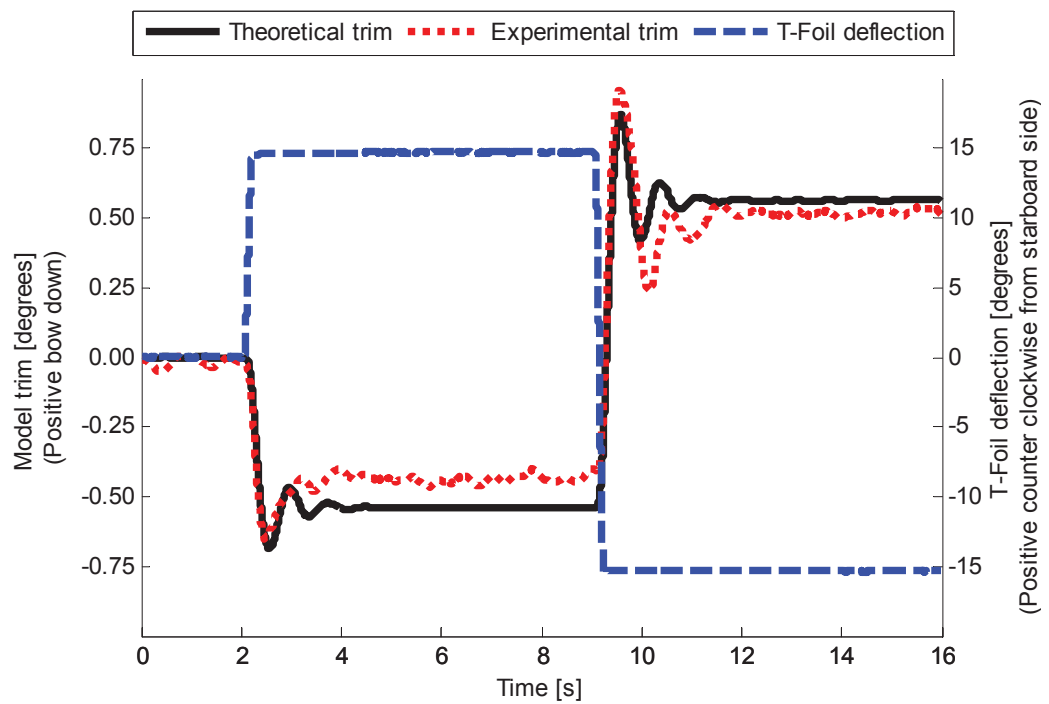


Figure 4.10: Trim response to T-Foil deflection of $\pm 15^\circ$ at model speed of 2.89 m/s.

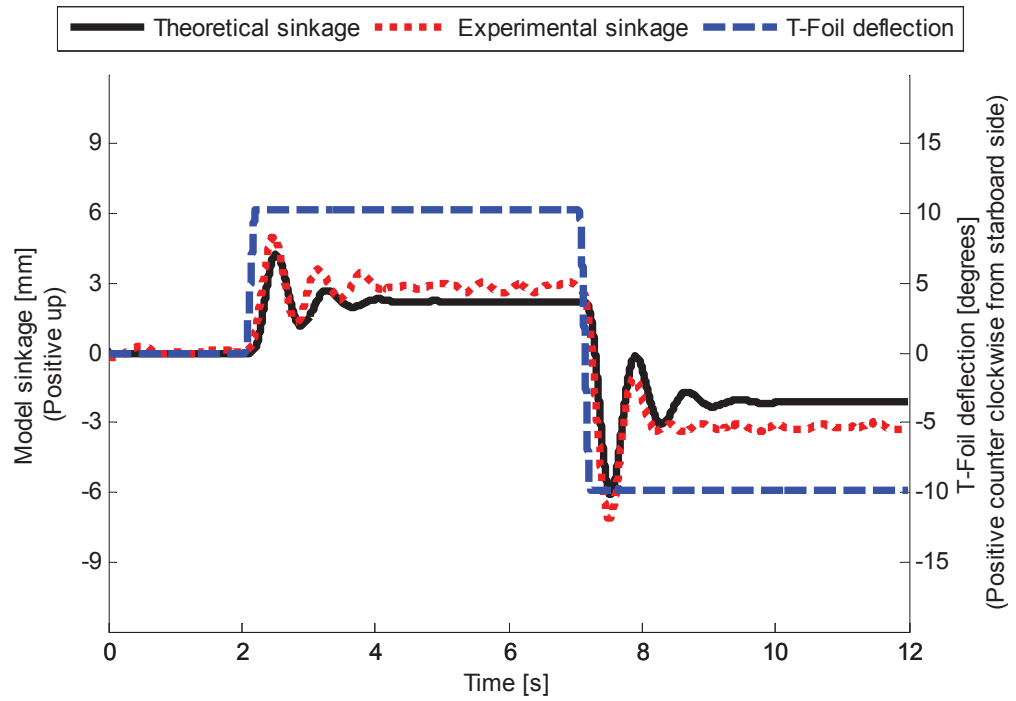


Figure 4.11: Sinkage response to T-Foil deflection of $\pm 10^\circ$ at model speed of 2.89 m/s.

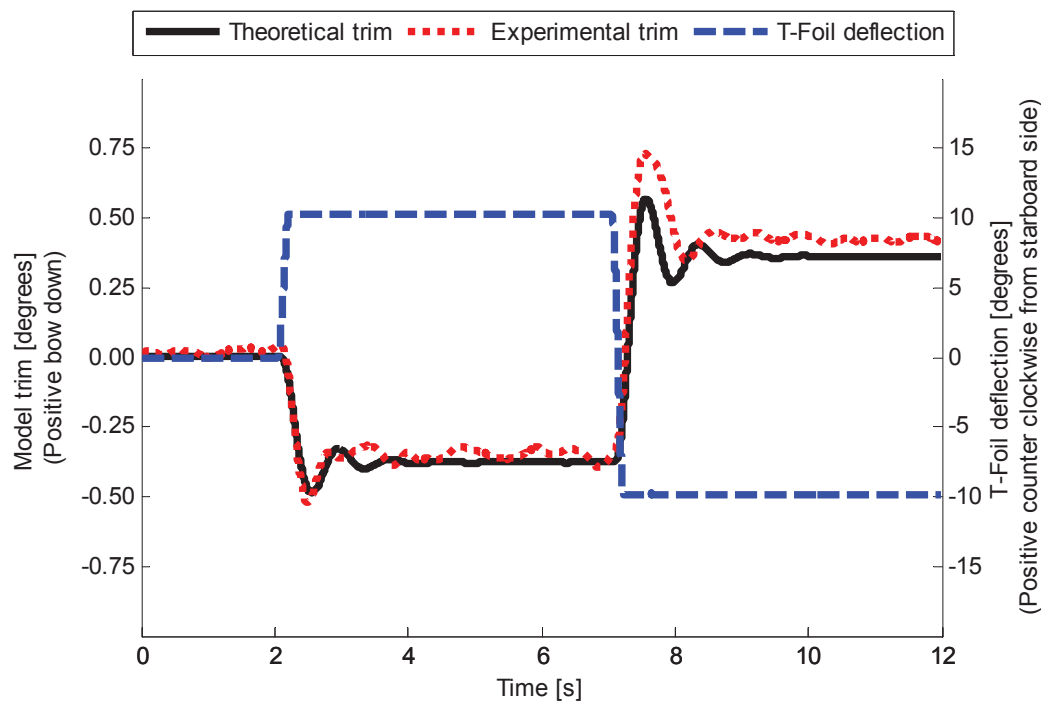


Figure 4.12: Trim response to T-Foil deflection of $\pm 10^\circ$ at model speed of 2.89 m/s.

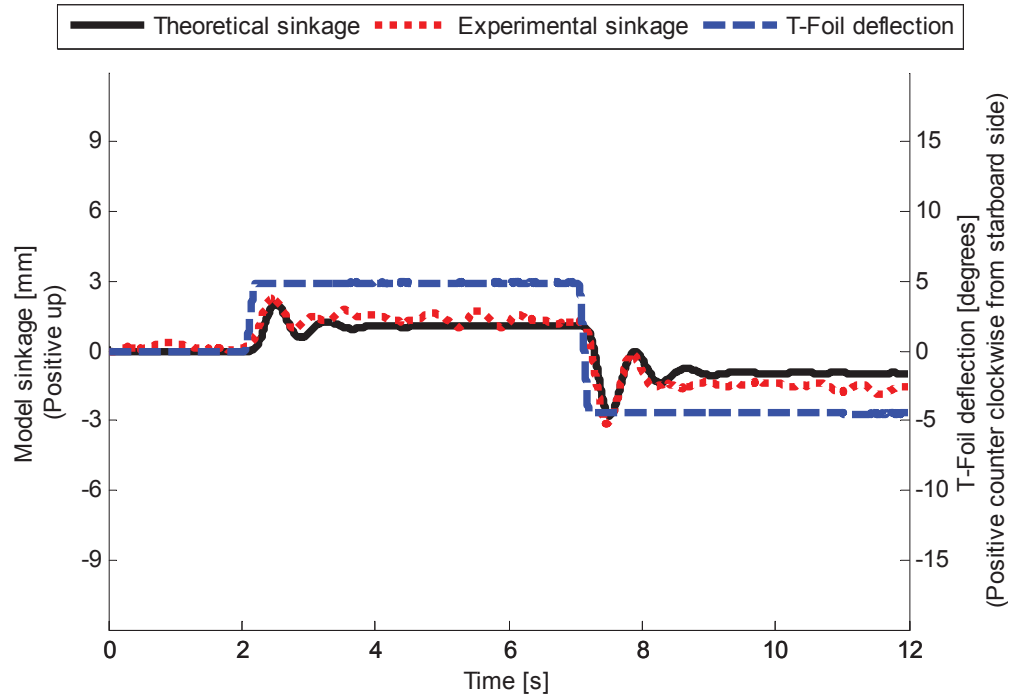


Figure 4.13: Sinkage response to T-Foil deflection of $\pm 5^\circ$ at model speed of 2.89 m/s.

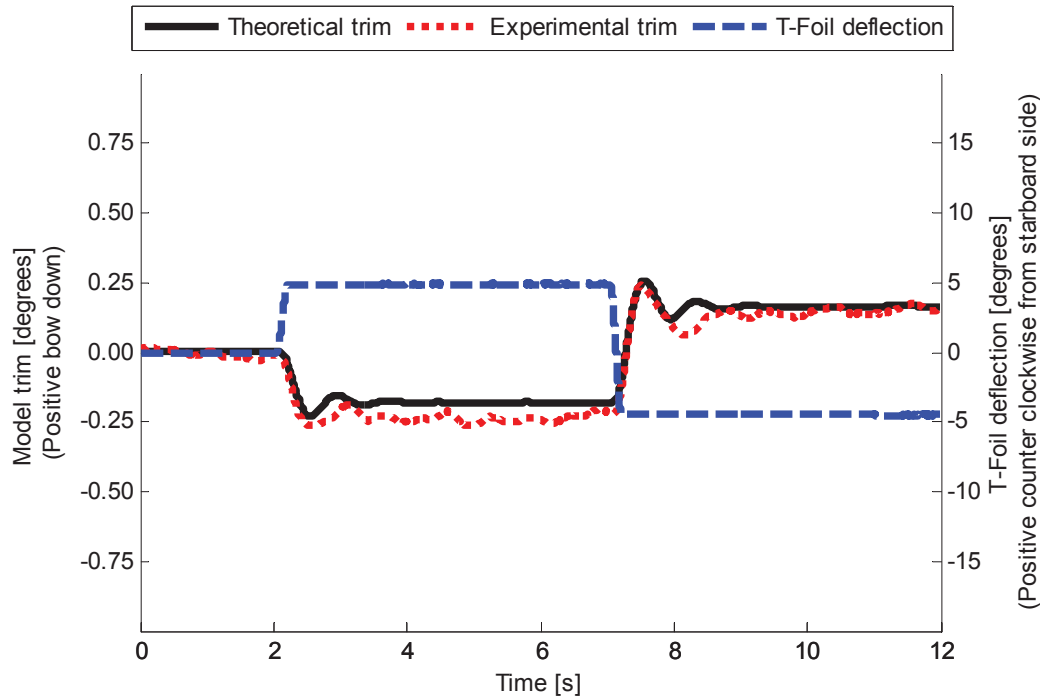


Figure 4.14: Trim response to T-Foil deflection of $\pm 5^\circ$ at model speed of 2.89 m/s.

range of about 1° (i.e. ranging over $\pm 0.5^\circ$). Although the theoretical calculation of sinkage is in good agreement with experimental sinkage, the theoretical calculation over predicted the trim response by about 0.1° when the T-Foil was deflected $+15^\circ$. A possible explanation for this is that the lift-curve coefficient ($\frac{dC_L}{d\alpha}$) was considered constant with control deflection in order to perform the theoretical prediction. However lift was not found to be exactly proportional to control surface deflection in the previous experiments [111]. This may explain the differences of trim responses seen by the comparison of the predicted and measured trim in Figures 4.10, 4.12 and 4.14. The comparison between Figures 4.9, 4.11 and 4.13 shows that experimental sinkage responses are generally consistent with the theoretical calculations of sinkage. However the deviation between theoretical sinkage and experimental sinkage is somewhat more evident in Figure 4.11.

Figures 4.15 and 4.16 show that the maximum deflection of the stern tabs from -18° to $+18^\circ$ can only lift the model by about 3.5 mm but can trim the model by about 1° . As shown in Figures 4.15 to 4.20, the agreement between theoretical predictions and experimental responses to the stern tabs deflection is not as good as the results of predicted responses to T-Foil deflections presented in Figures 4.9 to 4.14. There is a small theoretical over prediction of the sinkage for positive deflections of the stern tabs, which seems to be consistent for different tab deflections as shown in Figures 4.15, 4.17 and 4.19. Figures 4.16, 4.18 and 4.20 also show that the theoretical calculations somewhat under predicted the trim responses. The theoretical under prediction of trim is more significant for -10° deflection of stern tabs. A possible explanation for the stern tab results may be the variation of the lift coefficient derivative ($\frac{dC_L}{d\alpha}$) of the stern tabs. It should be noted that two lift-coefficient derivatives ($\frac{dC_L}{d\alpha}$) were considered for positive and negative deflections of stern tabs respectively and treated as constant in each case. This was because lift was reduced for negative (i.e. upward) stern tab deflections due to flow separation from the tab. The stern tab lift-coefficient derivatives ($\frac{dC_L}{d\alpha}$) were calculated according to the results of Bell et al. [107], and these had to be extrapolated to larger angles and higher velocities. Bell et al. [107] measured the coefficients only up to 2.31 m/s, while the tests shown in figures 4.15 to 4.20 were at 2.89 m/s. Bell et al. [107] also only measured the stern tab negative lift at an angle of attack of -7° , while up to -18° was used in the present tests. Thus some inaccuracy is expected from these extrapolations.

In these results it should be noted that a drift of the signal was observed for sinkage under the action of stern tabs only, which can be explained by carriage aerodynamic effects as reported by Yang [131]. Measurements undertaken by Yang in the same towing tank as used in the present experiments demonstrated that there was flow of air between the top of the carriage and the water surface that caused a pressure wave in the vicinity of and travelling with the test model, and a corresponding (but not constant) reduction in the local calm water surface height. The experimental results presented in this study are corrected using Yang's results. In order to perform the correction for each run, a run in the same condition was performed without the control surface deflection. The repeated run without control surface deflection was considered

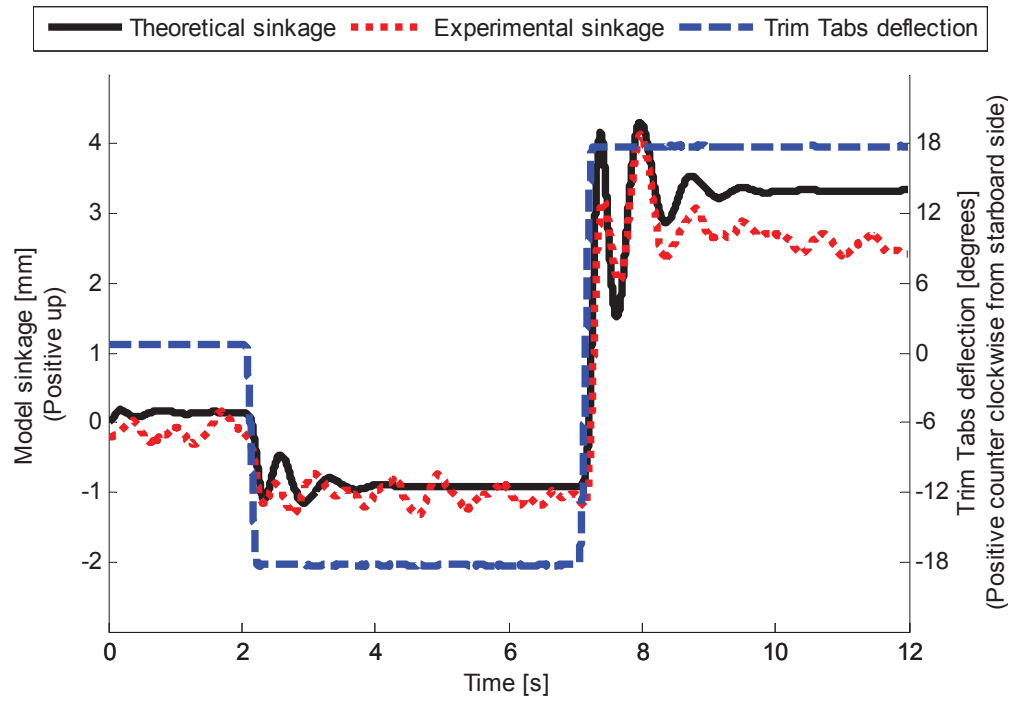


Figure 4.15: Sinkage response to stern tabs deflection of $\pm 18^\circ$ at model speed of 2.89 m/s.

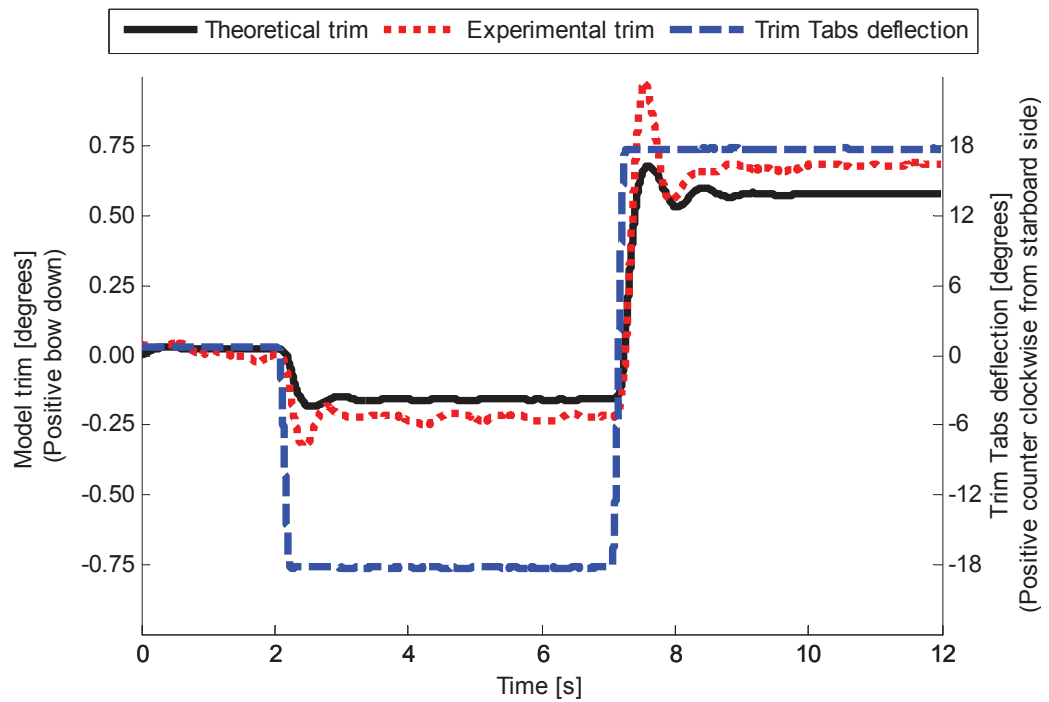


Figure 4.16: Trim response to stern tabs deflection of $\pm 18^\circ$ at model speed of 2.89 m/s.

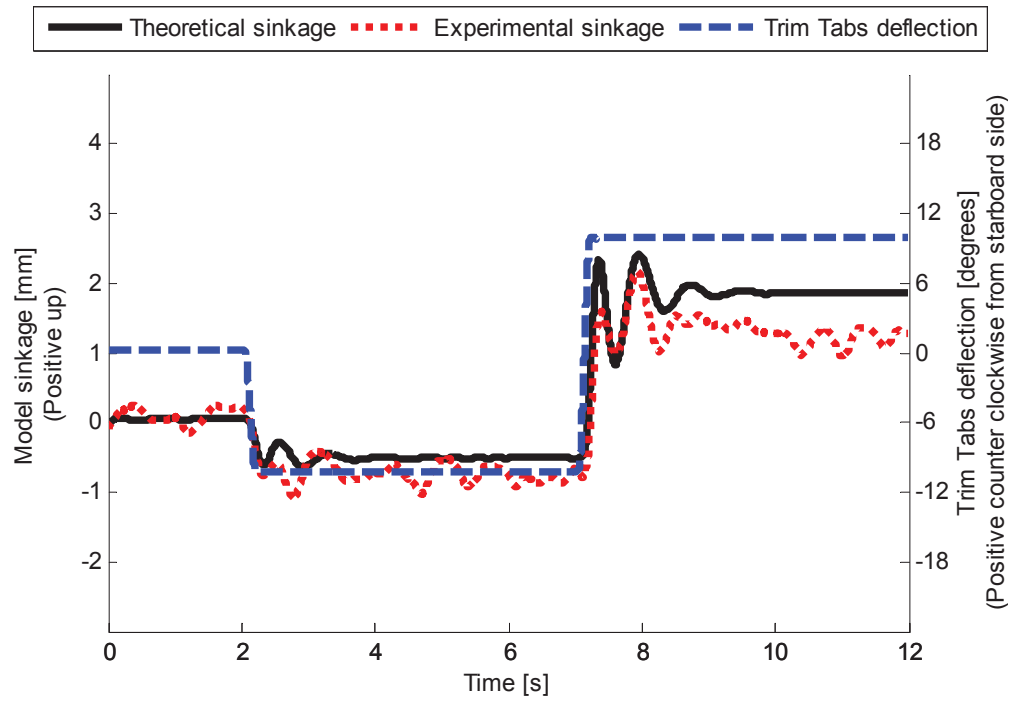


Figure 4.17: Sinkage response to stern tabs deflection of $\pm 10^\circ$ at model speed of 2.89 m/s.

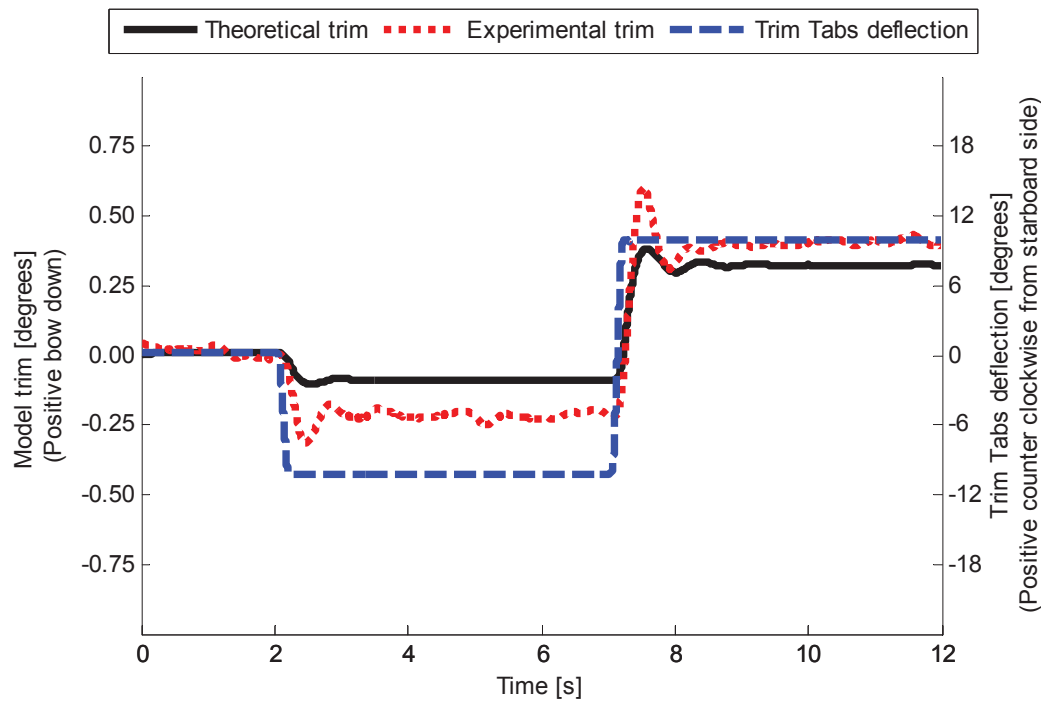


Figure 4.18: Trim response to stern tabs deflection of $\pm 10^\circ$ at model speed of 2.89 m/s.

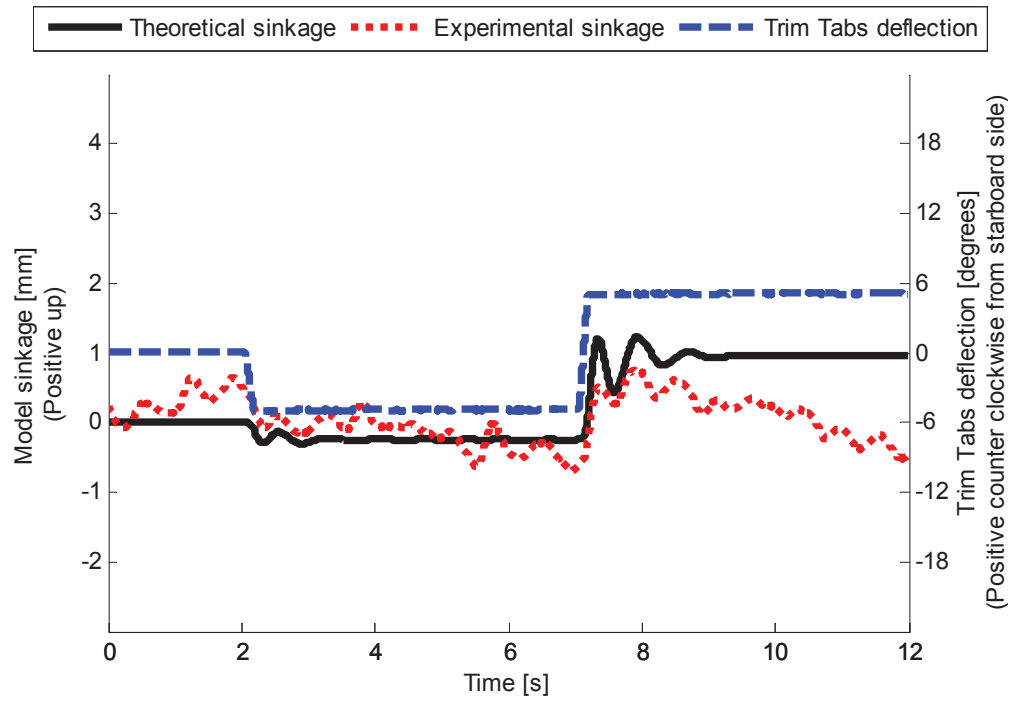


Figure 4.19: Sinkage response to stern tabs deflection of $\pm 5^\circ$ at model speed of 2.89 m/s.

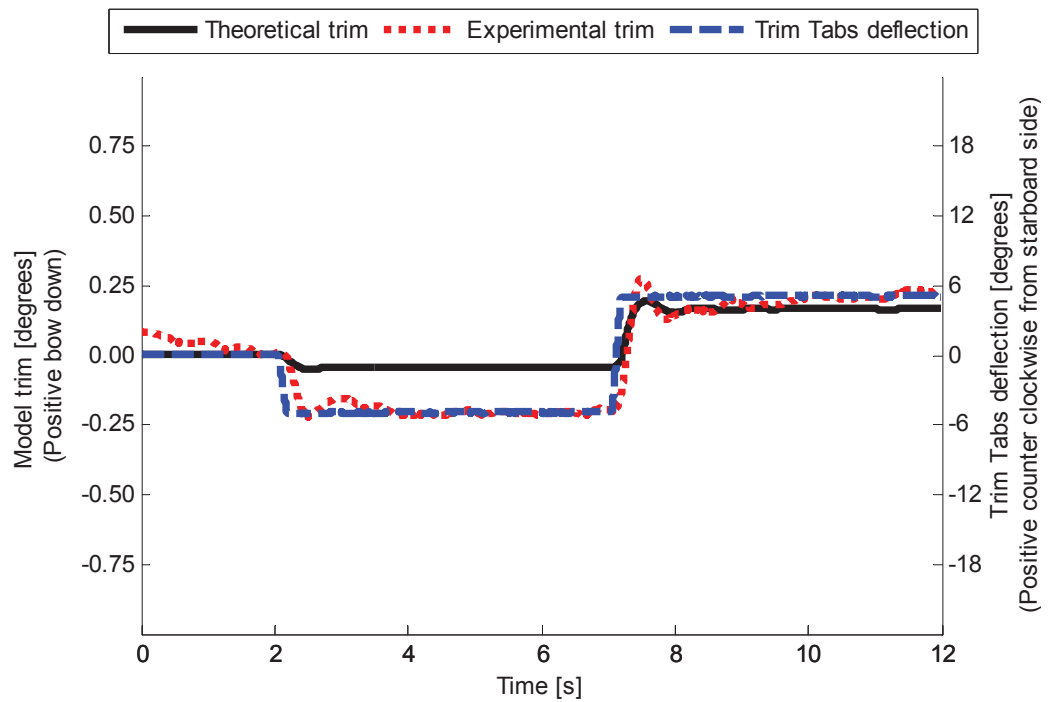


Figure 4.20: Trim response to stern tabs deflection of $\pm 5^\circ$ at model speed of 2.89 m/s.

as the zero and the actual experimental step responses results were determined by subtracting the measured zero to correct for the pressure wave generated by the moving carriage. The observed drift can still be seen in some of the presented results such as in Figure 4.19 for $t > 8$ s. This is due to the complexity of matching the time records of two different runs consisting of the non-deflected (zero) and deflected control surface model responses. This has a more significant effect when the number of repeated runs is less due to the limited data available for more accurate correction. It should be noted that the step responses of the model to the T-Foil deflection was investigated by a higher number of runs. This produced a more accurate set of results as shown in Figures 4.9, 4.11 and 4.13 as opposed to Figures 4.15, 4.17 and 4.19 where the number of runs was more restricted.

After measuring the effect of each control surface on the model sinkage and trim by deflecting each control surface individually, the T-Foil and stern tabs were activated together to investigate the effect of combined control surface activation on the model response. Figure 4.21 shows the model responses to the maximum step movements of the RCS when activated together at four model speeds to produce maximum trim change. The first step is T-Foil deflection of $+15^\circ$ together with stern tabs deflections of -18° . The second step is T-Foil deflection of -15° together with stern tabs deflection of $+18^\circ$.

As can be seen in Figure 4.21 the model step responses in exciting maximum trim change achieved good results with an overall maximum change in trim of 1.9 degrees bow down at a model test speed of 2.89 m/s. It can be seen in Figure 4.21 that the theoretical prediction of trim is in good agreement with experimental trim response at the three higher speeds but trim is under predicted for the first step at the lowest speed of 1.53 m/s. This is probably due to the variation of lift-curve coefficient derivatives ($\frac{dC_L}{d\alpha}$) of both T-Foil and stern tabs as well as the lower than predicted lift of the stern tabs with an upward deflection of -18° . Also, the model speed of 1.53 m/s is quite low and control forces will not be very large at that speed. Similarly, there is a small opposite prediction of sinkage at model speed of 1.53 m/s. However in all these cases the controls are being deflected with opposite sign and so the steady sinkage is relatively small.

Although the theoretical computations with these large opposite control deflections predicted the trim responses reasonably at the higher speeds, it significantly under predicted the sinkage responses to the second step at model speeds of 2.89 m/s and 2.50 m/s. This can be explained on the basis of the theoretical over prediction of the sinkage response to the stern tabs deflection of $+18^\circ$ presented in Figure 4.15. An over prediction in stern tab lift at the transom will produce a large net lift force resulting in a positive sinkage offset when compared to the measured sinkage.

Figure 4.22 shows the model responses to the maximum step movements of RCS when activated together at four model speeds to produce maximum sinkage change. The first step is a T-Foil deflection of $+15^\circ$ together with stern tab deflections of $+18^\circ$. The second step is a T-Foil deflection of -15° together with stern tab deflections of -18° .

These results show that there is good agreement of the sinkage responses between theoretical computations and experimental results. However, the theory did not appropriately predict the trim responses to the second step for speeds below 2.89 m/s. This is more obvious at lower speeds, where surprisingly the theoretical results predicted the trim in the opposite direction to that measured at the lowest speed of 1.53 m/s. This result is most likely related to the limitations in predicting the forces generated based on negative upward stern tab deflections especially at low model speeds as discussed previously.

Figure 4.23 shows a photograph of the model running at the low speed of 1.53 m/s when the stern tabs deflected -18° and the T-Foil is deflected -15° , the flow is seen to remain attached to the stern tabs. On the other hand, Figure 4.24 shows a photograph of the model running at the high speed of 2.89 m/s when the stern tabs deflected -18° and the T-Foil is deflected -15° , where the flow separated at the leading edge of the stern tabs, as expected at the higher test speed. The water flow fields observed in Figures 4.23 and 4.24 can be directly correlated to the model responses to RCS deflections based on the experimental results measured.

In general it can be seen that the deviation between theoretical results and experimental results is larger when the control deflections are smaller. This can be seen by comparing Figure 4.21 with Figure 4.22. Figure 4.21 shows for the maximum trim excitation that theory deviates from experiments more in the sinkage results. In contrast, in Figure 4.22 (maximum sinkage excitation) it is shown that the theoretical predictions deviate from the experimental results more in the trim responses. The sinkage prediction appears generally good and from the results presented in Figure 4.22 the maximum sinkage achievable at 2.89 m/s was 10 mm based on simultaneous activation of T-Foil and stern tab from $+15^\circ$ and $+18^\circ$ respectively to -15° and -18° respectively. During this condition the trim of the model only increased by 0.2° demonstrating the effectiveness of the RCS in exciting a maximum sinkage response.

Another purpose of the open loop step responses tests was to find an appropriate combination of control movements to excite the model only in sinkage or only in trim. This is required for setting the gains of the ride control system to implement different control algorithms, such as pitch control, local control and heave control. From the characteristics of the control surface actions and model step response to each control surface deflection, as discussed previously, a T-Foil deflection of $+15^\circ$ combined with stern tab deflections of $+10^\circ$ should excite the model only in sinkage. This case is called "pure sinkage excitation". Figure 4.25 shows the model responses to the step movements of control surfaces when deflected together to produce "pure sinkage excitation" at four different model speeds. As can be seen this combination at model speed of 2.89 m/s can change the sinkage of the model by about 4.5 mm and the trim of the model is not changed significantly. This successful outcome confirms the control system gains required to run the ride control system in a heave control mode. These results also show good agreement between theory and experiment.

From the previously measured control effects a T-Foil deflection of -8° together with a stern tab deflection of $+18^\circ$ should provide "pure trim excitation", and the responses are shown in

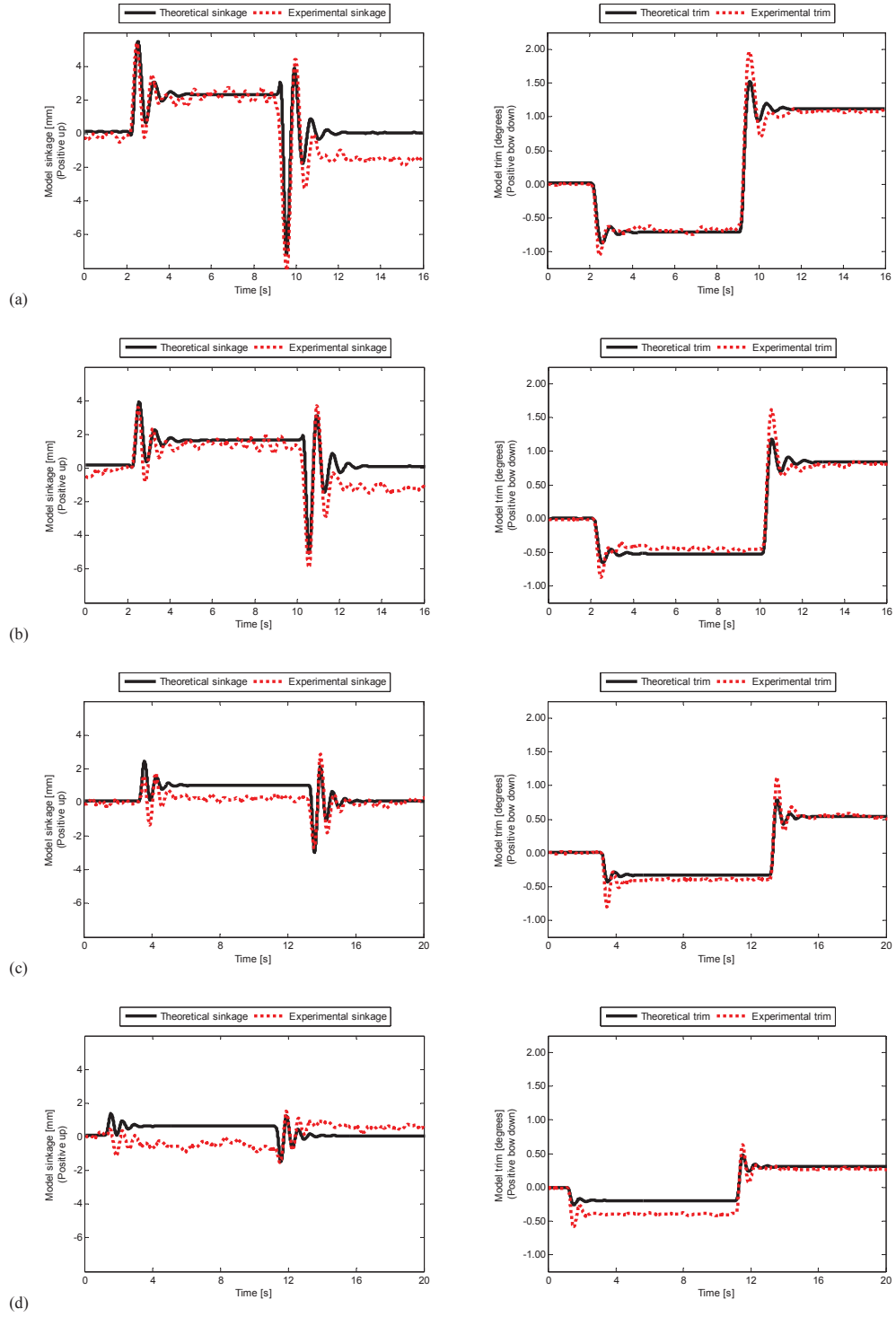


Figure 4.21: Model responses to maximum step movements of RCS when activated together to produce maximum trim change: (a) model speed of 2.89 m/s, (b) model speed of 2.50 m/s, (c) model speed of 2.0 m/s, (d) model speed of 1.53 m/s. First step: T-Foil deflection of $+15^\circ$ and stern tabs deflection of -18° . Second step: T-Foil deflection of -15° and stern tabs deflection of $+18^\circ$.

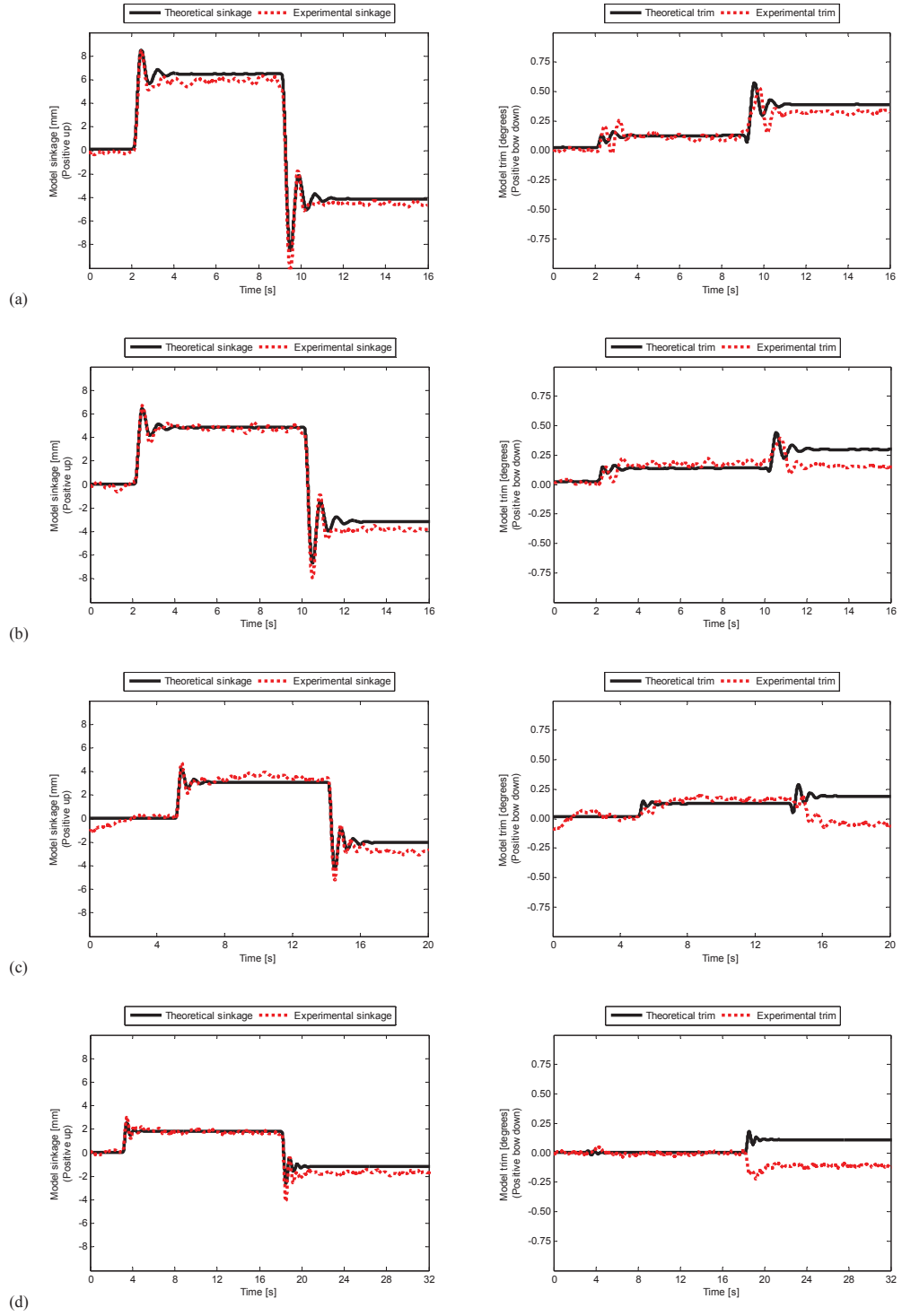


Figure 4.22: Model responses to maximum step movements of RCS when activated together to produce maximum sinkage change: (a) model speed of 2.89 m/s, (b) model speed of 2.50 m/s, (c) model speed of 2.0 m/s, (d) model speed of 1.53 m/s. First step: T-Foil deflection of $+15^\circ$ and stern tabs deflection of $+18^\circ$. Second step: T-Foil deflection of -15° and stern tabs deflection of -18° .

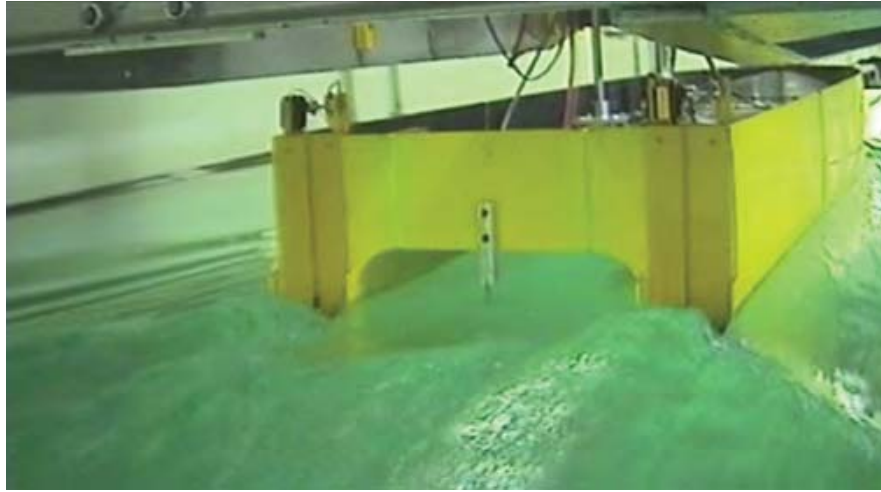


Figure 4.23: Photo of the model running at the low speed of 1.53 m/s when the stern tabs and the T-Foil are deflected at -18° and -15° respectively.

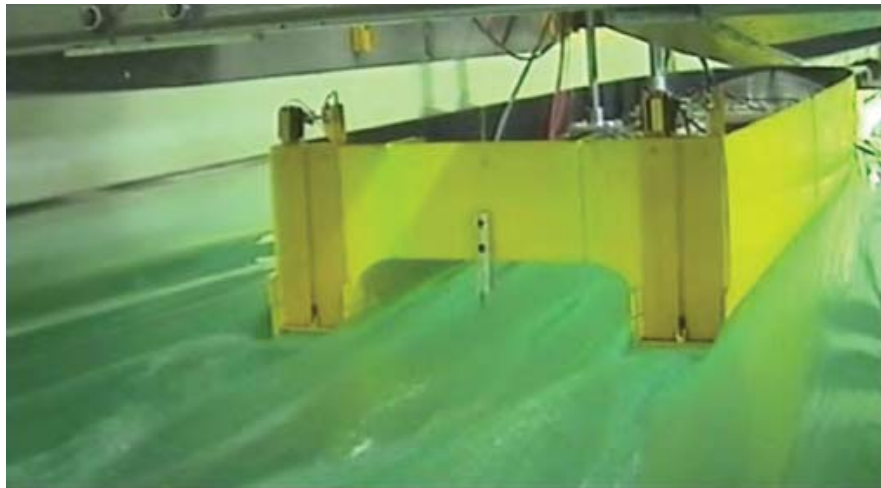


Figure 4.24: Photo of the model running at the high speed of 2.89 m/s when the stern tabs and the T-Foil are deflected at -18° and -15° respectively.

Figure 4.26. As can be seen, this combination at a model speed of 2.89 m/s changes the trim of the model by about 0.9° and the sinkage of the model is not changed. This successful outcome confirms the control system gains required to run the ride control system in a pitch control mode. These final results shown in Figures 4.25 and 4.26 demonstrate that the theoretical calculations predicted the experimental results adequately for the purpose of selecting the gains required to implement different motion control algorithms.

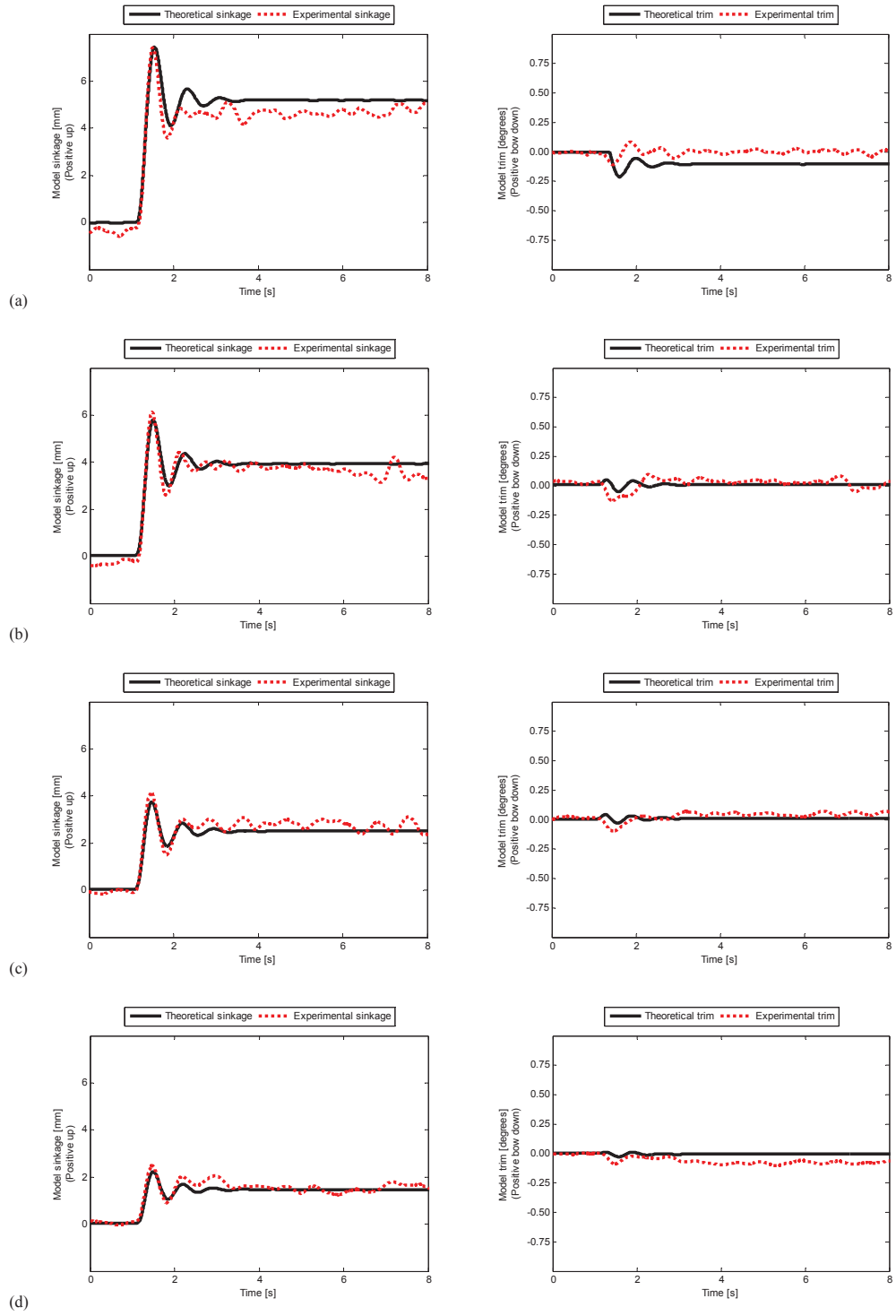


Figure 4.25: Model responses to step movements of RCS surfaces when activated together to produce pure sinkage excitation (T-Foil deflection of $+15^\circ$ and stern tabs deflection of $+10^\circ$): (a) model speed of 2.89 m/s, (b) model speed of 2.50 m/s, (c) model speed of 2.0 m/s, (d) model speed of 1.53 m/s.

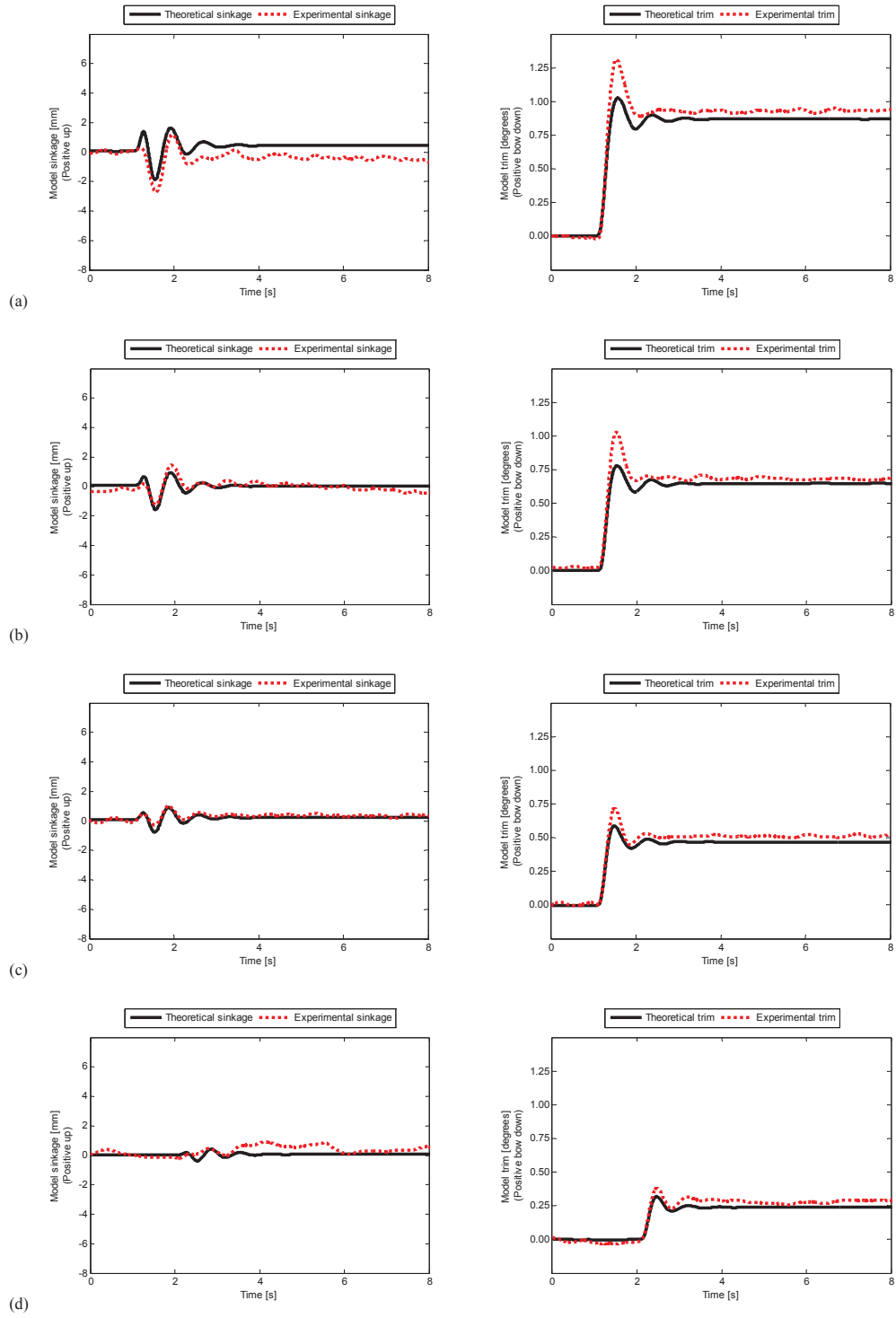


Figure 4.26: Model responses to step movements of RCS surfaces when activated together to produce pure trim excitation (T-Foil deflection of -8° and stern tabs deflection of $+18^\circ$): (a) model speed of 2.89 m/s, (b) model speed of 2.50 m/s, (c) model speed of 2.0 m/s, (d) model speed of 1.53 m/s.

4.5 Frequency responses results

After finalising the step responses tests, model testing was carried out in calm water to investigate the frequency responses of the model to the ride control system. The control surfaces were first deflected individually to their maximum allowance at different excitation frequencies in order to measure the effect of each control surface on heave and pitch. Firstly, the T-Foil was deflected at its maximum range from $+10^\circ$ to -10° while the stern tabs were fixed at $+9^\circ$ and secondly, the stern tabs were deflected at their maximum range from 0° to $+18^\circ$ while the T-Foil was passive at 0° . After that, two combinations of control surfaces deflection were applied at different frequencies in order to produce heave excitation and pitch excitation on the basis of the results obtained from the step responses tests (pure sinkage excitation and pure trim excitation). All the tests were conducted at the high speed of 2.89 m/s for 12 different frequencies ranging from 0.25 Hz to 2.00 Hz in 0.25 Hz increments and ranging from 2.00 Hz to 4.00 Hz in 0.50 Hz increments. The same numerical simulation as explained in 4.2.2 was applied in order to predict the heave and pitch motions. Figure 4.27 shows a sample time record of heave response while only the T-Foil was deflected at its maximum range from $+10^\circ$ to -10° at a frequency of 1.25 Hz.

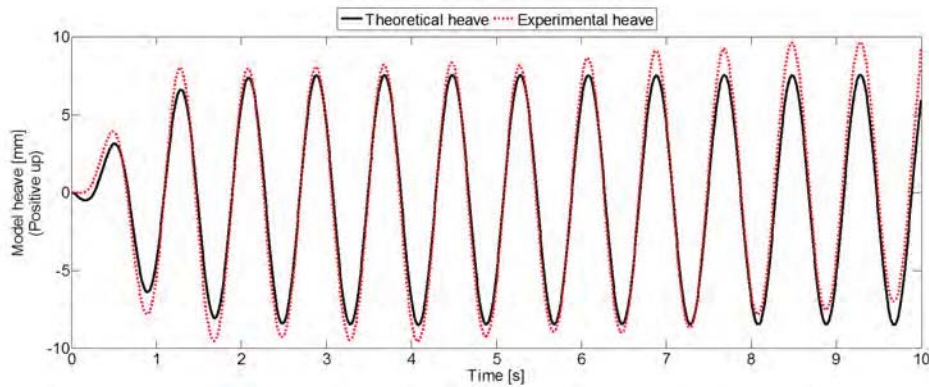


Figure 4.27: Heave response of the model in calm water at a model speed of 2.89 m/s excited by T-Foil deflection of $\pm 10^\circ$ at a frequency of 1.25 Hz with the stern tabs fixed at $+9^\circ$.

4.5.1 Amplitude responses

Figures 4.28 and 4.29 show the experimental and theoretical frequency responses for heave range and pitch range respectively. As can be seen in these figures, all modes produce peak responses at frequencies between 1.00 to 2.00 Hz.

Excitation of the model by T-Foil deflection at full range of $\pm 10^\circ$ can lead to a maximum heave range of 18 mm at frequency of 1.25 Hz, whereas the stern tabs full range excitation can only produce 7 mm heave range at frequency of 1.50 Hz. The T-Foil full range deflection can excite the model by 1.45° pitch range at frequency of 1.00 Hz and also the model pitch range

of 1.15° can be obtained by the stern tabs full range excitation at frequency of 1.00 Hz.

As expected, the pitch excitation mode produces the maximum pitch range as opposed to the heave excitation mode which led to the minimum pitch range. However, this fact is not true for the heave range results as the heave responses to the heave and pitch excitation modes are not the maximum and minimum respectively. In fact the T-Foil full range excitation produces the maximum heave range.

The results presented in Figures 4.28 and 4.29 show a reasonable agreement between the experimental and theoretical responses to the different excitation modes. However, there are some deviations between experimental and theoretical results which are obvious at the response peaks. This might be due to the fact that the applied gains into the numerical computation were obtained by experiments, whereas these gains are not necessarily true for the two degree of freedom rigid body simulation. It is also noted that the Salvesen, Tuck and Faltinsen strip theory is a low Froude number theory and is known to have significantly reduced validity in some cases at a Froude number approaching 0.6. This may be another potential source of the discrepancy between experimental and theoretical results presented in Figures 4.28 and 4.29.

4.5.2 Phase responses

In addition to the amplitude responses, the phase responses of the model to the different excitation modes were analysed. Figures 4.30 to 4.33 show the theoretical and experimental phase lag between the motion responses as well as the control surfaces for different excitation modes at different excitation frequencies.

As can be seen in Figure 4.30, the phase lag between pitch response and T-Foil deflection is about 180° at low frequency of 0.25 Hz and it increases with increase of excitation frequency. A similar trend can be seen for the phase lag between the heave response and the T-Foil deflection while it starts from 0° at low frequency of 0.25 Hz. Heave and pitch responses show a phase lag of about -180° and these results demonstrate a close agreement between theoretical and experimental responses.

Figure 4.31 shows that the phase lag between pitch response and stern tabs deflection tends to be zero at low frequency and dramatically increases with increase of frequency from 0.75 Hz to 2.00 Hz. The same trend can be seen for the phase between the heave response and the stern tabs deflection. It should be noted that it was impossible to measure the phase lag between the heave response and the stern tabs deflection at very low frequencies as the model heave response to the stern tabs full range deflection is negligible. This can be seen in the phase lag between heave and pitch response which are presented only above 1.25 Hz. This graph shows a very close agreement between theoretical and experimental responses to the stern tabs full range deflection.

Figure 4.32 shows the phase lag between the heave, pitch, T-Foil deflection and stern tabs deflection for the pitch excitation mode at different frequencies. It is clear that the T-Foil and

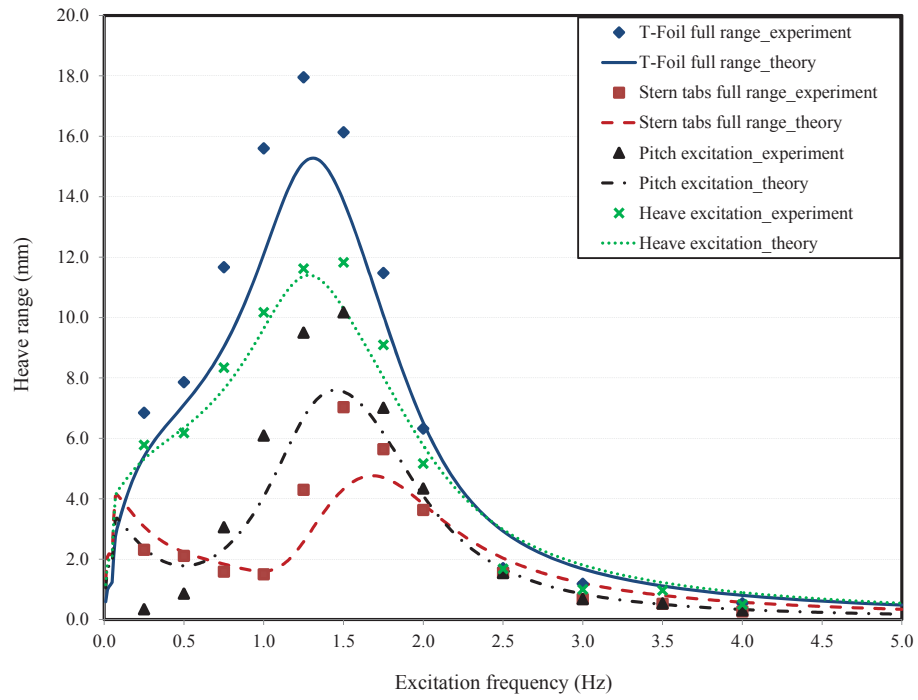


Figure 4.28: Heave range of the model excited by different combinations of the control surfaces at different frequencies in calm water at a model speed of 2.89 m/s.

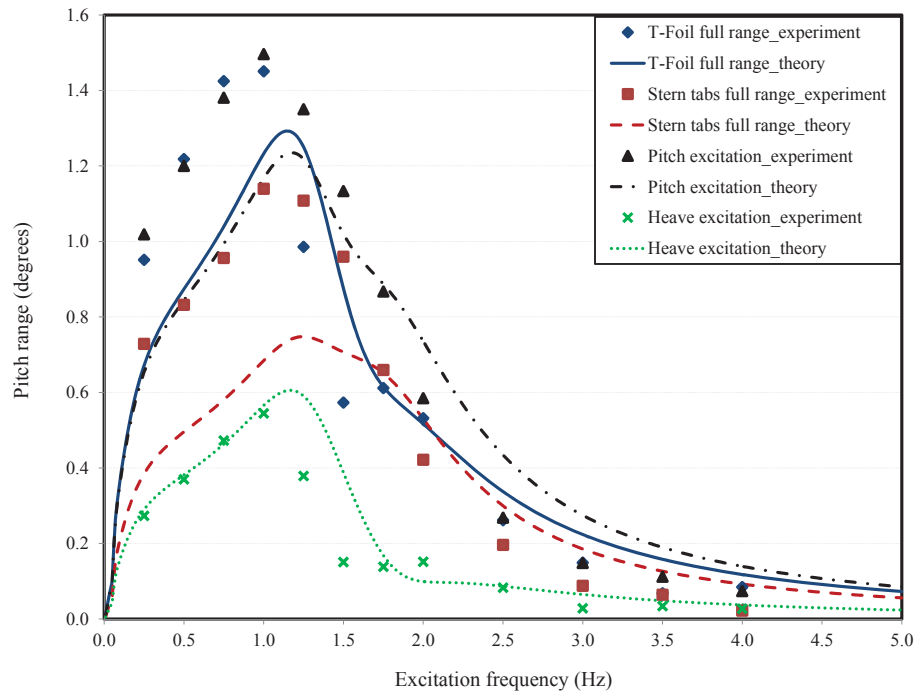


Figure 4.29: Pitch range of the model excited by different combinations of the control surfaces at different frequencies in calm water at a model speed of 2.89 m/s.

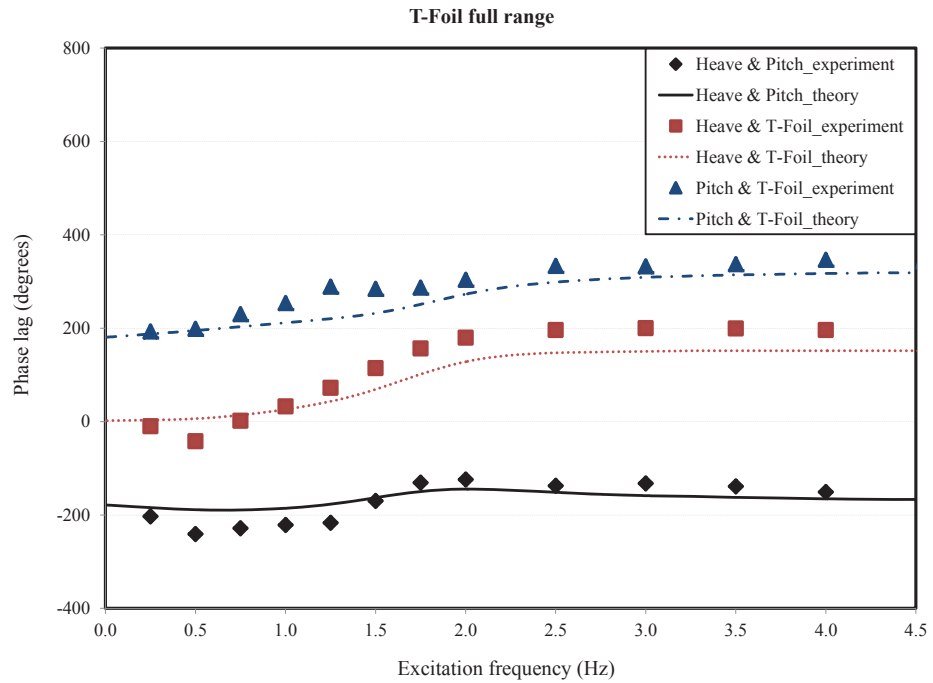


Figure 4.30: Phase lag between the motions as well as the control surface deflections for the T-Foil full range mode at different frequencies in calm water at a model speed of 2.89 m/s.

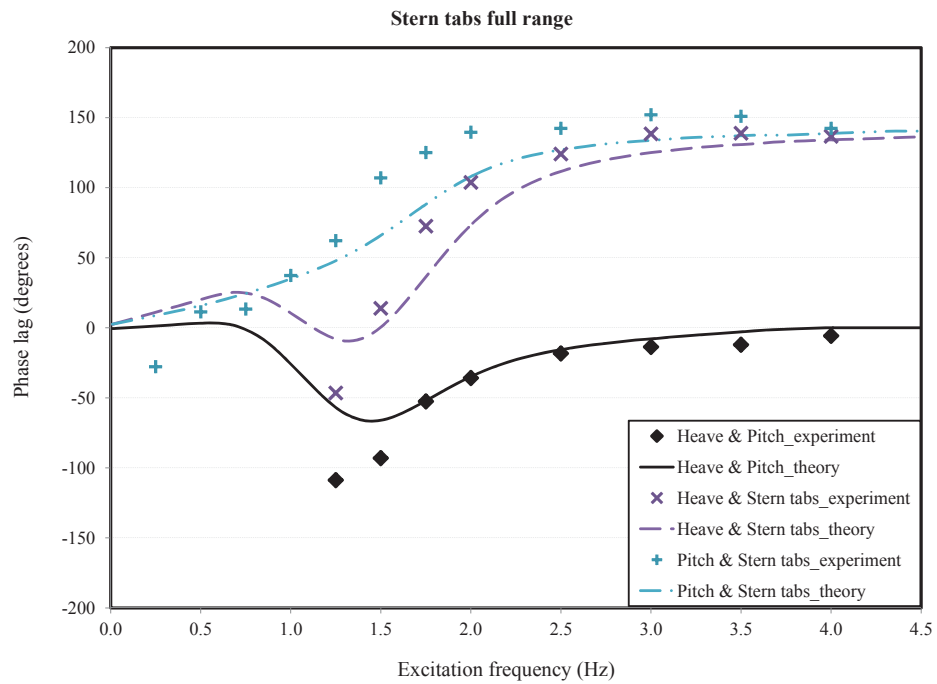


Figure 4.31: Phase lag between the motions as well as the control surface deflections for the stern tabs full range mode at different frequencies in calm water at a model speed of 2.89 m/s.

the stern tabs should be deflected by 180° phase lag in order to excite the model only in pitch. These results also show that experimental phase lags are in close agreement with theoretical analysis.

Finally, Figure 4.33 presents the results for the heave excitation mode. As it is required for the T-Foil and the stern tabs to be deflected in phase (i.e. 0° phase lag) in order to excite the model only in heave, the phase lag between heave and T-Foil deflection is equal to the phase lag between heave and the stern tabs. The same trend can be seen in the phase lag between the pitch response and the deflection of control surfaces.

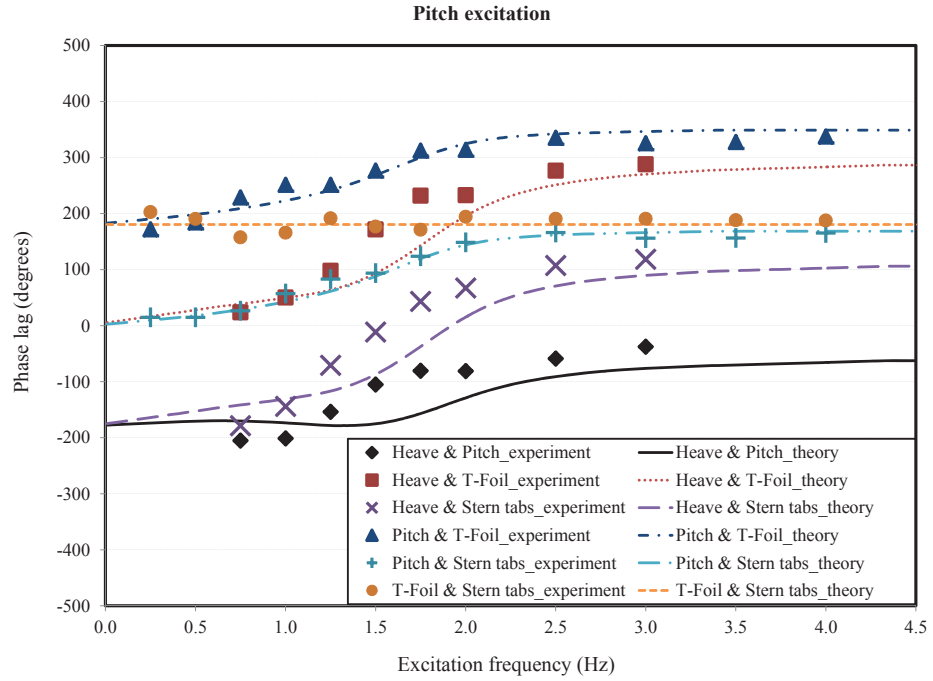


Figure 4.32: Phase lag between the motions as well as the control surface deflections for the pitch excitation mode at different frequencies in calm water at a model speed of 2.89 m/s.

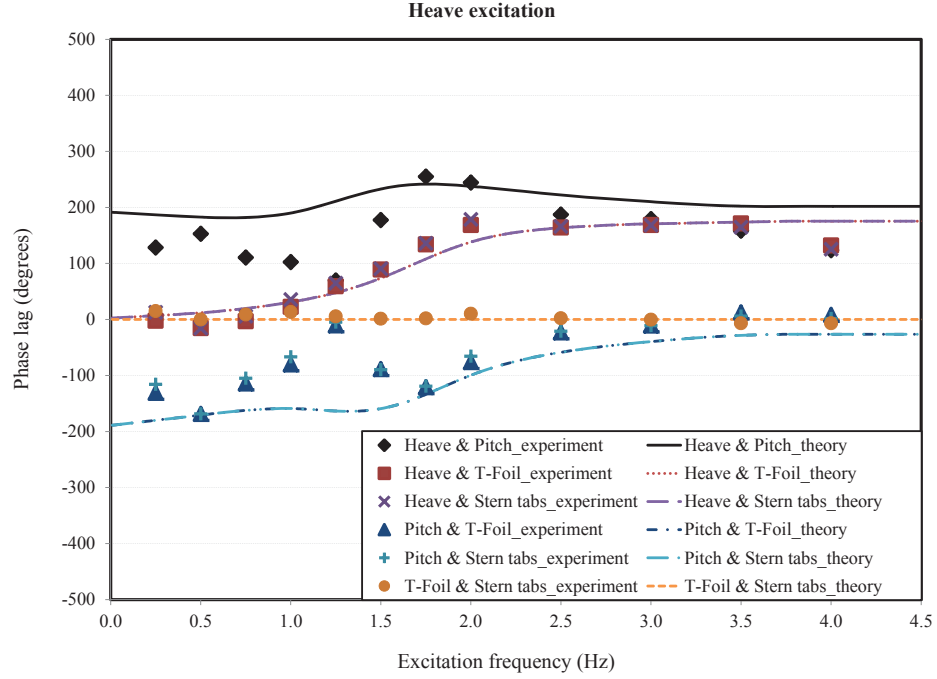


Figure 4.33: Phase lag between the motions as well as the control surface deflections for the heave excitation mode at different frequencies in calm water at a model speed of 2.89 m/s.

4.6 Conclusions

Two hydrostatic methods were applied to determine the T-Foil and stern tab responses, namely a static load experiment and a hydrostatic prediction, and there was close agreement between the two outcomes. This was extended by a dynamic prediction of the response of the moving model based on a two degree of freedom rigid body analysis using strip theory. The results from this analysis developed an equation of motion to predict the sinkage and trim response of the model based on T-Foil and stern tab control surface deflections. This analysis was based on an infinite flow region for the T-foil without including possible interaction effects between the water free surface and demihull surfaces.

The 2.5 m towing tank model was equipped with a Ride Control System (RCS) consisting of a centre bow mounted T-Foil and stern tabs located at the stern of the model. Towing tank tests were performed in calm water to measure the step and frequency responses according to ride control inputs to identify control gains for heave and pitch control and also to compare the response to a numerical simulation based on a two degree of freedom rigid body analysis using strip theory.

The model experiments show that a maximum deflection of the T-Foil from $+15^\circ$ to -15° when it is operated separately can sink the model over a range of about 7 mm and trim it by about 1° . Moreover a maximum deflection of the stern tabs from -18° to $+18^\circ$ lifts the model

by about 3.5 mm and trims the model by about 1° .

The theoretical calculation of sinkage response to the T-Foil deflection was found to be in good agreement with experimental sinkage, but over predicted the trim response by about 0.1° when the T-Foil was deflected $+15^\circ$. This is possibly due to the fact that the T-Foil lift-curve coefficient was considered constant in order to perform the theoretical analysis.

The deviation between theoretical calculations and experimental responses to the stern tabs deflection is somewhat greater than the results of predicted responses to T-Foil deflections mainly due to the lack of sufficient data to predict the lift-curve derivative of stern tabs for both positive and negative deflections at angles of $\pm 10^\circ$ and a speed of 2.89 m/s.

It was found that a T-Foil deflection of $+15^\circ$ and stern tab deflection of $+10^\circ$ produce pure sinkage, while a T-Foil deflection of -8° together with the stern tab deflections of $+18^\circ$ lead to pure trim. These outcomes indicate the control system gains required to run the ride control system in pure pitch and pure heave control modes.

The frequency response tests show that all four excitation modes produce peak responses at frequencies between 1.00 to 2.00 Hz. A maximum of 18 mm heave range at a frequency of 1.25 Hz can be obtained by excitation of the model with T-Foil deflection at full range of $\pm 10^\circ$. However, the stern tabs full range excitation can only produce 7 mm heave range at a frequency of 1.50 Hz.

The T-Foil full range deflection can produce a pitch range of 1.45° at a frequency of 1.00 Hz, moreover the model pitch range of 1.15° can be obtained by the stern tabs full range excitation at a frequency of 1.00 Hz.

This study presents a relatively simple method of predicting open loop control surface step and frequency responses using a simple strip theory, lumped parameter approach. This method and the test data obtained here can now form the basis for the optimisation of closed loop control ride control systems. The results also demonstrate that the ride control system can be operated in different control modes including pitch control and heave control when appropriate closed loop system gains are selected in the appropriate combinations for the control surfaces.

These are important outcomes and this work underpins a comprehensive model test program to determine the control system gains required to minimise ship motions and associated loads to be discussed in Chapters 5 and 6.

Chapter 5

Closed-Loop Influence of the Ride Control System on the Model Motion Responses

5.1 Introduction

After finalising the open loop step and frequency response tests in calm water and concluding the effect of the ride control system on the 2.5 m catamaran model motions, model testing was carried out in regular waves in order to investigate the influence of different ride control algorithms on the motions response of the model.

Six ideal motion control feedback algorithms were used to activate the model scale ride control system and surfaces in a closed loop control system: heave control, local motion control and pitch control, each in a linear and nonlinear version. The responses were compared with the responses with inactive control surfaces and with no control surfaces fitted.

A series of model tests in head seas at different wave heights and frequencies was conducted for the different control algorithms at the Australian Maritime College (AMC) towing tank in order to measure the heave and pitch motions. The Response Amplitude Operators (RAOs), Response Phase Operators (RPOs) and acceleration response of the model were evaluated from the heave and pitch data. In addition to the RAOs and RPOs, the amplitude and phase of the control surface motions were analysed in order to present the range of control surfaces deflection as well as the phase lag of the control surfaces deflection relative to the model motions.

5.2 Ride control algorithms

The towing tank model was tested with different ride control conditions including without RCS (i.e. no T-Foil and locked stern tabs), passive RCS (i.e. with locked T-Foil and stern tabs) and

active RCS. The active RCS mode consisted of heave control, local motion control and pitch control, while linear and nonlinear gains were applied for each control mode. The linear gains were selected so that the control motions remained within their maximum range of physical movement, the nonlinear gains were set at large values so that the control surfaces moved at maximum slew rate between their extreme positions thus generating maximum control force at all times. The general equations for demanded deflection for each control surface for all algorithms based on global motions are

$$\alpha_{TFd} = TF0 + aH + b\dot{H} + c\ddot{H} + dP + e\dot{P} + f\ddot{P} \quad (5.1)$$

$$\alpha_{STd} = ST0 + gH + h\dot{H} + i\ddot{H} + jP + k\dot{P} + l\ddot{P}, \quad (5.2)$$

where α_{TFd} and α_{STd} are the demanded T-Foil and the stern tabs deflection respectively, $TF0$ and $ST0$ are the T-Foil and the stern tabs initial angle respectively, H and P are the instantaneous heave and pitch, and the parameters a to l are the control gains. Over dots represent differentiation with respect to time.

At this point it should be noted that the small model scale control system has physical limitations due to its size. In particular it is known to have phase lags between demands and control motions as presented in Section 3.4 of Chapter 3. In general, commercial full scale ride control systems are operated as motion damping systems with the broad objective of reducing peaks in RAOs under circumstances of relatively small control forces (e.g. several hundred tonnes weight) in proportion to ship weight (e.g. several thousand tonnes). Under such conditions it appears that the control system is not capable of significantly modifying system stiffness and so control action is primarily directed at motion control by damping. However, some commercial systems do incorporate a small stiffness effect in the feedback, particularly for pitch control. In the present model scale investigation the approach of formally implementing damping feedback in the control system has been taken but it should be recognised that phase lags in the model system give rise to an effective combination of damping and stiffness in the control action.

Equations 5.1 and 5.2 can be simplified by considering only damping modes of feedback demand to the control surface actuators and zero magnitude of initial control surfaces deflection, giving 5.3 and 5.4, with coefficients b , e , h and k defined below for each different algorithm and the unused control coefficients set to zero.

$$\alpha_{TFd} = b\dot{H} + e\dot{P} \quad (5.3)$$

$$\alpha_{STd} = h\dot{H} + k\dot{P}. \quad (5.4)$$

Here α_{TFd} and α_{STd} represent demanded pitch deflections of the T-Foil and stern tabs respectively, the actual deflections being somewhat phase lagged from these demands.

5.2.1 Pitch control

Equations 5.3 and 5.4 can be further simplified to give equations for the demanded control deflections for the pitch control as

$$\alpha_{TF} = e\dot{P} \quad (5.5)$$

$$\alpha_{ST} = k\dot{P}. \quad (5.6)$$

Once again, these are the demanded control deflections and the actual control deflections will be somewhat phase lagged to the demanded deflections. The gains k and e must have a defined ratio to ensure that no net heave force is generated but only a pitch control moment. To calculate the parameter e for the linear deflection of the T-Foil, the maximum T-Foil deflection should be considered in relation to an estimated maximum pitch velocity. Thus, noting that a positive T-Foil force produces a negative pitching moment,

$$e = -\frac{(\alpha_{TFd})_{max}}{\dot{P}_{max}}. \quad (5.7)$$

Equation 5.7 can be solved with the following inputs:

- Maximum pitch rate, $\dot{P}_{max} = P_{max} \times \omega_e$
- Wave encounter angular frequency, $\omega_e = \omega_e^* \sqrt{\frac{g}{l}}$
- Maximum pitch, $P_{max} = (Maximum\ wave\ slope) \times (Maximum\ pitch\ RAO)$ where $Maximum\ wave\ slope = \frac{2\pi\zeta}{\lambda}$, ζ =wave amplitude and $\lambda = \frac{2\pi g}{\omega_0^2}$ is the wavelength.
- The wave angular frequency in fixed coordinates,

$$\omega_0 = \omega_0^* \sqrt{\frac{g}{l}} = \frac{-1 + \sqrt{1 + (4\omega_e^* Fr)}}{2Fr} \sqrt{\frac{g}{l}}$$
- The Froude number, $Fr = \frac{U}{\sqrt{gl}}$ where U = model forward speed, g = gravitational acceleration and l = model length.

In order to activate the ride control system in the pitch control mode, the total net force of control surfaces in the heave direction should be zero. It was assumed that the drag component of each control surface is negligible in the heave direction. It is also assumed that the control surfaces are sufficiently close to the hull that the local flow is parallel to the hull and therefore the

control surfaces respond only to their deflections relative to the hull, i.e. there is no additional effective angle of attack resulting from the global pitching of the model. Thus the lift forces are

$$L_{TF} = \frac{1}{2} \rho U^2 S_{TF} \alpha_{TF} (C_{L\alpha})_{TF} \quad (5.8)$$

$$L_{ST} = \frac{1}{2} \rho U^2 S_{ST} \alpha_{ST} (C_{L\alpha})_{ST}, \quad (5.9)$$

where α_{TF} and α_{ST} are actual surface deflections. For zero heave force we require $L_{TF} + 2L_{ST} = 0$ (noting that there are two tabs), therefore

$$\frac{\alpha_{ST}}{\alpha_{TF}} = \frac{-S_{TF}(C_{L\alpha})_{TF}}{2S_{ST}(C_{L\alpha})_{ST}}. \quad (5.10)$$

Combining Equation 5.10 with Equations 5.5 and 5.6, the control parameter k for the linear deflection of stern tabs is evaluated as

$$k = -e \frac{S_{TF}(C_{L\alpha})_{TF}}{2S_{ST}(C_{L\alpha})_{ST}}, \quad (5.11)$$

where the control surfaces lift coefficient derivative $(C_{L\alpha})$ was determined based on the results from previous studies on the T-Foil (Section 3.5 of Chapter 3) and stern tabs [107]. It should be noted that during control operations the T-Foil reaches the limit of its range before the stern tabs when the actions are balanced to give zero heave. Therefore the parameter e is determined by equation 5.7 in terms of the maximum T-Foil deflection and the parameter k is determined by equation 5.11 in terms of e . Thus, whilst the T-Foil can operate over its full range of action, the stern tabs operate at less than their full range of action in this control mode.

5.2.2 Heave control

In order to evaluate the control gains for the heave control Equations 5.3 and 5.4 are reduced to equations for the demanded control deflections:

$$\alpha_{TFd} = b\dot{H} \quad (5.12)$$

$$\alpha_{STd} = h\dot{H}. \quad (5.13)$$

The parameter b is evaluated by considering the maximum deflection of the T-Foil and the maximum heave velocity,

$$b = -\frac{(\alpha_{TFd})_{max}}{\dot{H}_{max}}, \quad (5.14)$$

where the maximum heave velocity is $\dot{H}_{max} = H_{max} \times \omega_e$ and maximum heave is $H_{max} = (Maximum\ Wave\ amplitude) \times (Maximum\ heave\ RAO)$.

For the heave control mode the total pitch moment about the *LCG* induced by the control surfaces must be zero, thus $L_{TF}x_{TF} - 2L_{ST}x_{ST} = 0$, giving

$$h = b \frac{x_{TF}S_{TF}(C_{L\alpha})_{TF}}{x_{ST}2S_{ST}(C_{L\alpha})_{ST}}, \quad (5.15)$$

where x_{TF} and x_{ST} are the distances between the *LCG* and the centre of pressure of the T-Foil and the stern tabs respectively. Once again the T-Foil reaches the limit of its range before the stern tabs when the actions are balanced to give zero pitch. Therefore the parameter b is determined by equation 5.14 in terms of the maximum T-Foil deflection and the parameter h is determined by equation 5.15 in terms of b .

5.2.3 Local control

In order to control the local control surface motions, the control surfaces act independently and have input demands to oppose the local vertical velocities. The vertical velocity of the model at the longitudinal location of each control surface are $\dot{H} - x_{TF}\dot{P}$ and $\dot{H} + x_{ST}\dot{P}$ for the T-Foil and stern tab respectively. Thus from Equations 5.3 and 5.4 we require control surface demands $\alpha_{TFd} = b(\dot{H} - x_{TF}\dot{P})$ and $\alpha_{STd} = h(\dot{H} + x_{ST}\dot{P})$, where

$$b = -\frac{(\alpha_{TFd})_{max}}{\dot{H}_{max}} \quad (5.16)$$

$$h = -\frac{(\alpha_{STd})_{max}}{\dot{H}_{max}}. \quad (5.17)$$

Written in the form of Equations 5.3 and 5.4 we thus specify

$$e = -b \times x_{TF} \quad (5.18)$$

$$k = h \times x_{ST}. \quad (5.19)$$

5.2.4 Nonlinear control algorithms

It is recognised that the control surfaces are not large enough to cancel motions altogether in large waves. Therefore a nonlinear version of each algorithm is proposed, in which the control

surfaces are moved to their maximum angular offsets as quickly as the mechanisms will allow, thus giving demand control surface deflections

$$\alpha_{TFd} = \pm b \dot{H}_{max} \pm e \dot{P}_{max} \quad (5.20)$$

$$\alpha_{STd} = \pm h \dot{H}_{max} \pm k \dot{P}_{max}. \quad (5.21)$$

The constants b , e , h and k are determined as described above for the respective operation mode, and the sign in each case is chosen so that the lift force or moment opposes the relevant velocity term (heave, pitch or local). While this does not change the maximum control forces at maximum control deflection at the extreme point of the motion vertical velocity, it will maintain the forces at maximum values opposing the velocities for a longer duration within the motion half cycles and so increase the impulse of those forces by a factor of approximately $\pi/2$ (an additional 57%) assuming the motions to be close to sinusoidal and the control mechanisms to be instantaneously responsive. This represents a significant potential increase of motion control performance.

5.3 Motion tests and analysis

Towing tank testing in head seas was undertaken in regular waves at a model speed of 2.89 m/s, simulating a full scale speed of 37 knots. The model was tested at two wave heights, 60 mm and 90 mm, simulating full scale wave height of 2.69 m and 4.03 m respectively. Wave frequencies ranging from 0.350 Hz to 0.900 Hz were generated by the towing tank wave maker for each test condition. Table 5.1 summarises the model test conditions. It should be noted that a sample frequency of 50 Hz was selected for the motion data acquisition system used to acquire the voltage signals including LVDTs.

As can be seen in Table 5.1, the model tests in 60 mm waves were conducted with different control conditions including without RCS, passive RCS, linear heave control, nonlinear heave control, linear local control, nonlinear local control, linear pitch control and nonlinear pitch control. In contrast, the model tests in 90 mm waves were only carried out with control conditions of passive RCS, linear heave control, linear local control, linear pitch control and nonlinear pitch control. The results obtained in 60 mm waves demonstrated that the nonlinear ride control system was not more effective than the linear system in heave and local control modes.

Figures 5.1 and 5.2 show a typical sample time record at model speed of 2.89 m/s ($Fr = 0.608$), wave height of 90 mm and dimensionless wave encounter frequency $\omega_e^* = 3.182$ for the passive RCS mode and pitch control mode respectively. It is to be noted that the wave profile at the LCG and the heave motion are positive up, the pitch motion is positive bow down and

Table 5.1: Towing tank catamaran model RCS test conditions.

Model speed, U (m/s)	Wave Height (mm)	Ride Control algorithm	Wave Frequency (Hz)
2.89	60	Without RCS	0.350
		Passive RCS	
		Heave control	0.400
		Nonlinear heave control	0.450
		Local control	0.500
		Nonlinear local control	0.525
		Pitch control	0.550
		Nonlinear pitch control	0.575
	90		0.600
		Passive RCS	0.650
		Heave control	0.700
		Local control	0.800
		Pitch control	0.900
		Nonlinear pitch control	

the control surfaces deflection are positive counter-clockwise viewed from the starboard side, producing upward lift. In order to evaluate the amplitude and phase of the signals, a range of the time record was analysed, starting when regular periodic motions had been reached and including at least five cycles, and an average of all these cycles was presented. The amplitude and phase analysis was carried out by finding the peak and trough of each cycle using the Matlab "Findpeaks" function. As can be seen from Figures 5.1 and 5.2, the pitch control mode significantly reduced the pitch motion, clearly demonstrating the significant effect of motion control on the response of the model in this mode.

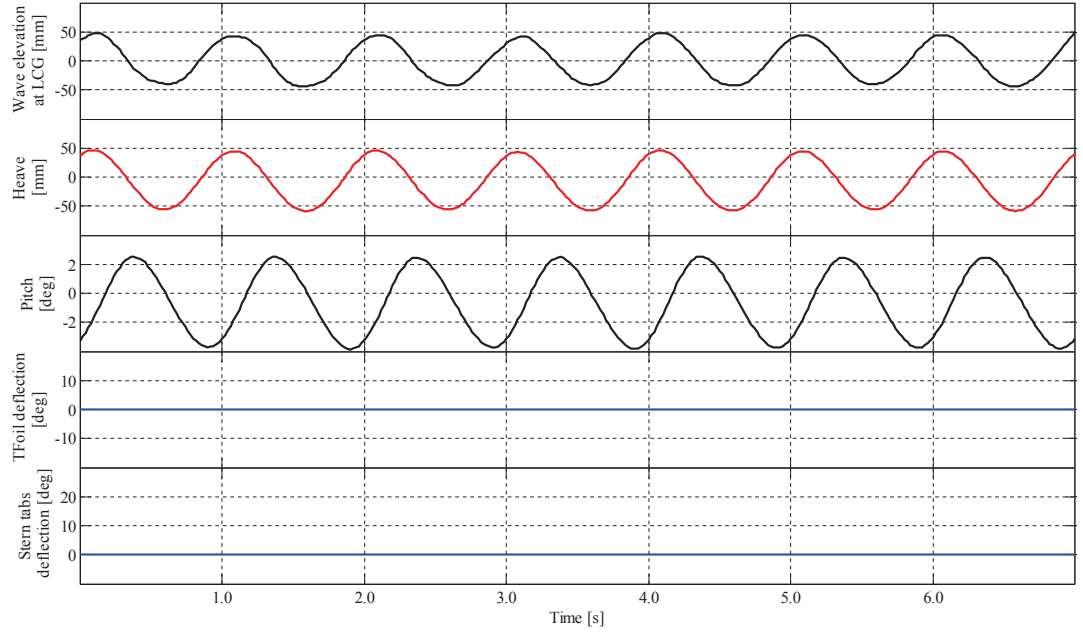


Figure 5.1: Time records at a model test speed of 2.89 m/s ($Fr = 0.608$), wave height of 90 mm, dimensionless wave encounter frequency $\omega_e^* = 3.182$ and passive RCS mode.

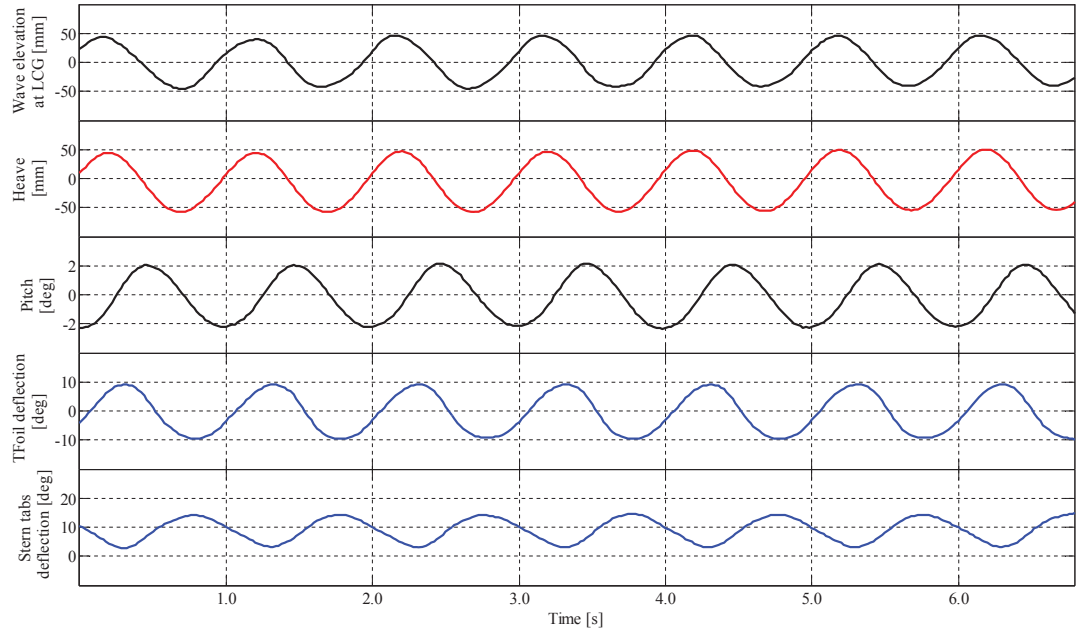


Figure 5.2: Time records at a model test speed of 2.89 m/s ($Fr = 0.608$), wave height of 90 mm, dimensionless wave encounter frequency $\omega_e^* = 3.182$ and pitch control mode.

5.4 Ride control system motions response

5.4.1 Uncertainty analysis

In order to establish the accuracy of the results an uncertainty analysis was performed based on the standard deviation of the results. For each run the time record included from 5 to 19 useable cycles after transients had dissipated and before either the run terminated or reflections or other forms of contamination became significant. The variation between the cycles in each run was analysed in order to quantify the accuracy of the results. The standard deviation analysis of the results shows an average of $\pm 2.5\%$ variation for the wave elevation, $\pm 2.0\%$ variation for the heave motion and $\pm 2.2\%$ variation for the pitch motion. Figures 5.3 and 5.4 illustrate these uncertainty results for some typical cases at a wave height of 60 mm, showing the error bars on the dimensionless pitch and heave respectively. Three of the ride control conditions including without RCS, pitch control and nonlinear pitch control were selected for demonstrating the error bars on the dimensionless pitch shown in Figure 5.3, while three ride control conditions without RCS, heave control and nonlinear heave control were chosen to show the error bars on the dimensionless heave demonstrated in Figure 5.4. These curves illustrate the substantial changes brought about by the most successful ride control algorithm, but as can be seen from Figures 5.3 and 5.4, the uncertainty in the results within each case is insignificant compared to the overall effect of the ride control system. Thus the experimental uncertainty has no impact on the key conclusions of this research, and in view of the quantity of data subsequent results will be presented without error bars.

It should be noted that all of the experimental set-up was calibrated prior to model tests and zeros were taken before each run. Items such as LVDTs and wave probes were calibrated daily. Therefore in addition to the uncertainty analysis, the bias error of the experimental set-up was estimated by comparing the daily calibration factor to quantify any possible drift. This showed an average fluctuation of about $\pm 1.5\%$ which clearly demonstrates the insignificant magnitude of the systematic errors. There are other effects that may be difficult to quantify precisely, for instance carriage aerodynamic effects as reported by Yang [131] in the same towing tank as used in the present experiments. Yang demonstrated that there was flow of air between the top of the carriage and the water surface that caused a pressure wave in the vicinity of and travelling with the test model, and a corresponding reduction in the local calm water surface height. However, this phenomenon will affect different tests in the same way, so will not change the ranking of results, nor the conclusions.

5.4.2 Response Amplitude Operators (RAOs)

The heave and pitch motions were measured using the LVDT data obtained from the towing tank data acquisition system (discussed in Section 4.3 of Chapter 4) and from this the Response Amplitude Operators (RAOs) were evaluated.

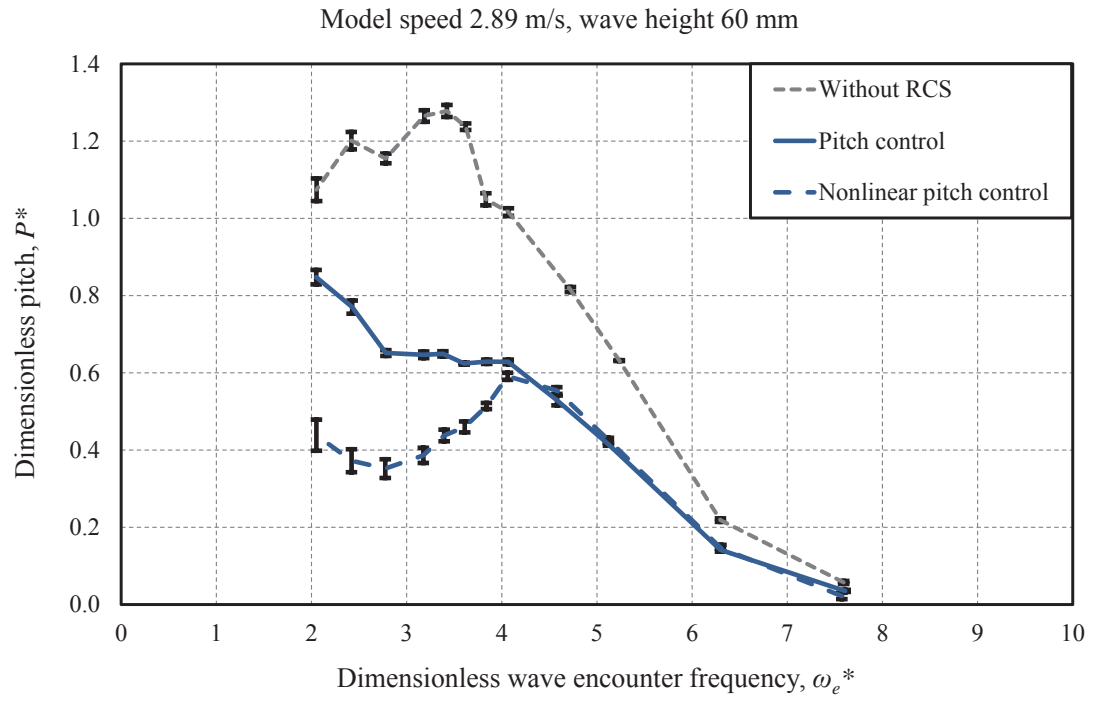


Figure 5.3: Pitch RAO at model speed of 2.89 m/s ($Fr = 0.608$) and wave height of 60 mm showing error bars.

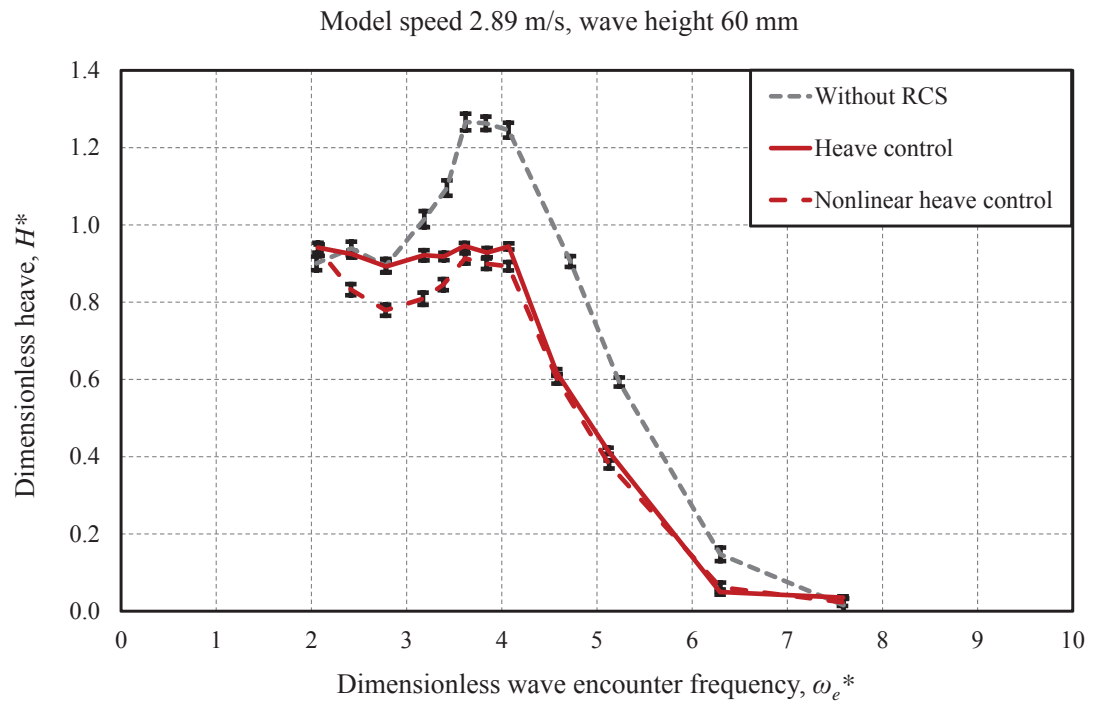


Figure 5.4: Heave RAO at model speed of 2.89 m/s ($Fr = 0.608$) and wave height of 60 mm showing error bars.

Figures 5.5 and 5.6 show the pitch RAO at wave height of 60 mm and 90 mm respectively and Figures 5.7 and 5.8 show the heave RAO at wave height of 60 mm and 90 mm respectively. In addition to the different control conditions, the results from a previous study with no ride control conducted on the same model by Lavroff [3] are presented in these figures to compare with the current results.

Comparing the results of the model tests without RCS and with a passive RCS it can be seen that the deployment of the T-Foil to a fixed position and acting as a passive control surface reduces the peak heave and pitch motions. As expected, heave and pitch were more strongly reduced by their respective control algorithms. This was more evident in the pitch control mode, where the pitch RAO is substantially reduced. Operation in local control mode led to similar results to those from operation in the heave control mode.

Figures 5.5 and 5.6 demonstrate that compared to the passive RCS mode, the local control algorithms increased the pitch motion at dimensionless wave encounter frequencies (ω_e^*) up to 4. A similar trend can be seen for the heave control mode, however it reduced the pitch motion at very low wave frequencies. As can be seen from Figure 5.5, the nonlinear action of the ride control system in the heave control mode increased the pitch motion and a clear benefit of nonlinearity could not be identified in the local control, although it shows some pitch motion reduction at very low wave frequencies. The most notable aspect of the data presented in Figures 5.5 and 5.6 is the significant effect of the nonlinear pitch control algorithm on the reduction of model pitch motion, where it reduced the peak pitch motion by about 50%.

As expected, Figures 5.7 and 5.8 show that heave motion was reduced by the heave control algorithm and was more strongly reduced in the nonlinear heave control mode. A similar outcome was obtained by the linear and nonlinear local motion control algorithms. Although the pitch control mode had a positive effect for $\omega_e^* > 3.5$, this control mode increased the heave motion at low frequencies.

In general the pitch control and heave control modes strongly reduced the pitch and heave motions respectively for all cases investigated. The nonlinear control modes demonstrated the most significant effect on reducing the motions response of the model, in particular when compared to the non RCS results of Lavroff [3] with a reduction of up to 50% in pitch motion.

5.4.3 Response Phase Operators (RPOs)

In addition to the RAOs, the Response Phase Operator (RPO) was studied at different wave heights and frequencies, because of the importance of phase lag between the wave profile and model motions. The pitch RPO is the phase lag of the model pitch motion relative to the wave profile measured at the model LCG. Similarly the heave RPO is the phase lag of the heave motion relative to the wave profile at the model LCG. In order to measure the phase lag of the model motions relative to the wave profile, a time record of recorded data that included at least five cycles of each signal was analysed. The peaks and troughs of the signals were found

and an average of all cycles was evaluated.

Figures 5.9 and 5.10 show the pitch RPO at wave heights of 60 mm and 90 mm respectively, while Figures 5.11 and 5.12 show the heave RPO at wave heights of 60 mm and 90 mm respectively. As can be seen from Figures 5.9 and 5.10, the pitch RPO tends to 90° at very low wave frequencies, as expected since the pitch follows the wave slope, and there is a progressive increase of phase lag of pitch relative to the encountered wave with increasing wave frequency, indicating an increasing lag as inertia becomes more significant at higher frequency. The increase of phase lag from zero to high frequency however remains below 180° in all cases, reaching about 120° of lag increase in the smaller waves and about 70° of lag increase in the larger waves. Broadly similar increases of 120° and 70° in phase lag with frequency in smaller and larger waves respectively are seen in the heave responses shown in Figures 5.11 and 5.12. However, the heave RPOs commence at 0° at low wave frequencies of course. Overall, we see that the pitch motion lags the heave motion by approximately 90° over the full range of frequencies tested, which extends well beyond the frequency of maximum motions (at about $\omega_e^* \approx 4$) into the frequency range of quite small motions ($\omega_e^* > 6$ approximately).

Since the controls are mechanical systems with inertia and a limited slew rate of about $300^\circ/\text{s}$ it is to be expected that their response will lag demand inputs. Although the ride control algorithms were designed on the basis of the control gains as explained in Section 5.4, any phase lag between the control surfaces deflection and model motions will appear as an increased effective stiffness of the control system.

Figures 5.13 and 5.14 show the phase lag of the T-Foil relative to pitch at wave heights of 60 mm and 90 mm respectively. It should be noted that all phase data are presented in the range from 0° to 360° therefore $+360^\circ$ was added to the negative results in order to present them in the positive zone of the phase lags. As can be seen from Figures 5.13 and 5.14, in pitch control mode the phase lag between detected motion and T-Foil movement lies between 270° and 360° . This corresponds to the control force comprising both damping and stiffness components. With heave or local motion control the phase lies between 0° and 90° , this also corresponding to the T-Foil force comprising both damping and stiffness components. When the system operates with higher nonlinear gains the limited slew rate of the model mechanism increases the phase lag in both modes of control. Similar effects are evident in the phase lag of the stern tabs shown in Figures 5.15 and 5.16, where in pitch control mode the phase lag lies between 90° and 180° approximately; this again corresponds to the control force being a mix of damping and stiffness components.

As expected the phase lag between the control surfaces presented in Figures 5.17 and 5.18 show that the T-Foil and the stern tabs are in phase in the heave and local control modes but out of phase in the pitch control mode. However, a rise of about 30° phase lag was observed in the pitch control mode at a wave height of 90 mm at ω_e^* in the range 4 – 6. The phase lag between the T-Foil deflection and the stern tabs deflection in the pitch control mode at a wave height of 90 mm starts from 180° at $\omega_e^* = 2$ and rises to 240° as ω_e^* increases to 5.

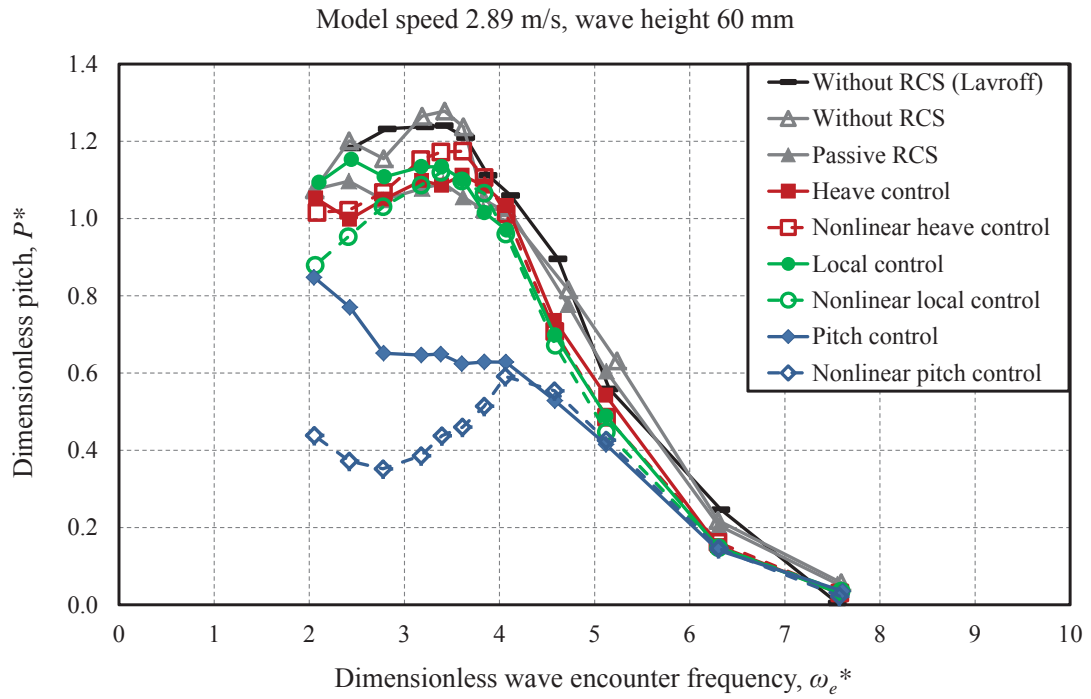


Figure 5.5: Pitch RAO at model speed of 2.89 m/s ($Fr = 0.608$) and wave height of 60 mm.

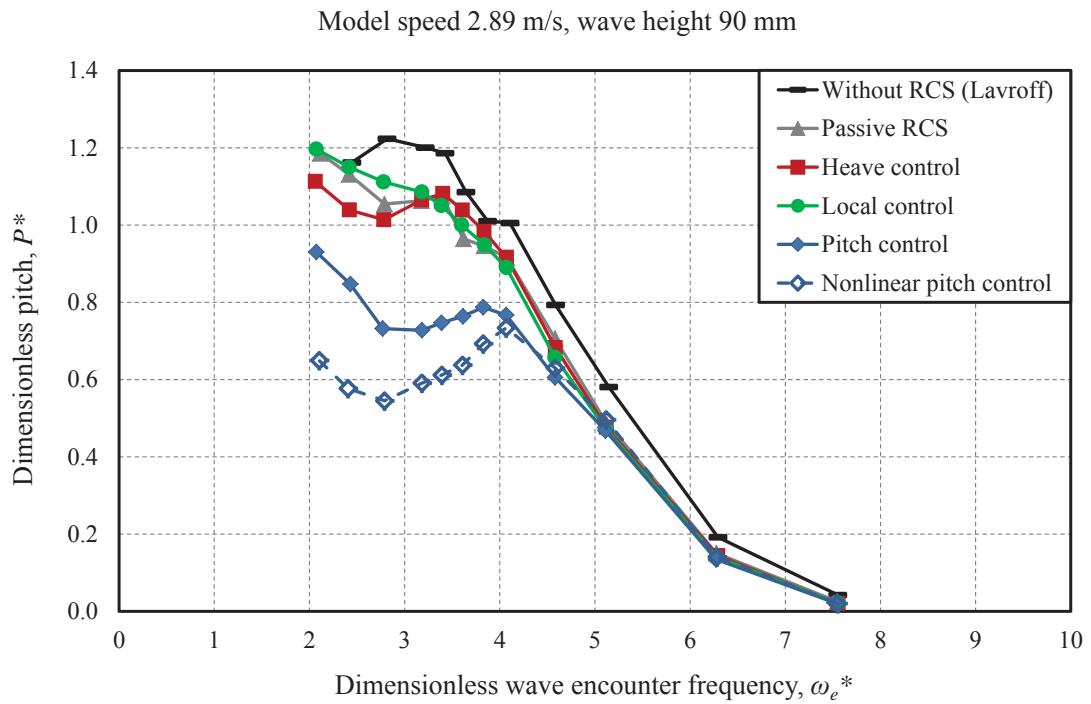


Figure 5.6: Pitch RAO at model speed of 2.89 m/s ($Fr = 0.608$) and wave height of 90 mm.

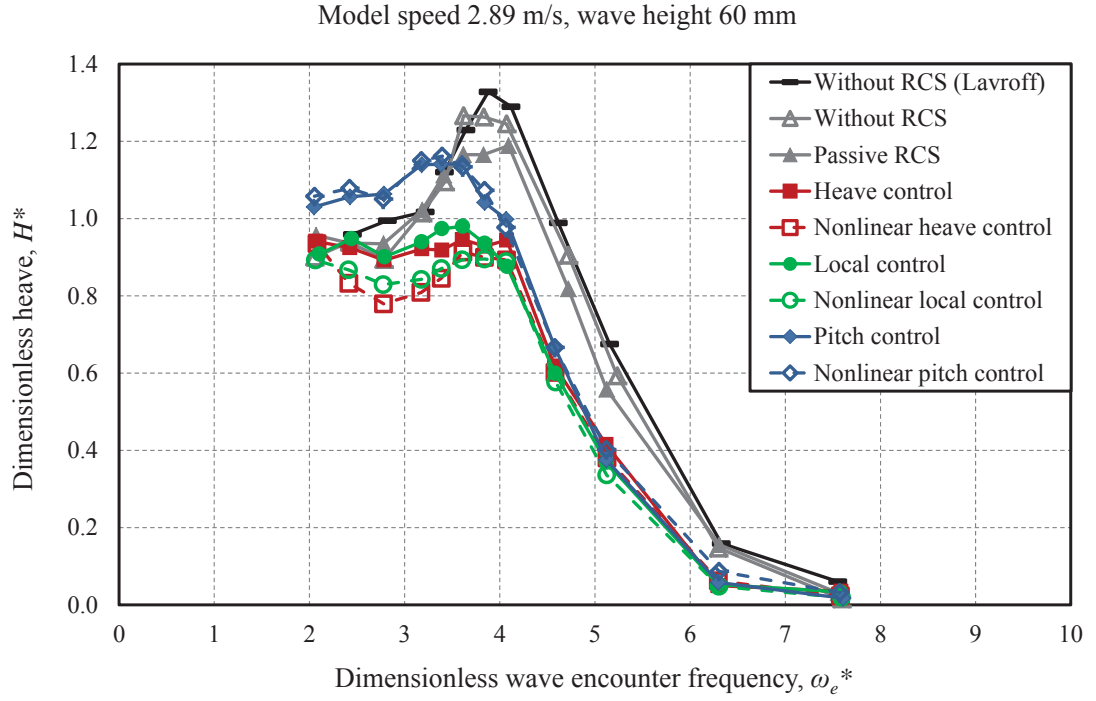


Figure 5.7: Heave RAO at model speed of 2.89 m/s ($Fr = 0.608$) and wave height of 60 mm.

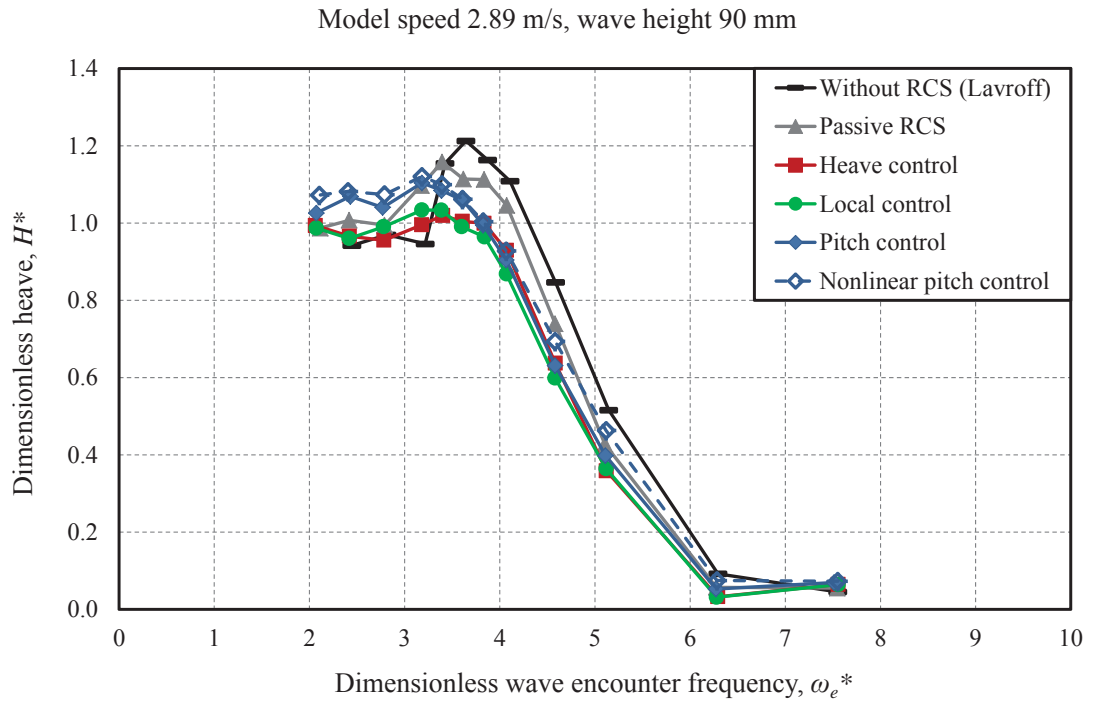


Figure 5.8: Heave RAO at model speed of 2.89 m/s ($Fr = 0.608$) and wave height of 90 mm.

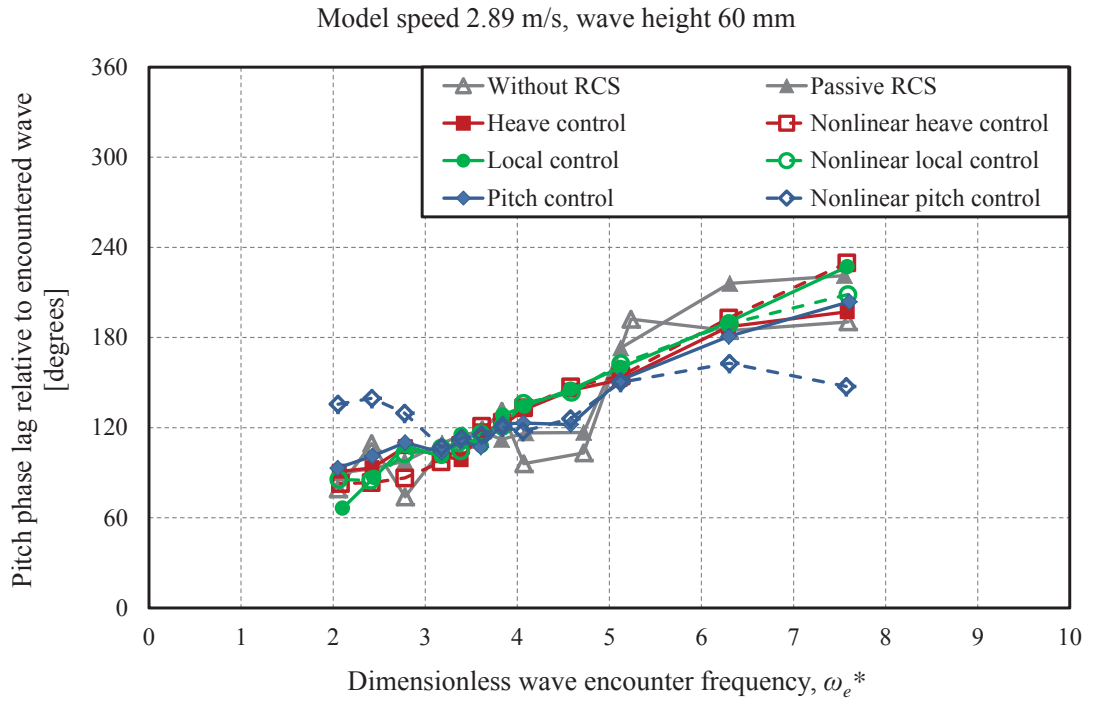


Figure 5.9: Pitch RPO (pitch phase lag relative to encountered wave at the LCG) at model speed of 2.89 m/s ($Fr = 0.608$) and wave height of 60 mm.

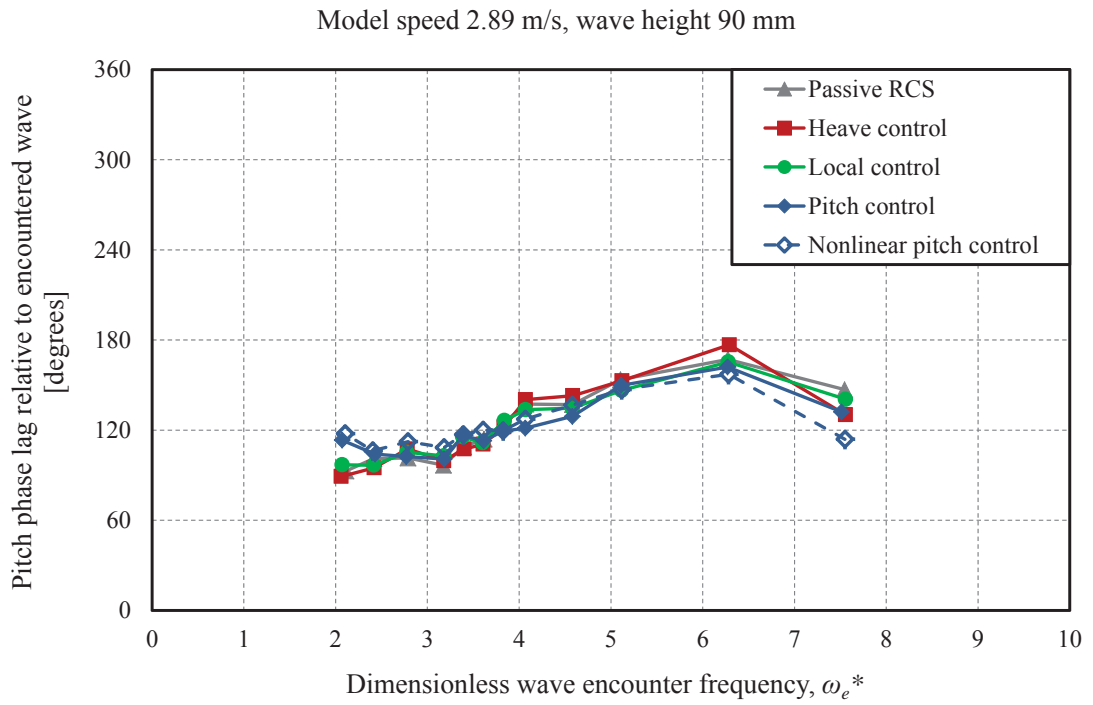


Figure 5.10: Pitch RPO (pitch phase lag relative to encountered wave at the LCG) at model speed of 2.89 m/s ($Fr = 0.608$) and wave height of 90 mm.

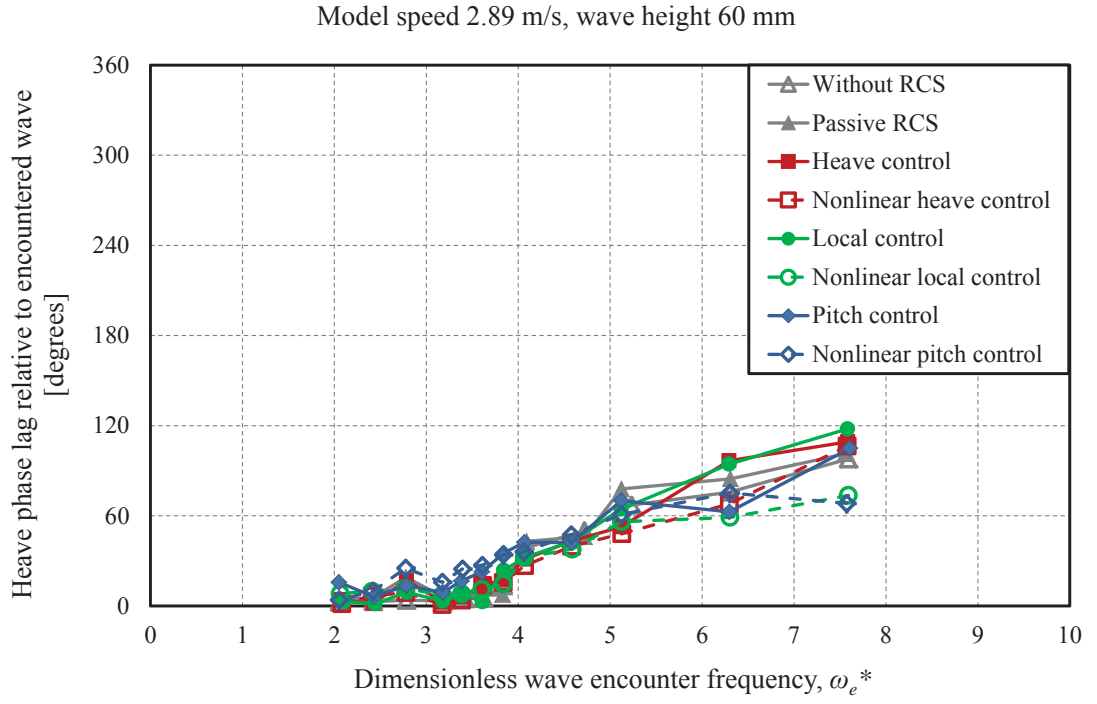


Figure 5.11: Heave RPO (heave phase lag relative to encountered wave at the LCG) at model speed of 2.89 m/s ($Fr = 0.608$) and wave height of 60 mm.

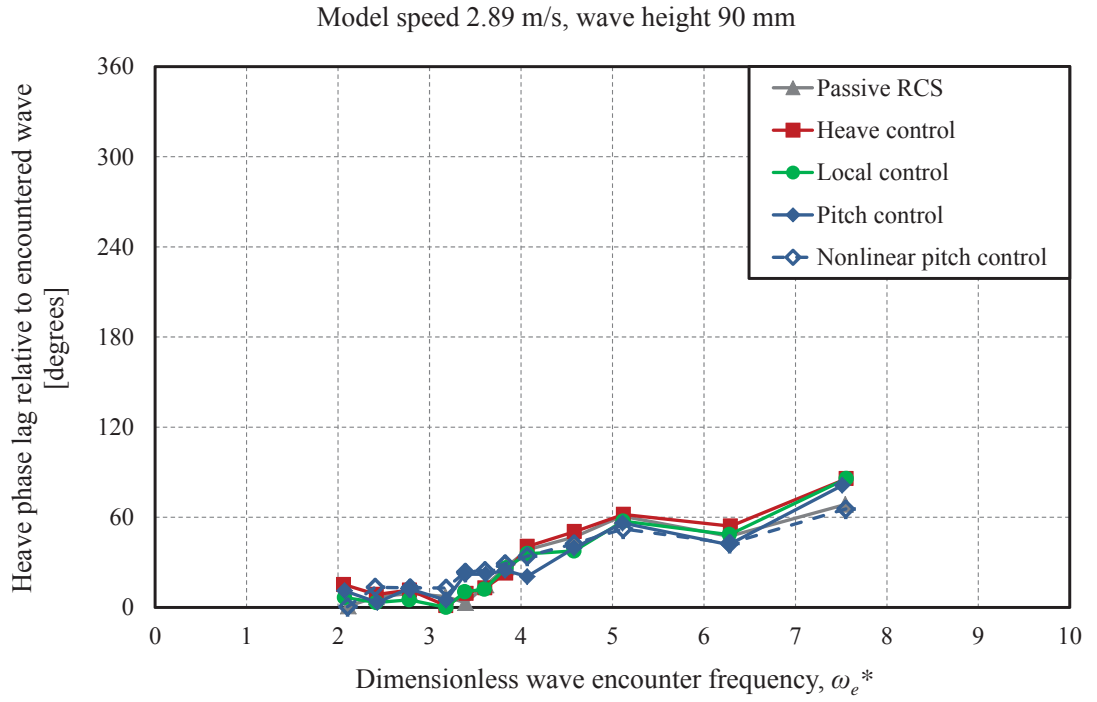


Figure 5.12: Heave RPO (heave phase lag relative to encountered wave at the LCG) at model speed of 2.89 m/s ($Fr = 0.608$) and wave height of 90 mm.

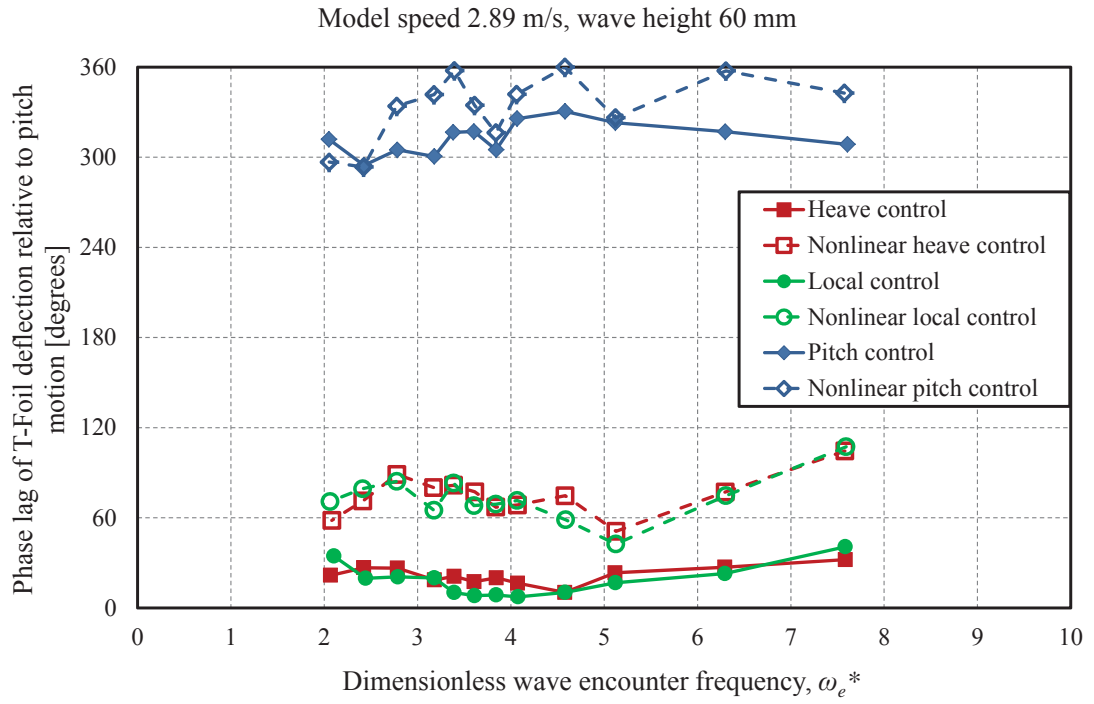


Figure 5.13: Phase lag of T-Foil relative to pitch motion at model speed of 2.89 m/s ($Fr = 0.608$) and wave height of 60 mm.

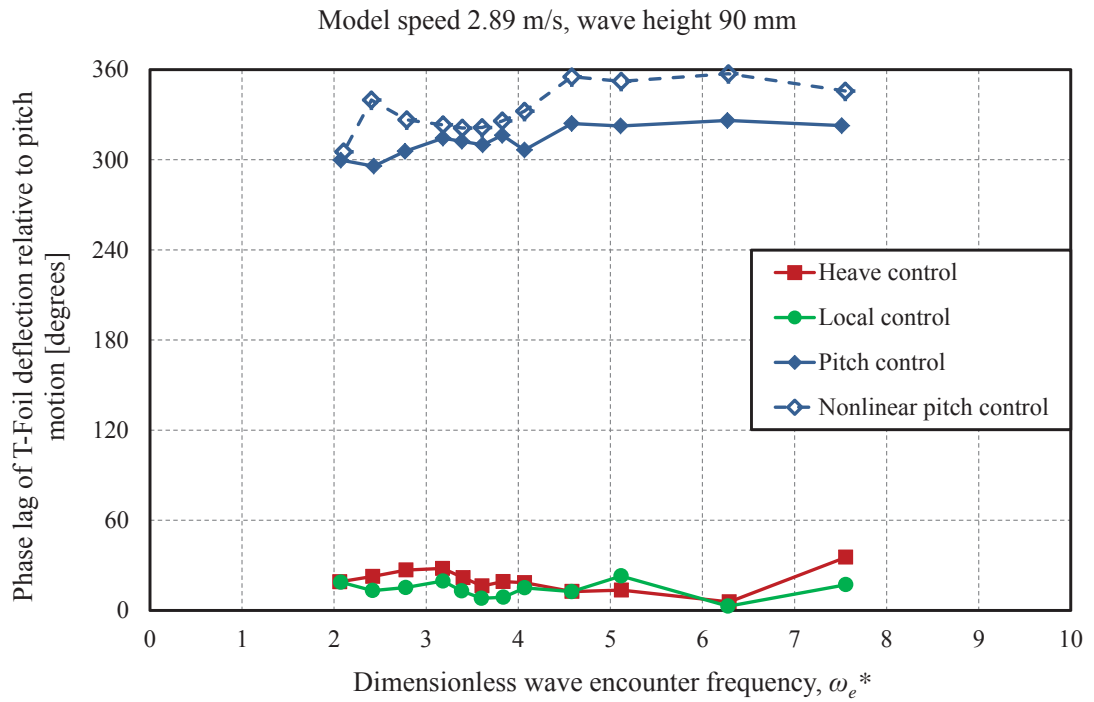


Figure 5.14: Phase lag of T-Foil relative to pitch motion at model speed of 2.89 m/s ($Fr = 0.608$) and wave height of 90 mm.

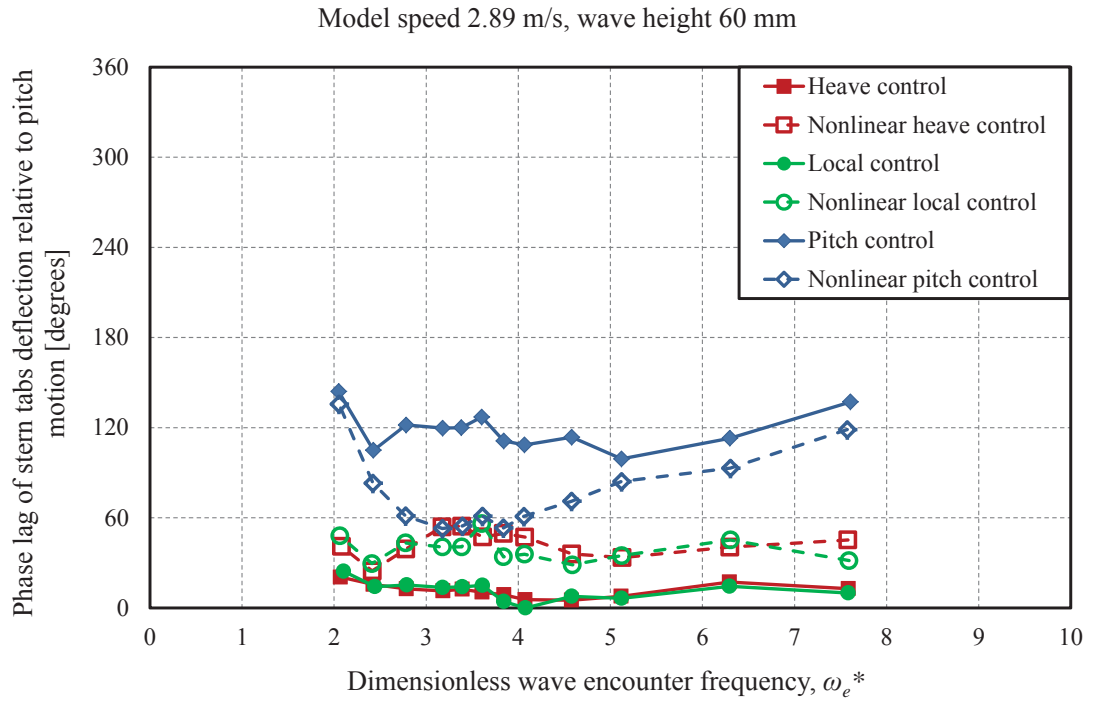


Figure 5.15: Phase lag of stern tabs relative to pitch motion at model speed of 2.89 m/s ($Fr = 0.608$) and wave height of 60 mm.

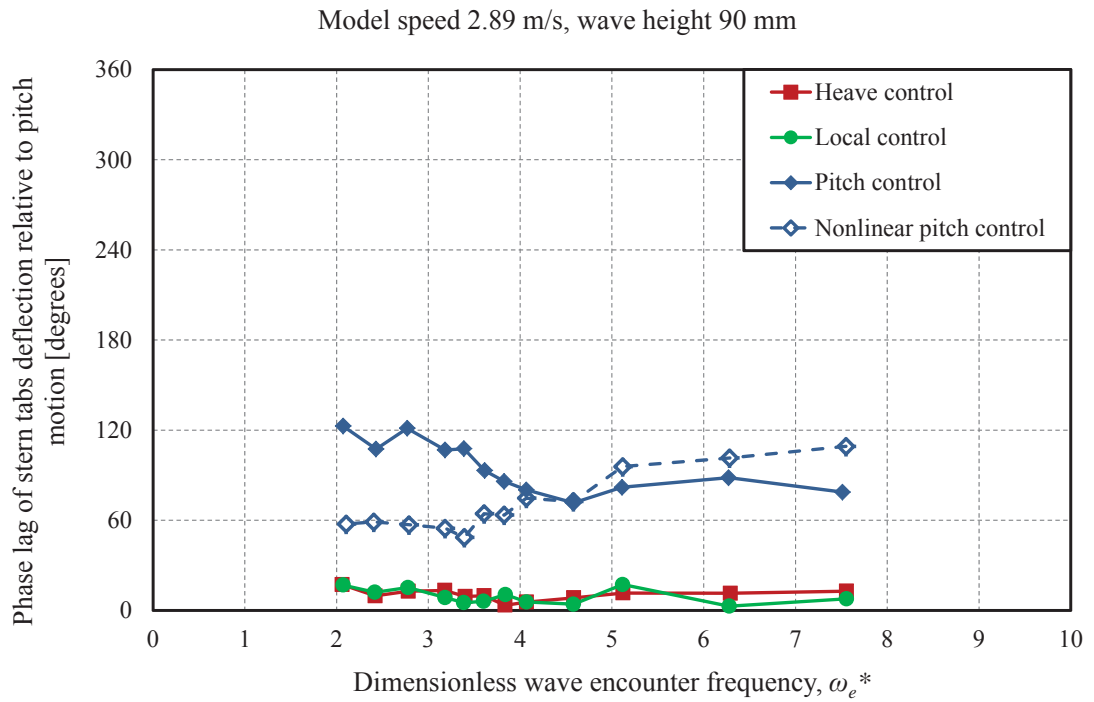


Figure 5.16: Phase lag of stern tabs relative to pitch motion at model speed of 2.89 m/s ($Fr = 0.608$) and wave height of 90 mm.

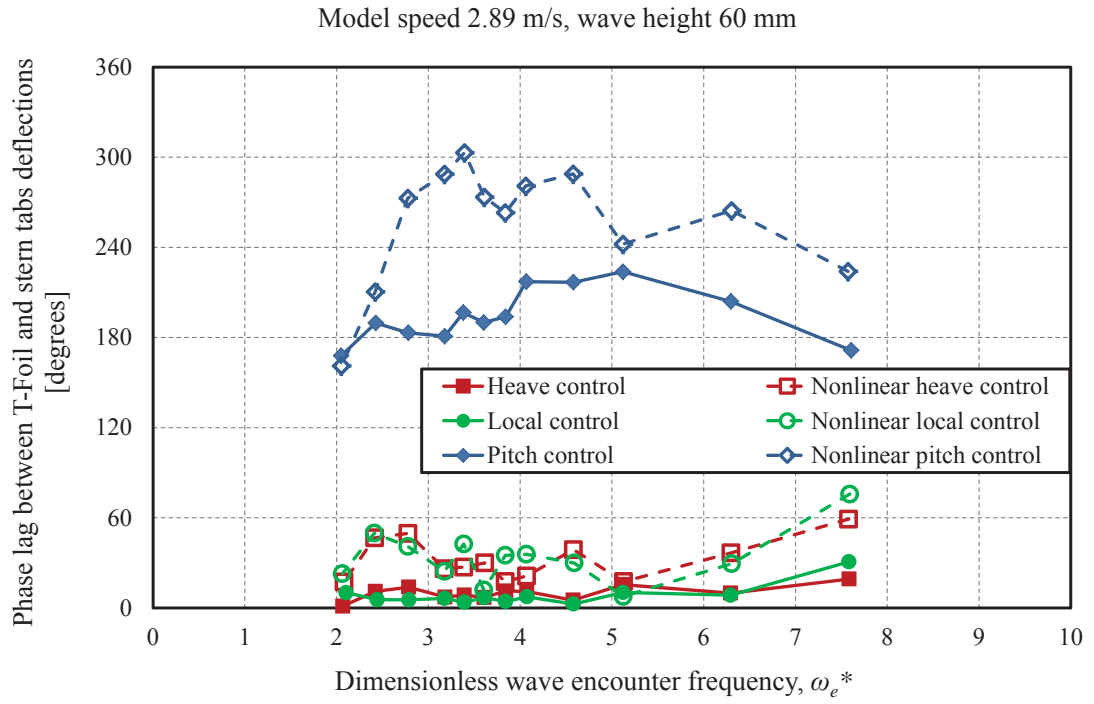


Figure 5.17: Phase lag between T-Foil and stern tabs deflection at model speed of 2.89 m/s ($Fr = 0.608$) and wave height of 60 mm.

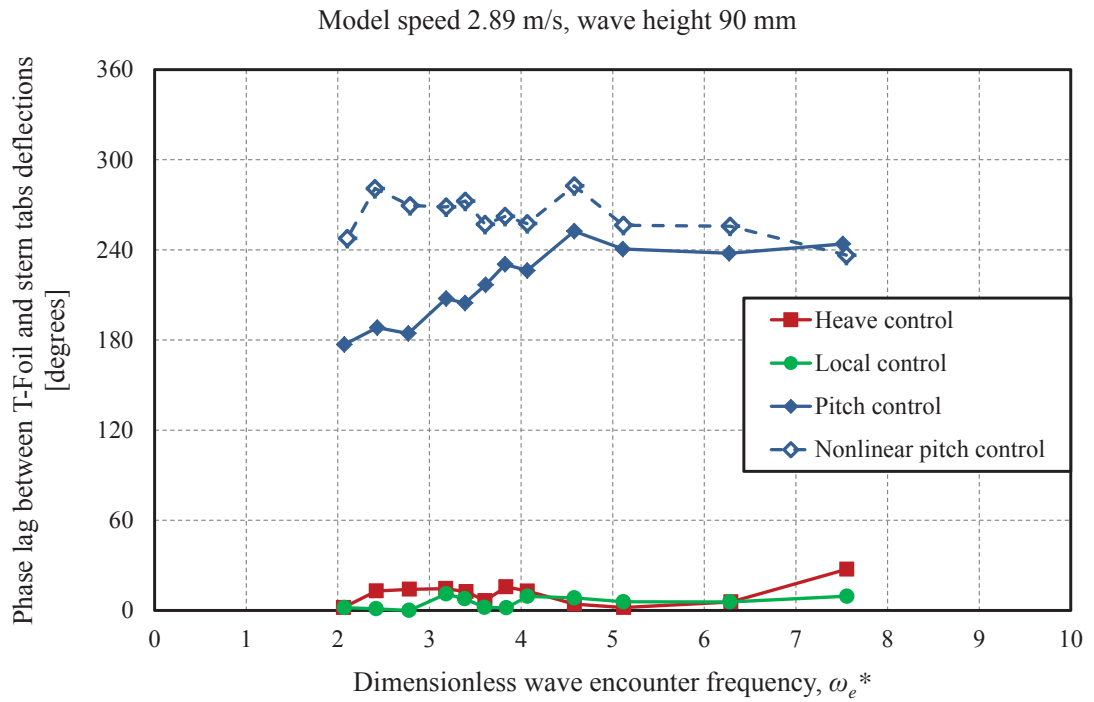


Figure 5.18: Phase lag between T-Foil and stern tabs deflection at model speed of 2.89 m/s ($Fr = 0.608$) and wave height of 90 mm.

5.4.4 Acceleration response

Although the ride control system has demonstrated significant effect in reducing the motion response of the catamaran model, the effect of the ride control system on the passenger comfort depends primarily on the vertical accelerations measured on the catamaran model. Furthermore, depending on the magnitude and phase of heave and pitch motions, the accelerations can be quite different at different locations on the hull. The vertical motion acceleration of the catamaran model was therefore investigated at three different longitudinal locations consisting of the LCG, the longitudinal location of the T-Foil and the longitudinal location of the stern tabs. The longitudinal location of the LCG and the T-Foil are 37% and 80% of LOA from the stern respectively, and the location of the T-Foil and the stern tabs represent approximate forward and aft most locations that passengers might be expected to occupy. Given that motions are close to sinusoidal, dimensionless heave accelerations were simply calculated by

$$\ddot{H}_x^* = H_x^* \times \omega_e^{*2} = \ddot{H}_x \frac{l}{g\zeta}, \quad (5.22)$$

where the subscript $_x$ refers to the location at which the motion was analysed.

The heave motion at the longitudinal location of the T-Foil and stern tabs were calculated respectively by

$$H_{TF}(t) = H(t) - x_{TF} \times P(t) \quad (5.23)$$

$$H_{ST}(t) = H(t) + x_{ST} \times P(t). \quad (5.24)$$

Figures 5.19 and 5.20 show the dimensionless heave acceleration at the LCG at wave heights of 60 mm and 90 mm respectively. As can be seen from Figures 5.19 and 5.20, the ride control system even in the passive mode reduced the heave acceleration at the LCG. There is a significantly larger reduction of accelerations in smaller waves as would be expected as the control system gains were set higher in the smaller waves so that at both wave heights the controls were acting with close to maximum range of movement. Figures 5.21 and 5.22 show the dimensionless vertical acceleration at the longitudinal location of the T-Foil at wave heights of 60 mm and 90 mm respectively. The accelerations at this forward location are much greater than at the LCG by a factor of about 2.5 showing that these forward on board locations are far less suitable for passenger accommodation. However, we see that the RCS in the pitch control mode has achieved approximately 40% reduction of these forward accelerations in the smaller waves. The dimensionless vertical acceleration at the location of the stern tabs at wave heights of 60 mm and 90 mm are shown in Figures 5.23 and 5.24 respectively. Here again the pitch control mode achieves a 40% reduction of vertical accelerations in the smaller waves. Overall the accelerations were greatest at the forward T-Foil location and smallest at the LCG, the forward

accelerations being approximately 2.5 times those at the LCG and the stern acceleration being about 1.9 times the LCG acceleration. The pitch control algorithm, especially in the nonlinear mode, demonstrated the strongest influence in reducing the vertical accelerations, which is the most important factor to improve passenger comfort. The results presented here can of course be used to determine the effect of the RCS on passenger motion sickness incidence (MSI). That determination depends very much on the spectrum of the encountered waves and so it is not possible to give a single answer as to the benefit of the RCS on MSI values. However in the range where MSI increases most rapidly with acceleration it is found that a 40% reduction of acceleration would approximately reduce the MSI by up to 50% [132].

5.4.5 Control surface response amplitude

During these experimental tests on the model with active RCS it was necessary to set pre-determined and fixed control system gains for each mode of control action. These gains were determined by the estimated maximum motion velocities relevant to each control mode as have been outlined in Section 5.4. Therefore it is of interest to determine the actual variation of control movement with encounter frequency, as in conditions of smaller motion the controls during these tests would not be acting over their maximum range of movement. This is an inevitable consequence of setting fixed control system gains.

Figures 5.25 and 5.26 show the range of T-Foil deflection for different ride control modes with wave heights of 60 mm and 90 mm respectively. The stern tab deflection range with wave heights of 60 mm and 90 mm are presented in Figures 5.27 and 5.28 respectively. As expected the maximum T-Foil deflection of $\pm 10^\circ$ (range of 20°) and the maximum stern tabs deflection range of 18° (from 0 to $+18^\circ$) were observed at all wave frequencies for all the nonlinear modes.

Figures 5.25 and 5.26 show a T-Foil range of 10° at $\omega_e^* = 2$ for the pitch control mode, which rises to the maximum range of 20° as ω_e^* increases to 3.5 near the peak model motions. The T-Foil range remains steady at ω_e^* in the range 3.5 – 5 and then decreases to 8° at $\omega_e^* = 7.5$. A similar trend can be seen for the heave and local control modes, however the T-Foil range reduces more strongly at ω_e^* above 4 for these two control modes. It can be seen from Figure 5.27 that the local control algorithm causes the stern tabs to reach their maximum range of deflection at lower wave frequencies. The sterns tab deflections for the pitch control mode has the maximum range of 18° at $\omega_e^* = 4.5$ while the heave control mode does not excite the stern tabs sufficiently to deflect to their maximum range. Figure 5.28 shows a similar trend for all the ride control algorithms in 90 mm waves, although the maximum range of stern tab deflections is not observed for the heave and local control.

These tests with linear control modes show that the control surface deflections rise from small values at low wave frequencies, where the vertical motion velocities are small, to the maximum range of movement at the wave frequencies of peak motions and then reduce to small values at high encounter frequency. However it should be borne in mind that where the control

gains are balanced so as to give only heave or only pitch control response, the ratios of control gains must take on specific values as explained in Section 5.4. Therefore it is not possible that both T-Foil and stern tabs in the heave and pitch control modes can be set to operate over their maximum range of movement. For this reason we see that the stern tabs are frequently not operating over their maximum range at the frequency of maximum motion. However, it is evident that the estimations of appropriate control gain for each control mode have generally resulted in operating one of the control surfaces, usually the T-Foil, over its maximum range at the frequency of maximum motion.

It can be noted from these results that there would be potential for further improving the performance of the RCS if the control gains were set by an automatic adaptive system so that whatever the wave conditions the RCS would be operating with maximum control movements.

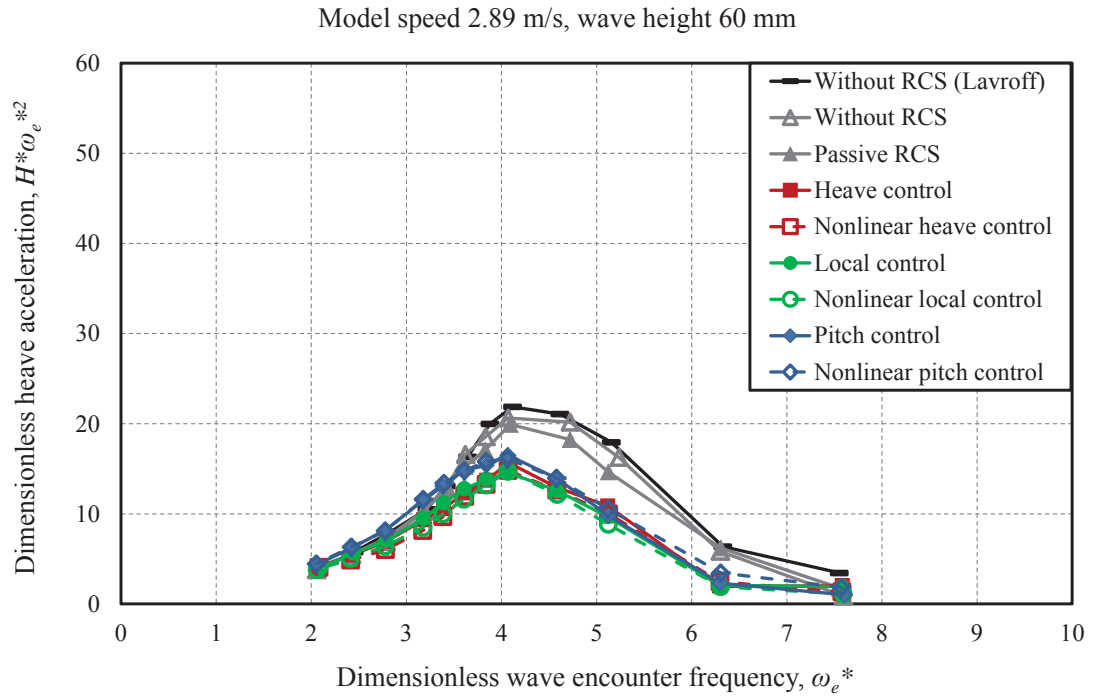


Figure 5.19: Dimensionless heave acceleration at LCG (37% LOA from the stern) at model speed of 2.89 m/s ($Fr = 0.608$) and wave height of 60 mm.

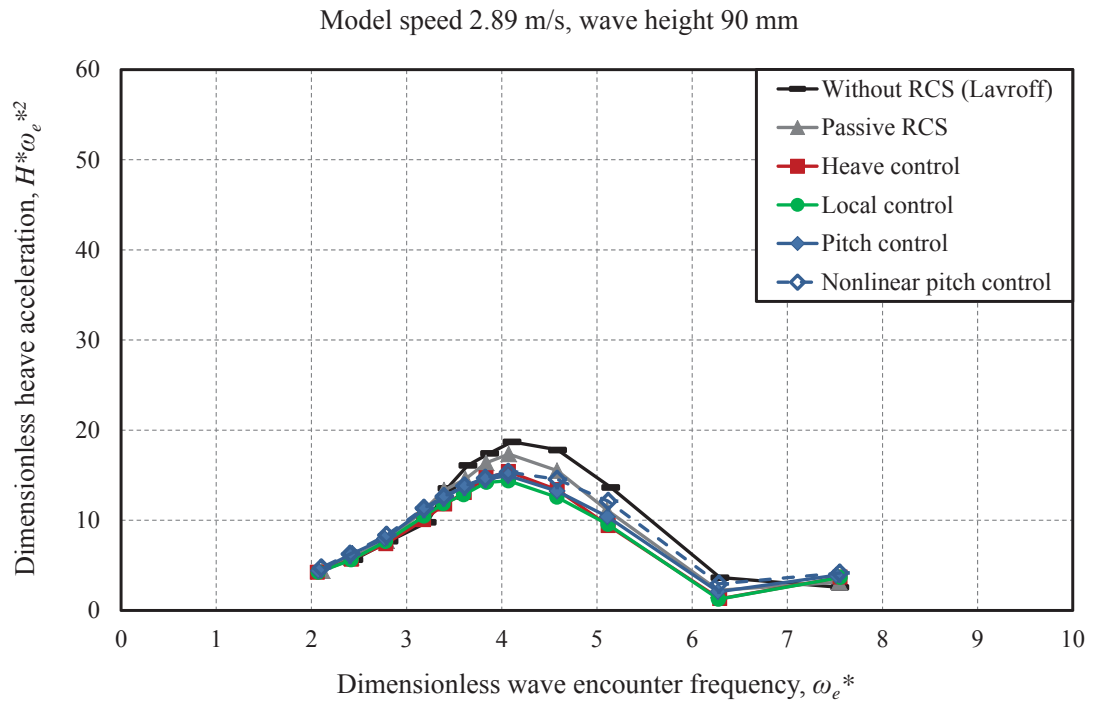


Figure 5.20: Dimensionless heave acceleration at LCG (37% LOA from the stern) at model speed of 2.89 m/s ($Fr = 0.608$) and wave height of 90 mm.

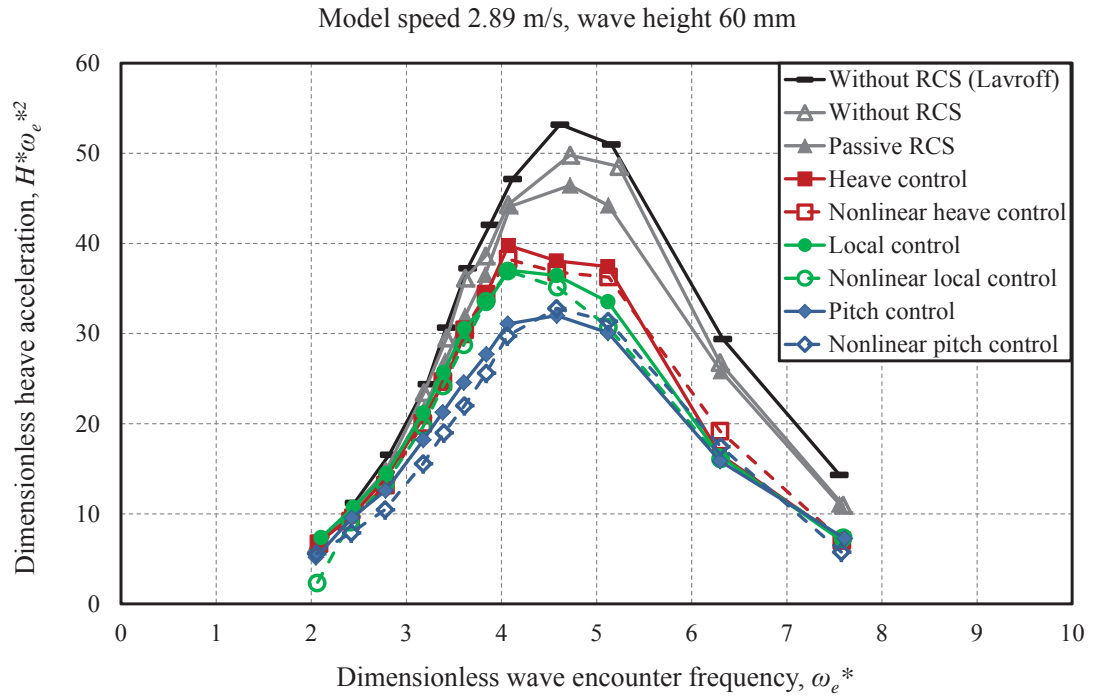


Figure 5.21: Dimensionless vertical acceleration at the longitudinal location of the T-Foil (80% LOA from the stern) at model speed of 2.89 m/s ($Fr = 0.608$) and wave height of 60 mm.

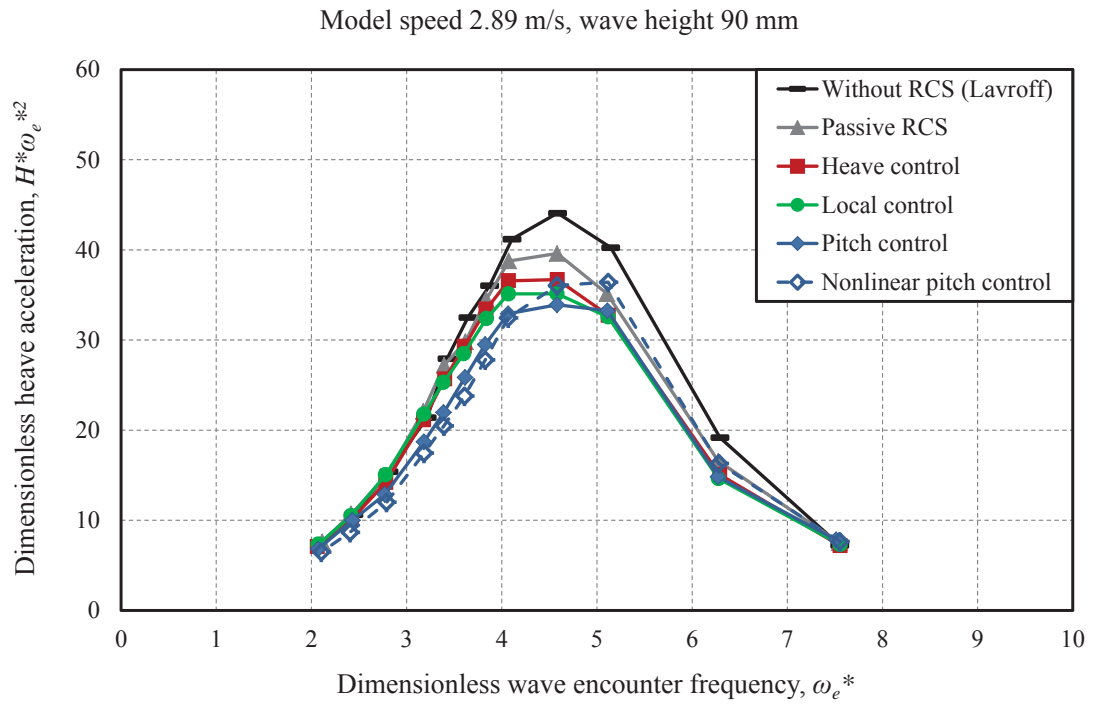


Figure 5.22: Dimensionless vertical acceleration at the longitudinal location of the T-Foil (80% LOA from the stern) at model speed of 2.89 m/s ($Fr = 0.608$) and wave height of 90 mm.

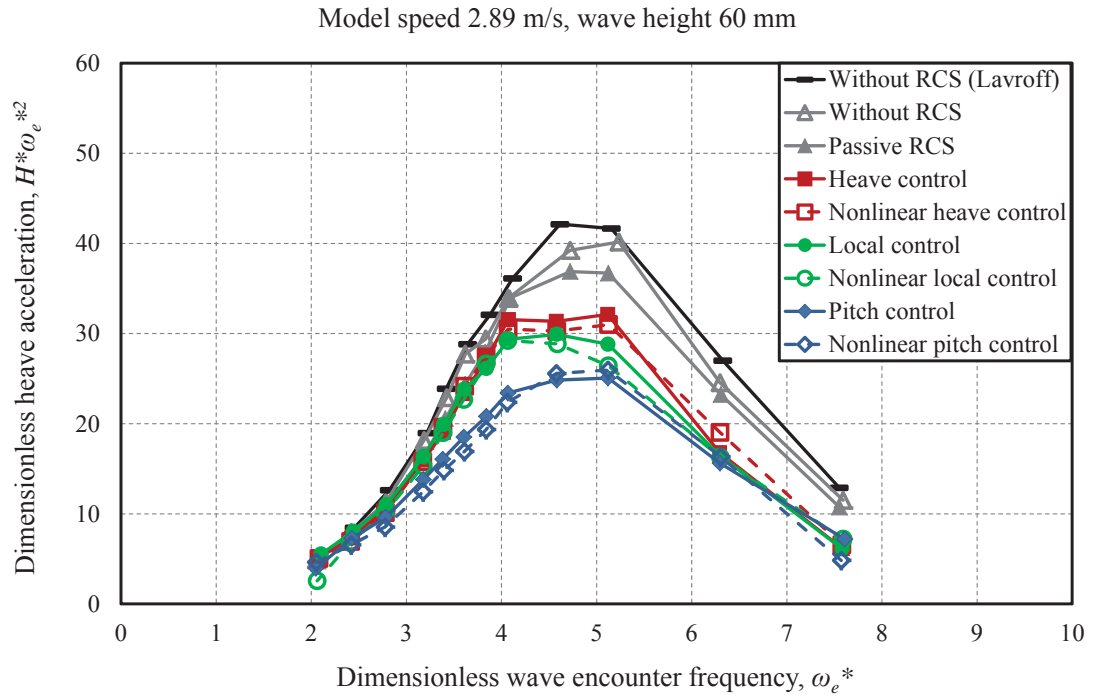


Figure 5.23: Dimensionless vertical acceleration at the longitudinal location of the stern tabs at model speed of 2.89 m/s ($Fr = 0.608$) and wave height of 60 mm.

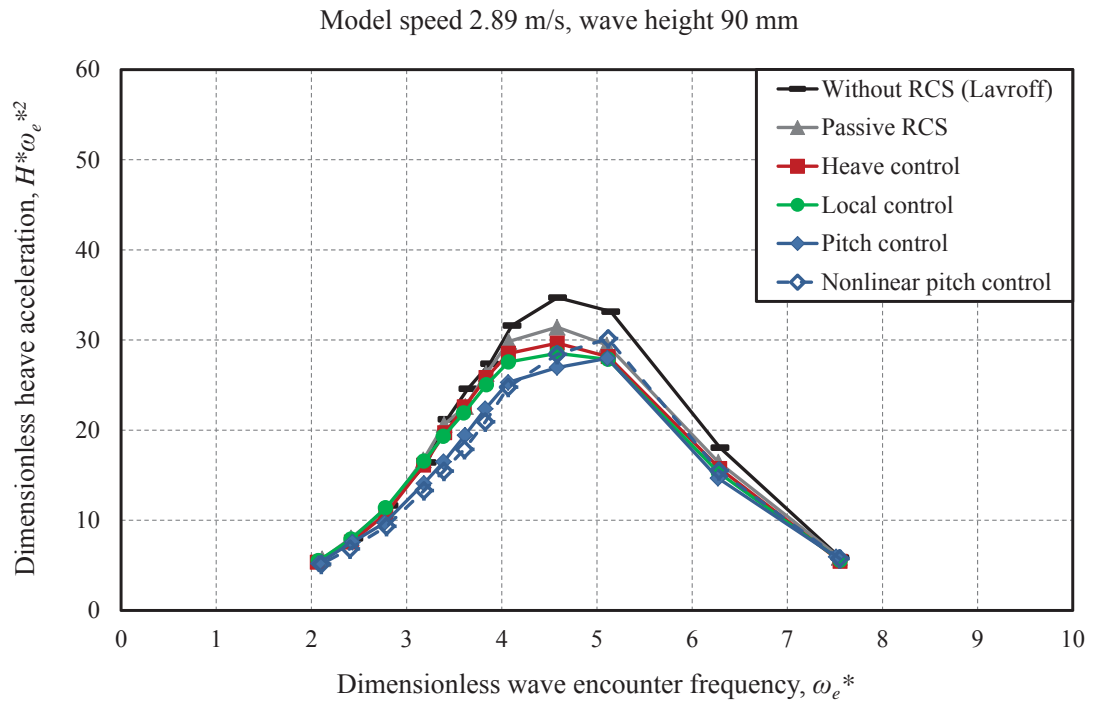


Figure 5.24: Dimensionless vertical acceleration at the longitudinal location of the stern tabs at model speed of 2.89 m/s ($Fr = 0.608$) and wave height of 90 mm.

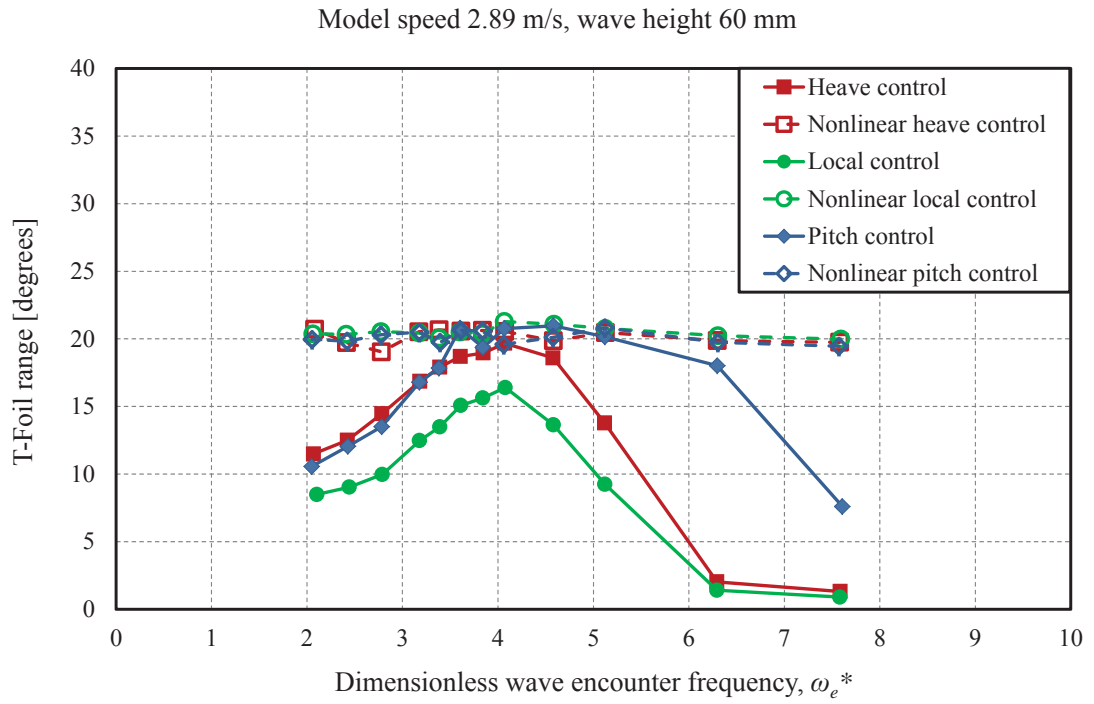


Figure 5.25: T-Foil deflection range at model speed of 2.89 m/s ($Fr = 0.608$) and wave height of 60 mm.

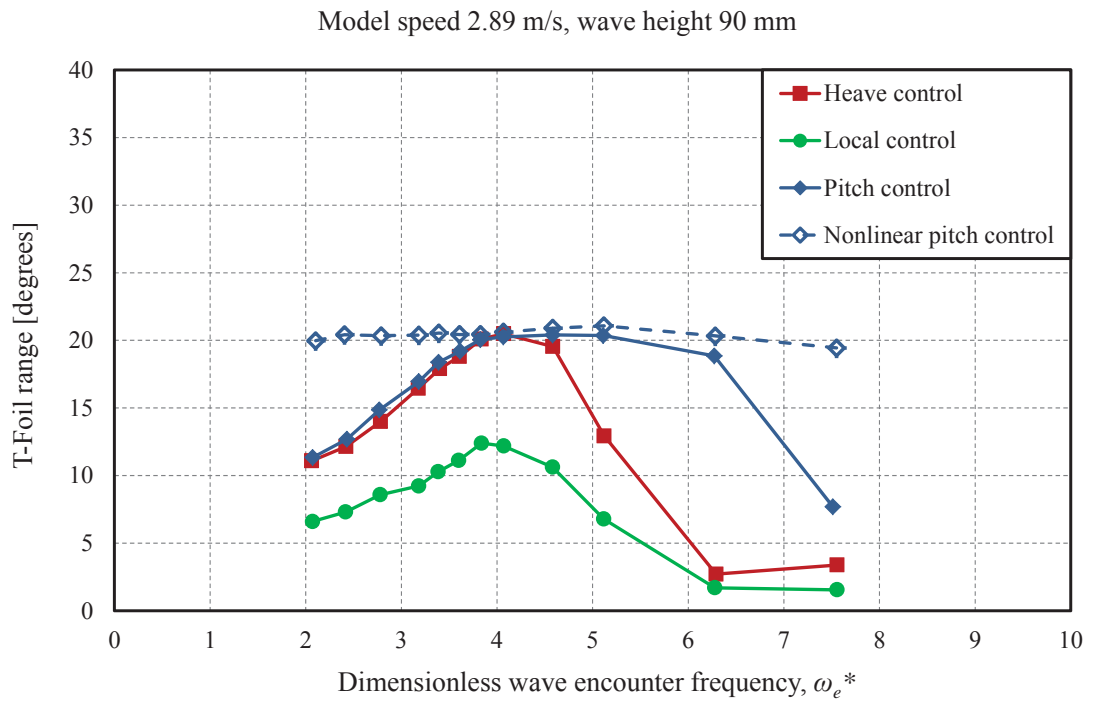


Figure 5.26: T-Foil deflection range at model speed of 2.89 m/s ($Fr = 0.608$) and wave height of 90 mm.

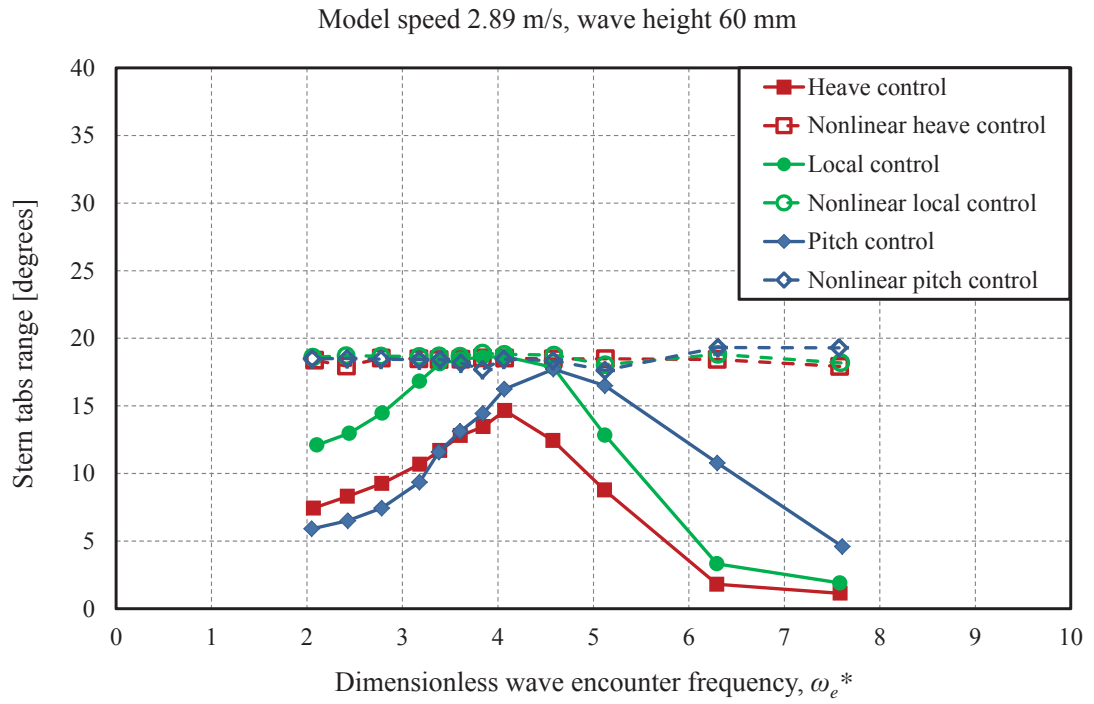


Figure 5.27: Stern tabs deflection range at model speed of 2.89 m/s ($Fr = 0.608$) and wave height of 60 mm.

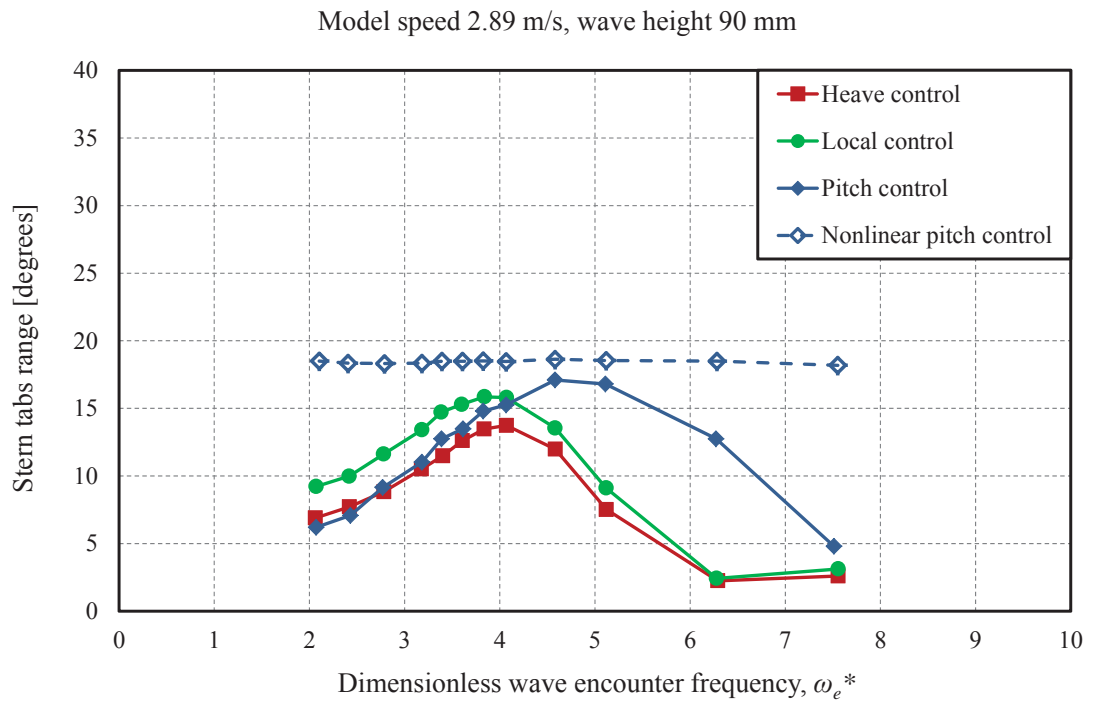


Figure 5.28: Stern tabs deflection range at model speed of 2.89 m/s ($Fr = 0.608$) and wave height of 90 mm.

5.5 Conclusions

In order to investigate the influence of different ride control methods on the motions of the 112 m INCAT high-speed wave-piercing catamaran the 2.5 m model was tested in the Australian Maritime College (AMC) towing tank with six different active ride control methods, a passive system and no system in head seas at different wave heights and frequencies. The Response Amplitude Operators (RAOs), Response Phase Operators (RPOs) and acceleration response of the model were determined using the heave and pitch data. The range of control surface deflections as well as the phase lag between the control surface deflections and the model motions were evaluated in order to investigate the performance of the model ride control system and the effectiveness of the different control methods. The active ride control systems were operated with heave control, local control and pitch control, each with linear and nonlinear operation.

It was found that the deployment of the T-Foil to a fixed position and acting as a passive control surface provides a modest reduction of the peak heave and pitch motions. The heave and pitch motions were much more strongly reduced with active ride controls. This was most evident with the pitch control modes where the nonlinear control action substantially reduced the pitch RAO by about 50% in 60 mm waves at model scale. The pitch motion was larger when the ride control system was operated in the nonlinear heave control mode, however the nonlinearity did not have significant effect on the pitch motions when applied in the local control mode.

The local vertical acceleration of the model at different longitudinal locations was significantly reduced by the ride control system. As was expected, this reduction was most obvious with pitch control, especially in the nonlinear mode, where it reduced the vertical acceleration near the bow by around 40% in 60 mm waves at model scale. The acceleration response of the catamaran model to the ride control system showed the potential for substantial improvement of passenger comfort and potentially reducing the structural loads, particularly with nonlinear pitch control where motion sickness incidence could be reduced by as much as 50% depending on encountered wave conditions.

The model RCS introduced significant phase lags between detected motions that generate the demand control deflections and the actual control deflections. The consequence of this was that the control action comprised a mixture of damping and stiffness feedback. However, in the case of pitch feedback control the presence of a significant stiffness component in the actual control actions was found to give substantial reductions in RAO in the lower range of encounter frequency.

The nonlinear control modes produced the maximum T-Foil and stern tab deflection ranges at all wave encounter frequencies. The linear control modes showed maximum range of movement only at the frequency of maximum motion due to operation with fixed control gains. These results thus show that there is significant potential for the application of adaptive gain control depending on the prevailing sea conditions. Also that operation of the controls in nonlinear

modes gives generally the best overall improvement of RAO and that the pitch control mode is most effective for improvement of passenger comfort.

In conclusion, the motions response results obtained here demonstrate the potential for significant benefit being obtained by using improved ride control algorithms. There is thus good potential for improving passenger comfort and reducing the incidence of motion sickness, an important consideration in particular for vessels operating in more exposed sea conditions.

Chapter 6

Closed-Loop Influence of the Ride Control System on the Model Load Responses

6.1 Introduction

This chapter investigates the influence of the ride control system on the model structural loads by analysing the data obtained from the strain gauges installed on the model centre bow and demihull links. Raw strain gauge data obtained from the towing tank tests were analysed and the forces on the centre bow and the slam induced bending moments in the demihulls were recorded as time records. These records were used to determine extreme loadings. The centre bow loads are presented in three parts: firstly, a centre bow entry force, which develops relatively slowly as the bow enters the water prior to a slam occurring, at which point water reaches the top of the arched cross section between demihulls; secondly, a rapidly rising slam force occurring when the cross section fills and water impacts the arch top; and thirdly, a total force comprising the sum of these two components. The position of the centre bow slam force from the transom is presented as a function of wave height and wave encounter frequency for different ride control algorithms. The slam induced bending moments are shown for the forward and aft segment of demihull. Extremes of all the above mentioned results are presented at two points in the whole slam event representing extreme sagging and hogging loads.

In addition to the structural loads results, the slamming kinematics results for the catamaran model are investigated in this chapter. The centre bow motion during the slamming process at the location of the T-Foil is investigated by using the heave and pitch motions data obtained during the towing tank tests performed in regular seas. The centre bow motion is calculated relative to the undisturbed wave profile.

A strain energy analysis is also performed in order to investigate the energy of the slam

force transmitted to the centre bow and demihull elastic links of the catamaran model.

6.2 Time record data analysis

The strain gauge data and the motion data were acquired simultaneously in order to investigate the key kinematic parameters controlling the slamming process. A sample frequency of 50 Hz was selected for the LVDT motion data acquisition system whilst a minimum sample frequency of the 1612.9 Hz was selected for the strain gauge data acquisition system. Figures 6.1 and 6.2 show a sample time record at model speed of 2.89 m/s ($Fr = 0.608$), wave height of 90 mm and dimensionless wave encounter frequency, $\omega_e^* = 4.581$ for the passive RCS and pitch control mode respectively. The kinematic parameters including bow height, bow immersion and relative bow velocity are measured at the longitudinal location of the T-Foil and relative to the undisturbed wave profile. These are not measured directly through model tests, but are derived from the recorded model motions and the method of calculation is explained in the following sections.

It should be noted that the wave profile at the LCG, bow height, centre bow total force and the heave motion are all positive upwards, the pitch motion and the relative bow velocity are positive bow down and the control surfaces deflection are positive counter-clockwise viewed from the starboard side, producing upward lift.

In order to evaluate the extremes of the signals, a range of the time record was analysed, starting when regular periodic motions had been reached and including at least five cycles. An average of the extremes of all these cycles is then presented. This analysis was carried out by finding the peak and trough of each cycle using the Matlab "Findpeaks" function.

As can be seen from Figures 6.1 and 6.2, the active ride control system not only reduced the motions of the catamaran model, but it also mitigated the centre bow total force, bow height, bow immersion and the relative bow velocity. Further details of the results are presented in the following sections.

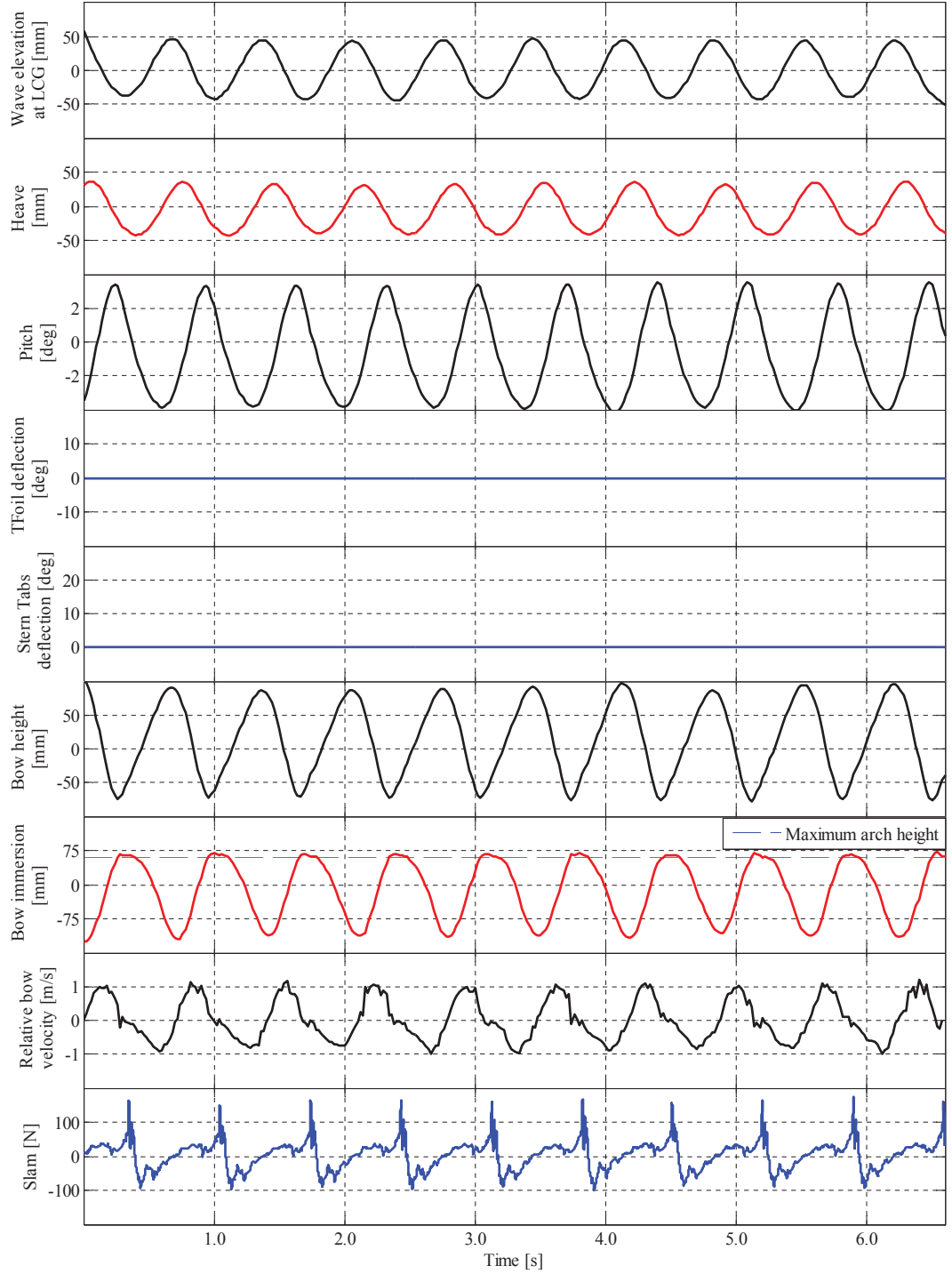


Figure 6.1: Time records showing kinematic data at model speed of 2.89 m/s ($Fr = 0.608$), wave height of 90 mm, ω_e^* of 4.581 and passive RCS mode.

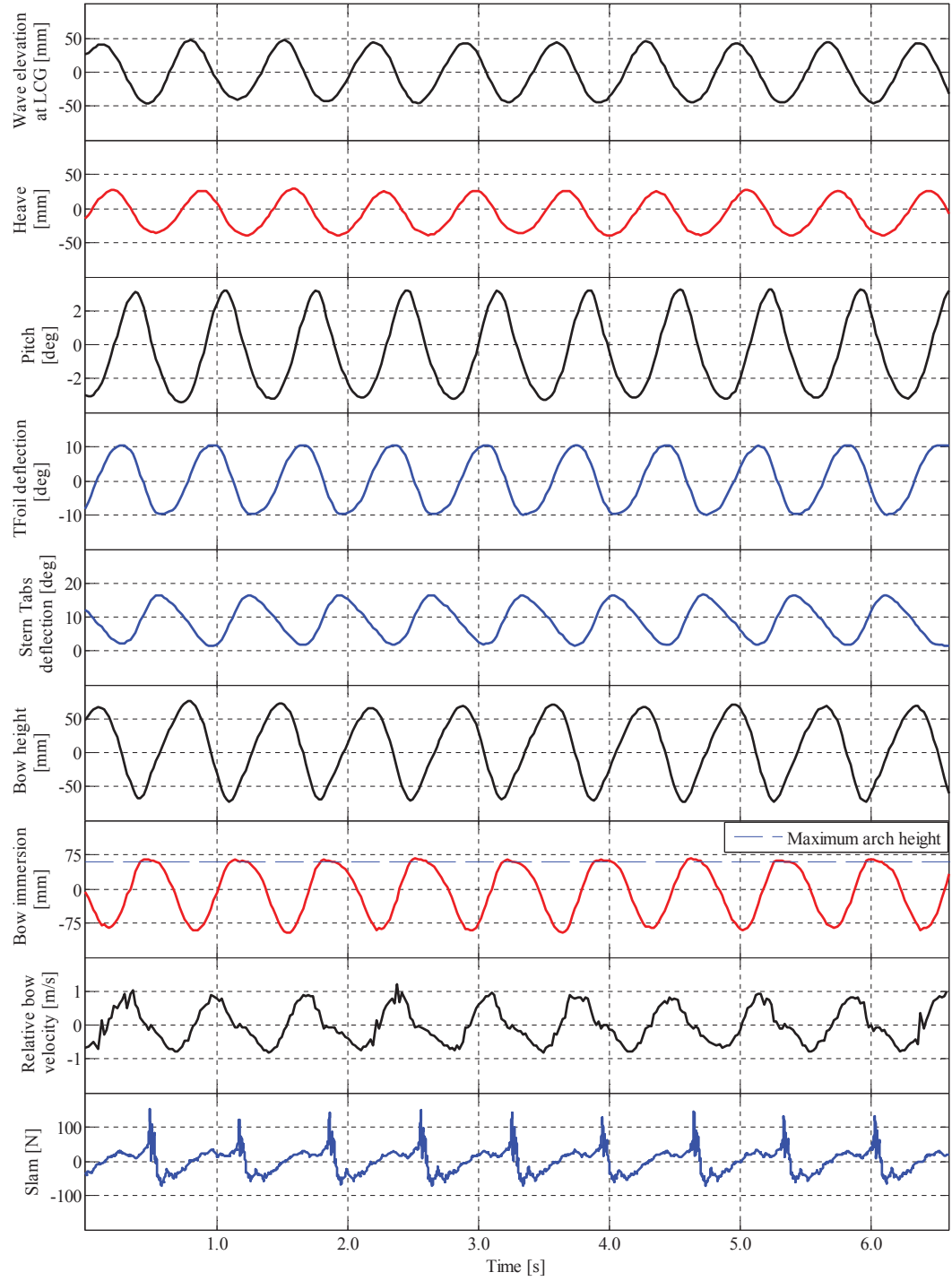


Figure 6.2: Time records showing kinematic data at model speed of 2.89 m/s ($Fr = 0.608$), wave height of 90 mm, ω_e^* of 4.581 and pitch control mode.

6.3 Dynamic structural loads analysis

The strain gauge data obtained during all towing tank tests undertaken on the catamaran model were analysed to identify the maximum centre bow entry force, the maximum total force and the slam force acting on the centre bow, and the maximum slam induced bending moments acting in the demihull. The onset of slamming and the relevant procedure has been previously discussed by Lavroff [3] where a minimum peak slam load threshold was developed to identify the onset of the wet-deck slam event. However, Lavroff [3] presented only the total centre bow force whereas here we have broken this down into the bow entry and slam components. The strains measured on the elastic links in the transverse bow mounting beams were converted to bending moments and thus used to calculate the force acting on the centre bow and its longitudinal location. The raw strain data acquired from the strain gauges installed on the demihull elastic links were used to calculate the bending moments measured on the catamaran model as discussed in Section 2.2.1.

As discussed in Chapter 2, the static loading tests on the model showed that the method used as illustrated in Figures 2.4 and 2.5 correctly identified the fore and aft location of the load on the bow using Equations 2.5 and 2.6 and that the pin mountings on the demihulls did not therefore transmit a significant torsional moment to the transverse bow support beams.

As before, in order to evaluate the extremes of the signals, a range of the time record was analysed, starting when regular periodic motions had been reached and including at least five cycles. An average of the extremes of all these cycles is then presented. This analysis was carried out by finding the peak and trough of each cycle using the Matlab "Findpeaks" function.

The accuracy of the results was established by uncertainty analysis performed based on the standard deviation of the results. For each run the time record included from 5 to 19 useable cycles after transients had dissipated and before either the run terminated or reflections or other forms of contamination became significant. The variation between the cycles in each run was analysed in order to quantify the accuracy of the results. The standard deviation analysis of the results shows an average of $\pm 3.0\%$ variation for the centre bow force and $\pm 3.5\%$ variation for the slam induced bending moment. Figures 6.3 and 6.4 illustrate these uncertainty of results for some typical cases at a wave height of 60 mm. They show the error bars on the centre bow total sagging force and demihull slam induced sagging bending moment for three of the ride control conditions: without RCS, passive RCS and pitch control mode. These curves illustrate the substantial changes brought about by the most successful ride control algorithm, but as can be seen from Figures 6.3 and 6.4, the uncertainty in the results within each case is insignificant compared to the overall effect of the ride control system. Thus the experimental uncertainty has no impact on the key conclusions of this study, and in view of the quantity of data subsequent results will be presented without error bars.

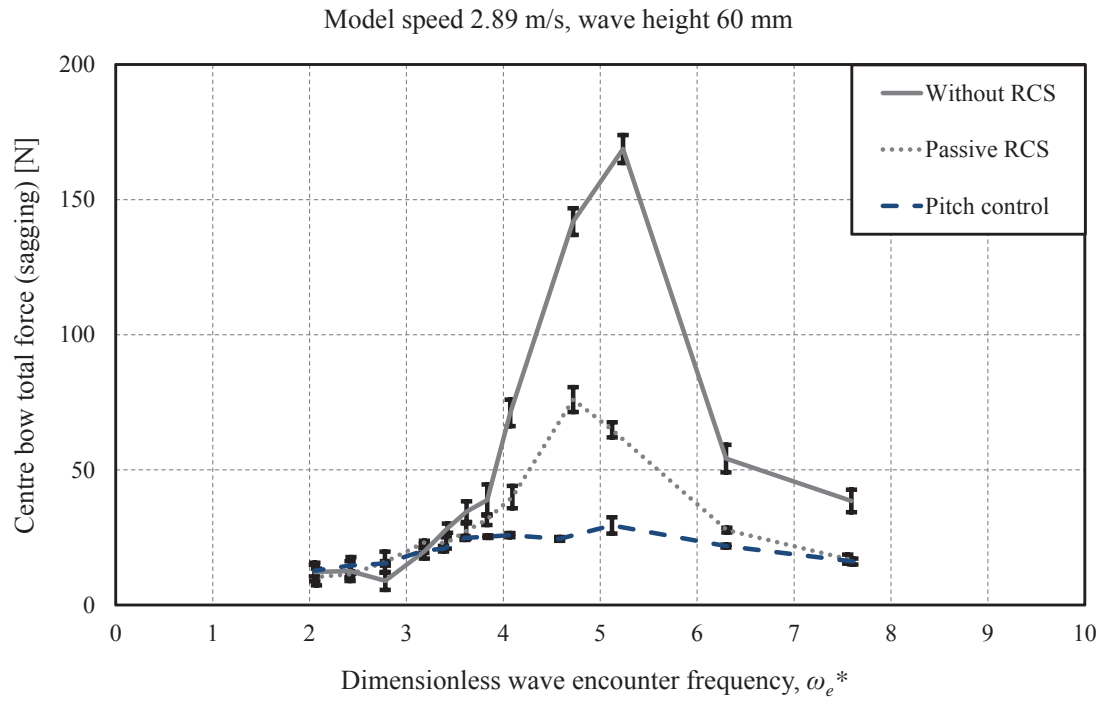


Figure 6.3: Error bars for centre bow total sagging force at a model test speed of 2.89 m/s ($Fr = 0.608$) and wave height of 60 mm.

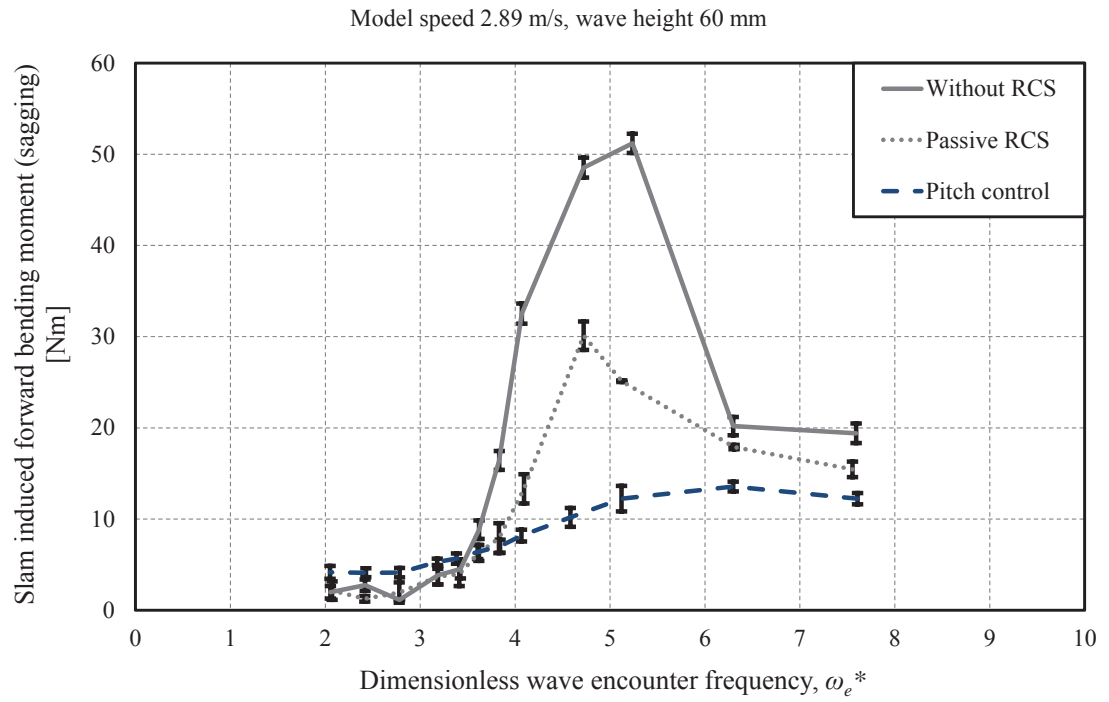


Figure 6.4: Error bars for demihull slam induced sagging bending moment at the forward segment position at a model test speed of 2.89 m/s ($Fr = 0.608$) and wave height of 60 mm.

6.3.1 Centre bow slamming forces

The centre bow forces, as previously explained, are divided into three parts: the centre bow entry force, the total centre bow force and the slam force. The slam force is actually the difference between the total force and the centre bow entry force. Figure 6.5 shows a sample time record of centre bow force demonstrating the centre bow entry force as well as the total sagging and hogging force acting on the bow. It is to be noted that the peak located between the total hogging force and total sagging force in each cycle was considered as the centre bow entry force for that particular cycle.

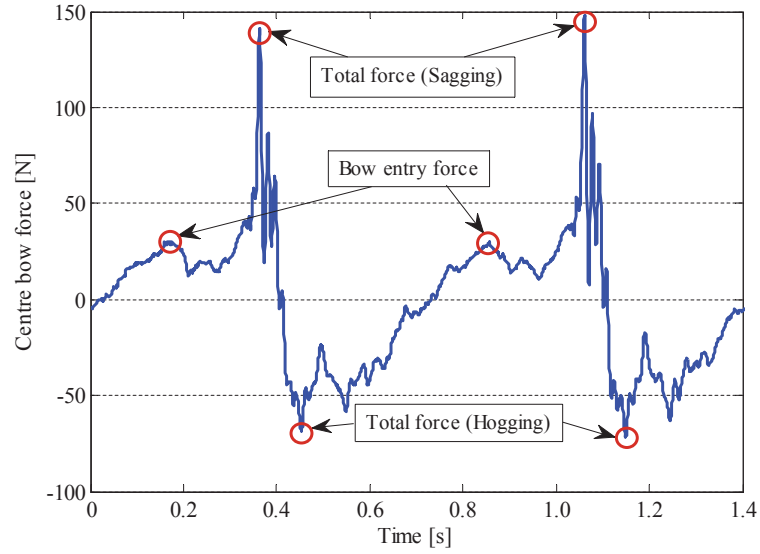


Figure 6.5: Designation of centre bow entry and total centre bow force using data obtained at model speed of 2.89 m/s ($Fr = 0.608$), wave height of 90 mm, ω_e^* of 4.581 and pitch control mode.

Centre bow entry force

Figures 6.6 and 6.7 show the centre bow entry force at a wave height of 60 mm and 90 mm respectively. As can be seen from Figure 6.6, although the passive RCS can reduce the peak centre bow entry forces, this force is more strongly mitigated when the ride control system is running in pitch control mode. Both local and heave control algorithms show a better reduction of the centre bow entry forces at the lower dimensionless wave encounter frequencies up to $\omega_e^* = 4.5$. The effect of nonlinearity of the ride control system on the centre bow entry forces is not significant. Figure 6.7 shows that both passive and active ride control systems do not have a strong influence on the centre bow entry force at the wave height of 90 mm, however the pitch control algorithm can slightly reduce the centre bow entry force.

It has been previously demonstrated by Lavroff [3] that the peak slam force is highly depen-

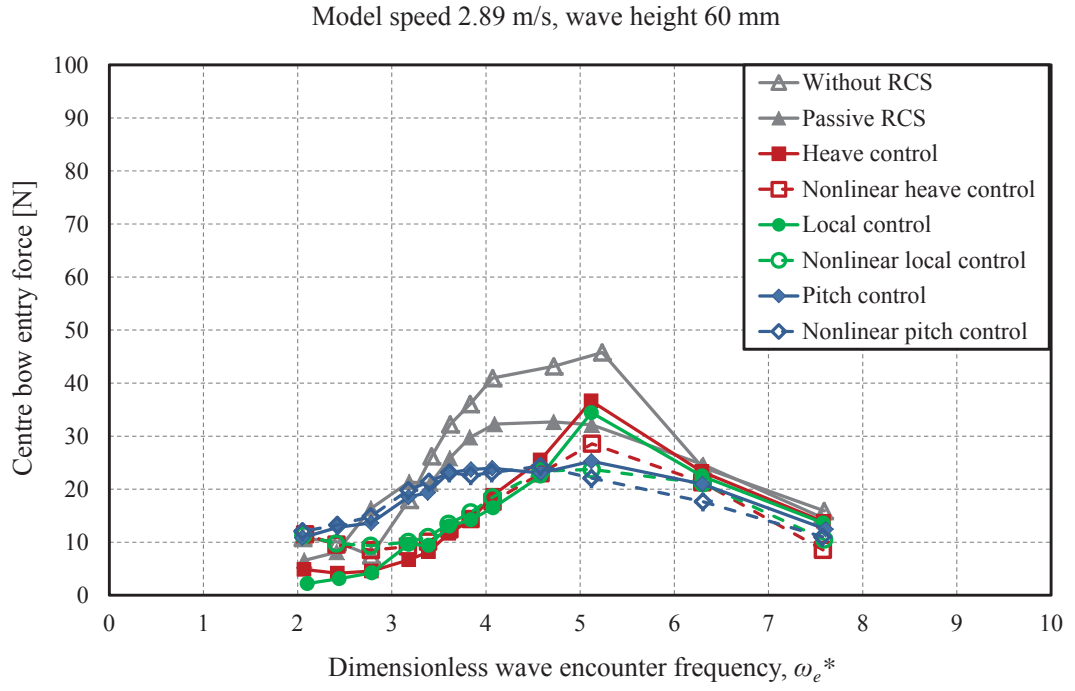


Figure 6.6: Centre bow entry force at model speed of 2.89 m/s ($Fr = 0.608$) and wave height of 60 mm.

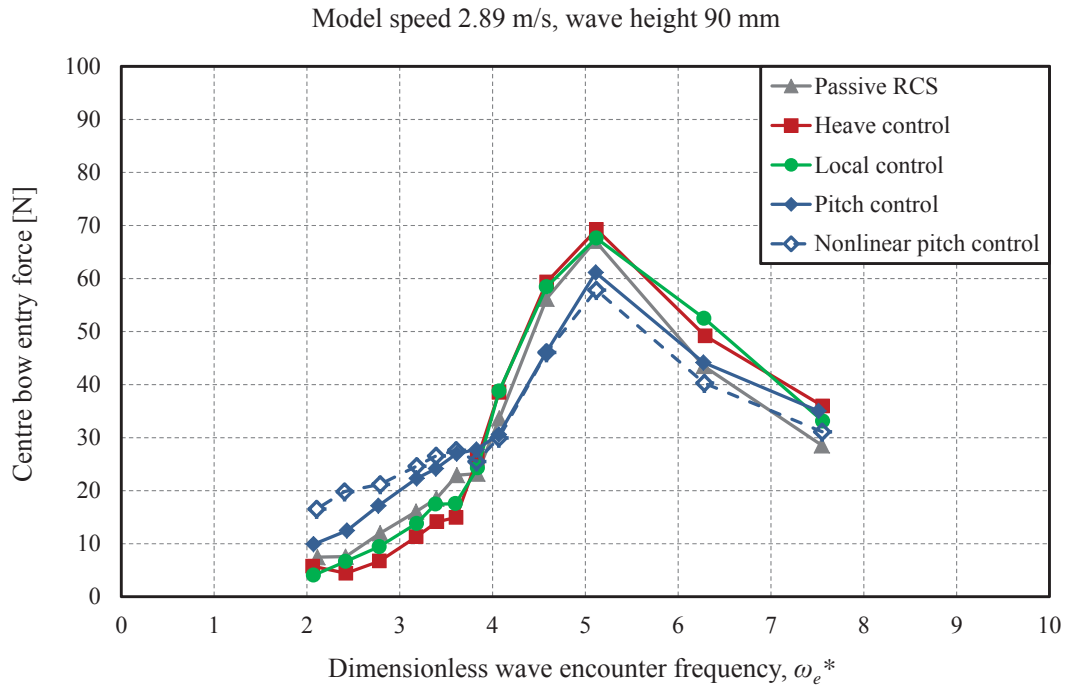


Figure 6.7: Centre bow entry force at model speed of 2.89 m/s ($Fr = 0.608$) and wave height of 90 mm.

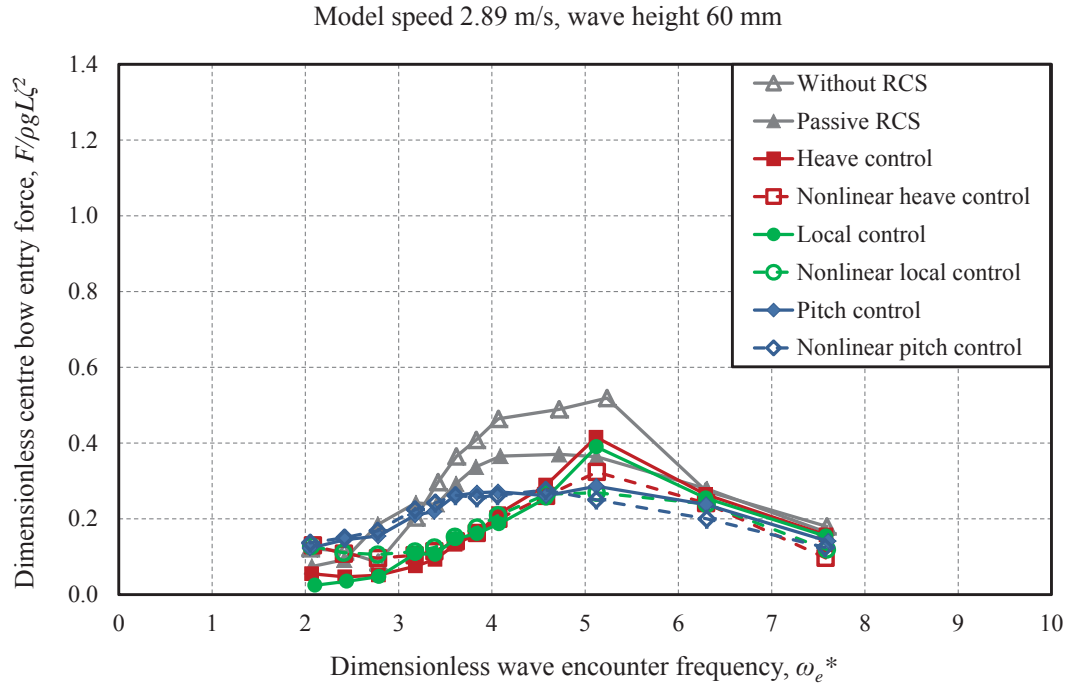


Figure 6.8: Dimensionless centre bow entry force at model speed of 2.89 m/s ($Fr = 0.608$) and wave height of 60 mm.

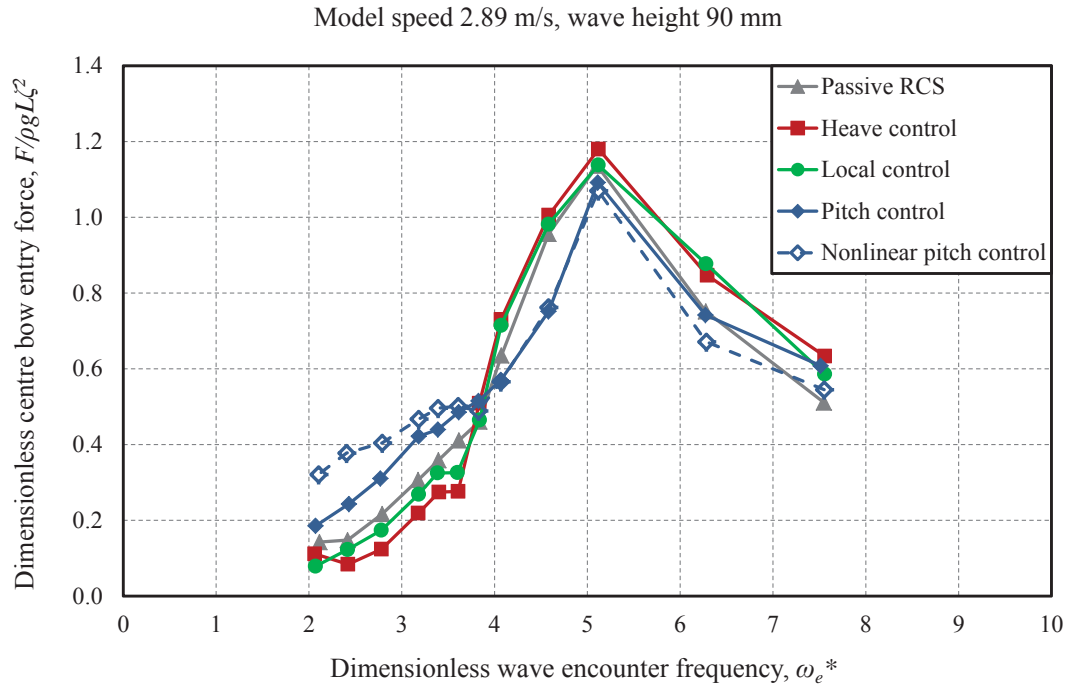


Figure 6.9: Dimensionless centre bow entry force at model speed of 2.89 m/s ($Fr = 0.608$) and wave height of 90 mm.

dent on the wave amplitude squared. Therefore, the centre bow entry forces as a function of wave height was reduced into dimensionless form as a function of the wave amplitude squared. Figures 6.8 and 6.9 show the results of the dimensionless centre bow entry forces, $F/\rho g L \zeta^2$, where F is the bow entry force, ρ is the density of water, g is the acceleration due to gravity, L is the overall length of the model and ζ is the actual measured wave amplitude at each model test run. It should be noted that although a specific wave height, either 60 mm or 90 mm, was demanded through the wave maker software, the actual wave height measured by wave probes was slightly different by about $\pm 5\%$. This led to a slightly different trend in dimensionless results compared to the dimensional results.

Centre bow total sagging force

As for the centre bow entry force, in order to evaluate the total sagging force acting on the centre bow at least five cycles at steady state were analysed and an average of the peaks was calculated. Simultaneously an average of the troughs was evaluated to specify the total hogging force acting on the centre bow of the catamaran model. The centre bow total forces were evaluated as a function of wave height and wave frequency for different ride control algorithms. In addition to the different ride control conditions, the results of the model test without RCS studied by Lavroff [3] are presented in order to compare with the results of the model test with RCS. Figures 6.10 and 6.11 show the centre bow total sagging force at wave heights of 60 mm and 90 mm respectively.

It is observed in Figure 6.10 that the maximum total sagging force measured on the bow at a model speed of 2.89 m/s and wave height of 60 mm was 169 N and occurred at $\omega_e^* = 5.235$ while the model was running without a ride control system. These results demonstrate that the ride control system can substantially reduce the centre bow total sagging force and is most effective in the pitch control mode, where the total sagging force was significantly reduced by about 85%. The local and heave control algorithms show a similar trend to the passive RCS, however compared to the passive RCS results they increased the total sagging force at the dimensionless wave encounter frequencies higher than 4.5.

As can be seen from Figure 6.11, although the pitch control algorithm reduced the total sagging force measured on the bow at a wave height of 90 mm, the ride control system at a wave height of 90 mm does not show the same effect on the centre bow total sagging force as the ride control system at wave height of 60 mm. This is simply due to the limited capacity of the controls, which become relatively less effective in larger seas.

Figures 6.12 and 6.13 show the results for the dimensionless centre bow total sagging force, $F/\rho g L \zeta^2$, where F is the centre bow total sagging force, ρ is the density of water, g is the acceleration due to gravity, L is the overall length of the model and ζ is the wave amplitude.

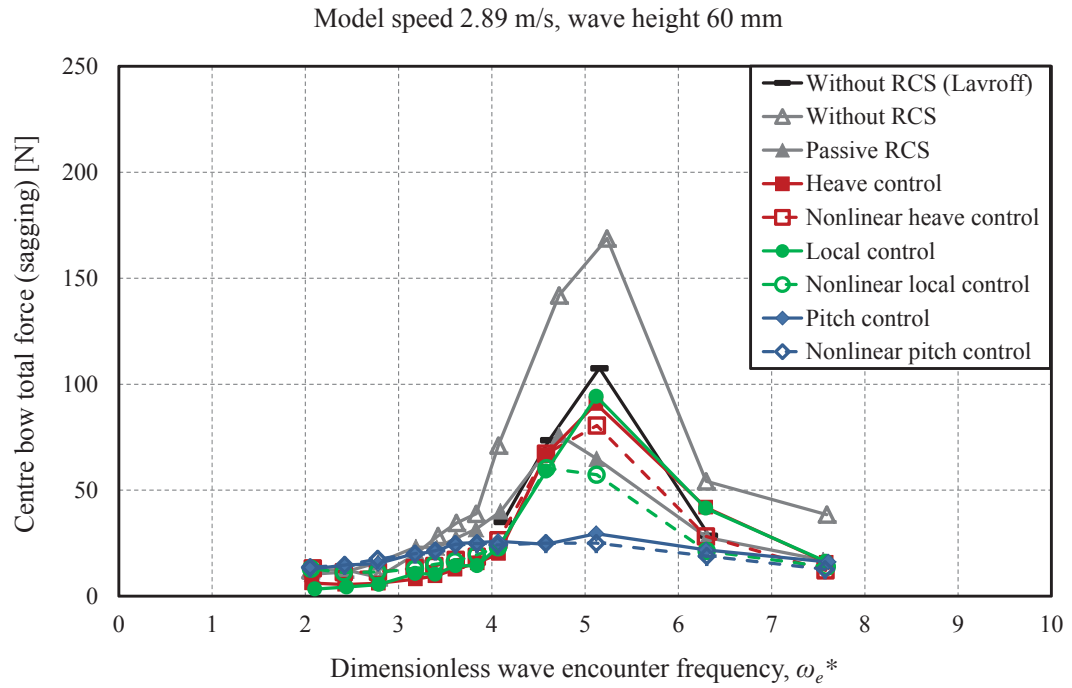


Figure 6.10: Centre bow total sagging force at model speed of 2.89 m/s ($Fr = 0.608$) and wave height of 60 mm.

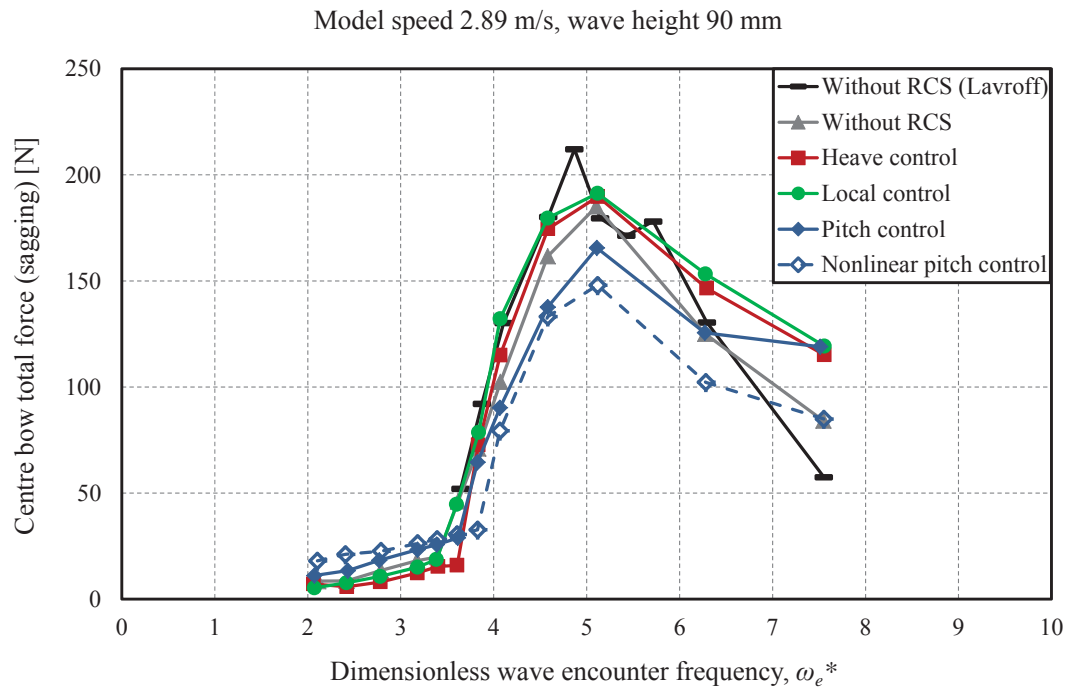


Figure 6.11: Centre bow total sagging force at model speed of 2.89 m/s ($Fr = 0.608$) and wave height of 90 mm.

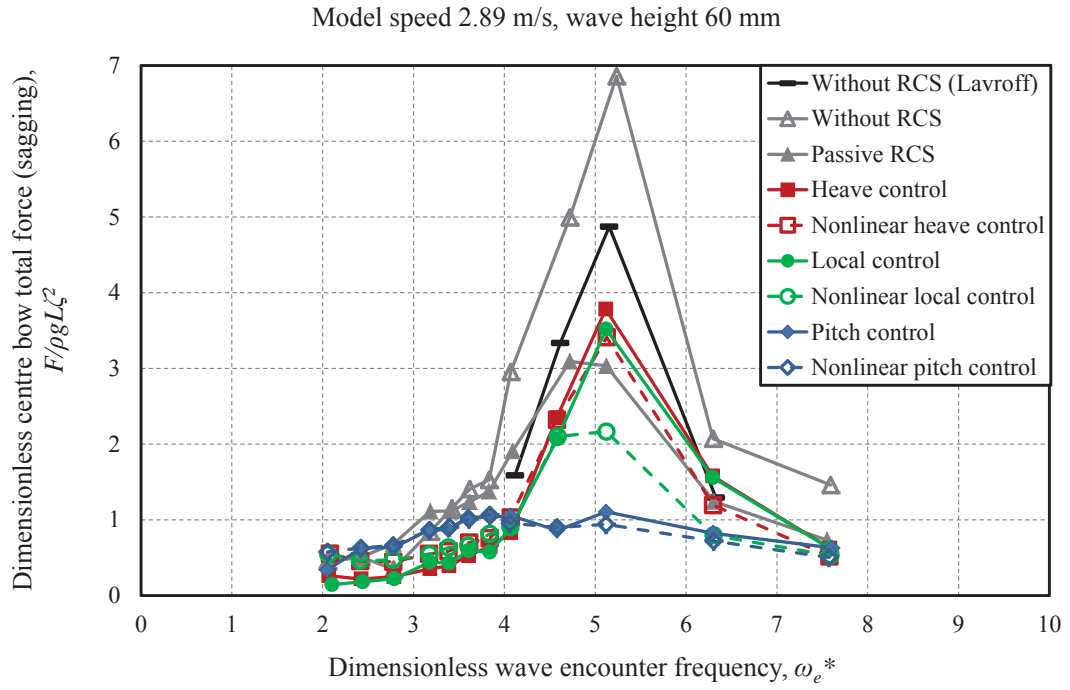


Figure 6.12: Dimensionless centre bow total sagging force at model speed of 2.89 m/s ($Fr = 0.608$) and wave height of 60 mm.

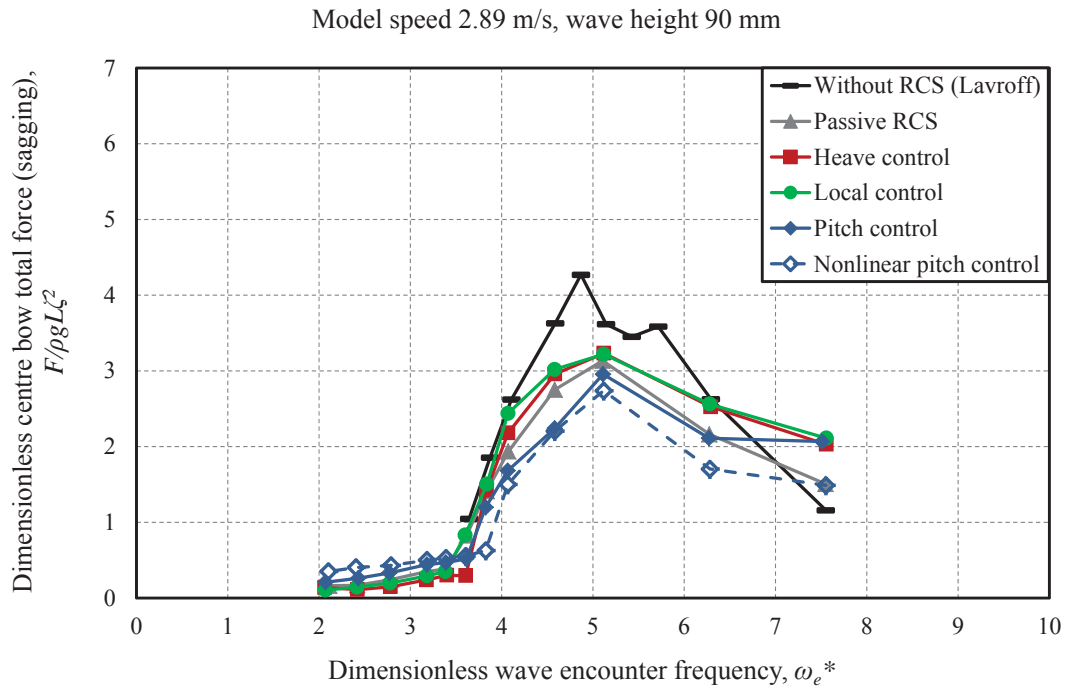


Figure 6.13: Dimensionless centre bow total sagging force at model speed of 2.89 m/s ($Fr = 0.608$) and wave height of 90 mm.

Centre bow total hogging force

Figures 6.14 and 6.15 show the centre bow total hogging force at wave heights of 60 mm and 90 mm respectively. As can be seen from Figure 6.14, the maximum total hogging force measured on the bow at a model speed of 2.89 m/s and wave height of 60 mm was 132 N and occurred at $\omega_e^* = 5.235$ when the model was without RCS. The passive ride control system can reduce the maximum peak total hogging force by about 25% from 132 N to 97 N. The heave and local control modes reduced the total hogging force and as expected from previous results, the pitch control mode had a significant influence on the reduction of the total hogging force, where it reduced the centre bow total hogging force by around 70%. It is observed in Figure 6.15 that the ride control system does not have a significant effect on the peak total hogging force at the wave height of 90 mm.

Figures 6.16 and 6.17 show the results for the dimensionless centre bow peak total hogging force. It can be seen from these figures that increases in the wave height resulted in increases of the magnitude of the total force measured on the bow of the catamaran model.

Centre bow slam force

Finally, Figures 6.18 and 6.19 show the centre bow sagging slam force at wave heights of 60 mm and 90 mm respectively, while the dimensionless centre bow sagging slam force at a wave height of 60 mm and 90 mm are presented in Figures 6.20 and 6.21 respectively. These results clearly demonstrate the effect of the ride control system on mitigating the centre bow peak slam force, which is most evident in the pitch control mode where it significantly reduced the peak slam force by about 90% in 60 mm waves. The effect of the RCS in 90 mm waves is again less profound when compared to the 60 mm case and follows a similar trend to the previous force results presented for the 90 mm test case.

Centre bow total force position

The force positions for both sagging and hogging were calculated based on the strains measured on the centre bow elastic links. Figures 6.22 and 6.23 show the positions of the total sagging force measured from the transom of the catamaran model as a function of wave encounter frequency at wave height of 60 mm and 90 mm respectively and Figures 6.24 and 6.25 similarly show the positions of the total hogging force. As can be seen in Figures 6.22 to 6.25, most of the total forces acting on the centre bow of the catamaran model occurred between 1800 mm and 2000 mm from the transom of the model for all the test cases considered with and without the RCS. This is close to the centre bow truncation at a distance of 1900 mm from the transom, a result consistent with the findings of Lavroff [3].

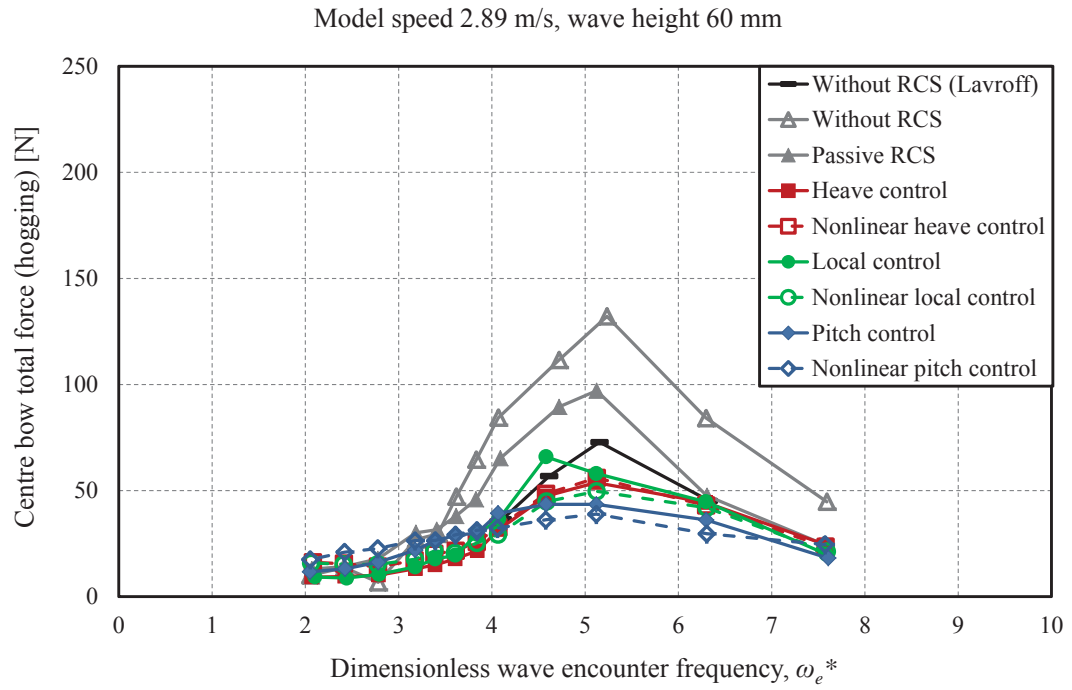


Figure 6.14: Centre bow total hogging force at model speed of 2.89 m/s ($Fr = 0.608$) and wave height of 60 mm.

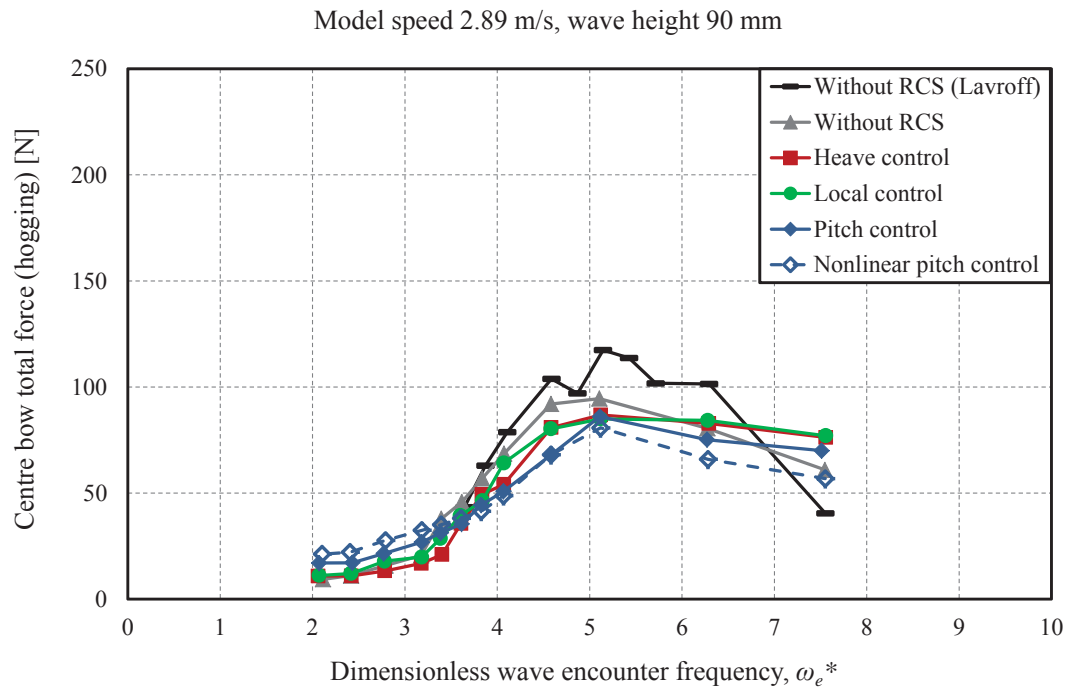


Figure 6.15: Centre bow total hogging force at model speed of 2.89 m/s ($Fr = 0.608$) and wave height of 90 mm.

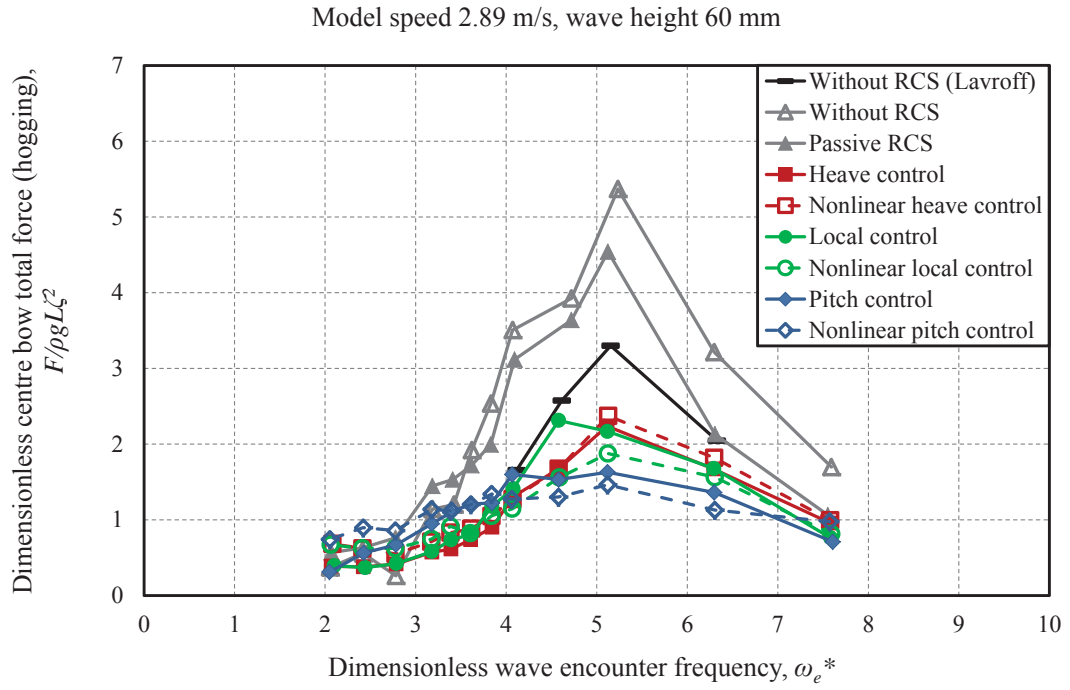


Figure 6.16: Dimensionless centre bow total hogging force at model speed of 2.89 m/s ($Fr = 0.608$) and wave height of 60 mm.

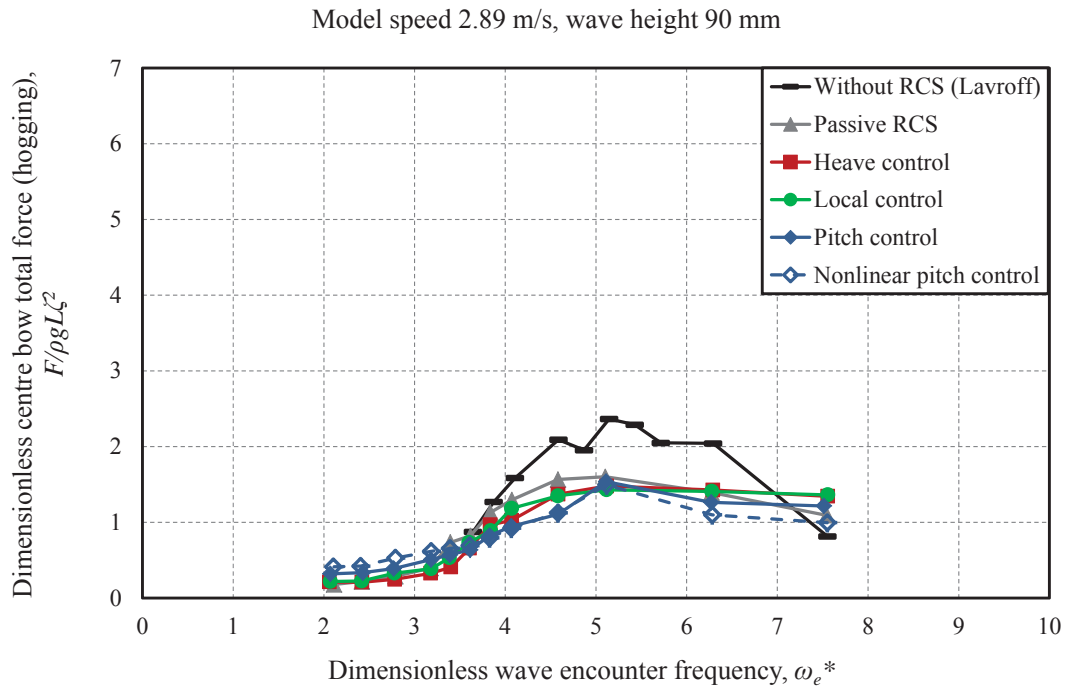


Figure 6.17: Dimensionless centre bow total hogging force at model speed of 2.89 m/s ($Fr = 0.608$) and wave height of 90 mm.

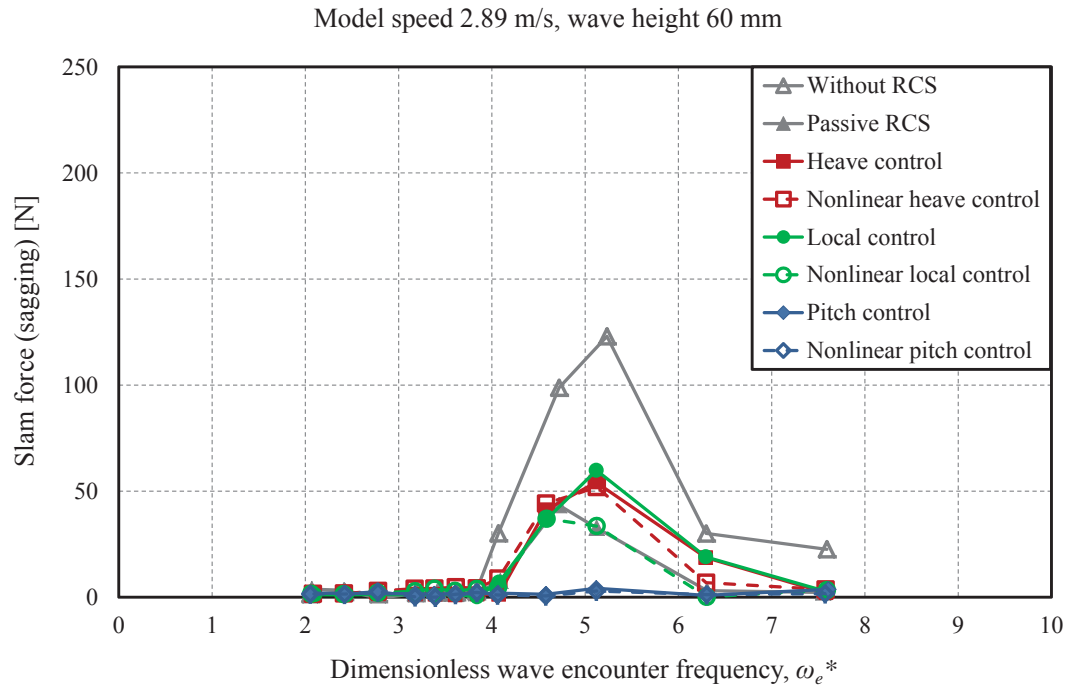


Figure 6.18: Sagging slam force at model speed of 2.89 m/s ($Fr = 0.608$) and wave height of 60 mm.

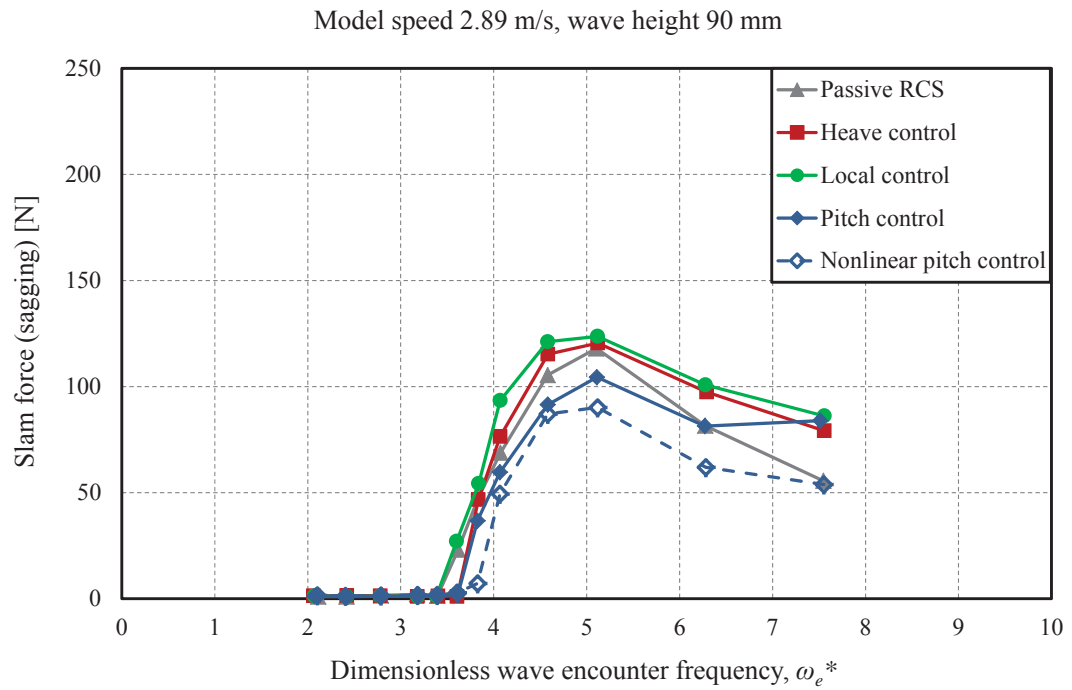


Figure 6.19: Sagging slam force at model speed of 2.89 m/s ($Fr = 0.608$) and wave height of 90 mm.

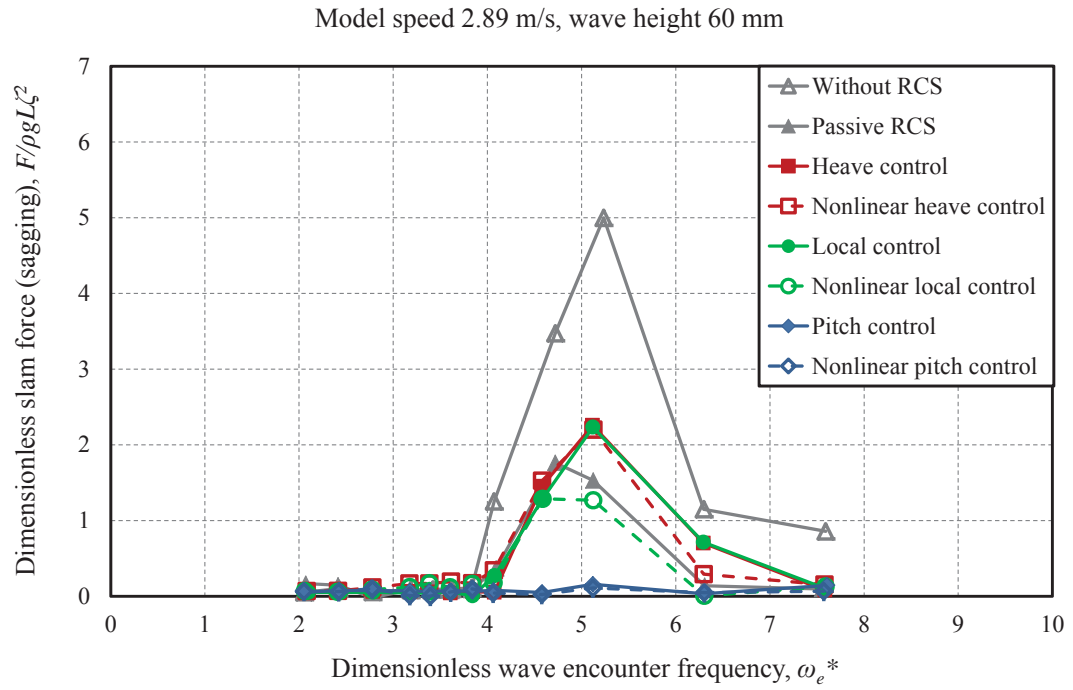


Figure 6.20: Dimensionless sagging slam force at model speed of 2.89 m/s ($Fr = 0.608$) and wave height of 60 mm.

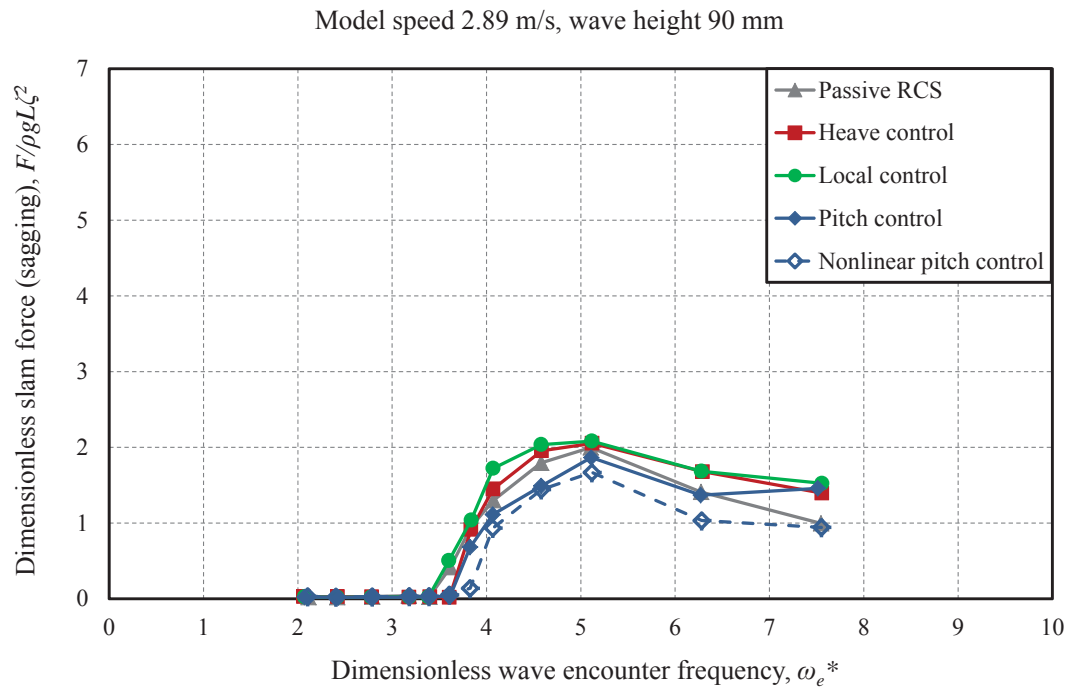


Figure 6.21: Dimensionless sagging slam force at model speed of 2.89 m/s ($Fr = 0.608$) and wave height of 90 mm.

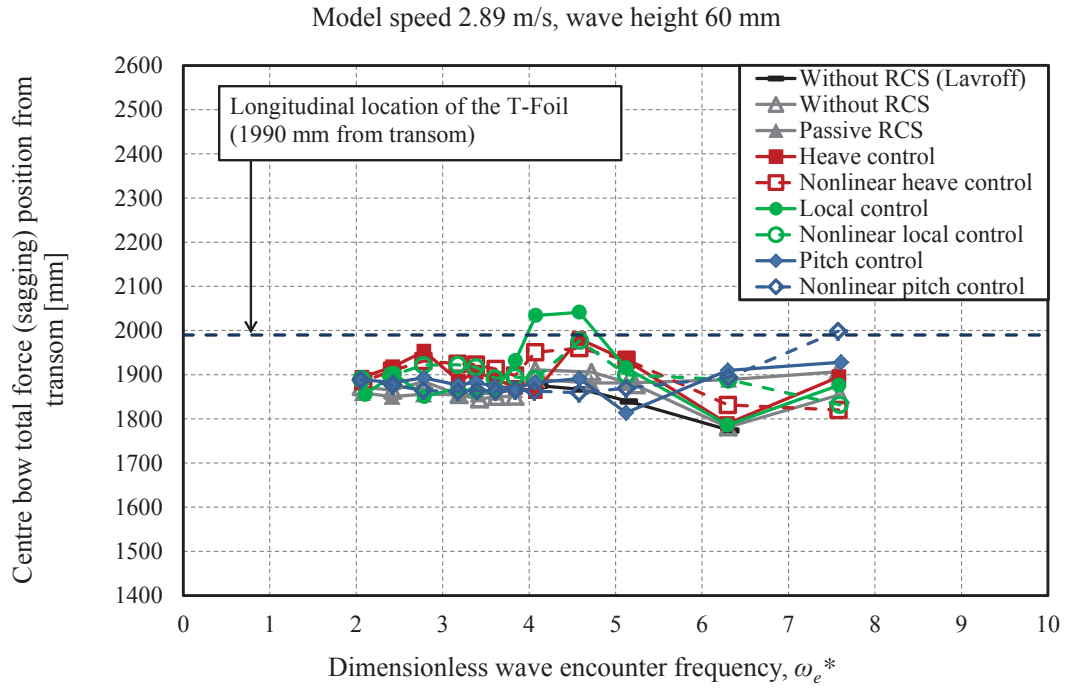


Figure 6.22: Centre bow total sagging force position from the transom at model speed of 2.89 m/s ($Fr = 0.608$) and wave height of 60 mm.

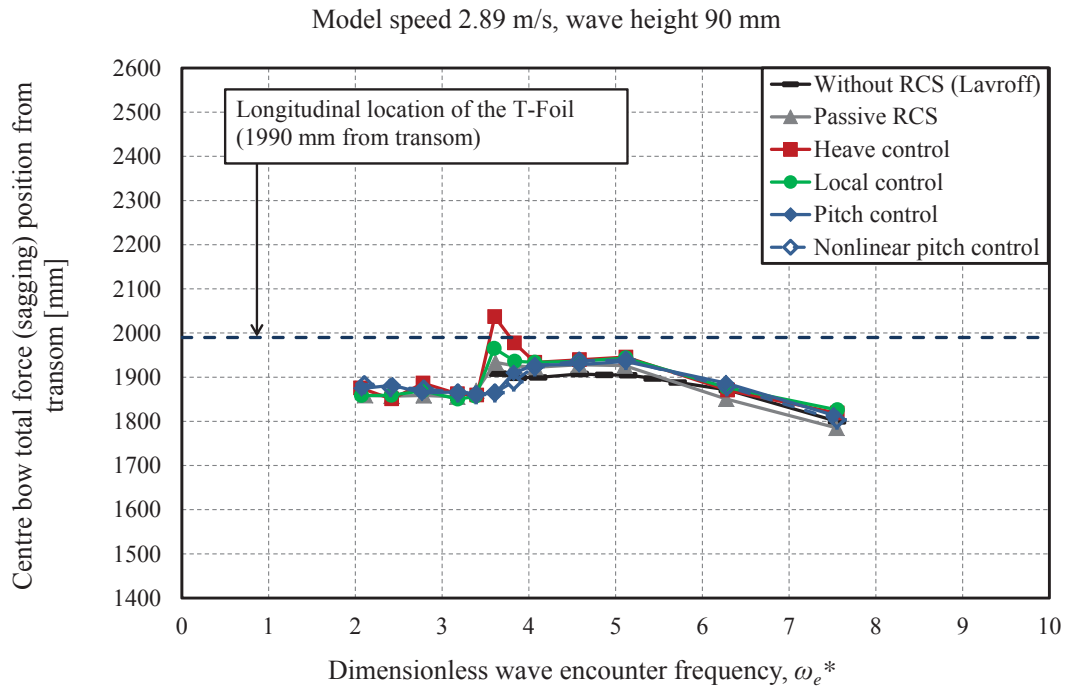


Figure 6.23: Centre bow total sagging force position from the transom at model speed of 2.89 m/s ($Fr = 0.608$) and wave height of 90 mm.

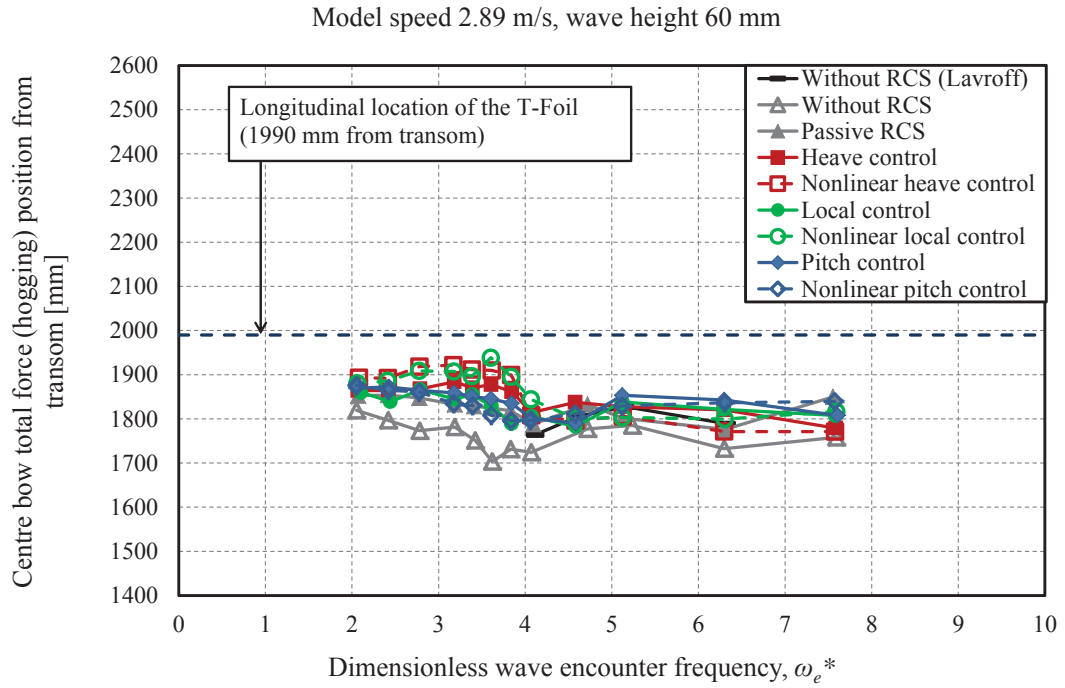


Figure 6.24: Centre bow total hogging force position from the transom at model speed of 2.89 m/s ($Fr = 0.608$) and wave height of 60 mm.

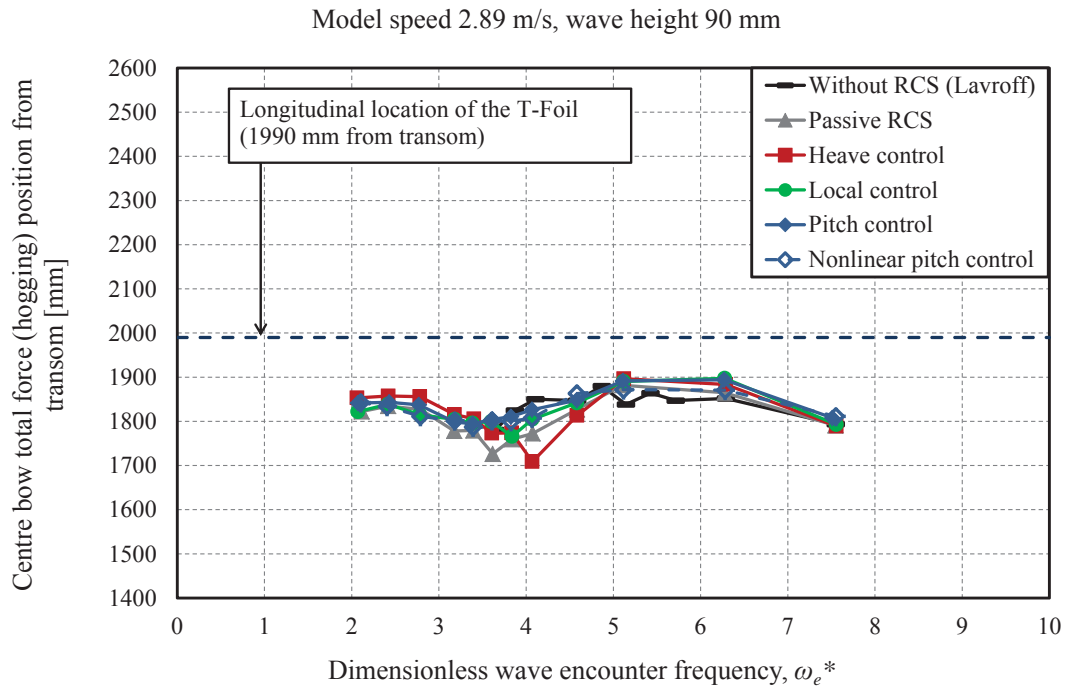


Figure 6.25: Centre bow total hogging force position from the transom at model speed of 2.89 m/s ($Fr = 0.608$) and wave height of 90 mm.

6.3.2 Demihull slam induced bending moments

The evaluation of the slam induced bending moments followed the same procedure as developed for calculating the centre bow forces. The peaks and troughs of the bending moment for at least five cycles at steady state of each individual model test run were selected and averaged to produce the hogging and sagging bending moment for the given test condition. The slam induced bending moments are presented for both forward and aft segments of the segmented catamaran model, as defined in Figure 2.1.

Figures 6.26 and 6.27 show the sagging slam induced bending moments measured in the forward segment of the catamaran model as a function of wave encounter frequency at wave heights of 60 mm and 90 mm respectively, while Figures 6.28 and 6.29 show the corresponding hogging moments. Similarly Figures 6.30 to 6.33 show sagging and hogging moments respectively measured in the aft segment at these two wave heights. The bending moment shown in each of these figures is the summation of the bending moments measured at the respective demihull port and starboard elastic links.

As can be seen from Figure 6.26, both linear and nonlinear pitch control modes significantly reduced the sagging slam induced forward segment bending moments by about 80%. The other ride control algorithms were still effective, giving about 50% reduction of the sagging slam induced forward bending moments. As expected, and evident in Figure 6.27, the ride control system at wave height of 90 mm was not as effective as it was at wave height of 60 mm, similar to the slam impact loads. However, the pitch control mode shows a reduction of about 30% in the sagging slam induced forward bending moments at wave height of 90 mm.

Figure 6.28 shows about 75% mitigation of the hogging slam induced forward segment bending moments by the pitch control algorithm at a wave height of 60 mm. However, Figure 6.29 demonstrates that there is no significant effect of the ride control system on the hogging slam induced forward bending moments at a wave height of 90 mm.

Figure 6.30 also shows a reduction of about 75% in the sagging slam induced bending moments measured in the aft segment by both linear and nonlinear control modes at a wave height of 60 mm, and as can be seen from Figure 6.32, the linear and nonlinear pitch control algorithms reduced the hogging slam induced bending moments measured in the aft segment by around 75% at a wave height of 60 mm.

Comparing the results of the slam induced bending moments presented in Figures 6.26 to 6.33 with the results of the centre bow forces presented in Figures 6.10, 6.11, 6.14 and 6.15, the direct influence of the centre bow forces on the model bending is immediately apparent. It is observed that increases in the wave height from 60 mm to 90 mm gave rise to increases in the centre bow forces as well as slam induced bending moments. The demihull slam induced sagging response was on average greater than the hogging response. The slam induced demihull bending moments were found to coincide with the centre bow slam forces.

In order to investigate the relationship between the slam induced bending moments and

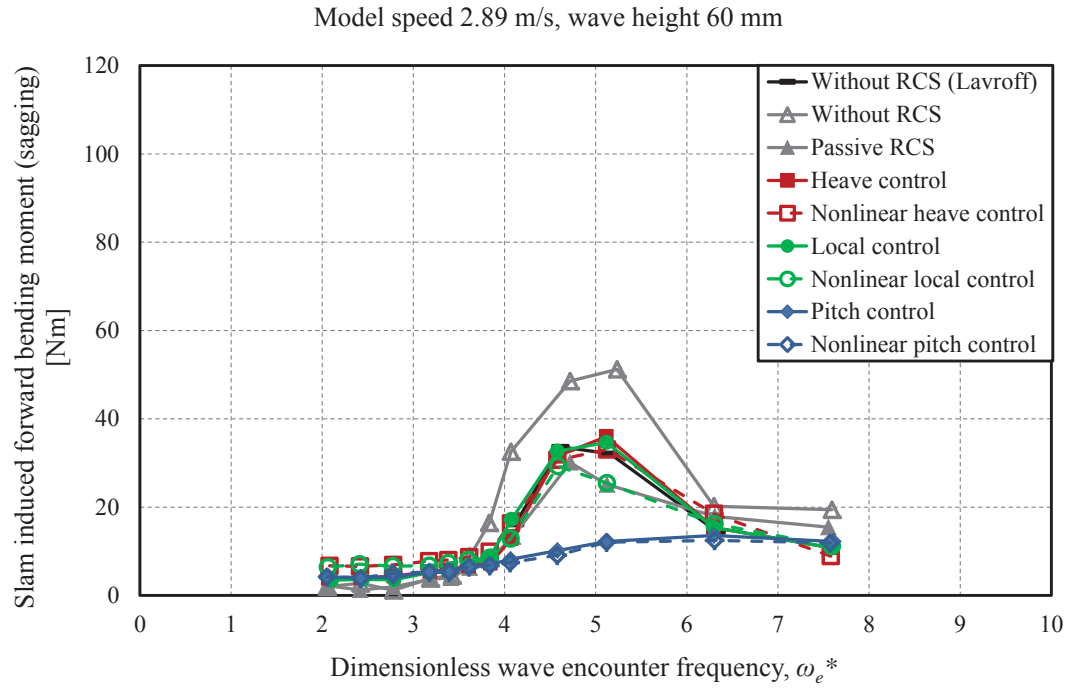


Figure 6.26: Demihull slam induced sagging bending moment at the forward segment position at model speed of 2.89 m/s ($Fr = 0.608$) and wave height of 60 mm.

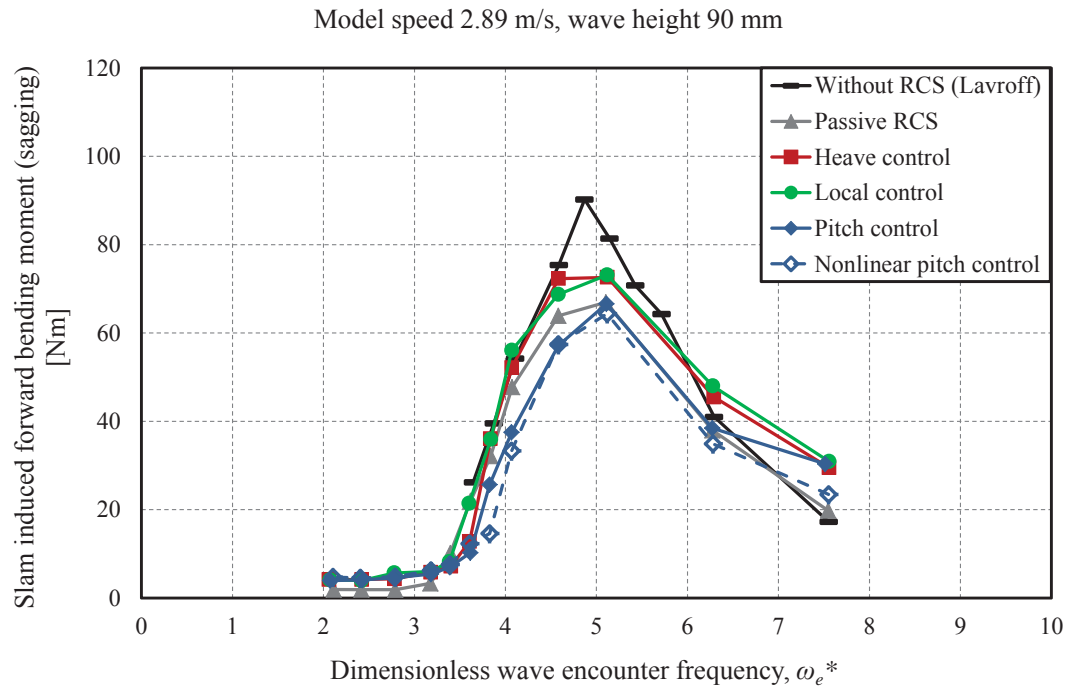


Figure 6.27: Demihull slam induced sagging bending moment at the forward segment position at model speed of 2.89 m/s ($Fr = 0.608$) and wave height of 90 mm.

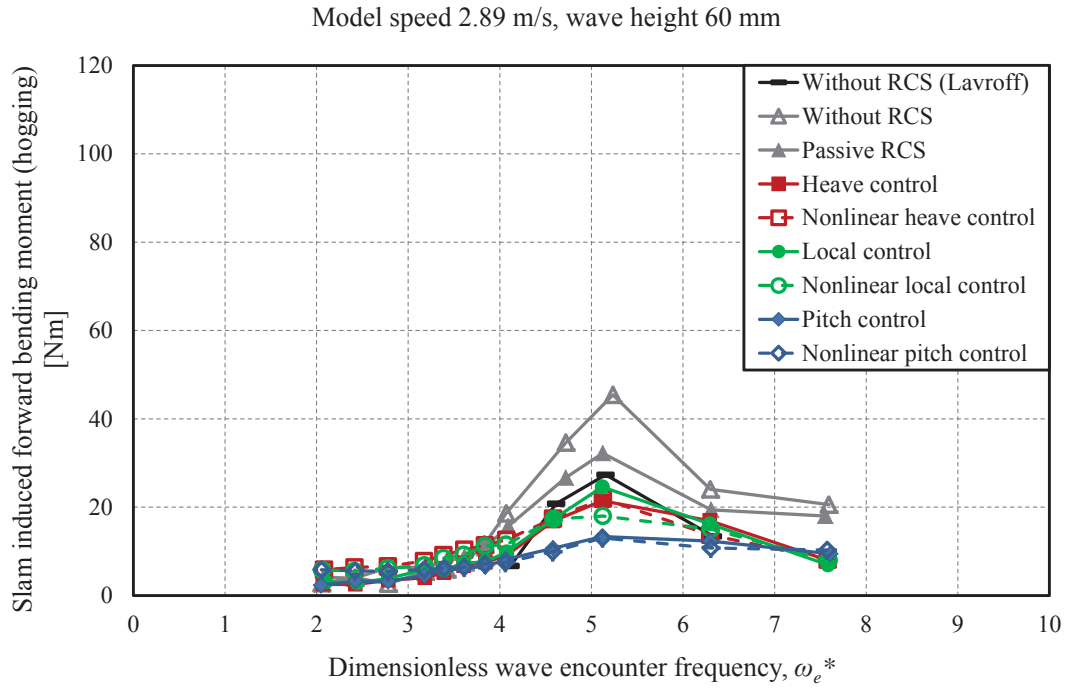


Figure 6.28: Demihull slam induced hogging bending moment at the forward segment position at model speed of 2.89 m/s ($Fr = 0.608$) and wave height of 60 mm.

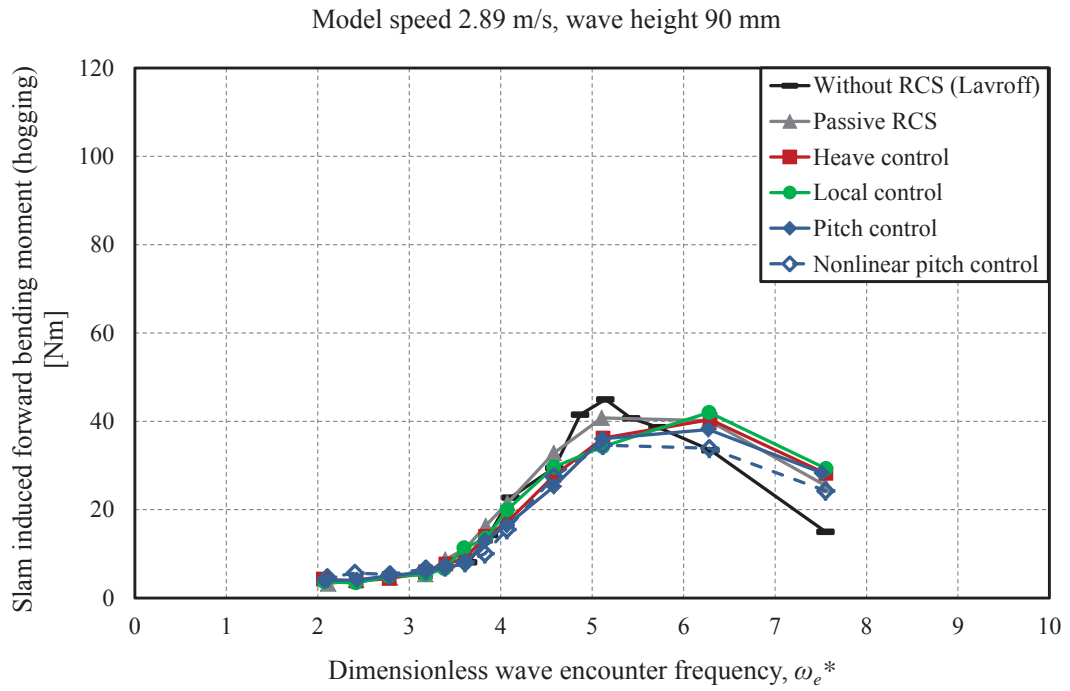


Figure 6.29: Demihull slam induced hogging bending moment at the forward segment position at model speed of 2.89 m/s ($Fr = 0.608$) and wave height of 90 mm.

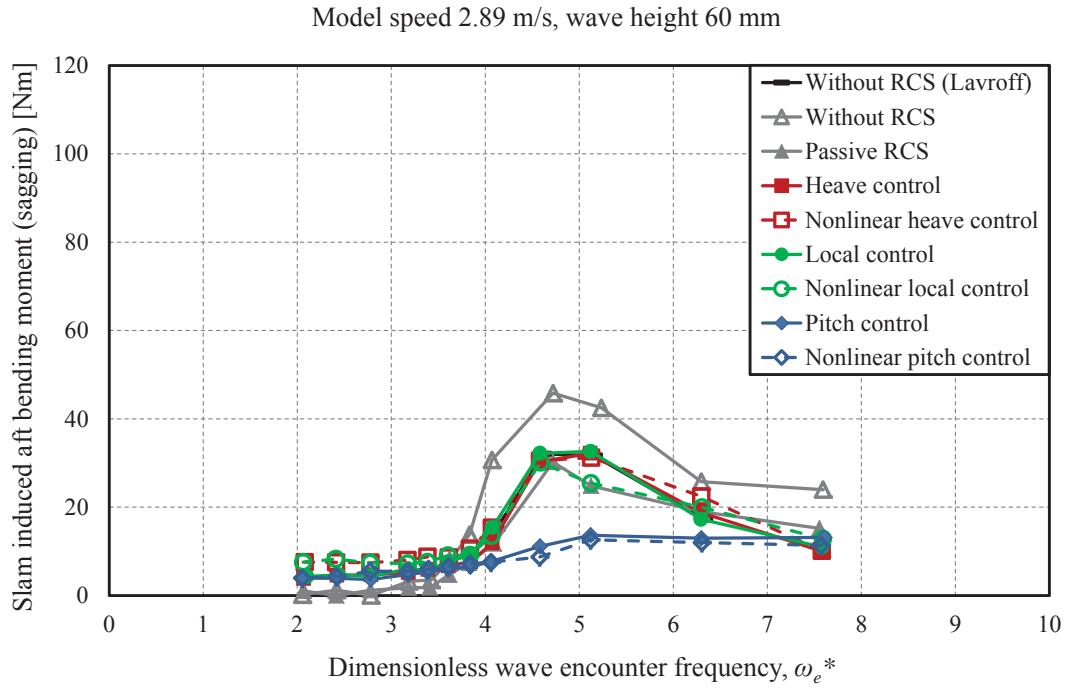


Figure 6.30: Demihull slam induced sagging bending moment at the aft segment position at model speed of 2.89 m/s ($Fr = 0.608$) and wave height of 60 mm.

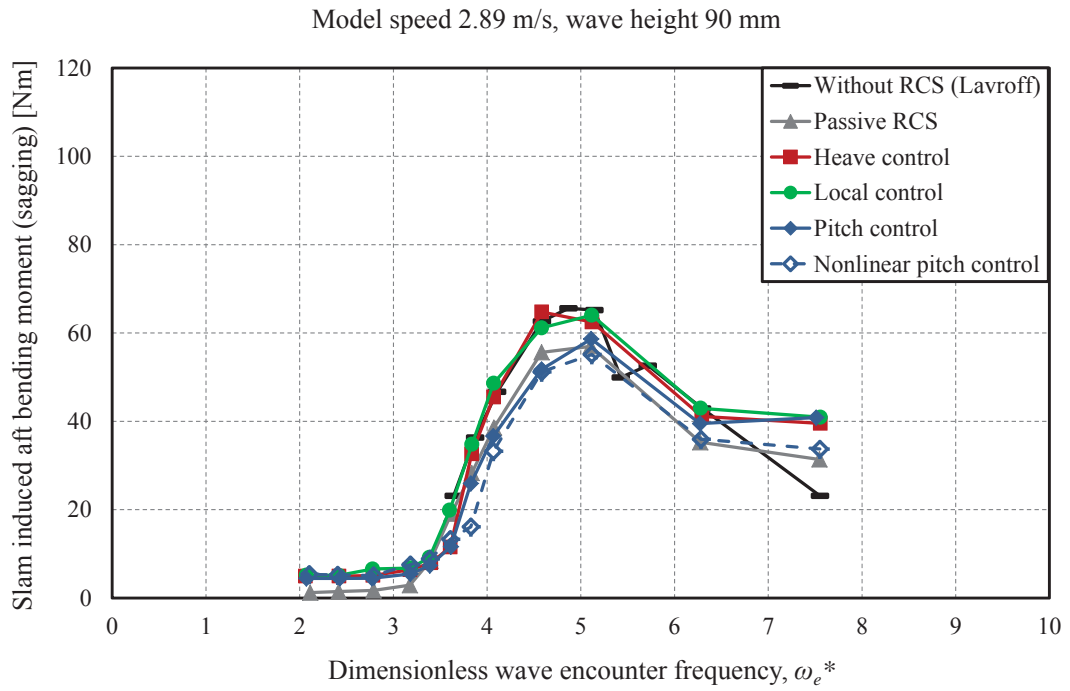


Figure 6.31: Demihull slam induced sagging bending moment at the aft segment position at model speed of 2.89 m/s ($Fr = 0.608$) and wave height of 90 mm.

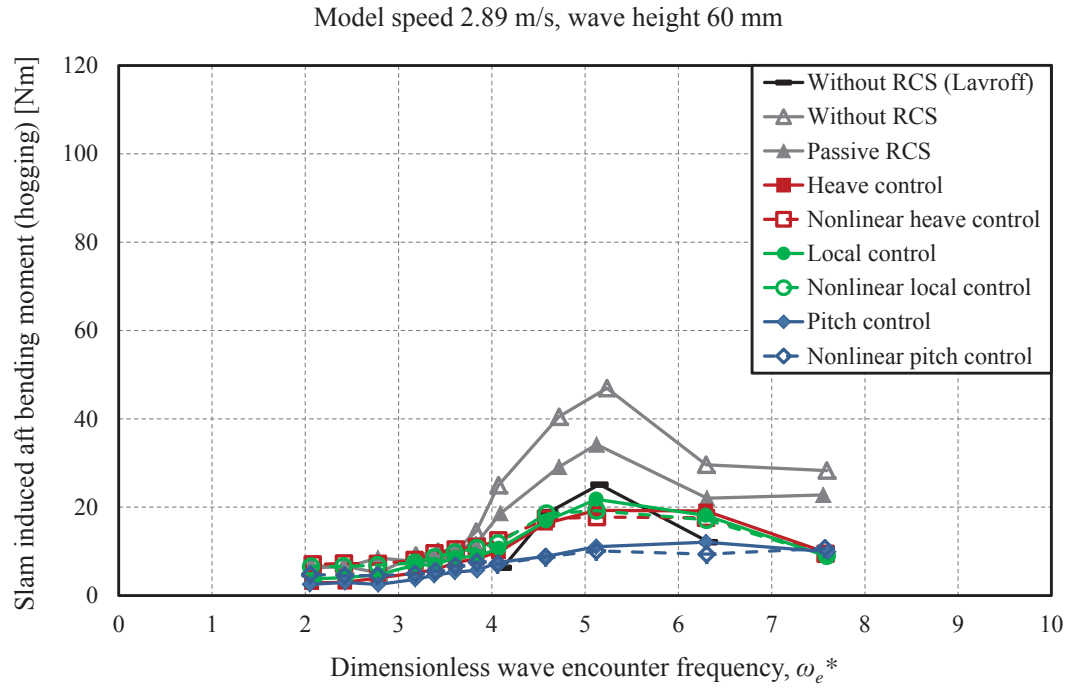


Figure 6.32: Demihull slam induced hogging bending moment at the aft segment position at model speed of 2.89 m/s ($Fr = 0.608$) and wave height of 60 mm.

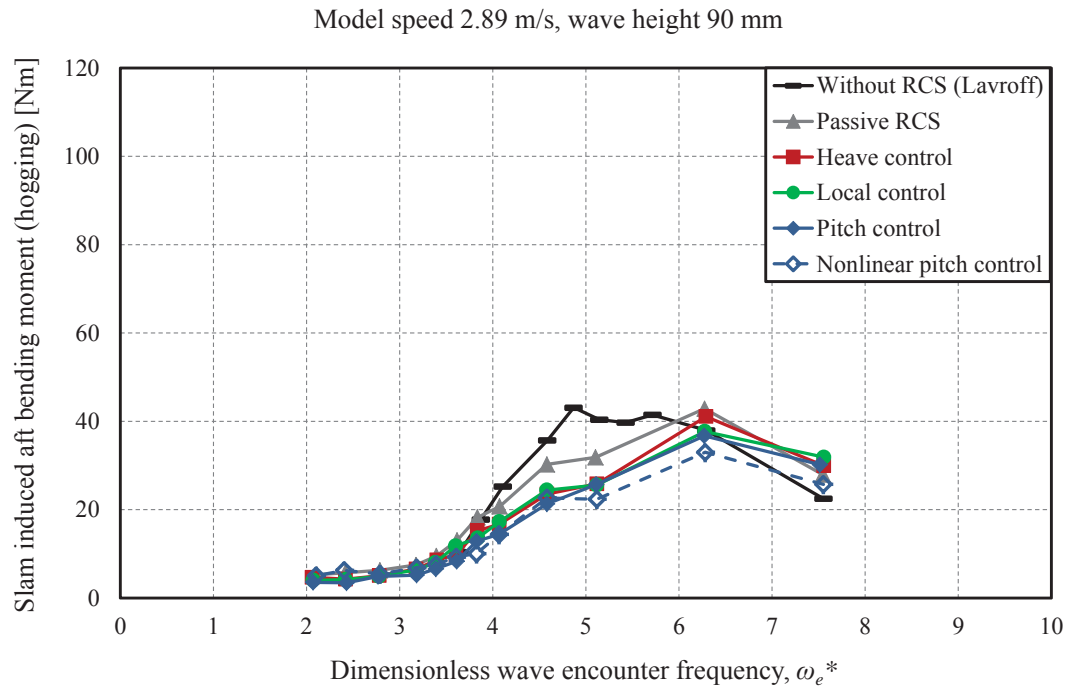


Figure 6.33: Demihull slam induced hogging bending moment at the aft segment position at model speed of 2.89 m/s ($Fr = 0.608$) and wave height of 90 mm.

the incident wave amplitude, the demihull bending moments were non-dimensionalised using the square of the wave amplitude since it has been previously demonstrated by Lavroff [3] that the the slam induced bending moments are highly dependent on the wave amplitude squared. Figures 6.34 to 6.41 show the non-dimensional slam induced bending moments, $M/\rho g L^2 \zeta^2$, where M is the bending moment, ρ is the density of water, g is the gravitational acceleration, L is the ship length and ζ is the wave amplitude.

As can be seen from Figures 6.34 and 6.35, the maximum value of non-dimensional sagging slam induced bending moments at the forward section for all the ride control conditions except pitch control mode is less variable over the change of wave height than was the dimensional parameter presented in Figures 6.26 and 6.27. This demonstrates that the peak sagging bending moments varied approximately with the wave amplitude squared.

Comparing Figures 6.36 and 6.37 with the dimensional parameter presented in Figures 6.28 and 6.29, indicates that the peak hogging bending moments variation with the wave amplitude squared is not as significant as the peak sagging bending moments variation with the wave amplitude.

Figures 6.38 to 6.41 show a similar trend for the slam induced bending moments measured at the aft segment of the catamaran model when compared with the results at the forward segment presented in Figures 6.34 to 6.37. However, these results show that the peak sagging slam force led to an increase in the dimensionless peak sagging bending moments measured at the forward segment of the catamaran model when compared to the aft segment position.

The non-dimensional slam induced bending moments demonstrate that both linear and nonlinear pitch control algorithms have significant influence on the reduction of the demihull bending moments when the model is tested at the wave height of 60 mm.

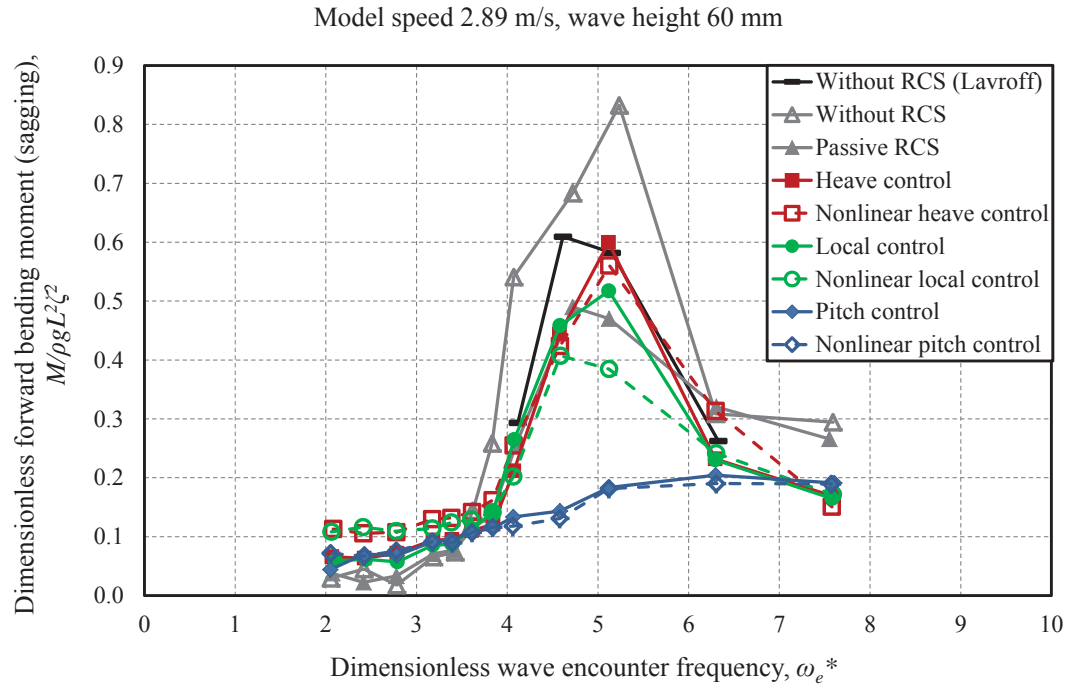


Figure 6.34: Dimensionless demihull slam induced sagging bending moment at the forward segment position at model speed of 2.89 m/s ($Fr = 0.608$) and wave height of 60 mm.

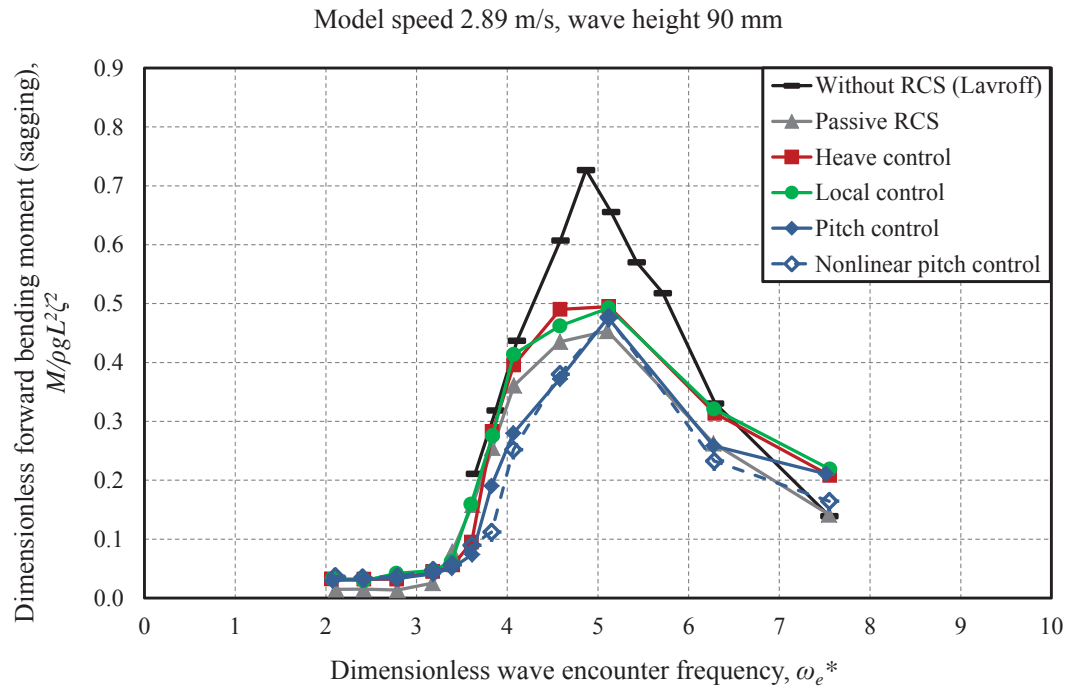


Figure 6.35: Dimensionless demihull slam induced sagging bending moment at the forward segment position at model speed of 2.89 m/s ($Fr = 0.608$) and wave height of 90 mm.

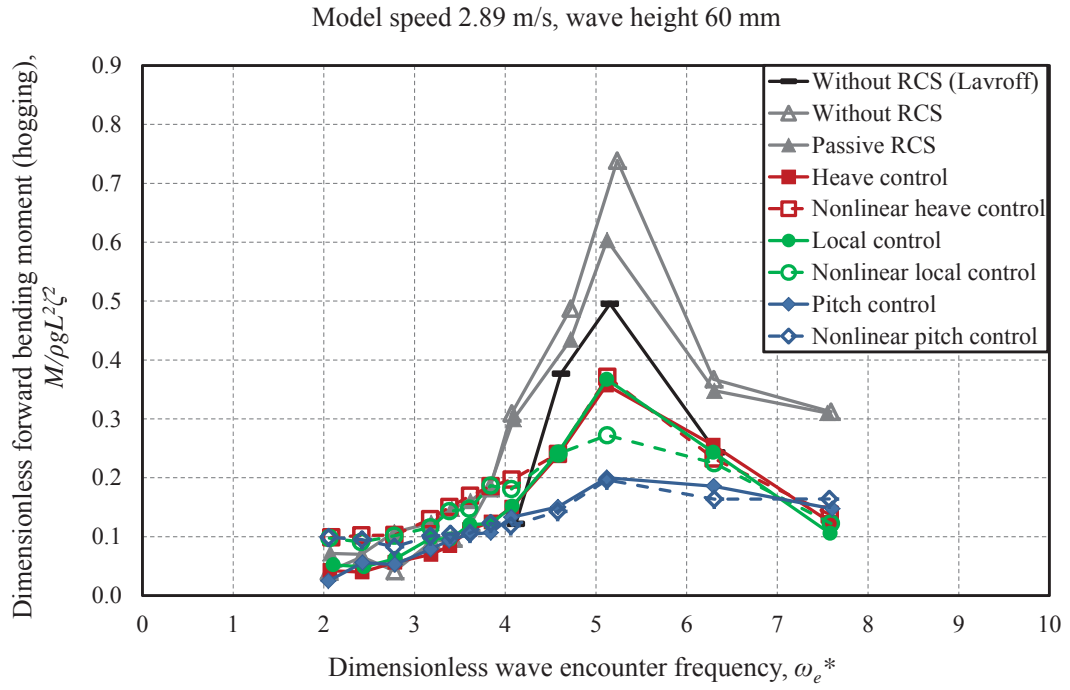


Figure 6.36: Dimensionless demihull slam induced hogging bending moment at the forward segment position at model speed of 2.89 m/s ($Fr = 0.608$) and wave height of 60 mm.

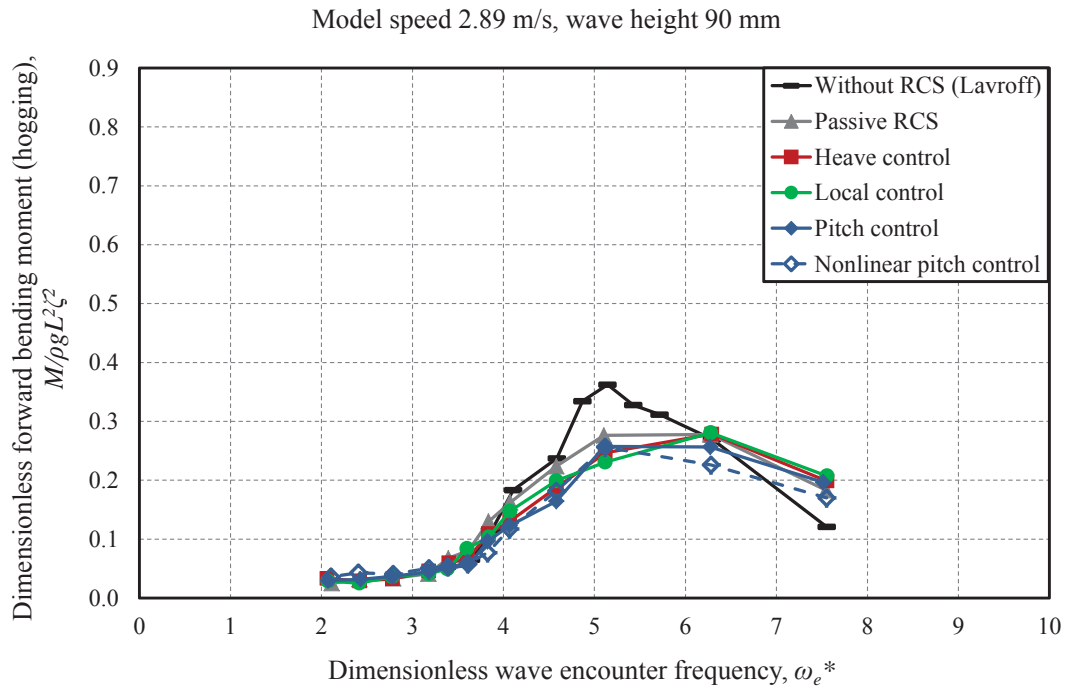


Figure 6.37: Dimensionless demihull slam induced hogging bending moment at the forward segment position at model speed of 2.89 m/s ($Fr = 0.608$) and wave height of 90 mm.

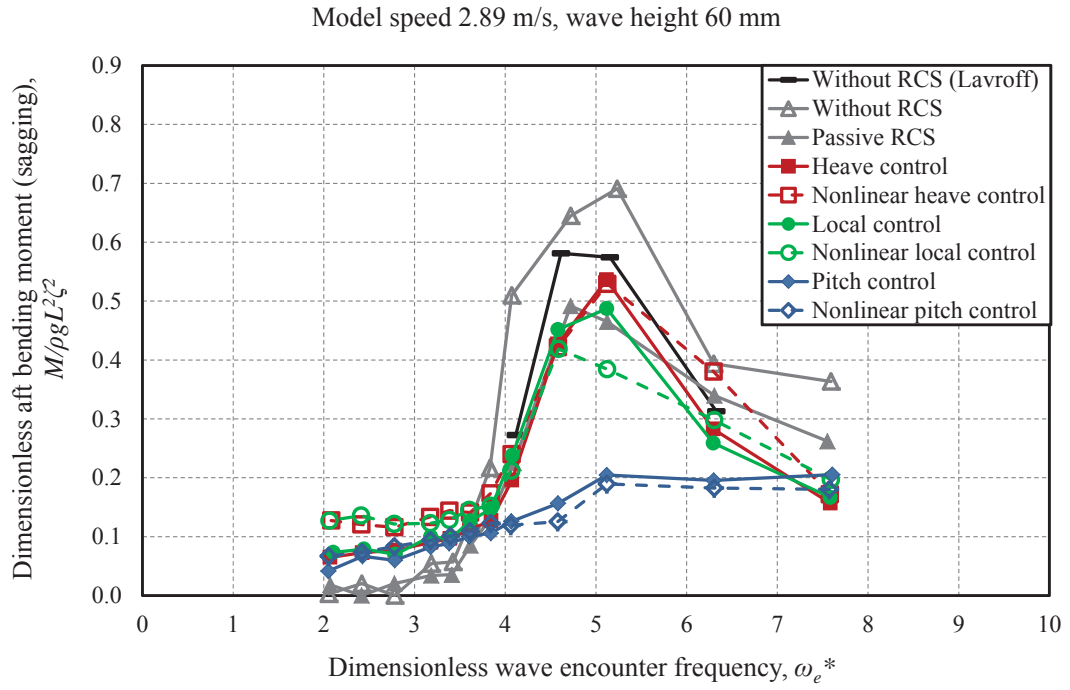


Figure 6.38: Dimensionless demihull slam induced sagging bending moment at the aft segment position at model speed of 2.89 m/s ($Fr = 0.608$) and wave height of 60 mm.

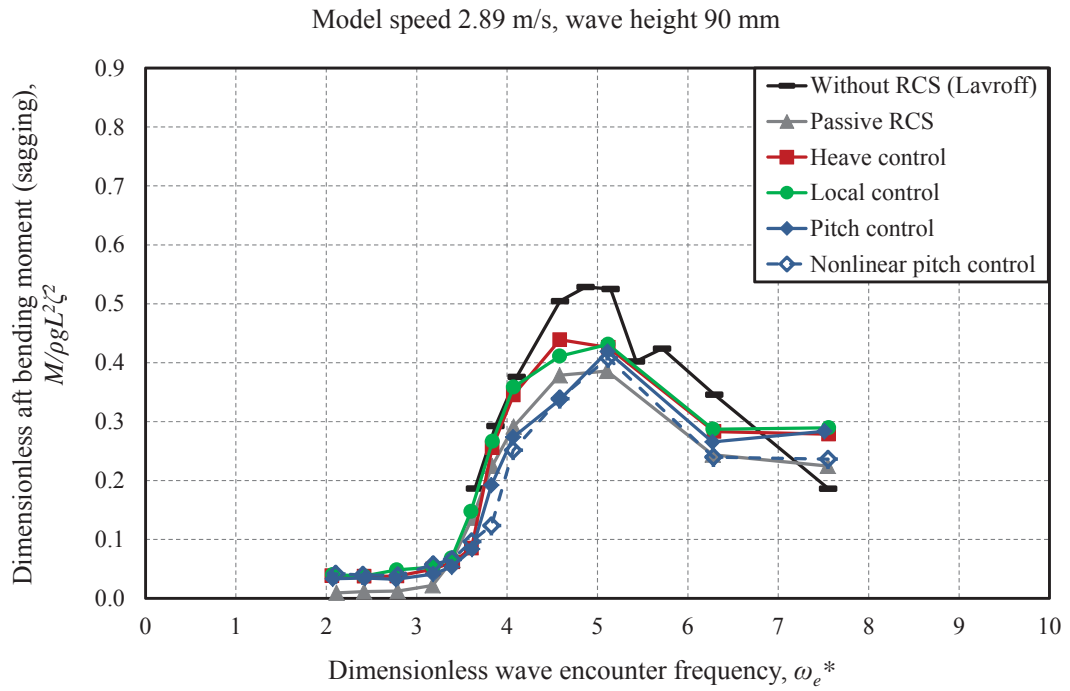


Figure 6.39: Dimensionless demihull slam induced sagging bending moment at the aft segment position at model speed of 2.89 m/s ($Fr = 0.608$) and wave height of 90 mm.

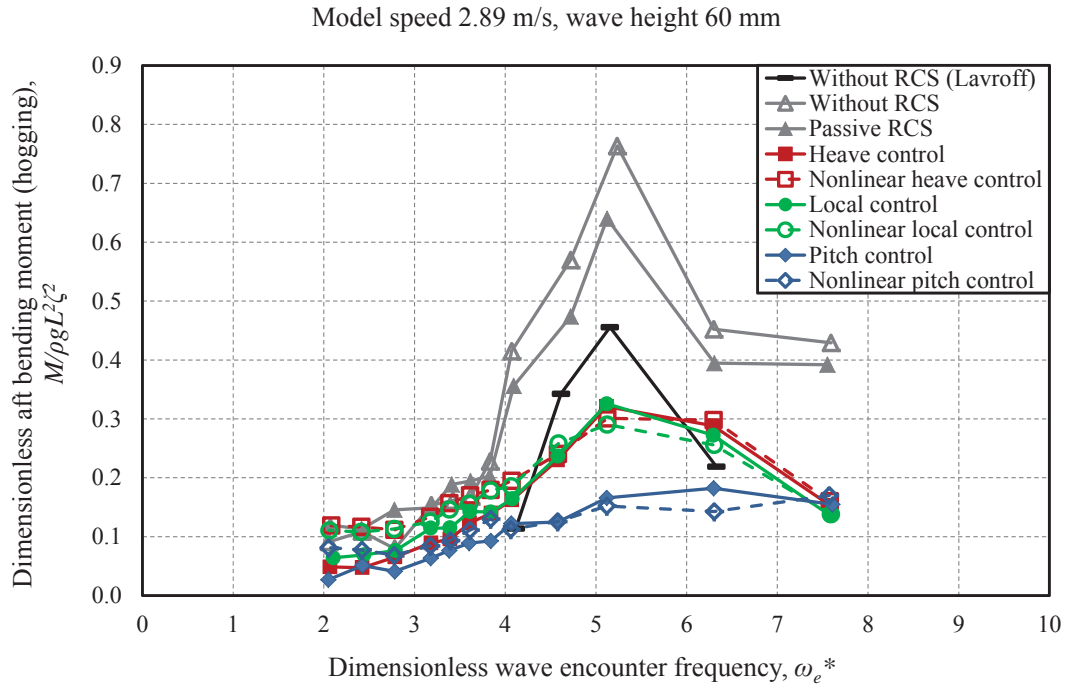


Figure 6.40: Dimensionless demihull slam induced hogging bending moment at the aft segment position at model speed of 2.89 m/s ($Fr = 0.608$) and wave height of 60 mm.

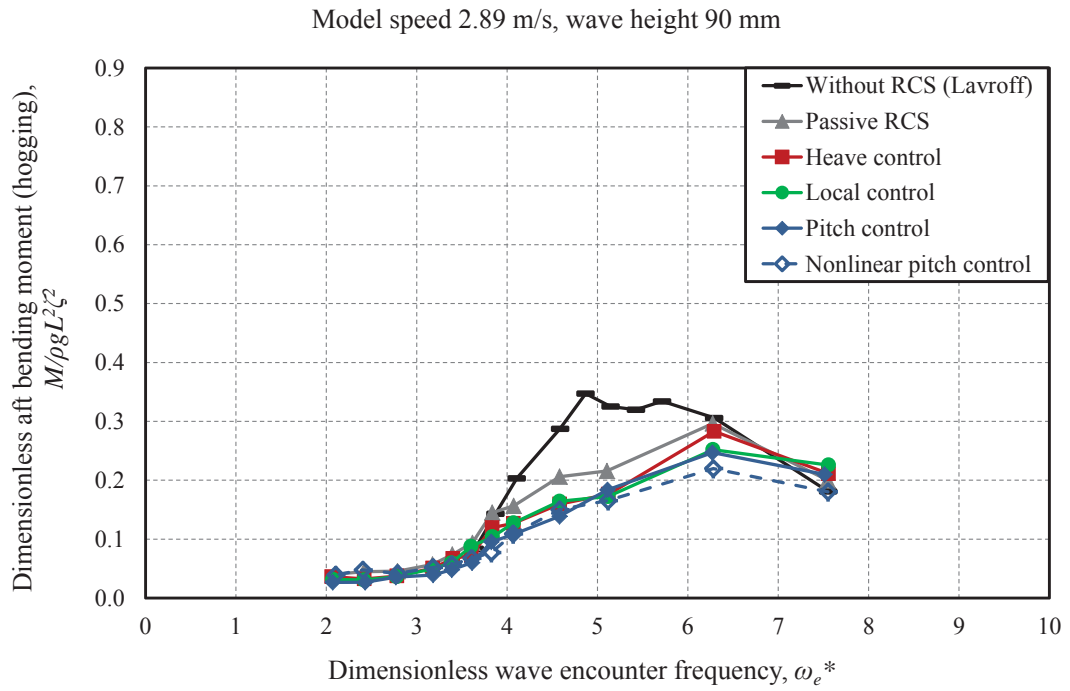


Figure 6.41: Dimensionless demihull slam induced hogging bending moment at the aft segment position at model speed of 2.89 m/s ($Fr = 0.608$) and wave height of 90 mm.

6.4 Slamming kinematics data analysis

The slamming kinematics results for the catamaran model were investigated by measuring the centre bow motion. The centre bow motion at the location of the T-Foil (1990 mm from the transom) relative to the undisturbed incident wave profile during the slamming process was investigated by using the heave and pitch motions data obtained during towing tank tests performed in regular seas. It should be noted that the same analytical procedure as described by Lavroff [133] was applied in order to proceed the slamming kinematic data analysis. Lavroff has developed a set of measurable kinematics parameters to investigate the relative bow immersion, relative bow velocity and the peak sagging slam force in order to identify key relationships for the purposes of providing a numerical slam model. Furthermore, data trends have been identified between the slam force, slam impulse and the maximum relative bow velocity to determine the relationships existing between the kinematics and slam force parameters [3]. Figure 6.42 shows the kinematics parameters developed for the analysis of the relative bow immersion, relative bow velocity and centre bow total force results using data obtained at a model test speed of 2.89 m/s, a wave height of 90 mm, ω_e^* of 6.272 and pitch control mode. Here h_{max} and V_{max} are respectively the maximum relative bow immersion and velocity, h_s and V_s are the immersion and velocity at the instant of the peak slam force, and Δt_s is the integration interval for determining the slam total impulse. Δt_s is defined by the zero crossings points of this force, hence the force is positive over this interval, producing the maximum calculated impulse.

The relative bow immersion was evaluated directly by subtracting the undisturbed wave height from the relative bow height while the relative bow velocity was calculated from the relative bow height using numerical differentiation with respect to time. The centre bow total force and the kinematics data were then analysed in order to investigate the relationship between the wave induced slam forces and the kinematics of the centre bow relative motion. Figures 6.43 to 6.54 show the slamming kinematic results.

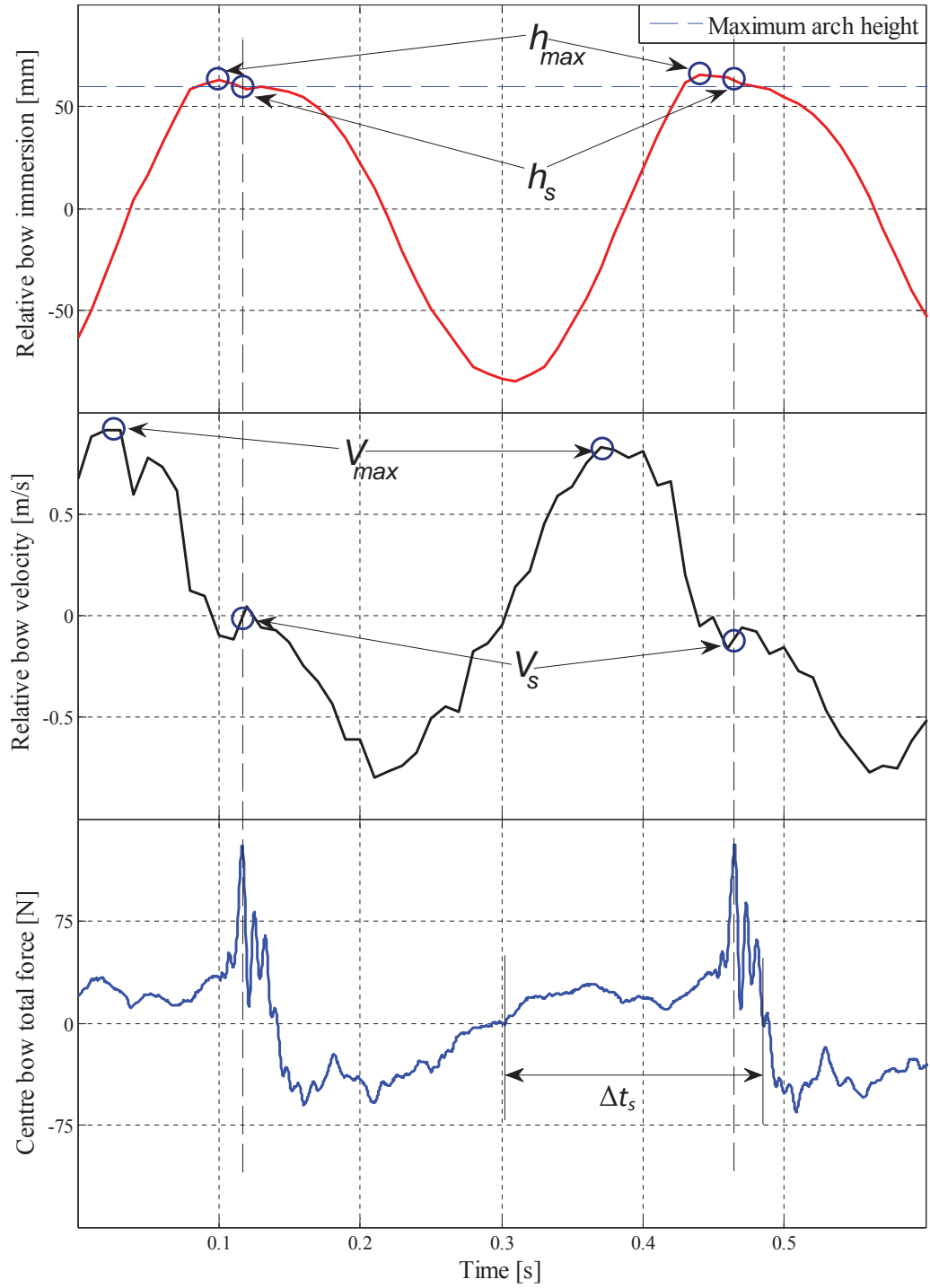


Figure 6.42: Designation of kinematics parameters using data obtained at model speed of 2.89 m/s ($Fr = 0.608$), wave height of 90 mm, ω_e^* of 6.272 and pitch control mode.

6.4.1 Relative bow immersion

Figures 6.43 and 6.44 show the maximum relative bow immersion, h_{max} , at wave heights of 60 mm and 90 mm respectively. Comparing Figures 6.43 with Figure 6.44, it can be seen that increases in the wave height gave rise to larger relative bow immersion, h_{max} . These results show that ride control system does not have significant effect on the maximum relative bow immersion, h_{max} , however the pitch control mode still is the most effective ride control algorithm.

Figures 6.45 and 6.46 show the relative bow immersion at the instant of peak sagging slam force, h_s , at wave heights of 60 mm and 90 mm respectively. As can be seen from Figure 6.45, the relative bow immersion at the instant of the peak sagging slam force, h_s , at a wave height of 60 mm was less than the maximum arch height for all ride control conditions. This indicates that the peak sagging slam force at a wave height of 60 mm occurred prior to the undisturbed water level reaching the top of the arch. Although all ride control conditions demonstrate close results of the relative bow immersion at the instant of peak sagging slam force, the pitch control mode shows the lowest bow immersion at a dimensionless wave encounter frequency between 4 to 6. Comparing Figure 6.45 with Figure 6.46, it is observed that increases in the wave height gave rise to only a modest increase of the relative bow immersion at the instant of peak sagging slam force, h_s , although the relative bow immersion is seen to approach and exceed the maximum arch height when compared to 60 mm waves where the bow immersion remained less than the maximum arch height.

6.4.2 Relative bow velocity

Figures 6.47 and 6.48 show the maximum relative bow velocity, V_{max} , at wave heights of 60 mm and 90 mm respectively. It can be seen from Figures 6.47 and 6.48 that the maximum relative bow velocity was significantly influenced by increase of wave height as further identified by Lavroff [133]. Comparing these results with the slam force results presented in Figures 6.10 to 6.17, the maximum relative bow velocity shows similar trends of variation. It is observed from Figure 6.47 that the ride control system, especially in the pitch control mode, can significantly reduce the maximum relative bow velocity at wave height of 60 mm whereas the results presented in Figure 6.48 demonstrate that ride control system does not have a significant influence on the maximum relative bow velocity at a wave height of 90 mm.

Figures 6.49 and 6.50 show the relative bow velocity at the instant of peak sagging slam force at wave heights of 60 mm and 90 mm respectively. Comparing these results with the results presented in Figures 6.47 and 6.48, it can be seen that the relative bow velocity at the peak sagging slam force was significantly less than the maximum relative bow velocity for most test conditions.

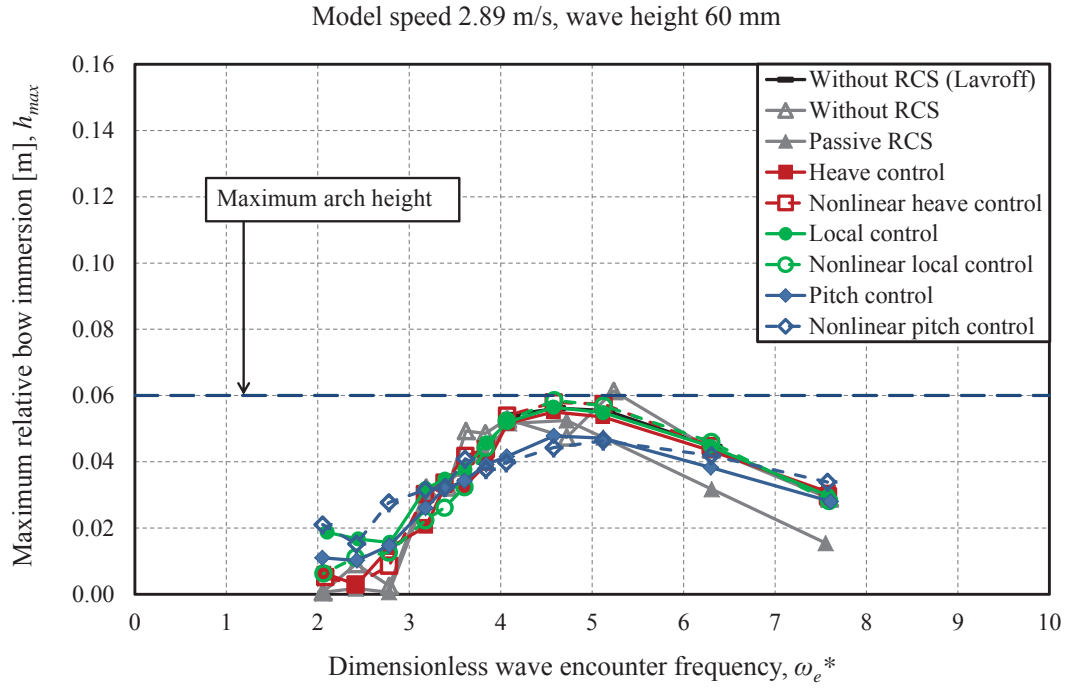


Figure 6.43: Maximum relative bow immersion at model speed of 2.89 m/s ($Fr = 0.608$) and wave height of 60 mm.

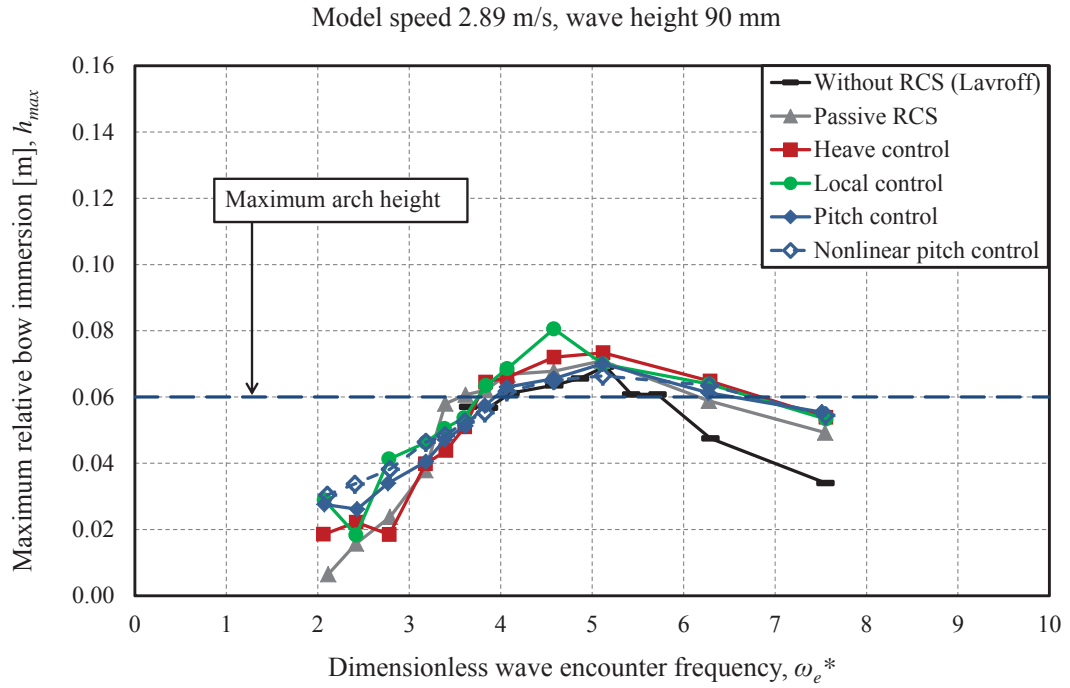


Figure 6.44: Maximum relative bow immersion at model speed of 2.89 m/s ($Fr = 0.608$) and wave height of 90 mm.

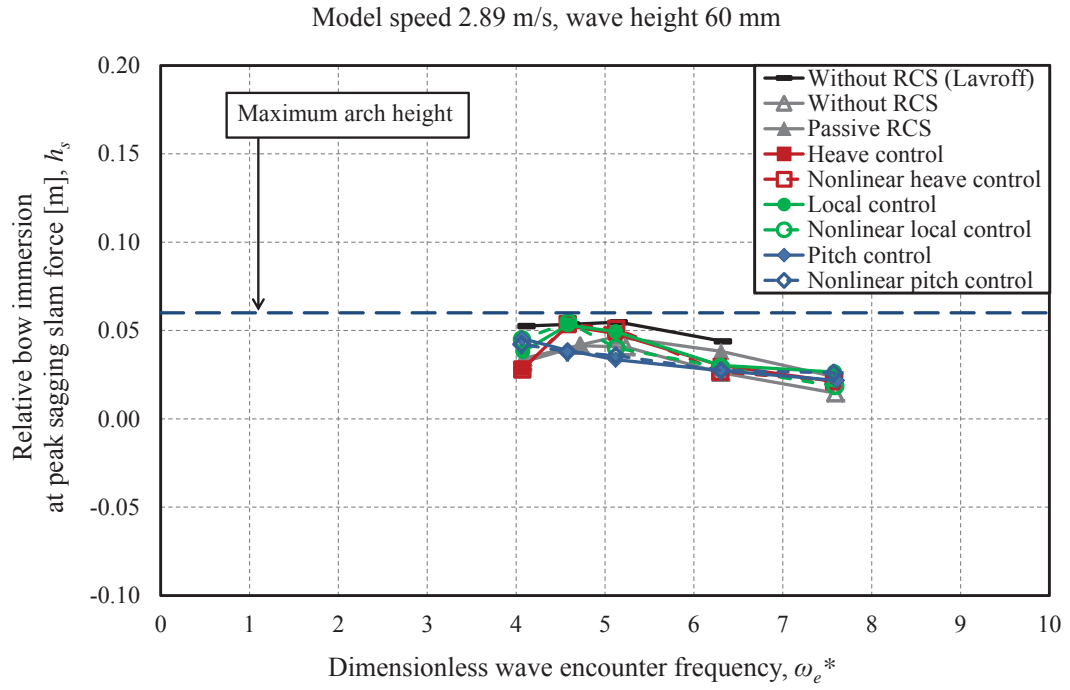


Figure 6.45: Relative bow immersion at the instant of sagging slam force at model speed of 2.89 m/s ($Fr = 0.608$) and wave height of 60 mm.

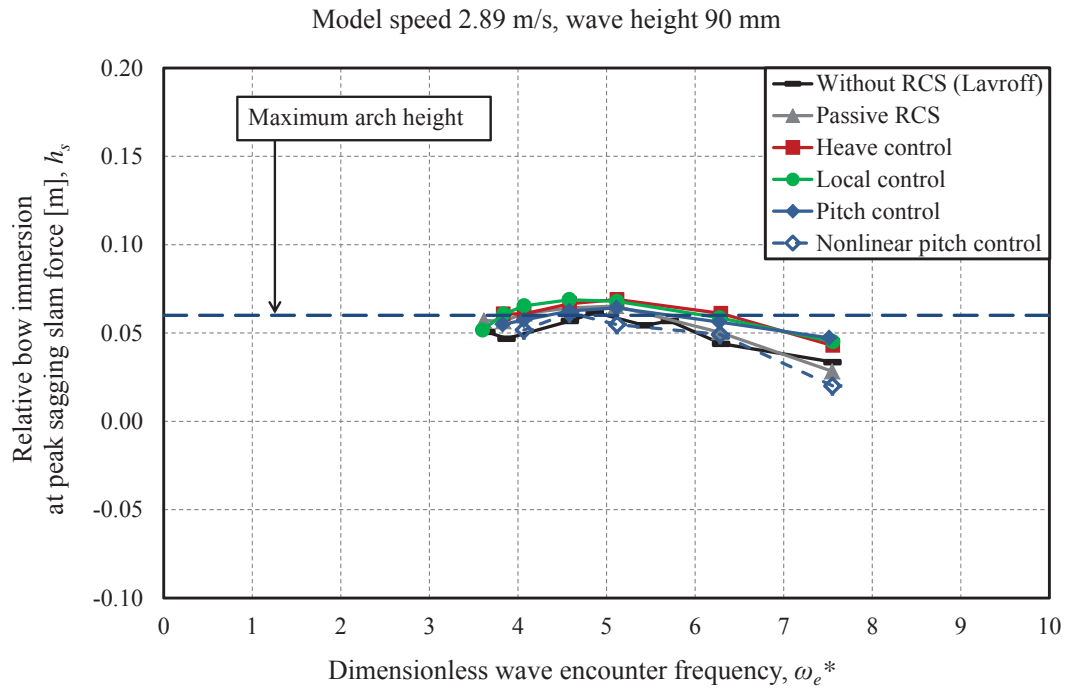


Figure 6.46: Relative bow immersion at the instant of sagging slam force at model speed of 2.89 m/s ($Fr = 0.608$) and wave height of 90 mm.

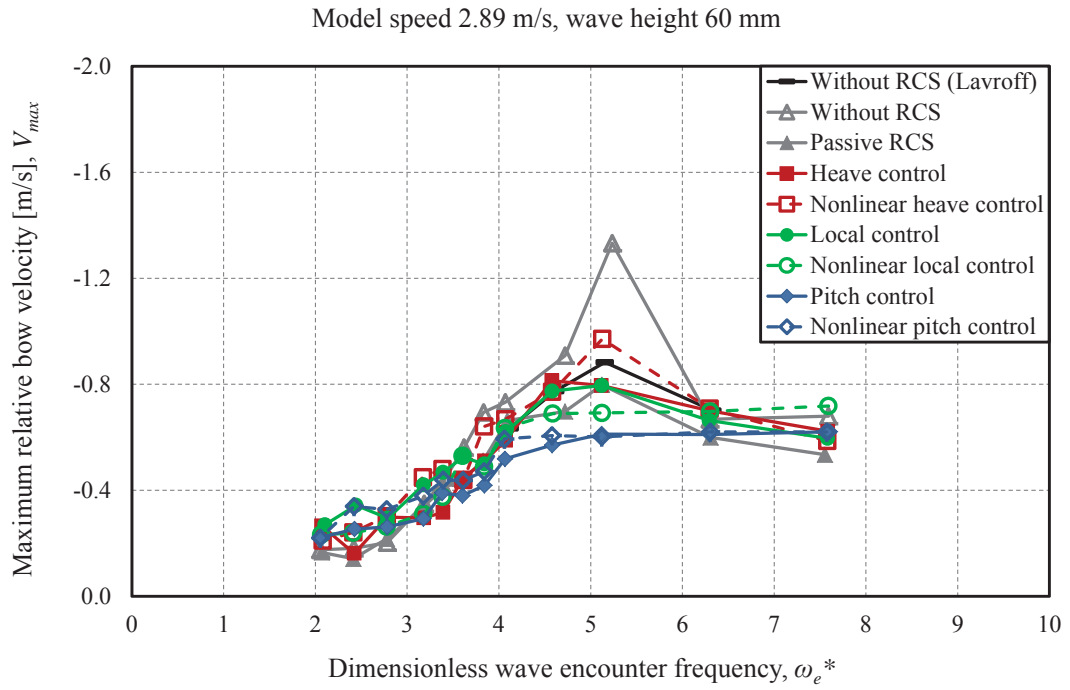


Figure 6.47: Maximum relative bow velocity at model speed of 2.89 m/s ($Fr = 0.608$) and wave height of 60 mm.

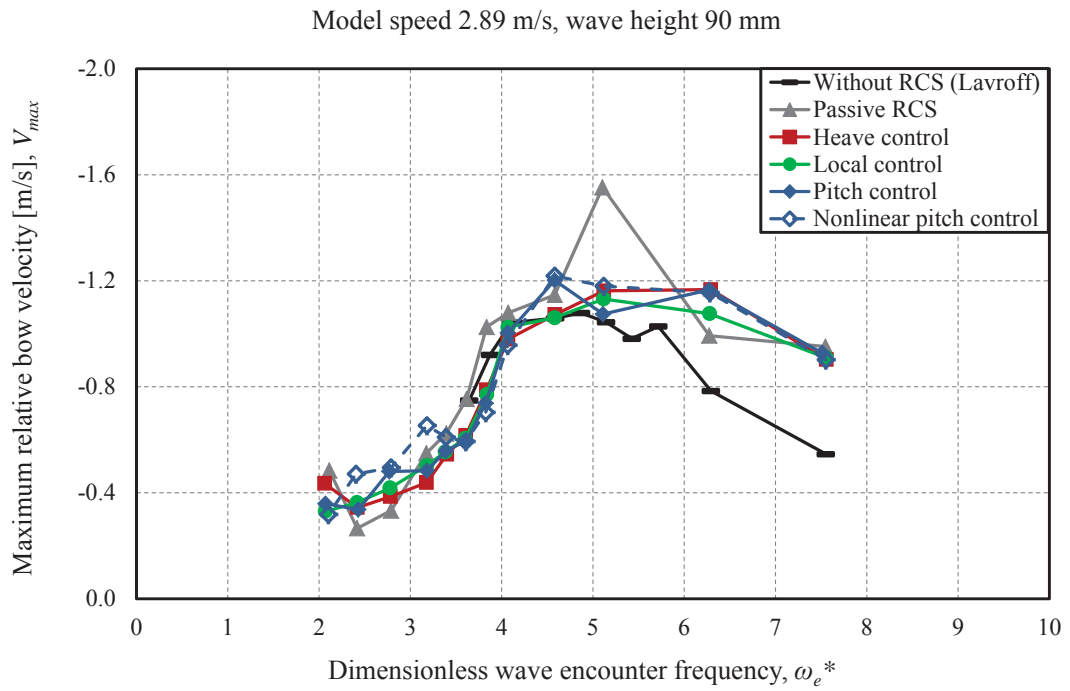


Figure 6.48: Maximum relative bow velocity at model speed of 2.89 m/s ($Fr = 0.608$) and wave height of 90 mm.

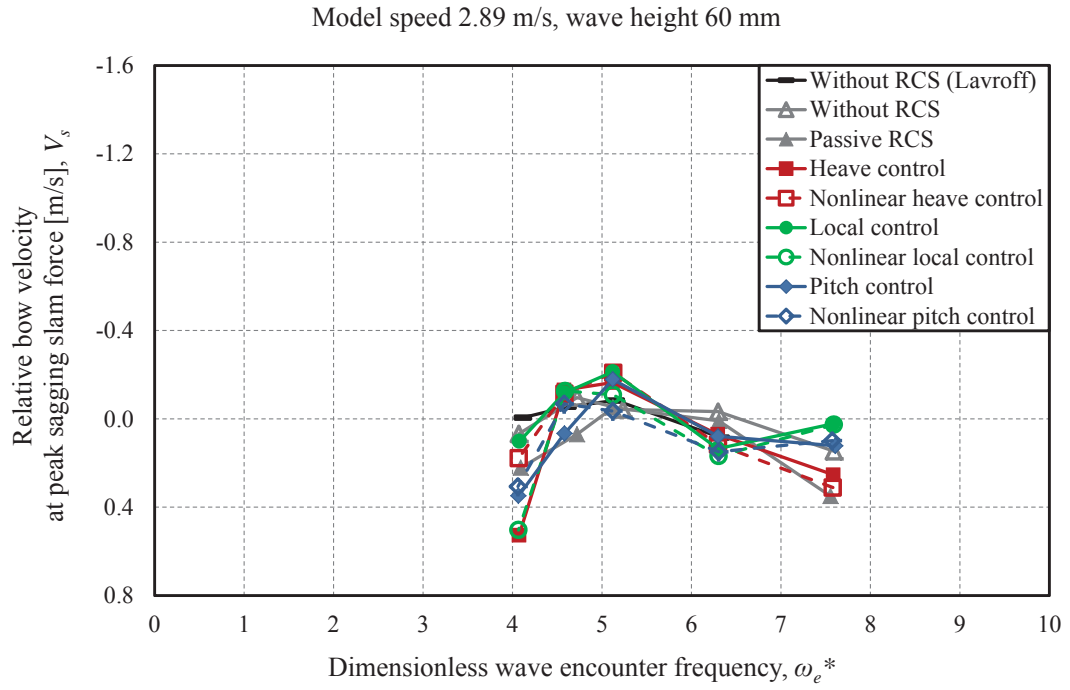


Figure 6.49: Relative bow velocity at the instant of sagging slam force at model speed of 2.89 m/s ($Fr = 0.608$) and wave height of 60 mm.

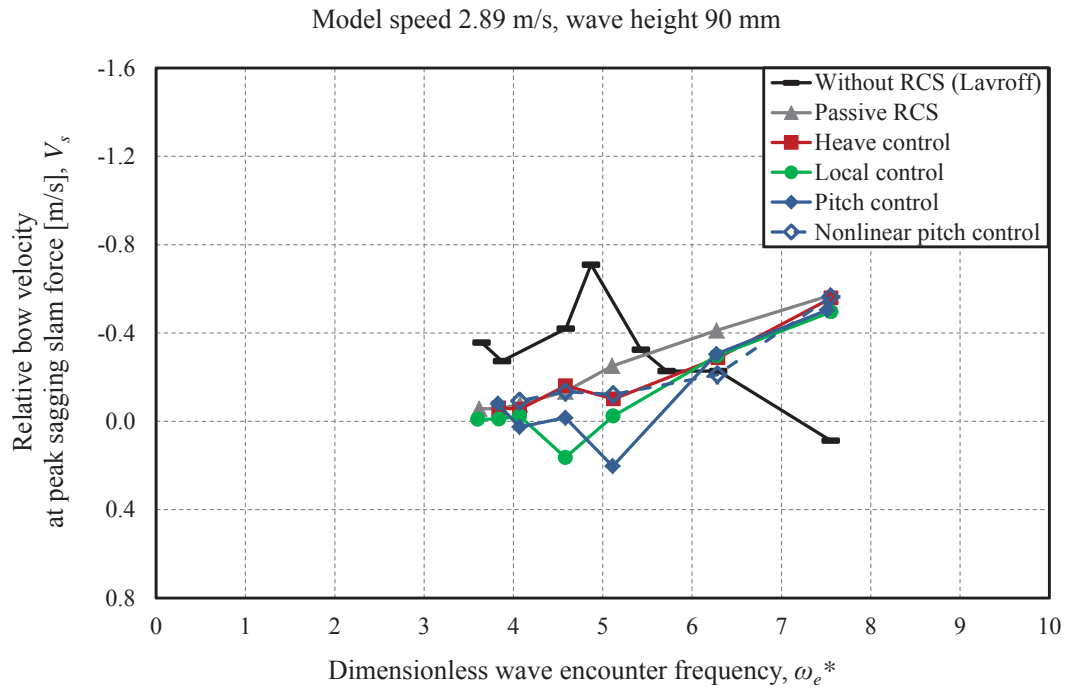


Figure 6.50: Relative bow velocity at the instant of sagging slam force at model speed of 2.89 m/s ($Fr = 0.608$) and wave height of 90 mm.

6.4.3 Slam duration and impulse

An integration time of Δt_s , as shown in Figure 6.42, was considered in order to evaluate the slam impulse. Figures 6.51 and 6.52 show the slam integration time, Δt_s , at wave heights of 60 mm and 90 mm respectively. These results show that the slam impulse integration time was relatively constant for all the test conditions.

And finally Figures 6.53 and 6.54 show the absolute slam impulse, $|I_s|$, at wave heights of 60 mm and 90 mm respectively. Comparing these results with the slam force results presented in Figures 6.10 to 6.17, similarities between the variations with frequency of the slam impulse and the slam force can be observed. Figures 6.53 and 6.54 show that increases in the wave height gave rise to similar variations with frequency of the magnitude of the slam impulse similar to the peak sagging slam forces. It is observed that the peak slam impulses measured during each test condition occurred at approximately the same dimensionless wave encounter frequencies as the peak slam forces due to the small variation of slam integration times as presented in Figures 6.51 and 6.52. As can be seen from Figures 6.53 and 6.54, the ride control system significantly reduced the slam impulse.

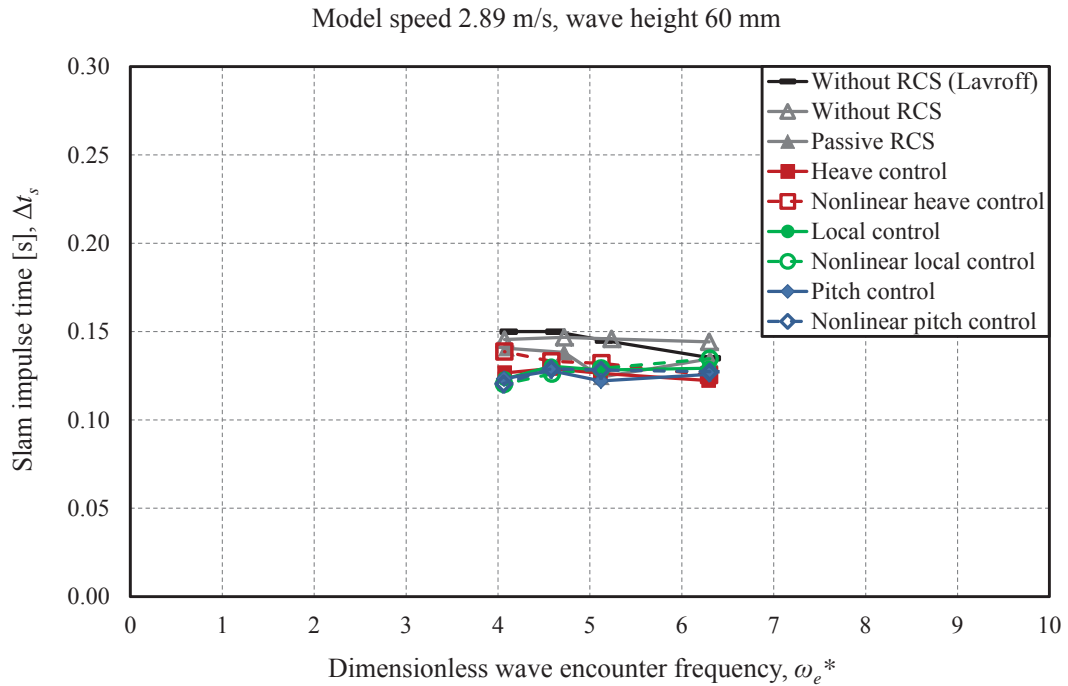


Figure 6.51: Slam impulse integration time at model speed of 2.89 m/s ($Fr = 0.608$) and wave height of 60 mm.

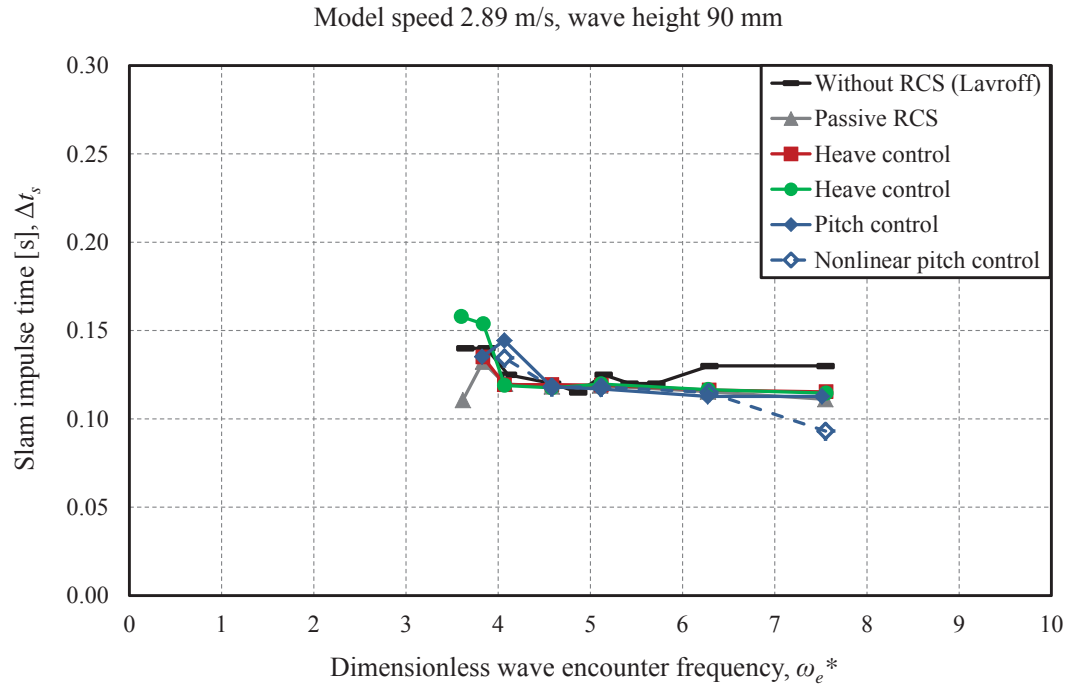


Figure 6.52: Slam impulse integration time at model speed of 2.89 m/s ($Fr = 0.608$) and wave height of 90 mm.

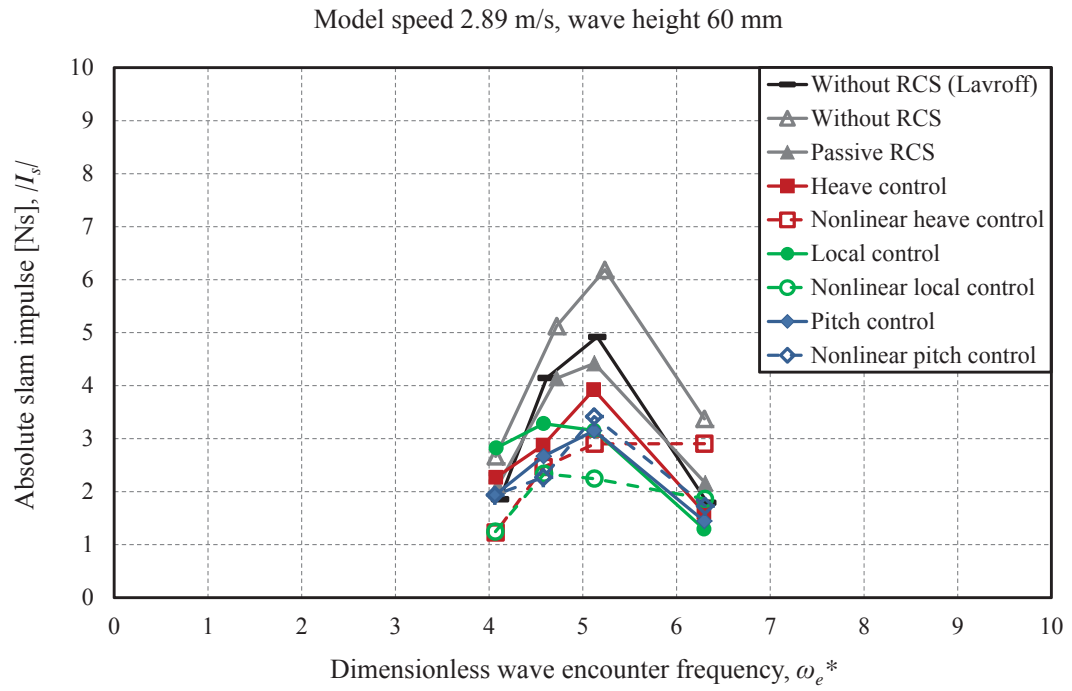


Figure 6.53: Absolute slam impulse at model speed of 2.89 m/s ($Fr = 0.608$) and wave height of 60 mm.

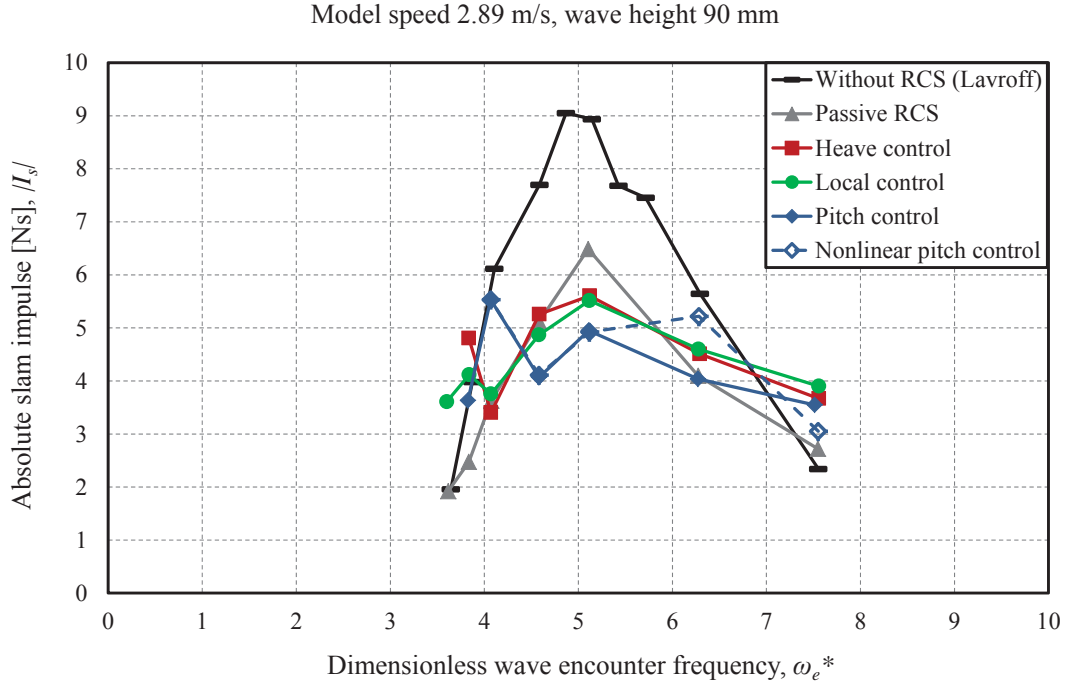


Figure 6.54: Absolute slam impulse at model speed of 2.89 m/s ($Fr = 0.608$) and wave height of 90 mm.

6.5 Slam induced strain energy analysis

It is of interest to investigate the strain energy in the elastic links due to several reasons. The strain energy is indicative of the impact energy associated with the slam. In addition, it is a measure of potential structural damage and also it represents the energy that goes into structural vibration such as whipping.

In order to identify relationships between the centre bow slam impulse, slamming kinematic data and the total strain energy, the slam induced strain energy was evaluated for all model test conditions on the basis of the method developed by Lavroff [3]. As discussed by Lavroff [3], the strain energy of an elastic hinge is $E_\epsilon = M\theta/2$, the work done by the applied moment M , at the angular deflection, θ . Therefore, the strain energy on an elastic hinge with effective stiffness of k_{eff} is $E_\epsilon = M^2/2k_{eff}$. Thus, the strain energy of an elastic hinge with a theoretical stiffness of $k_{th} = EI/l_b$, effective stiffness of k_{eff} , and measured surface strain $\epsilon = Mh/2EI$ can be evaluated by [3]

$$E_\epsilon = \left(\frac{2l_b^2 k_{th}^2}{h^2 k_{eff}} \right) \epsilon^2, \quad (6.1)$$

where l_b is the length of the elastic link beam, k_{th} is the elastic link theoretical stiffness, h is the cross-section height of the elastic link beam, k_{eff} is the effective stiffness of the elastic link and ϵ is the differential strain measured on the elastic link.

The peak strain energy of the centre bow and demihull elastic links were evaluated for all the ride control conditions in order to identify the effect of ride control system on the slam induced strain energy. The average peak sagging slam energy was calculated for each model test run by averaging the peak values of at least five cycles. Figures 6.55 to 6.60 show the peak strain energy of the centre bow and demihull elastic links as a function of wave height and dimensionless wave encounter frequency.

6.5.1 Peak strain energy of the centre bow elastic links

Figures 6.55 and 6.56 show the peak strain energy of the centre bow elastic links at wave heights of 60 mm and 90 mm respectively. As can be seen from Figures 6.55 and 6.56 the peak strain energy of the centre bow elastic links increased with increase of wave height and the influence of wave encounter frequency on the slam induced strain energy was in a manner similar to that observed with the slam impulse presented in Figures 6.53 and 6.54, which was consistent with the results presented by Lavroff [3]. Figures 6.55 and 6.56 show that the pitch control mode was the most effective ride control algorithm to mitigate the strain energy of the centre bow elastic links.

6.5.2 Peak strain energy of the demihull elastic links

Figures 6.57 and 6.58 show the peak strain energy of the demihull elastic links at wave heights of 60 mm and 90 mm respectively. Comparing these figures with Figures 6.55 and 6.56, it can be seen that the demihull elastic hinges produced the highest amount of strain energy in comparison to the centre bow elastic hinges. As can be seen from Figures 6.57 and 6.58, the pitch control mode strongly reduced the strain energy of the demihull elastic links.

6.5.3 Total peak strain energy of the centre bow and demihull elastic links

Finally, Figures 6.59 and 6.60 show the total peak strain energy of the centre bow and demihull elastic links at wave heights of 60 mm and 90 mm respectively. It is observed from Figure 6.59 that the ride control system even in the passive mode can significantly reduce the total strain energy imparted to the catamaran model. Although similar results can be seen at a wave height of 90 mm, presented in Figure 6.60, the pitch control algorithm demonstrates the greatest reduction of the total slam induced strain energy at a wave height of 60 mm and much less at a wave height of 90 mm.

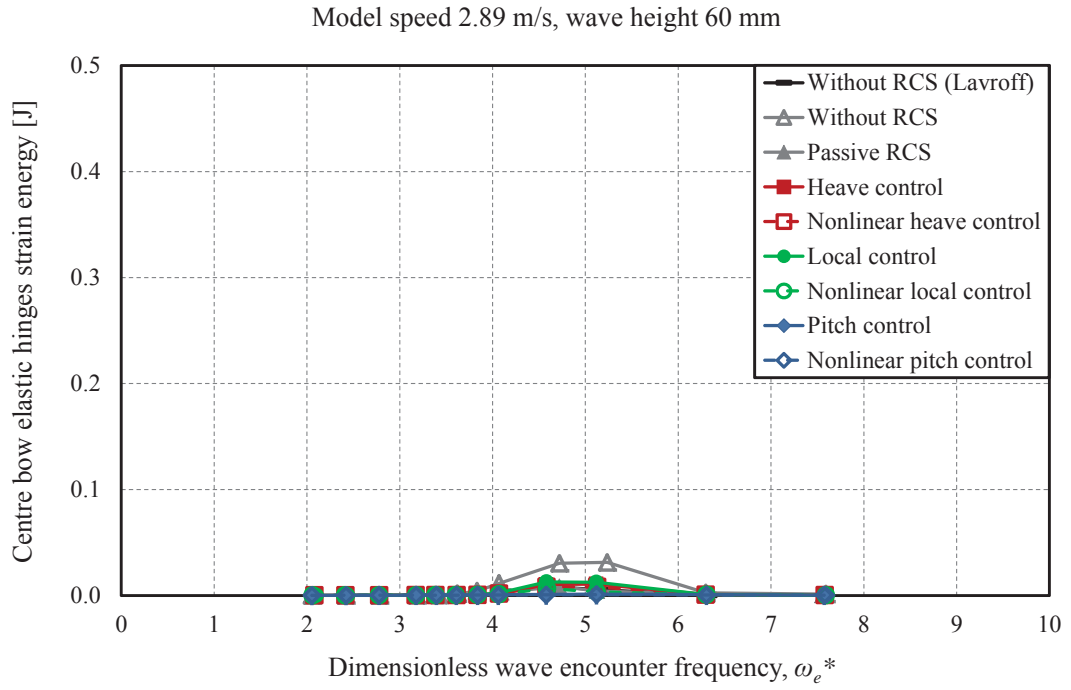


Figure 6.55: Peak strain energy of the centre bow elastic links at model speed of 2.89 m/s ($Fr = 0.608$) and wave height of 60 mm.

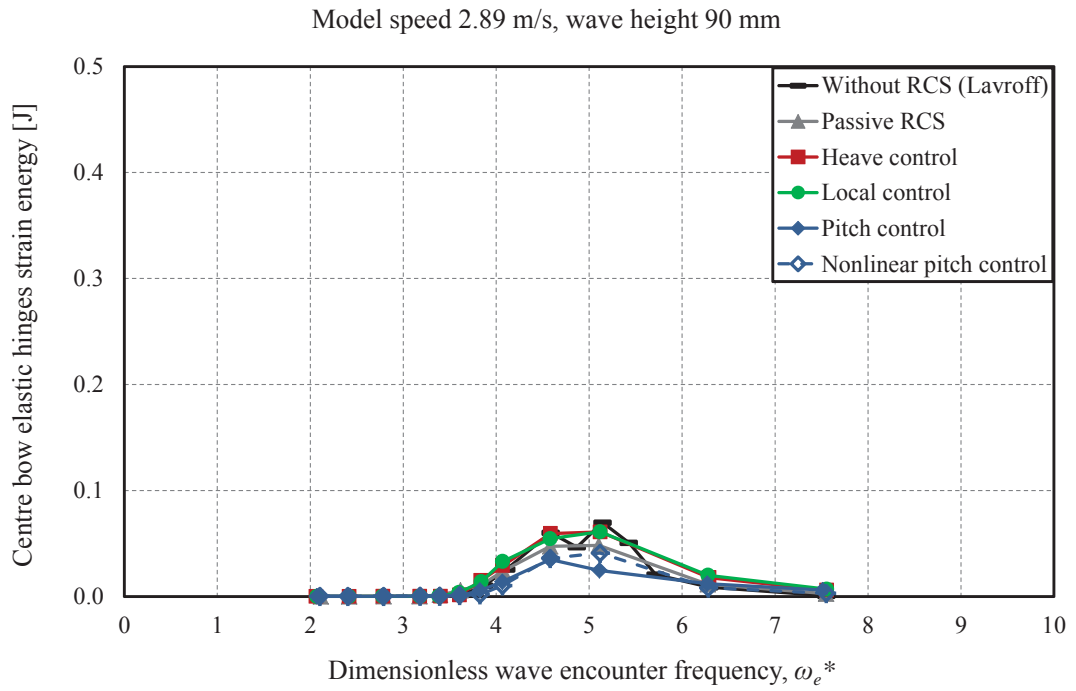


Figure 6.56: Peak strain energy of the centre bow elastic links at model speed of 2.89 m/s ($Fr = 0.608$) and wave height of 90 mm.

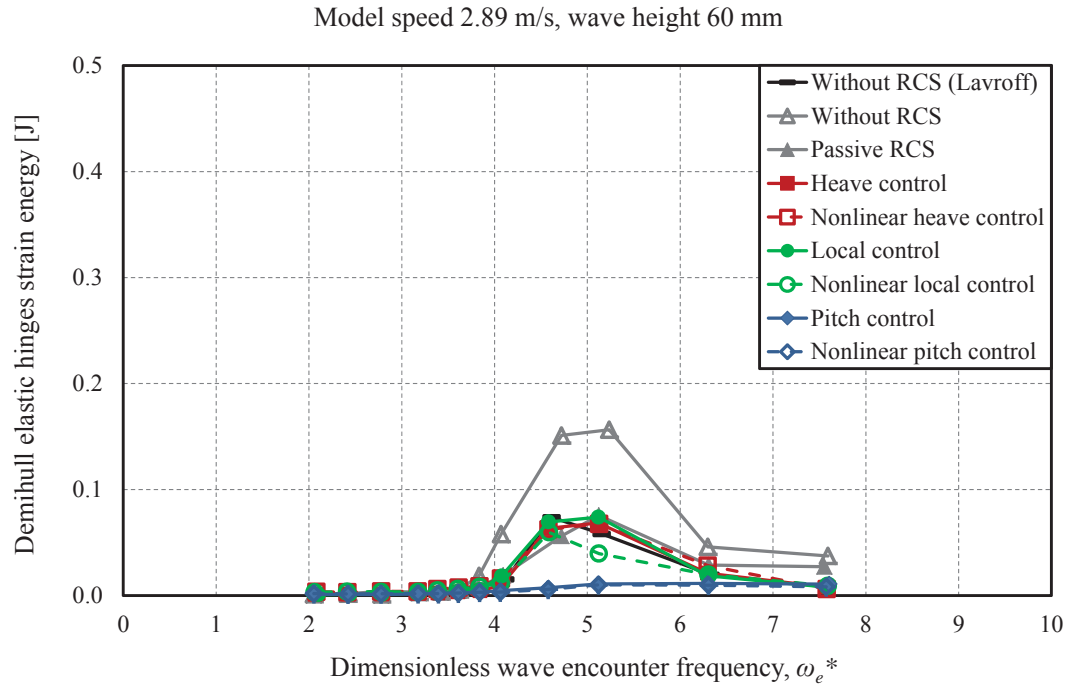


Figure 6.57: Peak strain energy of the demihull elastic links at model speed of 2.89 m/s ($Fr = 0.608$) and wave height of 60 mm.

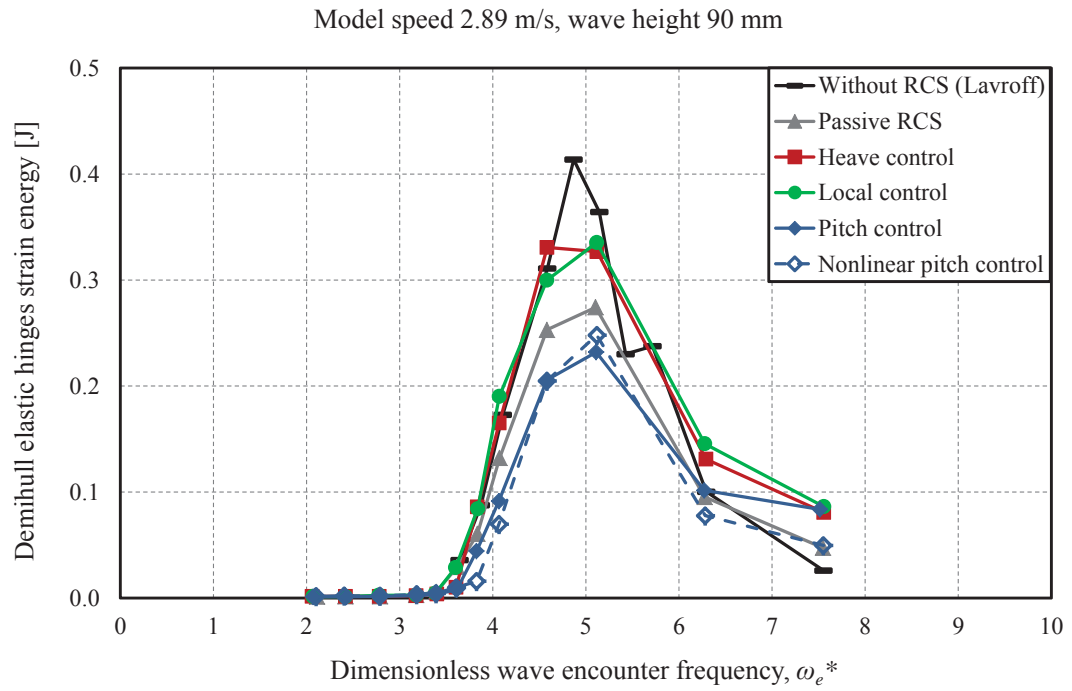


Figure 6.58: Peak strain energy of the demihull elastic links at model speed of 2.89 m/s ($Fr = 0.608$) and wave height of 90 mm.

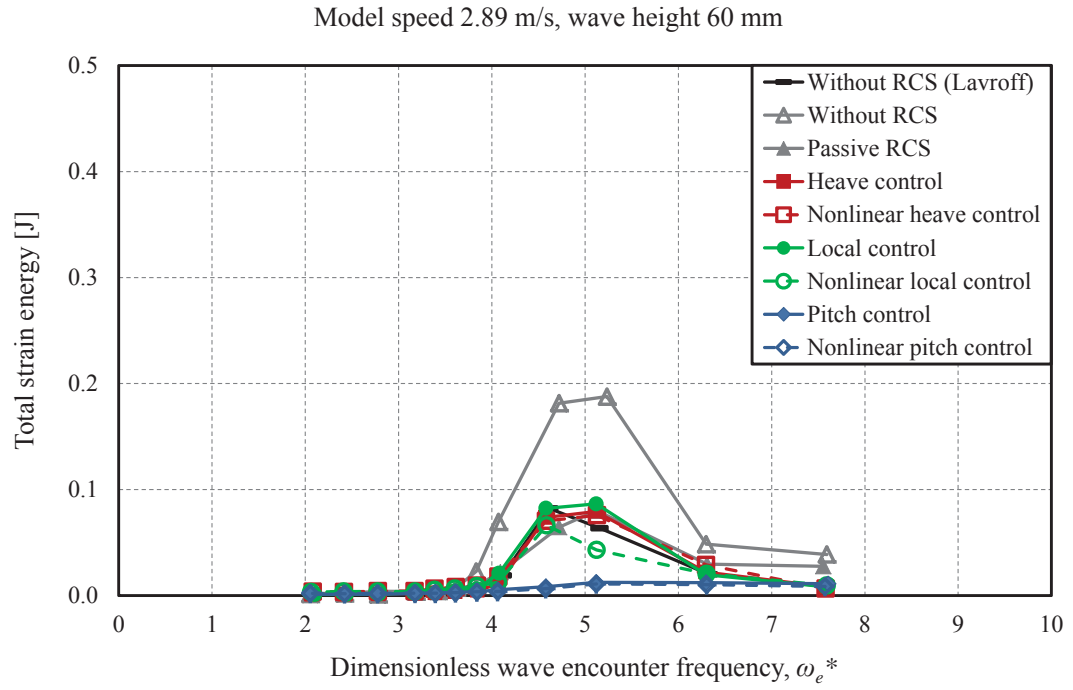


Figure 6.59: Total peak strain energy of the centre bow and demihull elastic links at model speed of 2.89 m/s ($Fr = 0.608$) and wave height of 60 mm.

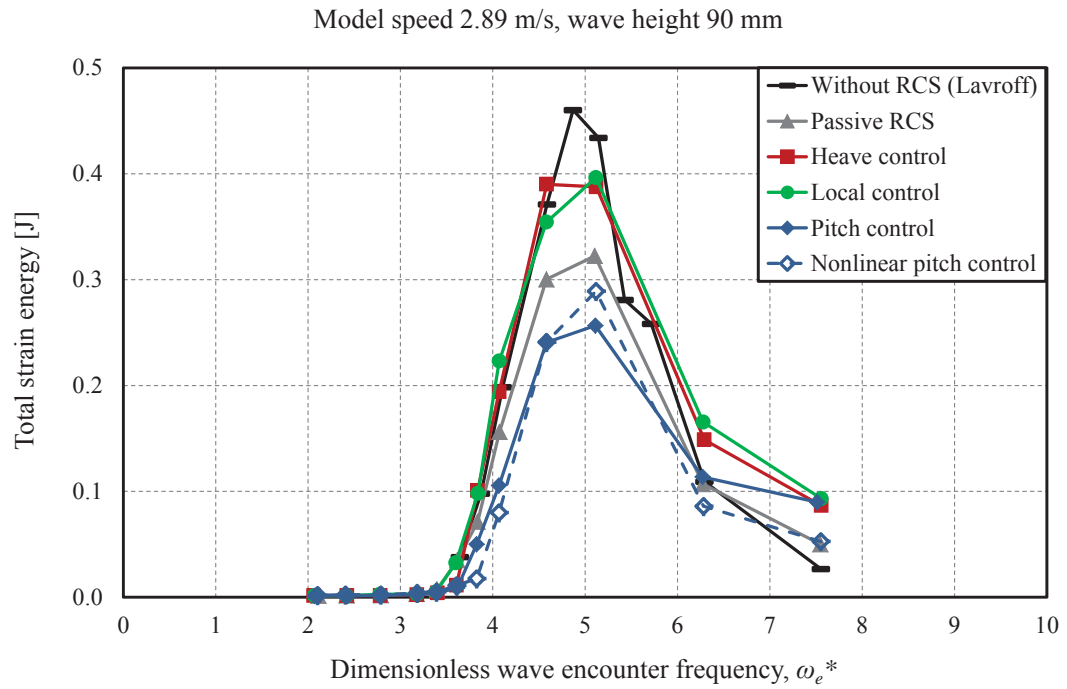


Figure 6.60: Total peak strain energy of the centre bow and demihull elastic links at model speed of 2.89 m/s ($Fr = 0.608$) and wave height of 90 mm.

6.6 Conclusions

The influence of the ride control system on the structural loads and internal forces of the catamaran model was investigated by analysing the data obtained from the strain gauges installed on the model centre bow and demihull links. The model structural loads were further compared with those using a passive control system and without control surfaces fitted.

The results show that a ride control system can reduce the centre bow slam force most strongly in the pitch control mode, where it reduced the peak slam force by about 90% in 60 mm waves at model scale compared to the model with no ride control system.

The centre bow slam forces had a direct association with the model bending moment. Increases in the wave height gave rise to increases in the slam induced bending moments. The demihull slam induced sagging bending moment was on average greater than the hogging bending moment. The peak slam induced demihull bending moments occurred simultaneously with the peak centre bow slam loads. The pitch control mode significantly reduced the slam induced bending moments by around 75% in 60 mm waves at model scale compared to the model with no control system.

The slamming kinematic results for the catamaran model were investigated using the centre bow motion at the location of the T-Foil relative to the undisturbed wave profile. The ride control system did not significantly affect the maximum relative bow immersion. The relative bow immersion at the instant of the peak sagging slam force at wave height of 60 mm was less than the maximum arch height for all ride control conditions indicating that the peak sagging slam force at wave height of 60 mm occurred prior to the undisturbed water level reaching the top of the arch. The relative bow immersion at the instant of peak sagging slam force increased with wave height. Increases in the wave height gave rise to an increase of the maximum relative bow velocity. The relative bow velocity at the instant of the peak sagging slam force was significantly less than the maximum relative bow velocity for most ride control conditions.

The catamaran model strain energy was analysed in order to investigate the energy of the slam force transmitted to the centre bow and demihull elastic links and it was found that most of the slam induced strain energy was transmitted to the demihulls. The peak strain energy of the centre bow and demihull elastic links increased with increase of wave height.

The ride control system, especially when it is running in the pitch control mode, could significantly reduce the total strain energy imparted to the catamaran model. Similar to the previous results, the ride control system at wave height of 90 mm was not as effective as it was at wave height of 60 mm.

In conclusion, the loads response results demonstrate the potential for significant benefit on structural loads reduction being obtained by using improved ride control algorithms. There is thus good potential for mitigating the dynamic structural loads experienced by vessels, an important consideration for future design in particular for vessels operating in severe sea conditions.

Chapter 7

Conclusions

This chapter summaries the main work and major outcomes of this research study and identifies possible future work in this area.

7.1 Summary

In order to investigate the influence of ride control systems on the motions and loads response of a 112 m INCAT high-speed wave-piercing catamaran a 2.5 m hydroelastic segmented catamaran model was equipped with model scale ride control systems. The catamaran model used for this research project was the hydroelastic segmented catamaran model (HSM01) which was designed, built and used by a team at the University of Tasmania.

A check up, calibration, modification of instrumentation and set-up was performed prior to installing the model scale ride control systems into the catamaran model. During the calibration of the centre bow load measurement system it was found that the existing instrumentation needed to be replaced and that the layout of the transverse beams pin joint mounts needed to be revised.

7.1.1 Steady and unsteady lift performance of low Reynolds number T-Foil

Although active ride control systems have been installed on all full scale 112 m INCAT Tasmania wave-piercer catamarans, the 2.5 m hydroelastic segmented model did not originally include an active ride control system in the previous model tests; stern tabs were statically mounted to correct bow up trim at speed and no T-Foil was fitted to the model. Therefore a model scale T-Foil was developed to fit to the model and the fixed tabs were replaced with moveable tabs.

In order to optimise the ride control system and design an appropriate algorithm to control ship motions, it was necessary to effectively activate the control surfaces according to vessel response. On this basis it was decided to investigate the lift and drag characteristics as well

as the frequency response of the model scale, low Reynolds number T-Foil by both static and dynamic tests. As the T-Foil was to be used in the ride control system and its angle of attack was to be changed based on the measured unsteady heave and pitch motion and designated algorithms, it was important to conduct dynamic tests on the T-Foil to investigate its performance prior to installation for testing on the 2.5 m catamaran model. The model scale T-Foil operates at a Reynolds number of approximately 10^5 , has an aspect ratio of 3.6 and a planform which is strongly tapered from the inboard to the outboard end.

Under steady conditions the effect of low Reynolds number on lift performance is not very significant and the results obtained show that the model scale T-Foil performs adequately to act as a control surface on the bow of the 2.5 m catamaran model. Similar results were found at different water flow velocities and it was evident that the T-Foil performance was not diminished due to the effect of low operating Reynolds number. The lift curve slope of the T-Foil was found to be 2.45 per radian, this being 61% of the value for an ideal foil of the same aspect ratio with elliptic load distribution.

It was found that there is a generally moderately good agreement between the temporal variation of experimentally measured lift coefficients and theoretical lift coefficients derived from a combination of the static lift curve slope and the Theodorsen theory [126] for unsteady lift. This leads to the conclusion that it is acceptable to use the Theodorsen theory [126] for the effect of frequency in combination with quasi-static predictions at low frequency to predict the dynamic lift coefficients.

The general conclusion of this investigation was that the unsteady performance of the low Reynolds number model scale T-Foil with a relatively low aspect ratio is adequate for application to scale model towing tank tests. It was therefore anticipated that tank testing of a complete 2.5 m catamaran model fitted with a model RCS system will lead to the identification of the effect of motion control algorithms for reducing ship motions.

7.1.2 Open-loop hull step and frequency responses to control actions in calm water

The first series of towing tank testing of the 2.5 m catamaran model was conducted at the Australian Maritime College (AMC) towing tank in Launceston, Tasmania, with a model displacement of 28.3 kg simulating a full scale displacement of 2545 tonnes. Testing was undertaken in calm water with a primary focus on measuring the responses to the ride control system at a model speed of 2.89 m/s, simulating the full scale speed of 37 knots, while the control surfaces were deflected to various angles with rapid step movements as well as periodic movement. These calm water open-loop test results were intended to assist in the next step of closed-loop active control system.

A specific purpose of these tests was to find an appropriate combination of control movements to excite the model only in heave or only in pitch. This then formed the basis of setting

the gains of the ride control system to implement different control algorithms, such as pitch control, local control and heave control.

Two hydrostatic methods were applied to determine the T-Foil and stern tab responses based on a static load experiment and a hydrostatic prediction and there was close agreement between the two outcomes. This was extended by a dynamic prediction of the response of the moving model based on a two degree of freedom rigid body analysis using strip theory. From this analysis the sinkage and trim of the model in response to the T-Foil and stern tab deflections could be predicted.

The model experiments show that a maximum deflection of the T-Foil from $+15^\circ$ to -15° when it is operated alone can sink the model over a range of about 7 mm and trim it by about 1° . Moreover a maximum deflection of the stern tabs from -18° to $+18^\circ$ lifts the model by a range of about 3.5 mm and trims it by about 1° .

The theoretical calculation of sinkage response to the T-Foil deflection was found to be in good agreement with experimental sinkage, but over predicted the trim response by about 0.1° when the T-Foil was deflected $+15^\circ$.

The deviation between theoretical calculations and experimental responses to the stern tabs deflection is somewhat greater than the results of predicted responses to T-Foil deflections mainly due to the lack of sufficient data to predict the lift-curve derivative of stern tabs for both positive and negative deflections at angles of $\pm 10^\circ$ and a speed of 2.89 m/s.

It was found that a combined T-Foil deflection of $+15^\circ$ and stern tab deflection of $+10^\circ$ produce pure sinkage, while a T-Foil deflection of -8° together with the stern tabs deflection of $+18^\circ$ leads to pure trim. These outcomes indicate the control system gains required to run the ride control system in pure pitch and pure heave control modes.

The frequency response tests show that all four excitation modes produce peak responses at frequencies between 1.00 to 2.00 Hz. A maximum of 18 mm heave range at a frequency of 1.25 Hz can be obtained by excitation of the model with T-Foil deflection at full range of $\pm 10^\circ$. However, the stern tabs full range excitation can only produce 7 mm heave range at a frequency of 1.50 Hz. The T-Foil full range deflection can produce a pitch range of 1.45° at a frequency of 1.00 Hz, moreover the model pitch range of 1.15° can be obtained by the stern tabs full range excitation at a frequency of 1.00 Hz.

This study presented a relatively simple method of predicting open loop control surface step and frequency responses based on a simple strip theory, lumped parameter approach. This method and the test data obtained here formed the basis for the optimisation of closed loop control ride control systems. The results also demonstrated that the ride control system can be operated in different control modes including pitch control and heave control when appropriate closed loop system gains are selected in the appropriate combinations for the control surfaces. These results were important outcomes and formed the basis of a comprehensive model test program to determine the control system gains required to minimise ship motions and associated loads.

7.1.3 Motion responses to waves with feedback ride control

After finalising the open loop step and frequency response tests in calm water and concluding the effect of the ride control system on the 2.5 m catamaran model motions, model testing was carried out in regular waves in order to investigate the influence of different ride control algorithms on the motions response of the model.

Six ideal motion control feedback algorithms were used to activate the model scale ride control system and surfaces in a closed loop control system: heave control, local motion control and pitch control, each in a linear and nonlinear version. The responses were compared with the responses with inactive control surfaces and with no control surfaces fitted.

A series of model tests in head seas at different wave heights and frequencies were conducted for the different control algorithms at the Australian Maritime College (AMC) towing tank in order to measure the heave and pitch motions. The Response Amplitude Operators (RAOs), Response Phase Operators (RPOs) and acceleration response of the model were determined using the heave and pitch data. The range of control surface deflections as well as the phase lag between the control surface deflections and the model motions were evaluated in order to investigate the performance of the model ride control system and the effectiveness of the different control methods.

It was found that the deployment of the T-Foil to a fixed position and acting as a passive control surface provides a modest reduction of the peak heave and pitch motions. The heave and pitch motions were much more strongly reduced with active ride controls. This was most evident with the pitch control modes where the nonlinear control action substantially reduced the pitch RAO by about 50% in 60 mm waves at model scale. The pitch motion was larger when the ride control system was operated in the nonlinear heave control mode, however the nonlinearity did not have significant effect on the pitch motions when applied in the local control mode.

The local vertical acceleration of the model at different longitudinal locations was significantly reduced by the ride control system. As was expected, this reduction was most obvious with pitch control, especially in the nonlinear mode, where it reduced the vertical acceleration near the bow by around 40% in 60 mm waves at model scale. The acceleration response of the catamaran model to the ride control system showed the potential for substantial improvement of passenger comfort and potentially reducing the structural loads, particularly with nonlinear pitch control where motion sickness incidence could be reduced by as much as 50% depending on encountered wave conditions.

The model RCS introduced significant phase lags between detected motions that generate the demand control deflections and the actual control deflections. The consequence of this was that the control action effectively comprised a mixture of damping and stiffness feedback. However, in the case of pitch feedback control the presence of a significant stiffness component in the actual control actions was found to give substantial reductions in RAO in the lower range

of encounter frequency.

The nonlinear control modes produced the maximum T-Foil and stern tab deflection ranges at all wave encounter frequencies. The linear control modes showed maximum range of movement only at the frequency of maximum motion due to operation with fixed control gains. These results thus show that there is significant potential for the application of adaptive gain control depending on the prevailing sea conditions. Also that operation of the controls in nonlinear modes gives generally the best overall improvement of RAO and that the pitch control mode is most effective for improvement of passenger comfort.

7.1.4 Load responses to waves with feedback ride control

The influence of the ride control system on the structural loads and internal forces of catamaran model was investigated by analysing the data obtained from the strain gauges installed on the model centre bow and demihull links. The model structural loads responses were further compared with those using a passive control system and without control surfaces fitted.

The loads results show that a ride control system can reduce the centre bow slam force most strongly in the pitch control mode where it reduced the peak slam force by about 90% in 60 mm waves at model scale compared to the model with no ride control system.

The centre bow slam forces had a direct association with the model bending moment. Increases in the wave height gave rise to increases in the slam induced bending moments. The demihull slam induced sagging bending moment was on average greater than the hogging bending moment. The peak slam induced demihull bending moments occurred simultaneously with the peak centre bow slam loads. The pitch control mode significantly reduced the slam induced bending moments by around 75% in 60 mm waves at model scale compared to the model with no ride control system.

The slamming kinematics results for the catamaran model were investigated using the centre bow motion at the location of the T-Foil relative to the undisturbed wave profile. The ride control system did not significantly affect the maximum relative bow immersion. The relative bow immersion at the instant of the peak sagging slam force at a wave height of 60 mm was less than the maximum arch height for all ride control conditions indicating that the peak sagging slam force at a wave height of 60 mm occurred prior to the undisturbed water level reaching the top of the arch. The relative bow immersion at the instant of peak sagging slam force increased with wave height. Increases in the wave height gave rise to an increase of the maximum relative bow velocity. The relative bow velocity at the instant of the peak sagging slam force was significantly less than the maximum relative bow velocity for most ride control conditions. The ride control system, specially in the pitch control mode, significantly reduced the slam impulse.

The catamaran model strain energy was analysed in order to investigate the energy of the slam force transmitted to the centre bow and demihull elastic links and it was found that most

of the slam induced strain energy was transmitted to the demihulls. The peak strain energy of the centre bow and demihull elastic links increased with increase of wave height.

The ride control system, especially when it is running in the pitch control mode, significantly reduced the total strain energy imparted to the catamaran model. Similar to the previous results, the ride control system at wave height of 90 mm was not as effective as it was at wave height of 60 mm.

In conclusion, the motions and loads response results demonstrated the potential for significant benefit on reduction of motion and structural loads being obtained by using improved ride control algorithms. There is thus good potential for improving passenger comfort, mitigating the dynamic structural loads experienced by vessels and reducing the incidence of motion sickness.

7.1.5 Key outcome

The motions and loads response results obtained during this research study clearly demonstrated that the pitch control mode, particularly in the nonlinear action, is the most effective ride control algorithm to reduce the motions and structural loads. This is an excellent outcome which can be implicated onto full scale vessel design where there are several important design criteria such as improving passenger comfort, enhancing structural efficiency, increasing payload and reducing manufacturing costs due to a reduction in use of materials with the associated weight savings.

7.2 Recommendations for future work

Recommendations for future works are as follows:

- The hydroelastic segmented catamaran model fitted with model scale ride control systems developed during the course of this research study provides significant potential for undertaking future model tests in order to measure the motions and dynamic wave slam forces in oblique sea directions.
- Model tests undertaken at the Australian Maritime College towing tank also present the opportunity for undertaking future model tests in irregular waves at both the Australian Maritime College towing tank and the model test basin.
- As discussed in Section 4.2.2 of Chapter 4, a numerical two Degree of Freedom (DOF) rigid-body simulation was developed to theoretically evaluate the experimental step and frequency response results. Although it was a relatively simple two DOF rigid-body simulation, the results obtained from this numerical simulation demonstrated that it can be a reliable method of predicting open loop control surface step and frequency responses based on a simple strip theory, lumped parameter approach. Therefore it may

be applicable in the future to develop the current numerical method in order to predict the motions response of the catamaran model to closed-loop ride control systems in waves and evaluate the experimental results.

- The accelerations of the catamaran model presented in Chapter 5 were actually dimensionless heave accelerations simply calculated by multiplying the dimensionless heave motion by dimensionless wave encounter frequency squared. Therefore, installation of accelerometers at different locations of the catamaran model for possible future studies would be recommended in order to accurately measure the acceleration of the catamaran model at different locations including centre bow to provide suitable inertia correction to slam loads.
- Further analysis of ride control system through full scale sea trial and numerical computational would be recommended. The motions and loads data at model scale, in conjunction with full scale sea trials data and numerical computations will ultimately assist in the optimisation of motion control system algorithms to improve ship motions, passenger comfort and reduce structural loads.

References

- [1] G. Thomas. *Wave slam response of large high-speed catamarans*. PhD thesis, University of Tasmania, 2003.
- [2] G. Thomas, S. Winkler, M. R. Davis, D. S. Holloway, S. Matsubara, J. Lavroff, and B. French. Slam events of high-speed catamarans in irregular waves. *Journal of marine science and technology*, 16(1):8–21, 2011.
- [3] J. Lavroff. *The slamming and whipping vibratory response of a hydroelastic segmented catamaran model*. PhD thesis, University of Tasmania, 2009.
- [4] G. A. Thomas, M. R. Davis, D. S. Holloway, T. Roberts, S. Matsubara, J. Lavroff, W. Amin, K. R. Chamberlin, and T. W. Dove. Characterisation of slam events of a high-speed catamaran in irregular waves. In *FAST: International Conference on Fast Sea Transportation*, volume 1, pages 177–188, 2009.
- [5] J. Kvålsvold and O. M. Faltinsen. Slamming loads on wetdecks of multihull vessels. In *Proc. Int. Conf. Hydroelasticity in Marine Technology, Trondheim, Norway*. (Ed. Faltinsen), 1994.
- [6] O. D. Okland, T. Moan, and J. V. Aarsnes. Structural response in large twin hull vessels exposed to severe wet deck slamming. In *Proc 7th Int Symp on Practical Design of Ships and Mobile Units (PRADS 98), The Hague, The Netherlands*, volume 2025, 1998.
- [7] E. M. Haugen and O. Faltinsen. Theoretical studies of wetdeck slamming and comparisons with full scale measurements. In *FAST. Proceedings of the 5th International Conference on Fast Sea Transportation. USA: FAST*, 1999.
- [8] <http://www.incat.com.au/>.
- [9] M. R. Davis, D. S. Holloway, and N. L. Watson. Validation of nonlinear wave loads predicted by time domain method in sea trials of an 86m catamaran. In *FAST: International Conference on Fast Sea Transportation*, pages 1–8, 2005.
- [10] G. Davidson, T. Roberts, and G. Thomas. Global and slam loads for a large wavepiercing catamaran design. *Australian Journal of Mechanical Engineering*, 3(2):155–164, 2006.

- [11] T. Roberts, G. Davidson, M. Davis, G. Thomas, and T. Brady. Global loads derivation of large high speed vessels. In *Pacific 2006 international maritime conference*, page 535. Pacific 2006 International Maritime Conference Managers, 2006.
- [12] M. R. Davis, J. R. Whelan, and G. A. Thomas. Computational modeling of wet deck slam loads with reference to sea trials. In *Proceedings of the 9th International Conference on Fast Sea Transportation, FAST*, volume 7, pages 616–624, 2007.
- [13] W. Amin, M. R. Davis, G. Thomas, and D. S. Holloway. Slamming quasi-static analysis of an INCAT 98-m high-speed wave piercing catamaran. In *Proceedings of the international conference for innovation in high speed marine vehicles, Fremantle, Australia*, 2009.
- [14] J. Lavroff, M. R. Davis, D. S. Holloway, and G. A. Thomas. The vibratory response of high-speed catamarans to slamming investigated by hydroelastic segmented model experiments. *International Journal of Maritime Engineering*, 151(4):1–13, 2009.
- [15] J. Lavroff, M. R. Davis, D. S. Holloway, and G. Thomas. Determination of wave slamming loads on high-speed catamarans by hydroelastic segmented model experiments. *International Journal of Maritime Engineering*, 153(A3):185–197, 2011.
- [16] J. Lavroff, M. R. Davis, D. S. Holloway, and G. Thomas. Wave slamming loads on wave-piercer catamarans operating at high-speed determined by hydro-elastic segmented model experiments. *Marine Structures*, 33:120–142, 2013.
- [17] B. J. French, G. A. Thomas, and M. R. Davis. Slam occurrences and loads of a high-speed wave piercer catamaran in irregular seas. *Proceedings of the Institution of Mechanical Engineers, Part M: Journal of Engineering for the Maritime Environment*, page 1475090213497705, 2013.
- [18] J. R. Shahraki, M. R. Davis, B. Shabani, J. AlaviMehr, G. A. Thomas, J. Lavroff, and W. Amin. Mitigation of slamming of large wave-piercing catamarans. In *The 30th Symposium on Naval Hydrodynamics*, pages 1–13, 2016.
- [19] M. R. Davis and D. S. Holloway. Motion and passenger discomfort on high speed catamarans in oblique seas. *International shipbuilding progress*, 50(4):333–370, 2003.
- [20] G. Jacobi, G. Thomas, M. R. Davis, D. S. Holloway, G. Davidson, and T. Roberts. Full-scale motions of a large high-speed catamaran: The influence of wave environment, speed and ride control system. *International Journal of Maritime Engineering*, 154:A143–A155, 2012.
- [21] G. Jacobi, G. Thomas, M. R. Davis, and G. Davidson. An insight into the slamming behaviour of large high-speed catamarans through full-scale measurements. *Journal of Marine Science and Technology*, 19:15–32, 2014.

- [22] A. J. Sørensen and O. Egeland. Ride control of surface effect ships using distributed control. *Modeling, identification and control*, 15(2):65–79, 1994.
- [23] A. J. Haywood, A. J. Duncan, K. P. Klaka, and J. Bennett. The development of a ride control system for fast ferries. *Control Engineering Practice*, 3:695–703, 1995.
- [24] A. J. Haywood, A. J. Duncan, K. P. Klaka, and J. Bennett. The role of simulation in the development of a ride control system for fast ferries. in *Proc. Conf. Maneuvering and Control of Marine Craft*, pages 261–269, 1994.
- [25] A. J. Haywood, B. H. Schaub, and C. M. Pappas. Recent developments in ride control. *Proceedings of FAST 2015, 13th International Conference on Fast Sea Transportation*, 2015.
- [26] S. Esteban, J. M. de la Cruz, , J. M. Giron-Sierra, B. De Andres, J. M. Diaz, and J. Aranda. Fast ferry vertical acceleration reduction with active flaps and T-Foil. in *Proc. IFAC intl. Symp. on Manoeuvring and Control of Marine Craft, Aalborg, Denmark*, pages 233–238, 2000.
- [27] S. Esteban, B. De Andres, J. M. Giron-Sierra, O. R. Polo, and E. Moyano. A simulation tool for a fast ferry control design. in *Proc. IFAC intl. Conf. Control Application in Marine Systems, Glasgow, UK*, 2001.
- [28] J. M. Giron-Sierra, S. Esteban, B. De Andres, J. M. Diaz, and J. M. Riola. Experimental study of controlled flaps and T-Foil for comfort improvement of a fast ferry. in *Proc. IFAC intl. Conf. Control Application in Marine Systems, Glasgow, UK*, 2001.
- [29] J. M. Giron-Sierra, R. Katebi, J. M. de la Cruz, and S. Esteban. The control of specific actuators for fast ferry vertical motion damping. *2002 IEEE international Symposium on Computer Aided Control System Design Proceedings. Glasgow, Scotland, U.K.*, 1:304–309, 2002.
- [30] S. Esteban, B. Andres-Toro, E. Besada-Portas, J. M. Giron-Sierra, and J. M. de la Cruz. Multiobjective control of flaps and T-Foil in high-speed ships. *Proceedings IFAC 2002 World Congress, Barcelona, Spain*, 2002.
- [31] J. M. Giron-Sierra, S. Esteban, J. M. de la Cruz, B. De Andres, and J. M. Riola. Fast ship’s longitudinal motion attenuation with T-Foil and flaps. *Novel Vehicle Concepts and Emerging Vehicle Technologies Symposium*, 2003.
- [32] S. Esteban, J. M. Giron-Sierra, B. Andres-Toro, and J. M. de la Cruz. Development of a control-oriented model of the vertical motions of a fast ferry. *Journal of Ship Research*, 48(3):218–230, 2004.

- [33] J. Aranda, J. M. Diaz, P. Ruiperez, T. M. Rueda, and E. Lopez. Decreasing of the motion sickness incidence by a multivariable classic control for a high speed ferry. *Proceedings of IFAC Conference on Control Applications in Marine Systems 2001 (CAMS 2001). Glasgow, (UK): Pergamon Press*, 2001.
- [34] J. Aranda, , J. M. de la Cruz, and J. M. Diaz. Design of a multivariable robust controller to decrease the motion sickness incidence in fast ferries. *Control Engineering Practice* 13, pages 985–999, 2005.
- [35] J. M. Díaz, S. Dormido, and J. Aranda. Interactive computer-aided control design using quantitative feedback theory: the problem of vertical movement stabilization on a high-speed ferry. *International Journal of Control*, 78(11):813–825, 2005.
- [36] J.M. Díaz. *Identification, modelling and control of the vertical dynamics of a high speed ship*. PhD thesis, University of Spain (UNED), Madrid, Spain, 2002.
- [37] J. M. de la Cruz, P. Perez de Lucas, J. Aranda, J. M. Giron-Sierra, F. Velasco, and A. Maron. A research on motion smoothing of fast ferries. *In Proceedings IFAC Intl. Conf. Control Applications in Marine Systems CAMS2001, Glasgow.*, 2001.
- [38] J. M. de la Cruz, J. Aranda, J. M. Giron-Sierra, F. Velasco, S. Esteban, J. M. Diaz, and B. Andres-Toro. Improving the comfort of a fast ferry, smoothing a ship’s vertical motion with the control of flaps and T-foil. *Control Systems Magazine*, 24(2):47–60, 2004.
- [39] J. M. Giron-Sierra, B. Andres Toro, S. Esteban, J. Recas, E. Besada, and J. M. de la Cruz. Model based analysis of seasickness in a fast ferry. *In Proceedings IFAC MCMC 2003, Gerona, Spain*, 2003.
- [40] J. M. Giron-Sierra, S. Esteban, J. Recas, B. Andres Toro, E. Besada, J. M. de la Cruz, and A. Maron. Distributed electronic system for monitoring and control of a fast ship. *Industrial Electronics Society, 2003. IECON’03. The 29th Annual Conference of the IEEE*, 2003.
- [41] J. M. Giron-Sierra, S. Esteban, B. Andres Toro, J. M. de la Cruz, J. M. Riola, J. Aranda, and F. Velasco. Overview of a research on actuators control for better seakeeping in fast ships. *16th IFAC, Prague, Czech Republic*, 1:620–625, 2003.
- [42] J. M. Giron-Sierra, B. Andres Toro, S. Esteban, J. Recas, E. Besada, J. M. de la Cruz, and A. Maron. First principles modelling study for the development of a 6 DOF motions model of a fast ferry. *Manoeuvring and Control of Marine Craft 2003 (MCMC 2003): A Proceedings Volume from the 6th IFAC Conference, Girona, Spain, 17-19 September 2003*, 2004.

- [43] S. Esteban, J. M. Giron-Sierra, B. Andres-Toro, and J. M. de la Cruz. A computer-based testbed for designing the control of vertical motions of a fast ferry. *Intl. Conf. on Marine Simulation and Ship Maneuvering, MARSIM, Orlando, USA*, pages 79–83, 2000.
- [44] S. Esteban, J. M. de la Cruz, and J. M. Giron-Sierra. Smoothing fast ferry vertical motions: a simulation environment for control analysis. *In Proceedings EUROSIM 2001 Congress, Delft, Netherlands*, 2001.
- [45] S. Esteban, J. M. Giron-Sierra, and J. M. de la Cruz. Nonlinear control design for fast ships. *In Proceedings 13th Intl. Ship Control Systems Symposium, Orlando, USA*, 2003.
- [46] S. Esteban, J. M. Giron-Sierra, J. Recas, J. M. Riola, B. De Andres, and J. M. de la Cruz. Actuators and control design for fast ferry using seasickness analysis. *In Proceedings IFAC Intl. Conf. Control Applications in Marine Systems CAMS2004, Ancona, Italy*, 2004.
- [47] S. Esteban, J. M. Giron-Sierra, B. De Andres, J. M. de la Cruz, and J. M. Riola. Fast ships models for seakeeping improvement studies using flaps and T-foil. *Mathematical and computer modelling*, 41(1):1–24, 2005.
- [48] S. Esteban, J. M. Giron-Sierra, B. De Andres, and J. M. de la Cruz. Frequency domain analysis for prediction of seasickness on ships. *Marine Technology*, 42(4):192–198, 2005.
- [49] L. Wu-Qiang and D. Zhu-Shun. Reducing the vertical motion in waves of round-bildge boat with controllable transom flaps. *Intl. Shipbuilding Progress*, 49(1):37–51, 2002.
- [50] P. D. Sclavounos and H. Borgen. Seakeeping analysis of a high-speed monohull with a motion-control hydrofoil. *J. Ship Research*, 48(2):77–117, 2004.
- [51] M. J. Hughes and K. M. Weems. Time-domain seakeeping simulations for a high speed catamaran with an active ride control system. *11th International Conference on Fast Sea Transportation FAST 2011, Honolulu, Hawaii, USA*, 2011.
- [52] A. A. K. Rijkens, J. A. Keuning, and R. H. M. Huijsmans. A computational tool for the design of ride control systems for fast planing vessels. *International Shipbuilding Progress*, 58(4):165–190, 2011.
- [53] A. A. K. Rijkens, H. M. A. Cleijssen, and J. A. Keuning. On the hydrodynamic performance of an improved motion control device for fast ships. *in Proceedings of the 12th International Conference on Fast Sea Transportation*, 2013.
- [54] M. R. Davis and D. S. Holloway. Passenger motions on equivalent monohulls, catamarans and trimarans. *5th International Conference on High Performance Marine Vehicles, Australia*, 2006.
- [55] M. R. Davis and D. S. Holloway. The influence of hull form on the motion of high speed vessels in head seas. *Ocean Engineering*, 30:2091–2155, 2003.

- [56] D. S. Holloway and M. R. Davis. Ship motion computations using a high Froude number time domain strip theory. *Journal of ship research*, 50:15–30, 2006.
- [57] M. R. Davis, N. Watson, and D. S. Holloway. Measurement of response amplitude operators for an 86 m high-speed catamaran. *Journal of ship research*, 49:121–143, 2005.
- [58] D. S. Holloway and M. R. Davis. Green function solutions for the transient motion of water sections. *Jnl. Ship Res.*, 46(2):99–120, 2002.
- [59] D. S. Holloway and M. R. Davis. Seakeeping computations for semi-SWATHs at high Froude number. *Trans. RINA, paper W303*, 2002.
- [60] R. Zhao. A complete linear time domain analysis for predicting ship motions at high Froude number. *Int. Shipbuilding Prog.*, 44(440):341–361, 1997.
- [61] R. Zhao and J. V. Aarsnes. Numerical and experimental studies of nonlinear motions and loads of a high speed catamaran. In *Proceedings of the Third International Conference on Fast Sea Transportation*, pages 1017–1030, 1995.
- [62] Z. Tao and A. Incecik. Nonlinear ship motion and global bending moment prediction in regular head seas. *International shipbuilding progress*, 47(452):353–378, 2000.
- [63] A. D. Papanikolaou and T. E. Schellin. A three dimensional panel method for motions and loads of ships with forward speed. *Ship Technology Research*, 39(4):147–156, 1992.
- [64] A. Colagrossi and G. Graziani. Time domain analysis of ship motions and loads by boundary-integral equations. *Ship Technology Research*, 49:22–32, 2002.
- [65] A. R. J. M. Lloyd, J. C. Brown, and J. F. W. Anslow. Motions and loads on ship models in regular oblique waves. *RINA Transaction*, 122:20–33, 1980.
- [66] M. K. WU and O. A. Hermundstad. Time-domain simulation of wave-induced nonlinear motions and loads and its applications in ship design. *Marine Structure*, 15(6):561–597, 2002.
- [67] O. A. Hermundstad, J. V. Aarsnes, and T. Moan. Linear hydroelastic analysis of high speed catamarans and monohulls. *Journal of Ship Research*, 43(1):48–63, 1999.
- [68] V. Bertram. Ship motions by a Rankine source method. *Ship Technology Research*, 37(4):143–152, 1990.
- [69] D. Kring, Y. F. Huang, and P. Slavounos. Nonlinear ship motions and wave induced loads by a Rankine method. *Proceedings of the 21st Symposium on Naval Hydrodynamic*, pages 45–63, 1996.
- [70] D. D. Nakos and P. D. Slavounos. Ship motions by a three dimensional Rankine panel method. *Proceedings of the 18th Symposium on Naval Hydrodynamic*, pages 21–39, 1990.

- [71] Y. F. Huang and P. D. Slavounos. Nonlinear ship motions. *Journal of Ship Research*, 42(2):120–130, 1998.
- [72] Y. S. Hong. Heave and pitch motions of SWATH ships. *Journal of Ship Research*, 30(1):12–25, 1986.
- [73] H. S. Chan. Prediction of motion and wave loads of twin hull ships. *Marine Structure*, 6(1):75–102, 1993.
- [74] P. D. Slavounos. The unified slender body theory: ship motions in waves. *15th Symposium of Naval Hydrodynamics*, pages 177–192, 1985.
- [75] H. K. YE and C. C. Hsiung. Time domain motion computations of twin and monohull ships in head seas. *International shipbuilding progress*, 46(445):91–123, 1999.
- [76] R. B. Inglis and W. G. Price. A three dimensional ship motion theory: calculation of wave loading and responses with forward speed. *Transaction RINA*, 124:183–192, 1982.
- [77] M. C. Fang. The effect of the steady flow potential on the motions of a moving ship in waves. *Journal of ship research*, 44(1):14–32, 2000.
- [78] P. A. Bailey, A. D. Hudson, W. G. Price, and P. Temarel. Theoretical and experimental validation of the seakeeping characteristics of high speed mono and multi-hulled vessels. *Fifth International Conference on Fast Sea Transportation*, pages 429–441, 1999.
- [79] E. Ballard, S. X. DU, D. Hudson, and P. Temarel. Motions of mono and multi-hulled vessels in regular waves using a partly non-linear time domain method. *Sixth International Conference on Fast Sea Transportation*, pages 219–234, 2001.
- [80] D. Hudson, A. F. Molland, W. G. Price, and P. Temarel. Seakeeping performance of high speed catamaran vessels in head and oblique waves. *Sixth International Conference on Fast Sea Transportation*, pages 247–258, 2001.
- [81] D. X. Zhu and M. Katory. A time domain prediction method of ship motions. *Ocean Engineering*, 25(9):781–791, 1998.
- [82] J. F. O’Hanlon and M. E. McCauley. Motion sickness incidence as a function of frequency and acceleration of vertical sinusoidal motion. *Aerospace Medicine*, pages 3566–3569, 1974.
- [83] J. A. Ewing and G. J. Goodrich. The influence on ship motions of different wave spectra and the ship length. *Trans. RINA*, 109:47–63, 1967.
- [84] S. Brizzolara. Hydrodynamic analysis of interceptors with CFD methods. *Proceedings of the 7th International Conference on Fast Sea Transportation*, 2003.
- [85] A. J. Haywood. Motion control systems. *Aquamarine 95*, 1995.

- [86] A. J. Haywood, A. J. Duncan, and K. P. Klaka. The development of a ride control system for a surface effect ship. *Interim report, Rep. CMST-C94-9, Curtin Univ., Perth, Australia*, 1994.
- [87] A. J. Duncan, A. J. Haywood, and K. P. Klaka. Ride control system (final report). *Rep. AMECRC-93-CP3, Curtin Univ., Perth, Australia*, 1993.
- [88] C. R. Swanton, A. J. Haywood, and B. H. Schaub. Simulation, an essential tool in the design of motion control systems. in *Proc. FAST 99*, pages 73–81, 1999.
- [89] R. P. Dallinga. Hydrodynamical aspects of the design of fin stabilizers. *Trans. RINA*, pages 189–200, 1993.
- [90] T. I. Fossen. *Guidance and Control of Ocean Vehicles*. John Wiley, New York, 1994.
- [91] T. J. Fossen. *Marine Control Systems*. Marine Cybernetics AS, Trondheim, 2002.
- [92] B. De Andres Toro, S. Esteban, J. M. Giron-Sierra, M. Jesus, and J. M. de la Cruz. Modelling the motion of a fast ferry with the help of genetic algorithms. *Proc. 3rd IMACS MATMOD, Vienna*, 2000.
- [93] J. Recas, J. M. Giron-Sierra, S. Esteban, B. Andres Toro, J. M. de la Cruz, and J. M. Riola. Autonomous fast ship physical model with actuators for 6 DOF motion smoothing experiments. In *Proceedings IFAC Intl. Conf. Control Applications in Marine Systems CAMS2004, Ancona, Italy*, 2004.
- [94] M. Ryle. Smoothing out the ride. *The Motor Ship*, pages 23–26, 1998.
- [95] M. A. Abkowitz. The effect of antipitching fins on ship motion. *Soc. Nav. Archit. Mar. Eng., Trans*, 62:210–252, 1959.
- [96] G. P. Stefun. Model experiments with fixed bow antipitching fins. *J. Ship Research*, 3(2):15–23, 1959.
- [97] F. J. Velasco, T. M. Rueda, E. Lopez, and E. Moyano. Pitch movement QFT control to reduce the msi of a turbo ferry. In *Proceedings IFAC Intl. Conf. Control Applications in Marine Systems CAMS2004, Ancona, Italy*, 2004.
- [98] J. H. Vugts. Pitch and heave with fixed and controlled bow fins. *Intl. Shipbuilding Progress*, 15(3):191–215, 1967.
- [99] K. M. Ochi. Hydroelastic study of a ship equipped with an antipitching fin. *SNAME Trans.*, 69:281–337, 1961.
- [100] M. Besso and Y. Kyojuka. On the ship motion reduction by antipitching fins in head seas. *Naval Hydrodynamics, Fifteenth Symposium: Seakeeping Problems, Hull-propeller Interactions, Nonlinear Free-surface Problems, Frontier Problems in Hydrodynamics*, pages 109–118, 1985.

- [101] J. Avis. Use of antipitch foil to reduce added resistance of a yacht in waves. *Marine Tech.*, 28(1):15–22, 1991.
- [102] T. Kawazoe, S. Nishikido, and Y. Wada. Effect of fin area and control methods on reduction of roll motion with fin stabilizers. *Bulletin of the MESJ*, 22(1):25–32, 1994.
- [103] T. Ulusoy. *State-space modelling and optimal control of ship motions in a seastate*. PhD thesis, Massachusetts Institute of Technology, 2006.
- [104] J. F. Tsai, J. L. Hwang, S. W. Chau, and S.K. Chou. Study of hydrofoil assistance arrangement for catamaran with stern flap and interceptor. *6th International Conference on Fast Sea Transportation FAST 2001, Southampton, UK*, 2001.
- [105] M. R. Davis, N. L. Watson, and D. S. Holloway. Measurement and prediction of wave loads on a high-speed catamaran fitted with active stern tabs. *Marine Structures*, 17(7):503–535, 2004.
- [106] N. Smith. Identification of ride control system parameters for a 98 metre high speed catamaran. BE (Hons) Thesis, University of Tasmania, 2013.
- [107] J. Bell, T. Arnold, J. Lavroff, and M. R. Davis. Measured loading response of model motion control stern tabs. *Royal Institution of Naval Architects. Transactions. Part A. International Journal of Maritime Engineering*, 155:A1–A7, 2013.
- [108] T. Shore. Frequency response of motion controls on INCAT catamaran model. BE (Hons) Thesis, University of Tasmania, 2011.
- [109] M. R. Davis, N. L. Watson, and D. S. Holloway. Wave response of an 86m high speed catamaran with active T-foils and stern tabs. *Transactions of the Royal Institution of Naval Architects, paper W302. International Journal of Maritime Engineering*, 145(A2):15–34, 2003.
- [110] M. R. Davis and D. S. Holloway. Effect of sea, ride controls, hull form and spacing on motion and sickness incidence for high speed catamarans. *Proceedings of FAST 03, 7th International Conference on Fast Sea Transportation*, 3:1–10, 2003.
- [111] J. AlaviMehr, M. R. Davis, and J. Lavroff. Low Reynolds number performance of a model scale T-Foil. *International Journal of Maritime Engineering*, 157:A175–A187, 2015.
- [112] J. AlaviMehr, M. R. Davis, J. Lavroff, D. S. Holloway, and G. A. Thomas. Response of a high-speed wave-piercing catamaran to an active ride control system. *International Journal of Maritime Engineering, In Press*, 2016.
- [113] J. AlaviMehr, J. Lavroff, M. R. Davis, D. S. Holloway, and G. A. Thomas. Motion response to waves of a high-speed catamaran with feedback ride control. *Submitted*, 2016.

- [114] J. AlaviMehr, J. Lavroff, M. R. Davis, D. S. Holloway, and G. A. Thomas. An experimental investigation of ride control algorithms to mitigate wave impact loads on high-speed catamarans. *Submitted*, 2016.
- [115] S. Matsubara. *Ship motions and wave-induced loads on high speed catamarans*. PhD thesis, University of Tasmania, 2011.
- [116] R. Eppler. *Airfoil design and data*. Springer-Verlag, Berlin ; New York, 1990.
- [117] J. Colman, J. M. Di Leo, J. S. Delnero, M. Martinez, U. Boldes, and F. Bacchi. Lift and drag coefficients behaviour at low Reynolds number in an airfoil with gurney flap submitted to a turbulent flow. Part 1. *Latin American Applied Research*, 38:195–200, 2008.
- [118] M. V. Ol, L. Bernal, C. K. Kang, and W. Shyy. Shallow and deep dynamic stall for flapping low Reynolds number airfoils. *Experiments in Fluids*, 46:883–901, 2009.
- [119] A. Pelletier and T. J. Mueller. Low Reynolds number aerodynamics of low-aspect-ratio, thin/flat/cambered-plate wings. *Journal of Aircraft*, 37:825–832, 2000.
- [120] K. Taira and T. Colonius. Three-dimensional flows around low-aspect-ratio flat-plate wings at low Reynolds numbers. *Journal of Fluid Mechanics*, 623:187–207, 2009.
- [121] A. Barton. *Friction, roughness and boundary layer characteristics of freshwater biofilms in hydraulic conduits*. PhD thesis, University of Tasmania, 2007.
- [122] J. Lavroff, M. R. Davis, D. S. Holloway, and G. Thomas. The vibratory response of high-speed catamarans to slamming investigated by hydroelastic segmented model experiments. *International Journal of Maritime Engineering*, 151:1–11, 2009.
- [123] J. Lavroff, M. R. Davis, D. S. Holloway, and G. Thomas. Determination of wave slamming loads on high-speed catamarans by hydroelastic segmented model experiments. *International Journal of Maritime Engineering*, 153:A185–A197, 2011.
- [124] J. Lavroff, M. R. Davis, D. S. Holloway, and G. Thomas. Wave slamming loads on wavepiercer catamarans operating at high-speed determined by hydro-elastic segmented model experiments. *Marine Structures*, 33:120–142, 2013.
- [125] H. Glauert. *The elements of aerofoil and airscrew theory*. University Press, Cambridge Eng., 1947.
- [126] D. H. Hodges and G. A. Pierce. *Introduction to structural dynamics and aeroelasticity*. Cambridge University Press, Cambridge, England ; New York, 2002.
- [127] O. M. Faltinsen. *Hydrodynamics of High-Speed Marine Vehicles*. Cambridge University Press, Cambridge ; New York, 2005.

- [128] D. S. Holloway. *A high Froude number time domain strip theory applied to the sea-keeping of semi-SWATHs*. PhD thesis, University of Tasmania, 1998.
- [129] N. Salvesen, E. Tuck, and O. Faltinsen. Ship motions and sea loads. *Transactions of Society of Naval Architects and Marine Engineers*, 78:250–287, 1970.
- [130] J. N. Newman. *Marine hydrodynamics*. MIT press, 1977.
- [131] F. Yang. Experimental investigation on wave propagation in Australian Maritime College (AMC) towing tank and the performance of resistance and acoustic wave probes in static and moving condition. BE (Hons) Thesis, University of Tasmania, 2015.
- [132] J. F. O’Hanlon and M. E. McCauley. Motion sickness incidence as a function of frequency and acceleration of vertical sinusoidal motion. *Technical Report Memorandum 1973-1, Human Factors Research Inc.*, 1973.
- [133] J. Lavroff and M. R. Davis. Slamming kinematics, impulse and energy transfer for wave-piercing catamarans. *Journal of Ship Research*, 59(3):145–161, 2015.